POLITECNICO

MILANO 1863

Department of Aerospace Science and Technology
Doctoral Program in Aerospace Engineering

NON-IDEAL STEADY SUPERSONIC FLOWS

Doctoral dissertation of:
Davide Vimercati

Supervisor:
Prof. Alberto Guardone

Co-supervisor:
Prof. Alfred Kluwick

Tutor:
Prof. Luigi Vigevano

The Chair of the Doctoral Program:
Prof. Pierangelo Masarati

January 2019 – Cycle XXXI

ACKNOWLEDGEMENTS

This work has been realised thanks to the support and dedication of many people.

Firstly, I would like to thank my supervisor, Prof. Alberto Guardone. You gave me the opportunity to join your research group and to learn from and with you. With your knowledge, enthusiasm and patience, you have been an extraordinary guide. Thanks for the constant encouragements, for each precious advice, for each enlightening discussion in your office. Thanks for supporting me in difficult times and for celebrating with me the results of our efforts. You have taught me much more than gasdynamics.

I am indebted to my co-supervisor, Prof. Alfred Kluwick, a giant of non-classical gasdynamics. Your outstanding work has inspired much of my research. Thank you for welcoming me at TU Wien, where I spent five amazing months, and for your insightful suggestions and generous guidance. This experience has contributed to my professional and personal growth. It has been a real privilege to collaborate with you.

I would like to thank Prof. Andrea Spinelli and Prof. Giacomo Persico for sharing some of their very broad knowledge of turbomachinery with me, and the reviewers, Prof. Edward Cox and Prof. Paolo Luchini, for the time devoted to evaluating this dissertation. Your ideas, remarks and suggestions have been very helpful and have contributed to the quality of this work.

I acknowledge the finantial support of the European Research Council, which enabled this research under the ERC Consolidator Grant 2013, project NSCHOCK 617603.

Many thanks to all my colleagues and friends at Politecnico di Milano. Barbara, Gianluca, Giulio, Luuc, Marta, thanks for providing such a nice environment for learning and research, and for the time spent together outside the university as well. The same goes to the mates of the Energy Department: Alessandro, Camilla, Giorgia and Simone. I would like to spend a few more words of gratitude for Gianluca, with whom I had the pleasure to work closely for more than one year. We faced great challenges together and helped each other through. Thanks also to Bob, Mauro, Tito and Vanessa for contributing to making our lunches a "cultural" moment.

I am very grateful to my closest friends, Cristina, Paolo, Sara, Andrea, Emanuele, Matteo, Riccardo, who have helped me taking important decisions, often listened to my complaints and cheered me up.

I want to express my deepest gratitude to Silvija, a turning point in my life. For encouraging me to give my best, for your understanding and your patience, for believing in me and being there for me. Simply thank you for all.

Saving the best for last, I wish to thank my parents and my brother for the unconditional support I received during these years. Thank you for making all this possible.

Davide Vimercati
Milano, January 2019

SUMMARY

Compressible flows in the neighbourhood of the vapour-liquid saturation curve and critical point are found in many technical applications, including hybrid rocket engines, power cycles, natural gas extraction and pharmaceutical processes. Operating at such high densities entails phenomena that have no counterpart in the dilute, ideal-gas regime which is often assumed in the theory of gasdynamics. Examples are: the increase of the speed of sound in adiabatic expansions, the increase of the Mach number across oblique shock waves and its reduction along isentropic expansions, the admissibility of rarefaction shocks, the reflection of oblique shocks as Prandtl-Meyer fans. At the basis of these gasdynamic effects is the peculiar thermodynamic behaviour of the substance which cannot be properly modelled, neither quantitatively nor qualitatively, using the ideal gas law. To emphasise their non-ideal thermodynamic nature, effects such as those mentioned above are referred to as non-ideal effects.

Progress in the field of Non-Ideal Compressible Fluid Dynamics (NICFD)—the branch of fluid mechanics devoted to the study of compressible flows whose behaviour deviates from that predicted by the ideal-gas model—will enable the improvement of existing industrial processes and machinery exploiting substances close to their critical point, as well as support the design of new ones. The contribution to NICFD given by the study documented herein is related to steady supersonic flows and in particular to those developing in confined geometries. In this context, a fundamental research question motivates the investigation: What are the physically admissible flow configurations in the non-ideal regime and how do they differ from those arising in ideal-gas flows? Also, what are the necessary conditions to observe a specific configuration, i.e. how is the flow field linked to the properties of the substance and the boundary conditions? These are key aspects in technical applications involving non-ideal supersonic flows and questions that this work will address.

To achieve the research goal, a thorough theoretical analysis of steady supersonic flows in the non-ideal gasdynamic context is performed. Efforts concentrate on three main complementary areas: flows in converging-diverging nozzles, flows around compressive/rarefactive ramps, shock reflections and interactions. These are elementary building blocks of general internal supersonic flows. A fully non-linear analysis is carried out to complement and extend previous studies relying on asymptotic expansion theory or numerics. The converging-diverging nozzle is the prototype of a variable area duct, the flow past ramps exemplifies the abrupt deflection of a supersonic stream (of course important for external flows as well), performed, e.g., though a shock wave which will be reflected by an opposing wall or interact with another incident shock. It is assumed that thermoviscous effects can be neglected and thus that the flow can be fully described by the Euler equations coupled with the Rankine-Hugoniot relations at points of jump discontinuity. On the other hand, an arbitrary equation of state of the fluid is allowed. In particular, the usual constraints of classical gasdynamics on the curvature of the isentropes in the pressure–density or pressure–specific volume plane, which ultimately determines the qualitative evolution of the flow, are dropped.

Flows in converging-diverging nozzle are studied using the quasi-one-dimensional approxima-

tion. A novel analytical approach sheds light on the connection between a general adiabatic flow field and the underlying local isentropic-flow features, including their qualitative change across shock waves. Isentropic flows are first classified to ease the construction and inspection of shocked flows, which are computed by means of shock-fitting techniques. The idea of functioning regime is introduced to analyse the response of the system to variations in the outlet pressure at fixed stagnation conditions at the nozzle inlet, i.e. fixed reservoir conditions, assuming the nozzle to be connected to an upstream reservoir. Extending previous results available in the scientific literature, ten different functioning regimes are singled out which include the ideal-gas-like scenario and nine non-ideal configurations. Key features of the non-ideal functioning regimes are the inclusion of rarefaction shocks to achieve arbitrarily large Mach numbers and the possibility of up to three shocks in nozzles with subsonic outflow. Then, the transition between the different classes of flow is investigated and ultimately a thermodynamic map of the reservoir conditions resulting in each functioning regime is produced. This map enables the identification of the thermodynamic region of interest for the observation of non-ideal nozzle flows.

To investigate supersonic flows past ramps, a general theory of oblique waves, i.e. waves generating a deflection of the supersonic stream, is developed. The analysis of oblique waves is performed by resorting to the concept of wave curves. The wave curve is the set of downstream states connected to a given upstream state by means of an oblique wave. Inspection of the wave curve structure for different upstream states reveals that, in addition to the conventional configuration consisting of compression oblique shocks and expansion Prandtl-Meyer fans, non-ideal configurations exist which include rarefaction shocks, compression fans and composite waves (combinations of shocks and fans). The connection between the upstream state and the configuration of the wave curve is explained and depicted through the use of thermodynamic maps. Further research in the context of oblique waves concerns oblique shocks featuring a non-ideal increase of the Mach number, which are systematically examined providing necessary conditions for their occurrence, and the extension of the typical shock angle–deflection angle diagram of oblique shocks with an additional half-plane corresponding to Prandtl-Meyer fans.

Then, the developed theory of oblique waves is applied to the investigation of shock reflections and interactions in non-ideal gasdynamics. The attention is placed on the neighbourhood of the singularity point where oblique waves intersect. Thanks to non-ideal effects such as the Mach number increase across shock waves, rarefaction shocks, compression fans and composite waves, the classical picture of shock reflections and interaction is enriched with new flow patterns. An overview of the most relevant configurations is given.

Finally, a realistic application where non-ideal supersonic flows occur is considered, namely the expansion in the turbine of an Organic Rankine Cycle (ORC) power plant. Focusing on supersonic stator vanes, firstly the flow is forced into a converging-diverging channel and then, at the trailing edge of each blade, oblique waves are generated due to the rotation imposed by the finite thickness of the trailing edge or to accommodate post-expansion or compression. The oblique waves generated on the pressure side of the blade propagate towards the suction side of the neighbouring blade and undergo a reflection when they impinge on the blade wall. The influence of non-ideal effects on the blade design and on the off-design performance is studied by means of numerical simulations. Advantages and disadvantages of operating in the non-ideal gasdynamic regime are discussed for a few specific examples, nonetheless providing more general considerations.

CONTENTS

x

CHAPTER 1

INTRODUCTION

1.1 Non-Ideal Compressible Fluid Dynamics

In the continuum-mechanical description of fluids, the general laws of conservation of mass, momentum and energy must be supplemented with constitutive relations characterizing the material properties of the fluid. For both constituents in this description, the level of approximation that is considered satisfactory dictates the choice of a model. For example, in many applications the effects of viscosity, heat conduction, chemical reactions, relaxation, etc. can often be neglected, thus resulting in simpler governing equations. Alongside, the selection of a suitable constitutive model is crucial, inasmuch as dynamical evolution of a fluid is largely influenced by its material properties. This issue is addressed here in the context of compressible fluid dynamics, namely the branch of fluid mechanics devoted to the study of fluid flows in the compressible regime.

Compressible fluid dynamics makes extensive use of the ideal-gas model (see, e.g. Hayes, 1958; Zucrow & Hoffman, 1976; Landau & Lifshitz, 1987; Thompson, 1988; Anderson, 2010), which is undeniably the simplest but nonetheless powerful, thanks to the capability of providing closed-form expressions in many occasions. For most applications involving dilute-gas flows, the ideal-gas model is reasonably accurate, both qualitatively and quantitatively. However, a significant departure from ideal-gas behaviour is observed when approaching the vapour-liquid saturation curve and critical point (see for example the generalised compressibility chart, e.g. in Callen 1985), i.e. when intermolecular attractive forces come into play, as first noticed by van der Waals (1873). In this (broad) range of thermodynamic conditions, the predictions of the ideal-gas model can be not only quantitatively, but also qualitatively, inaccurate (see, e.g., Menikoff & Plohr, 1989). It is in this context that Non-Ideal Compressible Fluid Dynamics (NICFD) is established as a branch of fluid mechanics studying the motion of compressible fluids not obeying ideal-gas thermodynamics. That is, the term non-ideal does not refer to dissipative mechanisms such as internal friction or heat conduction or to chemical reactions; rather it indicates the occurrence of phenomena that cannot be captured or predicted if the ideal-gas model is used to describe the substance.

NICFD encompasses fluid flows in the two-phase (vapour-liquid) region and in what is often referred to as the dense-gas region, by contrast with the dilute-gas region where the ideal-gas model is accurate. The boundary between ideal and non-ideal compressible fluid dynamics can be formalized by introducing the thermodynamic quantity Γ, known as the fundamental derivative of gasdynamics (Thompson, 1971), which is given by

$$\Gamma = \frac{v^3}{2c^2}\left(\frac{\partial^2 P}{\partial v^2}\right)_s = 1 + \frac{c}{v}\left(\frac{\partial c}{\partial P}\right)_s, \tag{1.1}$$

where P is the pressure, v the specific volume, s the specific entropy and $c = \sqrt{(\partial P/\partial \rho)_s}$ is the speed of sound, in which $\rho = 1/v$ is the density. The fundamental derivative is a non-dimensional measure of the curvature of isentropes in the (P, v)–plane or, equivalently, of the sound speed variation with pressure along an isentropic transformation. The fundamental derivative is so called because of its paramount role in delineating the dynamic behaviour of compressible flows in diverse areas, including shock-wave theory (Bethe, 1942; Weyl, 1949; Zel'dovich, 1946; Thompson & Lambrakis, 1973; Cramer & Sen, 1986, 1987; Cramer, 1989b; Cramer & Crickenberger, 1991; Kluwick, 2001; Zamfirescu et al., 2008; Guardone et al., 2010; Nannan et al., 2016; Alferez & Touber, 2017; Vimercati et al., 2018a), waves propagation in unsteady flows (Wendroff, 1972a,b; Cramer & Kluwick, 1984; Cramer et al., 1986; Menikoff & Plohr, 1989; Brown & Argrow, 1997; Guardone, 2007), steady duct flows (Chandrasekar & Prasad, 1991; Schnerr & Leidner, 1991; Cramer & Best, 1991; Cramer & Fry, 1993; Kluwick, 1993; Cramer et al., 1994; Kluwick, 2004; Cramer, 2006; Guardone & Vimercati, 2016), two-dimensional steady flows (Cramer & Crickenberger, 1992; Cramer & Tarkenton, 1992; Monaco et al., 1997; Cinnella & Congedo, 2007; Cinnella, 2008; Kluwick & Cox, 2018a; Vimercati et al., 2018b).

From these studies, a classification of different gasdynamic regimes emerges, which is based on the possible values of the fundamental derivative during the flow evolution:
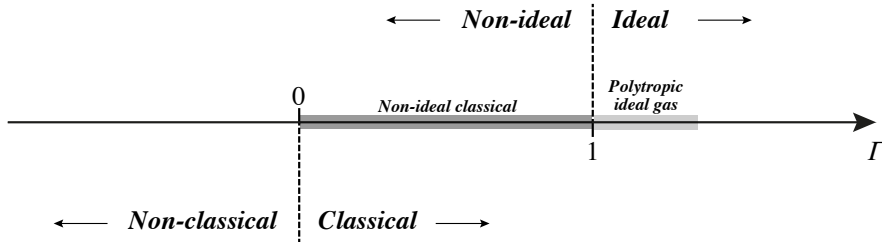
If the flow evolves through a sequence of thermodynamic states featuring $\Gamma > 1$, one speaks of *ideal gasdynamic regime*, since the usual behaviour of ideal gases is recovered. Indeed, for a polytropic ideal gas, equation (1.1) reduces to $\Gamma = (\gamma + 1)/2 > 1$, where $\gamma > 1$ is the ratio of the specific heats, which is constant under the polytropic assumption. By contrast, flows developing through states which possibly exhibit $\Gamma < 1$ are said to evolve in the *non-ideal gasdynamic regime*. Related phenomena of interest include, e.g., the decrease of the speed of sound in unsteady rarefaction fans (Thompson, 1971), the decrease of the flow Mach number in steady supersonic flows in nozzles (Cramer & Best, 1991) and around rarefactive ramps (Cramer & Crickenberger, 1992), the increase of the Mach number across oblique shock waves (Vimercati *et al.*, 2018*a*) and so-called *non-classical* gasdynamic phenomena, such as expansion shock waves (Thompson & Lambrakis, 1973), composite waves and split waves (Menikoff & Plohr, 1989), which are possible provided that $\Gamma < 0$. A further distinction can be therefore devised: in the following, we will refer to *non-classical gasdynamic regime* if the flow states are such that the fundamental derivative is possibly negative, and to *classical gasdynamic regime* otherwise. The overlapping region $0 < \Gamma < 1$ between the above classifications is referred to as *non-ideal classical gasdynamic regime*.

State-of-the-art thermodynamic models (e.g. Colonna *et al.*, 2012; Lemmon *et al.*, 2013) predict that $\Gamma < 1$ in the vapour-liquid equilibrium (VLE) region neighbouring the critical point, see figure 1.1 where three exemplary fluids are considered. In particular, a negative-Γ region is predicted to exist in the near-critical vapour-liquid equilibrium region (Nannan *et al.*, 2013). The behaviour in the single-phase vapour region, instead, depends on the molecular complexity of the fluid. In simple fluids such as carbon dioxide, $\Gamma > 1$ outside the two-phase region, see figure 1.1(*a*). In fluids characterized by moderate molecular complexity, such as toluene (figure 1.1(*b*)), a region $0 < \Gamma < 1$ occurs close to the dew line. Fluids composed of sufficiently complex molecules are predicted to exhibit a negative-Γ region in the vapour phase close to the dew line. This is named BZT region, after scientists Bethe, Zel'dovich and Thompson who pioneered non-classical gasdynamics in single-phase vapours, and fluids that are predicted to exhibit this region are referred to as BZT fluids. An example of such fluid is D_6 (dodecamethylcyclohexasiloxane, $C_{12}H_{36}O_6Si_6$), see figure 1.1(*c*).

Non-ideal flows are encountered in a variety of aerospace and industrial applications. Fluids in the vicinity of the vapour-liquid saturation curve can be adopted as oxidizers in hybrid rocket motors (e.g. N_2O) and can be exploited for surface cooling to reduce ablation and degradation of nozzle performance (Sutton & Biblarz, 2016; Guardone, 2011). Operation in the vicinity of the vapour-liquid saturation curve allows an increase of the heat transfer rates at a relatively constant fluid temperature and pressure, thanks to the contribution of the latent heat of vaporization. Gases made of complex molecules can be used in supersonic wind tunnels instead of air to achieve higher Reynolds numbers, which can be varied almost independently from the Mach number (Sagnier & Vérant, 1998).
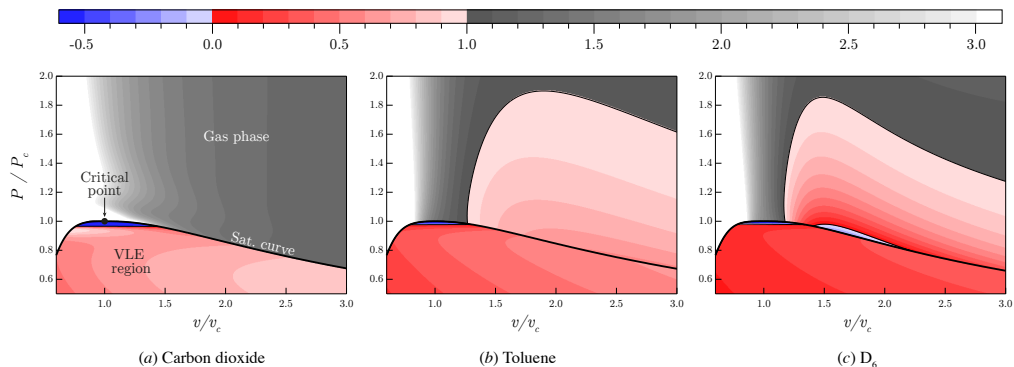
FIGURE 1.1. Fundamental derivative of gasdynamics for selected fluids modelled using reference EoS from the REFPROP library (Lemmon *et al.*, 2013).[1]

Organic Rankine Cycle (ORC) plants exploit organic compounds, e.g. hydrocarbons or siloxanes typically characterised by high molecular complexity, as working fluids instead of water (see, e.g., Angelino *et al.*, 1991; Colonna *et al.*, 2015; Macchi & Astolfi, 2016). The use of organic substances allows for higher cycle efficiencies, if compared to conventional steam cycles, when the temperature of the energy source is moderate or low, e.g. waste heat from industrial processes, geothermal reservoir, biomass combustion and concentrated solar radiation. Reduced complexity and maintenance, reduced costs and scalability are further advantages (see also Tchanche *et al.*, 2013, 2014). The expansion through the initial stages of ORC turbines typically occurs in the non-ideal regime, close to the vapour-liquid saturation curve and critical point. The combination of the large heat capacity of complex organic fluids and the thermodynamic conditions typical of ORC expanders results in low values of the speed of sound and, in turn, high values of the flow Mach number even modest flow velocities (especially in the initial stages due to the larger pressure ratio). High supersonic flows may result in large losses and mechanical stresses due to shock wave formation in the channel or at the trailing-edge of the blades (Denton & Xu, 1989; Mee *et al.*, 1990). Further non-ideal effects seem to exacerbate the problem (Wheeler & Ong, 2013; Galiana *et al.*, 2016; Vimercati *et al.*, 2017), at least for the non-BZT fluids that are currently employed as working fluids in ORCs. With working fluids of the BZT class, certain non-classical phenomena can in principle be exploited to improve the expander performances (Kluwick, 1994; Cramer & Park, 1999; Brown & Argrow, 2000).

Supercritical carbon dioxide cycles operate close to the critical point (see, e.g. Feher, 1968). Recent studies (Rinaldi *et al.*, 2015) indicates the possibility of expansion in the near-critical two-phase region, where non-classical phenomena are theoretically admissible. Other areas to which NICFD is relevant include refrigeration and heat pump systems (e.g. Bartosiewicz *et al.*, 2006; Zamfirescu & Dincer, 2009), oil and gas industry (e.g. Jassim *et al.*, 2008) and pharmaceutical industry (e.g. Helfgen *et al.*, 2003).

Driven by the growing interest of the industrial and scientific community, NICFD is a very active research field, as recent advancements and ongoing efforts, embracing theory, numerics and experiments, demonstrate. The theoretical side is undoubtedly the most developed; efforts

---

[1]In the very close proximity of the critical point, the analytical models of the REFPROP library might be inaccurate since they do not include scaling laws accounting for the non-analyticity of the Helmholtz free energy at the critical point (see, e.g., Levelt-Sengers, 1970). Nevertheless, the sign and the qualitative behaviour of Γ in that region is correctly predicted, see Nannan *et al.* (2013).

in this direction brought to a fairly good degree of knowledge of the thermodynamic modelling and phenomenological features of non-ideal flows, see Kluwick (2017) for a concise review. If compared to the well-established theory of ideal-gas flows, the understanding of non-ideal (and especially non-classical) flows is at a more basic level, as recent studies on fundamentals of NICFD confirm (see, .e.g, Nannan *et al.*, 2016; Kluwick & Cox, 2018*a*; Vimercati *et al.*, 2018*a,b*). Nowadays the community can rely on a number computational tools capable of dealing with and accurately treat non-ideal flows. Notable examples are FlowMesh (Guardone & Vigevano, 2002; Guardone, 2007; Re *et al.*, 2017, 2018; Re & Guardone, 2018), zFlow (Colonna & Silva, 2003; Colonna & Rebay, 2004) and the recent suite SU2 (Palacios *et al.*, 2013; Vitale *et al.*, 2015; Gori *et al.*, 2015), which is an open-source platform for solving multi-physics PDE problems and PDE-constrained optimization problems, and it is becoming the tool of choice in NICFD simulations and design (see also Gori *et al.*, 2017*b*; Pini *et al.*, 2017). Developing reliable CFD softwares is of great important to facilitate the comprehension and the prediction of non-ideal flows.

The experimental aspect is the most unexplored in NICFD, due to the difficulties in measuring high-temperature and high-pressure flows close to condensation or the thermal stability limit of the working fluid. To fill this gap, a number of research efforts are currently being performed. The list of experimental facilities dedicated to the investigation of NICFD flows includes: the Ludwieg-type shock tube FAST (Flexible Asymmetric Shock Tube, see Colonna *et al.*, 2008*a*; Mathijssen *et al.*, 2015), the supersonic blow-down wind tunnel TROVA (Test Rig for Organic VApours, see Spinelli *et al.*, 2010, 2013; Guardone *et al.*, 2013) at Politecnico di Milano and the supersonic closed-circuit wind tunnel ORCHID (Organic Rankine Cycle Hybrid Integrated Device, see Head *et al.*, 2016) at Delft University of Technology, the ORC Ludwieg tube of University of Cambridge (Galiana *et al.*, 2016), the micro-ORC test rig of Lappeenranta University of Technology (Uusitalo *et al.*, 2017; Turunen-Saaresti *et al.*, 2017), the closed-loop wind tunnel CLOWT (Closed Loop Organic Wind Tunnel, Reinker *et al.*, 2017) at Münster University of Applied Sciences. Special reference needs to be made to experiments of non-classical gasdynamics.

No experimental evidence of non-classical behaviour is available to date. A first attempt was carried out by Borisov *et al.* (1983) who claimed they measured a rarefaction shock wave in trifluorochloromethane, but the result were adversely interpreted at a later stage (Cramer & Sen, 1986; Kutateladze *et al.*, 1987; Thompson, 1991; Fergason *et al.*, 2003), who pointed towards critical-point phenomena and two-phase effects. The experiments devised by Fergason *et al.* (2003) and Guardone (2007) failed due to thermal decomposition of the working fluid. Although no clear proof of the existence of non-classical gasdynamic phenomena has been given yet, a promising experimental program is underway at the FAST facility, close to and inside the expected BZT region of dodecamethylcyclohexasiloxane (Mathijssen, 2017).

1.2 Research motivation and objectives

In spite of the considerable theoretical efforts of the last few decades, to date, theoretical knowledge of non-ideal compressible flows is still far from being complete and its progress represents a great challenge for the scientific community. Partially understood problems and open questions in NICFD include, among others, the characterization of multi-dimensional shock waves, the response and stability of shock waves to perturbations, the admissibility of shock reflection patterns and interactions. These are all examples of problems which have been completely or mostly solved, or which simply have no counterpart, in the theory of ideal-gas flows. Advancements in the theory of non-ideal compressible flows will have a beneficial impact on the above-mentioned industrial applications, not only directly, e.g. by driving ORC turbomachinery devices to higher efficiencies, but also indirectly by supporting numerical and experimental activity with improvements in current

5

FIGURE 1.2. Computed Mach number distribution in the first-stage stator of an ORC turbine. Flow from left to right. Three characteristic flow regions are identified: expansion through a converging-diverging nozzle (A), generation of oblique shocks at the trailing edge (B), shock reflection on the blade wall (C). Details on the numerical simulation are given in §6.
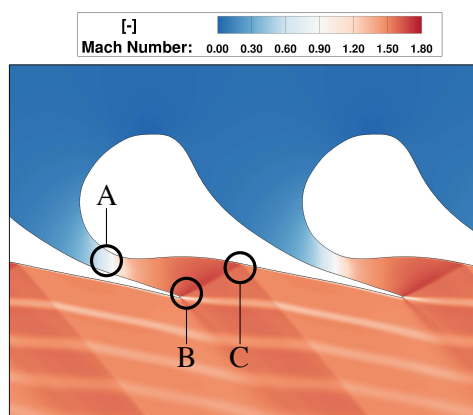
methods and development of new ones (e.g. aimed at answering the long-lasting question of the existence of non-classical phenomena) and in the interpretation of results.

The objective of this work is to investigate the effects of non-ideal thermodynamics on the general features of steady supersonic flows of single phase vapours or gases (the non-classical regime is thus treated in the vapour region of BZT fluids). To this end, original research is presented which covers the theories of (a) steady-state flows in converging-diverging nozzles, (b) flows around compressive/rarefactive ramps, (c) shock reflections and interactions. The purpose of the nozzle flow analysis is to determine the possible functioning regimes in the non-ideal gasdynamic context and the link between the functioning regimes and the flow stagnation conditions at the nozzle inlet (i.e. the reservoir conditions, if the nozzle is assumed to be connected to a reservoir). The study of the ramp problem is aimed at understanding oblique waves in supersonic flows, i.e. waves which can produce the deflection of a steady supersonic stream. On the basis of specific non-ideal effects, several types of oblique waves are identified and, again, a link is established between the type of wave and the unperturbed state of the fluid. The characterization of oblique waves lays the ground work for the analysis of shock reflections and interactions in non-ideal flows. The primary contribution of this document to the theory of NICFD is thus a classification of relevant phenomena occurring in steady supersonic flows in the non-ideal regime (both classical and non-classical) and the identification of the connection between the predicted phenomenon and the flow conditions.

Understanding the precise conditions under which non-ideal and non-classical phenomena can possibly occur is important for at least two reasons. Firstly, from the point of view of practical applications, it constitutes valuable knowledge at the design stage, where the ability to anticipate potential advantages/disadvantages associated with a particular operating condition is crucial. A second reason is connected with the constant endeavour to observe experimentally the non-classical phenomena that theory predicts, first and foremost the rarefaction shock. As noted by Kluwick & Cox (2018a), steady flow conditions offer an interesting and promising alternative to the previous attempts (all based on shock-tube techniques) of acquiring experimental evidence of non-classical behaviour. In this perspective, knowing how various parameters of interest influence the flow field is extremely useful for the selection of experimental conditions suitable for the purpose. Remarkably, despite the theoretical predictions always depend on the EoS used to model the fluid, the analytical framework delineated in this work is of general nature and delivers conclusions that are independent of the specific choice of the EoS, from the qualitative point of view. As such, the concepts developed here are suitable to future improvements of thermodynamic modelling and at the same time provide a solid basis for further advancements in gasdynamics.

The theories of nozzle flows, oblique waves, shock reflections and shock interactions have direct practical application. In the specific context of non-ideal flows, a prominent example is

represented by ORC turbines, where the subjects of the present study are all key elements of the flow field, as shown in figure 1.2. The flow is expanded from stagnation up to supersonic speed through a converging diverging nozzle (region A). At the trailing edge of the blade, shock waves are formed due to the rotation imposed by its finite thickness or to accomplish post-expansion (region B). The oblique shock generated on the pressure side propagates towards the suction side of the neighbouring blade and is reflected at the wall (region C). These different aspects of compressible flow will be individually examined and then considered collectively in a realistic ORC application.

1.3 Outline of the thesis

The thesis is structured as follows.

Chapter 2 outlines the theoretical background of compressible flows, in particular with respect to shock waves, which are discussed in a general perspective appropriate for non-ideal and non-classical gasdynamics.

Chapter 3 deals with steady flows expanding from a reservoir through a converging-diverging nozzle. Firstly, isentropic flows are examined. Isentropic-flow analysis allows one to anticipate and explain, to a certain degree, the exact solutions of the nozzle flow which possibly includes shock waves. The concept of functioning regime is introduced to analyse the response of the system to variations in the downstream boundary condition (outlet pressure). According to the reservoir conditions, several non-ideal functioning regimes are singled out. The connection between the reservoir conditions and the functioning regime is explained and depicted through the use of thermodynamic maps.

Chapter 4 reports an extensive analysis of the properties of oblique waves in steady supersonic flows. The first part is focused on non-ideal oblique shocks in classical gasdynamics. Non-ideal oblique shocks increase the flow Mach number and thus might have important implications for practical applications. The necessary conditions for the formation of non-ideal oblique shocks are examined for several fluids of industrial interest. The second part of the chapter deals with the admissible wave configurations in non-classical gasdynamics. Wave curves consisting of states connected to a given initial state (the uniform state upstream of the ramp) by an oblique wave are constructed. The link between the wave curve and the upstream state is clarified and depicted in a thermodynamic map.

Chapter 5 deals with shock reflections and interactions in non-ideal steady flows. Following the same lines as chapter 4, in the first part the classical theory is enriched by taking into account the potential non-ideal increase of the Mach number across oblique shock waves. Subsequently, moving from the theory of non-classical oblique waves established in the previous chapter, shock-reflection and shock-interaction patterns in non-classical gasdynamics are examined.

Chapter 6 presents the study of non-ideal steady flows in ORC turbine cascades featuring hex-amethyldisiloxane (MM) as the working fluid. This application case embraces each of the basic phenomena analysed in the thesis and is particularly relevant in view of the recent tendency towards higher pressures and temperatures at the turbine inlet (e.g. supercritical ORC). In the context of supersonic nozzle cascades, the influence of non-ideal effects on the optimal blade shape and its off-design behaviour is investigated by means of numerical simulations. Advantages and disadvantages of operating in the non-ideal gasdynamic regime are discussed for a number of specific examples, nonetheless providing more general considerations.

Chapter 7 summarizes conclusions and recommendations for future research activities.

CHAPTER 2

STEADY COMPRESSIBLE FLOW

This chapter recalls the equations that govern steady compressible flows under the assumption that effects such as viscosity, heat conduction, chemical reactions and relaxation can be neglected. The general description of the fluid motion is provided by the integral conservation laws of mass, momentum and energy. For a local description of the flow field, the smoothness of the conservative variables must be taken into account. Thus, in regions where the variables are continuously differentiable, the flow is locally described by the Euler equations, while at points of jump discontinuity by the Rankine-Hugoniot relations. The salient features of smooth flows and shock waves are discussed to prepare the ground for the original analysis presented in the subsequent chapters.

2.1 Conservation laws

This section introduces the integral form of the conservation laws, specialized to the case of steady and single-phase flow in which thermoviscous, body-forces and non-equilibrium effects are negligible or are not the focus of attention. Let us consider a volume V in the domain of the fluid with boundary ∂V. The principle of conservation of mass, momentum and energy are written as

$$\int_{\partial V} \rho \, \boldsymbol{u} \cdot \boldsymbol{n} = 0, \tag{2.1}$$

$$\int_{\partial V} \rho \boldsymbol{u} \, \boldsymbol{u} \cdot \boldsymbol{n} = - \int_{\partial V} P \, \boldsymbol{n}, \tag{2.2}$$

$$\int_{\partial V} \rho e^t \, \boldsymbol{u} \cdot \boldsymbol{n} = - \int_{\partial V} P \, \boldsymbol{u} \cdot \boldsymbol{n}, \tag{2.3}$$

where $\boldsymbol{u}$ is the fluid velocity, $e^t = e + u^2/2$ is the specific total energy, in which e is the specific internal energy and $u = \|\boldsymbol{u}\|$ is the velocity magnitude and $\boldsymbol{n}$ is the outward-pointing unit vector normal to the surface ∂V. These integral relations must be satisfied for each volume V of fluid.

2.2 Euler equations

If the variables appearing in the integrals of equations (2.1)-(2.3) are continuously differentiable, the surface integrals can be transformed into volume integrals and Gauss's theorem can be applied obtaining the well-known Euler equations, reported here in so-called quasi-linear form:

$$\boldsymbol{u} \cdot \nabla \rho + \rho \nabla \cdot \boldsymbol{u} = 0, \tag{2.4}$$

$$(\boldsymbol{u} \cdot \nabla)\boldsymbol{u} + \frac{\nabla P}{\rho} = 0, \tag{2.5}$$

$$\boldsymbol{u} \cdot \nabla e + \frac{P}{\rho} \nabla \cdot \boldsymbol{u} = 0. \tag{2.6}$$

The above equations can be recast in a more enlightening form involving the specific entropy s and specific total enthalpy $h^t = h + u^2/2$, where h is the specific enthalpy. This reads

$$\nabla h^t - T \nabla s = \boldsymbol{u} \times \nabla \times \boldsymbol{u}, \tag{2.7}$$

$$\boldsymbol{u} \cdot \nabla s = 0, \tag{2.8}$$

$$\boldsymbol{u} \cdot \nabla h^t = 0, \tag{2.9}$$

where T is the temperature. Thus, in smooth flows (i) the fluid particles maintain their entropy and total enthalpy unaltered and (ii) rotational motion ($\nabla \times \boldsymbol{u} \neq 0$) generates either entropy or total enthalpy non-uniformities (unless the velocity and vorticity vectors are parallel).

2.3 Shock wave and contact discontinuities

The integral equations (2.1)-(2.3) admit discontinuous solutions as well. These discontinuities are the limit of thin layers, carrying an abrupt variation of the fluid properties, for vanishing viscosity

and thermal conductivity (see, e.g., Zel'dovich, 1946; Landau & Lifshitz, 1987). At each point on a surface of discontinuity, the laws of conservation of mass, momentum and energy, namely the well-known Rankine-Hugoniot relations, locally assume the form

$$[\rho u_n] = 0, \tag{2.10}$$

$$[P\boldsymbol{n} + \rho u_n \boldsymbol{u}] = 0, \tag{2.11}$$

$$[\rho u_n h^t] = 0, \tag{2.12}$$

where $[\cdot]$ denotes the jump across the discontinuity, $\boldsymbol{n}$ is the unit vector normal to the surface of discontinuity and $u_n = \boldsymbol{u} \cdot \boldsymbol{n}$ is the normal component of the velocity. Note that the above relations hold not only for a steady flow, but also for the unsteady case if the reference frame is locally attached to the discontinuity.

Two different types of discontinuity can be distinguished based on the value of the mass flux $m = \rho u_n$ across the discontinuous front. Discontinuities having $m = 0$ are called contact discontinuities. Of course, $\rho \neq 0$ so that $u_n = 0$ on both sides of a contact discontinuity. Moreover, projection of (2.11) onto the normal direction gives $[P] = 0$ across a contact surface. A contact discontinuity can thus sustain jumps in density, entropy or any other thermodynamic quantity except the pressure and jumps in the tangential velocity $\boldsymbol{u}_t = \boldsymbol{u} - u_n \boldsymbol{n}$. Contact discontinuities presenting a purely thermodynamic jump (at constant pressure) are referred to as entropy waves, while those featuring different tangential velocities across the front but equal thermodynamic states are called vorticity waves or slip lines.

Shock waves are discontinuities through which there is flow of matter ($m \neq 0$). Thus, we can distinguish a pre-shock state where fluid particles enter the shock and a post-shock state where the fluid leaves the shock, as shown figure 2.1. In other words, if the shock-attached coordinate system is chosen such that $u_n > 0$, the post-shock state lies on the side pointed by the normal $\boldsymbol{n}$ and the pre-shock state on the opposite side. Hereinafter, when referring to shock waves, the pre-shock and post-shock states will be indicated as states A and B, respectively, and $[\cdot] = ()_B - ()_A$.

The energy balance across the shock reduces to $[h^t] = 0$, thus the total enthalpy is conserved across the shock. In addition, by projecting (2.11) onto the normal direction and tangent plane, one obtains

$$[P + \rho u_n^2] = 0, \tag{2.13}$$

$$[\boldsymbol{u}_t] = 0, \tag{2.14}$$

so that a shock front of arbitrary shape can be locally studied by examining the properties of normal shocks to which a parallel velocity field is superposed. After straightforward manipulations, the energy and normal momentum balance equations are recast in the well-known form

$$[h] - \tfrac{1}{2}[P](v_A + v_B) = 0, \tag{2.15}$$

$$[P] + m^2[v] = 0. \tag{2.16}$$

Equation (2.15), known as the Hugoniot relation, determines the set (Hugoniot locus) of thermodynamic states that can be connected by a shock wave. In the (P, v)–plane, the Hugoniot locus is commonly referred to as the shock adiabat, while the straight line connecting the pre-shock and post-shock states, defined by relation (2.16), is known as the Rayleigh line.

2.3.1 Shock admissibility criteria

In the case of shock waves, the Rankine-Hugoniot relations must be complemented with suitable admissibility criteria in order to rule out unphysical solutions. The second law of thermodynamics
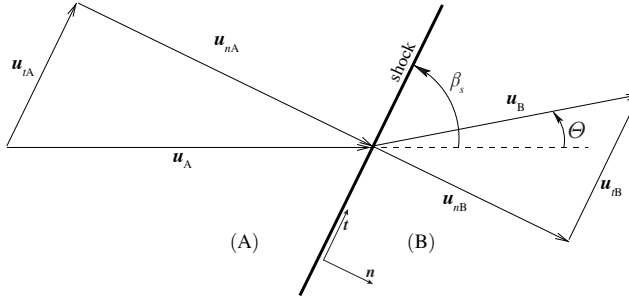
FIGURE 2.1. Qualitative illustration of the local shock front. States A and B represent the pre-shock and post-shock states, respectively. For ease of representation, the shock-attached reference frame is such that the plane spanned by unit vectors $\boldsymbol{n}$ and $\boldsymbol{t}$ contains the fluid velocity $\boldsymbol{u}$. The angles β_s and Θ are the shock angle and flow deviation angle, respectively, both computed with respect to the pre-shock flow direction.

requires that the entropy does not decrease across the shock, namely

$$[s] \geqslant 0. \tag{2.17}$$

Further admissibility conditions stem from mechanical stability requirements. In order that the shock front be stable against one-dimensional perturbations of the normal flow, the well-known speed-ordering relation

$$M_{n\mathrm{B}} \leqslant 1 \leqslant M_{n\mathrm{A}}, \tag{2.18}$$

must be satisfied along the shock front, where $M_n = u_n/c$ denotes the normal Mach number (Lax, 1957). The conditions for stability with respect to multidimensional perturbations can be conveniently related to geometric properties of the shock adiabat and Rayleigh line, namely as bounds on their relative slope Π,

$$\Pi = m^2 \left| \frac{\mathrm{d}}{\mathrm{d}v} P^{\mathcal{H}}(v; P_{\mathrm{A}}, v_{\mathrm{A}}) \right|_{v=v_{\mathrm{B}}}, \tag{2.19}$$

where $P^{\mathcal{H}}(v; P_{\mathrm{A}}, v_{\mathrm{A}})$, $P_{\mathrm{B}} = P^{\mathcal{H}}(v_{\mathrm{B}}; P_{\mathrm{A}}, v_{\mathrm{A}})$ is the functional form of the relationship between the post-shock pressure and the post-shock specific volume for given P_{A} and v_{A}, as defined by equation (2.15). D'yakov (1954) and Erpenbeck (1962) showed that the shock front is stable against ripple perturbations if and only if

$$-1 \leqslant \Pi \leqslant 1 + 2M_{n\mathrm{B}}. \tag{2.20}$$

The stability range (2.20) was further restricted by Kontorovich (1958) to

$$-1 \leqslant \Pi \leqslant \frac{1 - M_{n\mathrm{B}}^2(1 + v_{\mathrm{A}}/v_{\mathrm{B}})}{1 - M_{n\mathrm{B}}^2[v]/v_{\mathrm{B}}}, \tag{2.21}$$

by noting that in the interval

$$\frac{1 - M_{n\mathrm{B}}^2(1 + v_{\mathrm{A}}/v_{\mathrm{B}})}{1 - M_{n\mathrm{B}}^2[v]/v_{\mathrm{B}}} < \Pi < 1 + 2M_{n\mathrm{B}} \tag{2.22}$$

the shock front is only neutrally stable against transverse perturbations and can spontaneously emit acoustic waves (see also Fowles, 1981). Gardner (1963) and Erpenbeck (1963) also pointed out

that violating the second inequality in (2.20) leads to non-uniqueness of solutions of the Riemann problem. Despite conditions (2.20) and (2.21) derive from linear stability analysis of planar shocks, it turns out that an arbitrarily curved shock front is uniformly stable provided (2.21) is satisfied locally at each point of the front (Majda, 1983). Yet, for some cases, the above conditions may not be sufficient to rule out unphysical solutions of the Rankine-Hugoniot relations. Further and more selective criteria may solve the problem of defining the admissible shocks. For non-convex shock adiabats, requiring that the shock wave admits a one-dimensional thermoviscous profile allows to rule out inadmissible shocks that are not detected by the above conditions. It must be noticed, however, that there is no general theory for defining appropriate admissibility conditions that applies to arbitrary equations of state (Menikoff & Plohr, 1989; Kluwick, 2001).

2.3.2 Properties of the shock curve

The locus of the states that can be connected to a given initial state A constitutes a shock curve. Choosing a parametrization for the shock curve that is valid both in the classical and non-classical gasdynamic regime and for the most general equations of state might be a difficult task. In the following we restrict our attention to shock curves that satisfy condition

$$2 + \frac{[v]}{v_{\mathrm{B}}} G_{\mathrm{B}} > 0, \tag{2.23}$$

where $G = v(\partial P/\partial e)_v$ is the Grüneisen coefficient, which has the same sign of the coefficient of thermal expansion. The above relation is satisfied in the limit of weak shocks, but may be violated, e.g., for finite-strength compression shocks if G is sufficiently large. As a matter of fact, the choice of limiting the discussion to shock waves satisfying relation (2.23) is motivated by the fact that this is the typical behaviour of the shock curves for most real fluids below the dissociation (ionization) threshold, regardless of anomalies due to negative nonlinearities $\Gamma < 0$ or phase transitions (see, e.g., Landau & Lifshitz, 1987; Cramer, 1989b; Menikoff & Plohr, 1989; Kluwick, 2001). As a result of our assumption, the post-shock specific volume parametrizes the shock curve, see below. If $G > 0$ and thus the substance expands upon isobaric heating, which is true in most situations of interest (with the notable exception of water near freezing), equality in (2.23) determines the maximum density increase across compression shock waves.

We now report the variation of relevant quantities along the shock curve of a given state A, as a function of the downstream specific volume. To establish notation, the functional dependence of a given quantity X evaluated on the shock curve of the initial state A is denoted as $X^{\mathcal{H}}(v; \mathbf{A})$, being $\mathbf{A}$ a triplet of the form $\mathbf{A} = (P_{\mathrm{A}}, v_{\mathrm{A}}, \boldsymbol{u}_{\mathrm{A}})$ describing the complete thermodynamic and kinematic initial state. Any other equivalent triplet can be obtained by simple manipulation. Of course, $X_{\mathrm{B}} = X^{\mathcal{H}}(v_{\mathrm{B}}; \mathbf{A})$. Note also that if X is a purely thermodynamic quantity, then it will depend on the pre-shock thermodynamic state only (e.g. P_{A}, v_{A}), thanks to equation (2.15). When there is no risk of confusion, the notation will be simplified using $\mathrm{d}X_{\mathrm{B}}/\mathrm{d}v_{\mathrm{B}}$ as a shorthand for $\mathrm{d}X^{\mathcal{H}}(v; \mathbf{A})/\mathrm{d}v\big|_{v=v_{\mathrm{B}}}$.

First of all, the pressure variation is considered, which determines the local structure of the shock adiabat:

$$\frac{\mathrm{d}P_{\mathrm{B}}}{\mathrm{d}v_{\mathrm{B}}} = -\frac{P_{\mathrm{B}}}{v_{\mathrm{B}}} \left(\frac{c_{\mathrm{B}}^2}{P_{\mathrm{B}} v_{\mathrm{B}}} - \frac{[P]}{2P_{\mathrm{B}}} G_{\mathrm{B}} \right) \left(1 + \frac{[v]}{2v_{\mathrm{B}}} G_{\mathrm{B}} \right)^{-1}. \tag{2.24}$$

By requiring that relation (2.23) is satisfied, the slope $\mathrm{d}P_{\mathrm{B}}/\mathrm{d}v_{\mathrm{B}}$ is finite and P_{B} is a single valued function of v_{B}; therefore the Hugoniot locus can be parametrized using the post-shock specific volume. If $G > 0$, the quantity in (2.23) approaches zero for a finite value of v_{B}, thus defining a vertical asymptote for which the pressure goes to positive infinity. Since all real materials satisfy the condition $G \leqslant 2c^2/Pv$ introduced by Smith (1979), see also Menikoff & Plohr (1989), the first bracketed term in (2.24) is positive. Thus, under the assumption that relation (2.23) holds, the slope

13

of the shock adiabat is always negative (this implies that the Hugoniot locus can be parametrised also by the post-shock pressure). An equivalent form of equation (2.24) is the following

$$\frac{\mathrm{d}P_B}{\mathrm{d}v_B} = \frac{[P]}{[v]} + \frac{c_B^2}{v_B^2}\left(M_{nB}^2 - 1\right)\left(1 + \frac{[v]}{2v_B}G_B\right)^{-1}, \tag{2.25}$$

see Cramer (1989b), in which the post-shock normal Mach number explicitly appears (this will be particularly useful when interpreting the admissibility criteria in a graphical way). At post-shock states such that $M_{nB} = 1$ (for which the shock is termed post-sonic, from the nomenclature of one-dimensional flows), the shock adiabat has the same slope of the Rayleigh line. From the above equation, it is easy to obtain an expression for the variation of the squared mass flux $m^2 = -[P]/[v]$ (corresponding to the slope of the Rayleigh line changed of sign) along the shock curve:

$$\frac{\mathrm{d}m^2}{\mathrm{d}v_B} = \frac{1}{[v]}\frac{c_B^2}{v_B^2}\left(1 - M_{nB}^2\right)\left(1 + \frac{[v]}{2v_B}G_B\right)^{-1}, \tag{2.26}$$

showing that the mass flux and the slope of the Rayleigh line have local extrema at points $M_{nB} = 1$. The entropy variation along the Hugoniot locus can be written as

$$\frac{\mathrm{d}s_B}{\mathrm{d}v_B} = \frac{c_B^2}{T_B}\frac{[v]}{v_B^2}\left(1 - M_{nB}^2\right)\left(2 + \frac{[v]}{v_B}G_B\right)^{-1}, \tag{2.27}$$

which also vanishes if $M_{nB} = 1$. In the above expression, the terms $[v]$ and $\left(1 - M_{nB}^2\right)$ both vanish as v_B approaches v_A. Thus, not only $\mathrm{d}s_B/\mathrm{d}v_B$ vanishes as v_B approaches v_A, but also the second derivative $\mathrm{d}^2 s_B/\mathrm{d}v_B^2$. In this respect, we report the celebrated result

$$[s] = -\frac{\Gamma_A c_A^2}{6T_A v_A^3}[v]^3 + \mathcal{O}([v]^4), \qquad [v] \to 0 \tag{2.28}$$

first derived by (Duhem, 1909) and independently by (Bethe, 1942). Equation (2.28) expresses the well-known fact that the slope and curvature of the shock adiabat at P_A, v_A equal those of the isentrope passing through this point. Using equation (2.27), relations for the internal energy and temperature variations can be obtained from the fundamental thermodynamic identities $de = Tds - pdv$ and from $dT = T/c_v ds - GT/v dv$:

$$\frac{\mathrm{d}e_B}{\mathrm{d}v_B} = c_B^2\frac{[v]}{v_B^2}\left(1 - M_{nB}^2\right)\left(2 + \frac{[v]}{v_B}G_B\right)^{-1} - P_B \tag{2.29}$$

and

$$\frac{\mathrm{d}T_B}{\mathrm{d}v_B} = \frac{c_B^2}{c_{vB}}\frac{[v]}{v_B^2}\left(1 - M_{nB}^2\right)\left(2 + \frac{[v]}{v_B}G_B\right)^{-1} - \frac{G_B T_B}{v_B}. \tag{2.30}$$

In the same way, the variation of the speed of sound along the shock curve is computed from $dc = (1 - \Gamma)c/v dv + \mathcal{K}T/c ds$ and reads

$$\frac{\mathrm{d}c_B}{\mathrm{d}v_B} = \frac{c_B}{v_B}\left(1 - \Gamma_B\right) - \mathcal{K}_B\frac{[P]}{c_B}\left(\frac{1}{M_{nB}^2} - 1\right)\left(2 + \frac{[v]}{v_B}G_B\right)^{-1}, \tag{2.31}$$

which involves both the fundamental derivative of gasdynamics and the dimensionless isochoric derivative of the speed of sound with the entropy $\mathcal{K} = (c/T)(\partial c/\partial s)_v$.

Next, we consider post-shock kinematic quantities, specifically the post-shock velocity magnitude u_B and the shock angle $\beta_s \in [\sin^{-1}(1/M_A), \pi/2]$, computed with respect to the pre-shock flow direction ($u_{nA} = u_A \sin \beta_s$). Recall that the pre-shock kinematic state is fixed by assumption, thus the variation of post-shock quantities corresponds to a change in the shock angle. These derivatives along the shock curve are

$$\frac{\mathrm{d}u_B}{\mathrm{d}v_B} = \frac{u_B}{v_B}\left\{1 + \left(1 + \frac{v_A}{v_B}\right)\left(\frac{1}{M_{nB}^2} - 1\right)\left(2 + \frac{[v]}{v_B}G_B\right)^{-1}\right\} \tag{2.32}$$

and

$$\frac{\mathrm{d}\beta_s}{\mathrm{d}v_B} = \tan \beta_s \frac{1 - M_{nB}^2}{M_{nB}^2[v]}\left(2 + \frac{[v]}{v_B}G_B\right)^{-1}, \tag{2.33}$$

as given in Gori *et al.* (2017*a*).

Finally, by combining the variation of the post-shock velocity (2.32) and speed of sound (2.31), an expression for the Mach number variation is obtained as

$$\frac{\mathrm{d}M_B}{\mathrm{d}v_B} = -\frac{M_B}{v_B}\left\{J_B + \frac{[v]}{v_B}\left(1 - M_{nB}^2\right)\left(\mathcal{K}_B + \frac{1 + G_B}{M_B^2}\right)\left(2 + \frac{[v]}{v_B}G_B\right)^{-1}\right\}, \tag{2.34}$$

in which

$$J = 1 - \Gamma - \frac{1}{M^2} \tag{2.35}$$

corresponds to the non-dimensional isentropic derivative of the Mach number with the density at constant total enthalpy, see equation (3.6).

We now report relevant results concerning the type of shocks that are admissible in the classical and non-classical gasdynamic regimes. In classical gasdynamics, an important result is the Bethe-Weyl theorem (Bethe, 1942; Weyl, 1949), which states that if $\Gamma > 0$ throughout the thermodynamic domain of interest, the Hugoniot locus is parametrized by the post-shock entropy and satisfies

$$\begin{cases} [v] < 0 \text{ and } M_{nB} < 1, & \text{if } [s] > 0, \\ [v] > 0 \text{ and } M_{nB} > 1, & \text{if } [s] < 0. \end{cases} \tag{2.36}$$

The impossibility of sonic points $M_{nB} = 1$ also implies that the mass flux is monotonic and therefore can parametrize the shock curve. Because the shock adiabat is convex near the initial state if $\Gamma > 0$ (equation 2.28), $M_{nA} > 1$ ($M_{nA} < 1$) on the compression (rarefaction) side of the shock curve. Therefore, in classical gasdynamics compressive shock waves only satisfy the entropy inequality and the speed ordering relation (and also possess a thermoviscous profile, see §2.3.4).

This, instead, is not always the case in non-classical gasdynamics, as is it seen from equation (2.28) when $\Gamma_A < 0$. Non-classical shock adiabats are typically non-convex and characterized by entropy extrema, where the Rayleigh line is tangent to the shock adiabat. A useful result, in this respect, is

$$T_B \frac{\mathrm{d}^2 s_B}{\mathrm{d}v_B^2}\bigg|_{M_{nB}=1} = -\frac{[v]}{2}\frac{\mathrm{d}^2 P_B}{\mathrm{d}v_B^2}\bigg|_{M_{nB}=1} = -\Gamma_B c_B^2 \frac{[v]}{v_B^3}\left(1 + \frac{[v]}{2v_B}G_B\right)^{-1}, \tag{2.37}$$

which follows from differentiation of equations (2.25) and (2.27) and by noting that

$$\frac{\mathrm{d}M_{nB}^2}{\mathrm{d}v_B}\bigg|_{M_{nB}=1} = 2\frac{\Gamma_B}{v_B}, \tag{2.38}$$

which is obtained by evaluating relation (2.34) at a post-shock sonic state. Thus, since sonic points are local extrema in entropy, the sign of Γ alternates at successive sonic points and the curvature of the shock adiabat and the local isentrope have the same sign. The admissibility conditions, in non-classical gasdynamics, are most conveniently interpreted in a graphical way, as shown in the following section.

2.3.3   Graphical interpretation of the admissibility criteria

The entropy condition (2.17), the speed ordering relation (2.18) and the further requirement of the existence of a thermoviscous profile can be checked graphically in the (P, v)–plane. Note that condition (2.20) is always satisfied within our assumptions, since the slope of the shock adiabat is always negative, and therefore the shocks considered here are not unstable to transverse perturbations. It is still possible, however, that the conditions for acoustic emission (2.22) are satisfied. This situation cannot be detected from graphical analysis, thus admissible/non-admissible shocks presented in the following are understood with reference to the other criteria.

Application of the fundamental identity $T ds = de + P dv$ across the shock wave gives

$$\int_{s_A}^{s_B} T ds = [e] + \int_{P_A}^{P_B} P dv = -\frac{P_B + P_A}{2}[v] + \int_{P_A}^{P_B} P dv, \tag{2.39}$$

where we used the equivalent form $[e] - [v](P_B + P_A)/2 = 0$ of relation (2.15). Thus, according to the above relation, for an entropy increasing shock wave, the area between v_A and v_B under the shock adiabat must be larger than that under the Rayleigh line. Thanks to relation (2.25), the stability requirement (2.18) can be graphically read as differences in the slope of the shock adiabat and Rayleigh line, namely

$$\left.\frac{d}{dv} P^{\mathcal{H}}(v; \mathbf{A})\right|_{v=v_B} \leqslant \frac{[P]}{[v]} \leqslant \left.\frac{d}{dv} P^{\mathcal{H}}(v; \mathbf{A})\right|_{v=v_A}, \tag{2.40}$$

where the extended notation is used for better clarity. This means that, for a shock wave satisfying the speed ordering relation, (i) the absolute value of the slope shock adiabat, evaluated in the pre-shock state, is less than or at most equal to the absolute value of the slope of the Rayleigh line and (ii) the absolute value of the slope shock adiabat, evaluated in the post-shock state, is greater than or at most equal to the absolute value of the slope of the Rayleigh line. Equality on one side of relation (2.40) implies that the shock wave has unitary normal Mach number on that side. If $M_{nB} = 1$ (post-sonic shock), the Rayleigh line is tangent to the shock adiabat at the post-shock state (equality between the first two terms in 2.40); if $M_{nA} = 1$ (pre-sonic shock), the Rayleigh line is tangent to the shock adiabat at the pre-shock state (equality between the last two terms in 2.40); if $M_{nA} = 1 = M_{nB}$ (double-sonic shock), the Rayleigh line is tangent to the shock adiabat both at the pre-shock and post-shock states (equalities in 2.40). Moreover, the further requirement that the shock wave admits a thermoviscous profile associated with the normal flow translates graphically into the requirement that the Rayleigh line does not cut the shock adiabat in interior points (see §2.3.4 below).

On the basis of these observations, the admissibility of compression/rarefaction shocks has a simple graphical interpretation: for an admissible compression shock, the Rayleigh line must be located completely above the shock adiabat; for an admissible rarefaction shock, the Rayleigh line must be located completely below the shock adiabat. Exemplary shock waves in the (P, v)–plane are sketched in figure 2.2. For shock adiabats that do not cross the negative-Γ region, only ordinary (non-sonic) compression shocks are admissible (e.g., shock A_1-B_1).

Two non-classical shock adiabats are reported, which cross the $\Gamma < 0$ region, but are centred on states featuring $\Gamma > 0$. The shock adiabat centred on state A_2 crosses the negative-Γ region
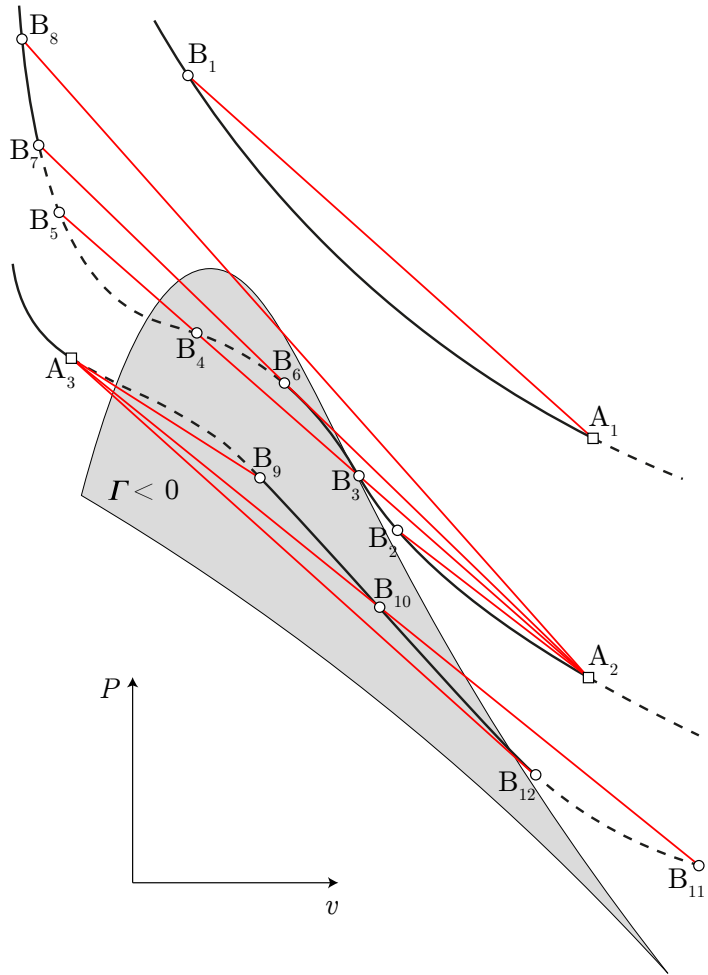
FIGURE 2.2. Qualitative illustration of shock adiabats (thick lines) crossing the region $\Gamma < 0$. The non-admissible portion of the shock adiabat is represented by the dashed line. Rayleigh lines in red. The curvature of the shock adiabats is intentionally exaggerated for explanatory purposes.

in its compression branch. Shock A_2-B_2 is an admissible shock. By increasing the mass flux (i.e. steepening the Rayleigh line), the situation arises in which three intersections between the Rayleigh line and the shock adiabat occur, namely points B_3, B_4, B_5. Of these points, only B_3 represents an admissible post-shock state. The others are cases in which the shock does not admit a thermoviscous structure (shock A_2-B_4 also violates the speed ordering relation). The Rayleigh line corresponding to the post-sonic shock A_2-B_6 and to the non-sonic shock A_2-B_7 delimits the range in which multiple intersections are possible. A further increase in the mass flux produces ordinary non-sonic shocks such as A_2-B_8.

The shock adiabat centred on state A_3 crosses the negative-Γ region in its rarefaction branch and encompasses rarefaction shocks. In the branch from point A_3 to point B_9, the speed ordering relation is not satisfied because $M_{nA} < 1$. Thus, the rarefaction-shock of smallest intensity from A_3 is the pre-sonic shock A_3-B_9. By increasing the mass flux, the condition is created in which

two intersections between the Rayleigh line and the shock adiabat occur (points B_{10}, B_{11}). Of these intersections, only B_{10} corresponds to an admissible rarefaction shock. Shock A_3-B_{11} instead violates the speed ordering relation and does not possess a thermoviscous profile. For rarefaction shocks there exists a maximum pressure jump for which the shock becomes post-sonic, see shock A_3-B_{12}. Any further increase in the mass flux yields no intersections on the rarefaction branch. For other examples of non-classical shock adiabats (including the case where the pre-shock state is selected in the region $\Gamma < 0$), the reader is referred to Kluwick (2001).

2.3.4 Remarks on the shock structure

The idealised picture of shock waves given in the preceding section is a result of ignoring thermoviscous effects and relaxation processes in the gas (such as the retarded energy transfer between various molecular degrees of freedom), which have in the statistical non-equilibrium a common basis. Accounting for these aspects allows to determine the structure of the transition layer that a shock wave in reality is.[1]

As discussed by Stupochenko *et al.* (1967), two opposing situations can be distinguished by comparing the characteristic macroscopic length L (in this case, the thickness of the transition layer) with the largest characteristic length l for the relaxation processes occurring in the fluid (defined as those of establishing thermodynamic equilibrium). Usually, the characteristic lengths for translational and rotational relaxation (excitation of molecular degrees of freedom) are comparable with the mean-free path l_0, while vibrational relaxation might be much slower and thus associated with larger characteristic lengths (especially for the complex molecules composing candidates BZT fluids). The establishment of chemical and ionization equilibrium is even slower.

If $L \gg l$, the equilibrium thermoviscous shock structure obtained by adding viscosity and thermal conductivity to equations (2.4)-(2.6) is appropriate. The resulting picture is that of a continuous transition between the pre-shock and post-shock states (Taylor, 1910). The limit of this description is in fact the requirement that the gradients of the flow variables are sufficiently small. This condition is evidently satisfied for weak shocks, but for strong shocks the situation is quite different.

When the spatial dishomogeneity grows, the state of the fluid may change so rapidly to cause significant disturbances to the statistical equilibrium. Using the concept of statistical mechanics, it is found that sufficiently strong shock waves are characterised by a thin leading layer in which a sharp transition occurs over distances of the order of l_0. In this layer, the assumption of continuum is no longer valid, thus showing that in the case of sufficiently strong shock waves, consideration of thermoviscous processes does not eliminate the necessity of introducing geometric discontinuity surfaces.[2] When $l \gg l_0$ (e.g. in moderately or complex fluids due to vibrational relaxation) the thin leading layer in strong shocks is followed by a relaxation zone of width l which ultimately determines the thickness of the shock. Since $l \gg l_0$, the relaxation region can be studied under the continuum model, but of course local thermodynamic equilibrium cannot be assumed.

Turning now to the case of shocks of relatively small amplitude, which are those of main interest in the following, relevant results are reported concerning the shock structure obtained, as previously mentioned, from the Navier-Stokes equations. Assuming one-dimensional steady flow, the balance equations of mass, momentum and energy can be recast, after integration along the

---

[1]If the characteristic lengths of the considered phenomena are large, compared with the thickness of the transition layer, the shock structure can be disregarded and thus the approximation of the shock as a geometric discontinuity surface is justified.

[2]The same order of magnitude for the width of the leading transitional layer of a strong shock can be estimated accidentally from considerations pertaining macroscopic, equilibrium fluid dynamics.

streamwise direction x, as

$$\rho u = m = \text{const},\tag{2.41}$$

$$m\left(\frac{4}{3}\mu + \zeta\right)\frac{\mathrm{d}v}{\mathrm{d}x} = F_v(v,T) \equiv P - P_i + m^2\left(v - v_i\right),\tag{2.42}$$

$$\frac{k}{m}\frac{\mathrm{d}T}{\mathrm{d}x} = F_T(v,T) \equiv e - e_i - \frac{1}{2}m^2\left(v^2 - v_i^2\right) + \left(P_i + m^2 v_i\right)\left(v - v_i\right),\tag{2.43}$$

where $\mu \geqslant 0$ is the shear viscosity, $\zeta \geqslant 0$ the volume viscosity, $k \geqslant 0$ the thermal conductivity and subscript i refers to either the pre-shock state ($i = $ A) or post-shock state ($i = $ B). The boundary conditions for the shock layer are

$$(v,T) \rightarrow (v_A, T_A) \quad \text{as} \quad x \rightarrow -\infty\tag{2.44}$$

$$(v,T) \rightarrow (v_B, T_B) \quad \text{as} \quad x \rightarrow \infty\tag{2.45}$$

and imply that

$$F_v(v_i, T_i) = 0, \qquad F_T(v_i, T_i) = 0.\tag{2.46}$$

Inserting the above condition into relations (2.41)-(2.43) yields the Rankine-Hugoniot relations for a stationary normal shock. The states satisfying (2.46) are singular points of the autonomous system (2.42)-(2.43). The analysis of these points was first performed by Weyl (1949) and subsequently extended by Gilbarg (1951), Liu (1976), Pego (1986), Menikoff & Plohr (1989), Cramer (1989b) and Cramer (1991). Here we simply report the final, important result: (i) a subsonic critical point is a saddle point while a supersonic critical point is a repulsive node and (ii) there exist trajectories connecting neighbouring critical points, but no solution connecting non-neighbouring ones. It follows that the Rayleigh line of shocks having a thermoviscous structure must not cut the shock adiabat in intermediate points. This is clearly satisfied if the fundamental derivative is strictly positive, since the Rayleigh line intersects the shock adiabat in two points only (see for example Landau & Lifshitz, 1987). Conversely, if the shock adiabat crosses a negative-Γ region, multiple intersections are possible, as shown in figure 2.2. The non-uniqueness can be resolved by requiring that the shock possess a thermoviscous profile. This criterion is more stringent than the entropy inequality and speed ordering relation, which in fact are not sufficient to rule out shocks such as A$_2$-B$_5$ in figure 2.2.

In the classical case of fluids with positive Γ, properties such as density, pressure, temperature, velocity and Mach number vary monotonically through the shock layer, while the entropy features a local maximum and then decreases to the post-shock value (see, e.g, Zel'dovich & Raizer, 1968; Thompson & Lambrakis, 1973). The transitional layer of shock waves in the non-classical gasdynamic regime was examined by Cramer & Crickenberger (1991), who presented numerical solutions of equations (2.41)-(2.43). Specifically, the investigation concentrated on compression shocks taking the fluid across the negative-Γ region and on rarefaction shocks. Following Kluwick (2001), the main results of the analysis of Cramer & Crickenberger (1991) are as follows:

- Compression shock waves that are slightly stronger (i.e. higher pressure jump) than the limiting shock whose Rayleigh line touches the shock adiabat in an intermediate point where $\Gamma < 0$ (e.g. case A$_2$-B$_7$ in figure 2.2) exhibit a sort of double layer structure. The density distribution features three inflexion points, rather than a single one, and the entropy distribution develops a second local maximum. The result is a significantly thick shock layer[3]. Increasing the shock strength, at fixed pre-shock state, causes the additional inflexion

---

[3]Note the obvious arbitrariness of the concept of thickness of the transition layer, as the length over which the change in the state can be regarded as completed, taking into account the asymptotic nature of this process. For example, Thompson & Lambrakis (1973) use the criterion of 98.7% of the overall speed change across the shock wave to determine its thickness.

points in the density and the local maximum in the entropy to disappear, along with a rapid decrease in the shock thickness.

- In contrast with the case of compression shocks, rarefaction shocks feature a local minimum of the entropy. Over most of the shock layer $s < s_A$, while the ultimate entropy increase is realised in the final stage of the transition to the post-shock state.

- At fixed pre-shock state, the thickness of rarefaction shocks first decreases with increasing shock strength and then decreases when the maximum strength (post-sonic shock) is approached.

- The transition from supersonic to subsonic flow might be non-monotonic. Extrema in the Mach number are found near $\Gamma = 0$ points. For compression and rarefaction shocks that bridge the negative-Γ region, both a local minimum and a local maximum of the Mach number develop in the shock layer. In the case of compression shocks, the local minimum is encountered first (moving from the pre-shock towards the post-shock state). The local maximum might be be supersonic, i.e. such shocks may exhibit an internal layer of supersonic flow. For rarefaction shocks, the ordering of the Mach number extrema is reversed and thus there exist regions where the Mach larger is larger/smaller than the pre-shock/post-shock value.

Also of interest is the estimate of the shock thickness Δ that is obtained for weak shocks (in the limit of vanishing shock strength) sufficiently far from the $\Gamma = 0$ curve that relation (2.28) is valid and effects related to Γ changing its sign can be neglected. The estimate for Δ, see Kluwick (2001) and Thompson & Lambrakis (1973) for an equivalent formula, is

$$\Delta \propto \left(\frac{4}{3}\mu_A + \zeta_A + k_A \frac{T_A G_A}{c_A^2} \right) \frac{6c_A}{\Gamma_A[P]}, \tag{2.47}$$

showing that the thickness of weak shocks increases with a reduction in the shock strength or in the fundamental derivative. It is also seen that in the limit of vanishing viscosity and thermal conductivity, the shock thickness is zero, as expected.

NON-IDEAL FLOWS IN CONVERGING-DIVERGING NOZZLES

The present chapter describes the computation of exact solutions for the steady flow of single-phase fluids expanding from a reservoir into a stationary ambient state with constant pressure through a conventional converging-diverging nozzle. The fluids considered are molecularly complex fluids in the non-ideal, possibly non-classical, gasdynamic regime. A novel analytical approach is introduced which makes it possible to elucidate the connection between a general adiabatic flow field and the underlying local isentropic-flow features, including their possible qualitative alterations in passing through shock waves. The global layout of the flow configurations produced by a monotonic decrease in the ambient pressure, namely the functioning regime, is examined for each possible reservoir conditions resulting in single-phase flows. Flow conditions determining the transition between the different classes of flow are investigated and each functioning regime is associated with the corresponding thermodynamic region of reservoir states. The discussion is carried out using the simple polytropic van der Waals model; the main findings are then confirmed by accurate thermodynamic models applied to fluids of practical interest.

Selected contents from:

Guardone, A. & Vimercati, D. 2016 Exact solutions to non-classical steady nozzle flows of Bethe-Zel'dovich-Thompson fluids. *J. Fluid Mech*, 800, 278-306.

3.1   Introduction and theoretical background

Nozzle flows play a central role in many applications, from rocket engines to turbines, and are also used extensively as test cases in the development and comparison of numerical schemes. The theory of nozzle flows of ideal gases is well-established and exploited in many applications that involve gases operating in dilute conditions. Here the focus is on the properties of nozzle flows in the non-ideal, possibly non-classical, gasdynamic regime.

Previous studies on non-ideal nozzle flows are as follows. Thompson (1971) first investigated the role of Γ in accelerating flows through a sonic throat, demonstrating that an anti-throat is required to accelerate to supersonic speed if $\Gamma < 0$. Cramer & Best (1991) examined steady isentropic flows of fluids in the dense-gas regime, focusing on the relation between the Mach number and the density. The main result is that the Mach number no longer increases monotonically with decreasing density if $\Gamma < 1$. In addition, if $\Gamma < 0$, the number of sonic points may increase from one only to three. Steady quasi-one-dimensional flows containing multiple sonic points were investigated also by Chandrasekar & Prasad (1991) and Kluwick (1993) in the context of transonic flows. Their work pointed out the existence of unconventional shocks, namely expansion and sonic shocks, in the neighbourhood of the throat of a converging-diverging nozzle. Moreover, these authors provided examples of stagnation conditions at the nozzle inlet (viz. reservoir states, if the nozzle is assumed to be connected to a reservoir) not allowing for shock-free flows expanding to arbitrarily large Mach numbers. The reference work of Cramer & Fry (1993) shed further light on the admissible flows of BZT fluids in a conventional converging-diverging nozzle. Solutions accounting for the entropy rise across shock waves were produced for the first time, by employing a shock fitting technique based on a sixth-order Runge-Kutta scheme. Two types of non-classical nozzle flows were introduced, in addition to the classical case (e.g. nozzle flows qualitatively similar to those of ideal gases). In a complete expansion from rest to arbitrarily large exit Mach numbers, *Type-1* flows include a rarefaction shock in the diverging section of the nozzle. Conversely, in *Type-2* nozzle flows a rarefaction shock is observed in the converging section of the nozzle.

The present research is aimed at complementing the theoretical framework delineated in the above-mentioned studies. The main focus is on the possible flow configurations that occur in a conventional converging-diverging nozzle connected to a reservoir with fixed thermodynamic state. The layout of the exact solutions produced by monotonically decreasing values of the ambient pressure determines the so-called functioning regime. As many as 10 functioning regimes are singled out: one of these is possible only if $0 < \Gamma < 1$, 8 of these are possible only if $\Gamma < 0$ (which also include the two classes of flow introduced by Cramer & Fry 1993, whose findings are confirmed by the present analysis), while the remaining one is the standard functioning regime of ideal gasdynamics $\Gamma > 1$. The leading goal of this study is to investigate the connection between reservoir conditions and functioning regimes. To this end, the precise conditions leading to the transition between different functioning regimes are determined.

The present chapter is organized as follows. Section 3.2 describes the mathematical formulation of the steady nozzle flow problem. In §3.3, nozzle flows in the non-ideal classical regime are discussed. In this framework, the main concepts of the novel analytical approach are introduced and applied to the computation of exact solutions, the identification of functioning regimes and the computation of the thermodynamic map of the reservoir conditions resulting in each functioning regime. On this basis, extension to the non-classical gasdynamic regime is presented in §3.4. Concluding remarks are given in §3.5.

3.2   Formulation

In the present study, the flow is assumed steady, inviscid, non-heat-conducting, non-reacting and single-phase. The quasi-one-dimensional approximation is used to model the fluid flow through the nozzle (see, e.g., Thompson, 1988). The quasi-one-dimensional governing equations for smooth, i.e. shock-free, flows are the algebraic equations enforcing the conservation of mass, of total enthalpy and entropy, namely

$$\rho u A(x) = \text{const}, \tag{3.1}$$

$$h^t = \text{const}, \tag{3.2}$$

$$s = \text{const}, \tag{3.3}$$

where $A(x)$ is the known cross-sectional area distribution along the axial coordinate x. The variables appearing in (3.1)-(3.3) should be regarded as averaged values over the cross section. Discontinuous solutions including shock waves are accounted for by means of the Rankine-Hugoniot jump relations discussed in §2.3. Because the flow is quasi-one-dimensional, only normal shocks needs to be considered.

In the following, we consider a converging-diverging nozzle $x \in [-1, 1]$ described by a fifth-order polynomial, whose coefficients are computed to set the inlet area $A(-1) = 1.2$, the throat area $A(0) = 1$ and an exit area $A(1) = 1.5$, and by imposing that the inlet, the throat and the exit stations are stationary points of the area distribution. The resulting law is

$$A(x) = -0.225x^5 - 0.35x^4 + 0.375x^3 + 0.7x^2 + 1, \qquad x \in [-1, 1] \tag{3.4}$$

and is sketched in figure 3.1. The above area distribution is chosen as an example for plotting purposes. In fact, the results presented in the following are qualitatively independent from the actual geometry, provided that the nozzle is a converging-diverging duct.

In order to complete the problem, a suitable thermodynamic model of the fluid must be specified. For explanatory purposes, nozzle flows are first illustrated using the polytropic van der Waals model (see van der Waals 1873 and Appendix A), which predicts the correct qualitative behaviour in the thermodynamic region of interest in this work, as shown for instance by Thompson & Lambrakis (1973), Kluwick (2001), Guardone *et al.* (2004), Guardone & Argrow (2005). For van der Waals fluids, the topology of Γ depends exclusively on the dimensionless isochoric specific heat c_v/R, where c_v is the isochoric specific heat and R is the gas constant. In the single-phase vapour or gas region, $\Gamma > 1$ if $c_v/R \lesssim 3.78$, $\Gamma > 1$, a region $0 < \Gamma < 1$ exists if $3.78 \lesssim c_v/R \lesssim 16.66$ while the BZT region $\Gamma < 0$ exists provided $c_v/R \gtrsim 16.66$, see Colonna & Guardone (2006). Subsequently, the predictions of the simple van der Waals model are verified against those of accurate multi-parameter models from the REFPROP library.

3.3   Classical nozzle flows

The general framework for the inspection of non-ideal nozzle flows is established in this section devoted to the classical gasdynamic regime. Many of the concepts familiar to nozzle flows of ideal gases are reviewed and extended to the non-ideal context. Functioning regimes and their exact solutions described in §3.3.3 are conveniently anticipated and explained through the isentropic flow model of §3.3.1. The link between the functioning regime and the reservoir conditions is investigated in §3.3.4.
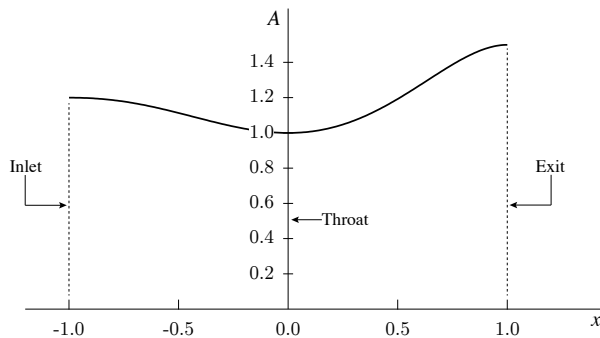
FIGURE 3.1. Cross-sectional area distribution considered in this work.

3.3.1 Isentropic flow

According to the governing equations of quasi-one-dimensional steady flows, the mass flow rate $\dot{m} = \rho u A(x)$ and the total enthalpy h^t are uniform both in shock-free and in shocked flows. The entropy s, on the other hand, is piecewise uniform with finite jumps occurring across shock waves. It follows that the general features of quasi-1D steady nozzle flows can be explained in a comprehensive manner by examining the isentropic flows with constant total enthalpy.

We start by commenting on the relation between the Mach number

$$M = u/c = \sqrt{2(h^t - h)}/c \qquad (3.5)$$

and the density in non-ideal compressible flows. Following Thompson (1971) and Cramer & Best (1991), the first derivative of the Mach number with respect to the density is recast in non-dimensional form as

$$J = \frac{\rho}{M}\frac{\mathrm{d}M}{\mathrm{d}\rho} = 1 - \Gamma - \frac{1}{M^2}. \qquad (3.6)$$

In flows of fluids having $\Gamma > 1$, the Mach number always decreases upon isentropic compression. Conversely, if $\Gamma < 1$, the Mach number can possibly increase with density. The variation of the Mach number along exemplary non-ideal isentropic flows is sketched in figure 3.2(a), where the van der Waals model with $c_v/R = 15$ is used. The current model specification allows for the existence of region $0 < \Gamma < 1$ in the vapour phase and is used throughout this section to illustrate qualitative aspects. The (M, ρ)–diagram of figure 3.2(a) is generated for a fixed value of the total enthalpy. Thus, each curve corresponds to a different entropy value along the same isenthalpic line $h = h^t$.

Isentropes in figure 3.2(a) intersect the vapour-liquid phase boundary along curve labelled M^{sat}. A wide portion of the saturated vapour boundary of the fluid considered is retrograde (see Thompson et al., 1986; Menikoff & Plohr, 1989), meaning that isentropes cross the phase boundary from the mixed towards the pure phase, in the direction of decreasing density.[1] We limit the present analysis to single-phase flows, i.e. to the subset of isentropes not crossing the saturated phase boundaries. Two-phase effects, as well as critical-point phenomena which affect near-to-critical isentropes are outside the scope of this work.

The stationary points of the Mach number form the locus $J = 0$, whose general shape can be explained by analysing the evolution of Γ along isentropes featuring $\Gamma < 1$ (see, e.g., Bethe, 1942;

---

[1]All isentropes eventually enter the two-phase region crossing a non-retrograde saturated phase boundary. The ultimate intersection with the non-retrograde portion of the saturated vapour boundary typically occurs at extremely low density values, compared to those characterizing the thermodynamic region of interest in this work, that it is reasonable to assume that isentropes cross saturation boundaries only if $s < s_{vle}$, where s_{vle} denotes the isentrope tangent to the vapour dome.
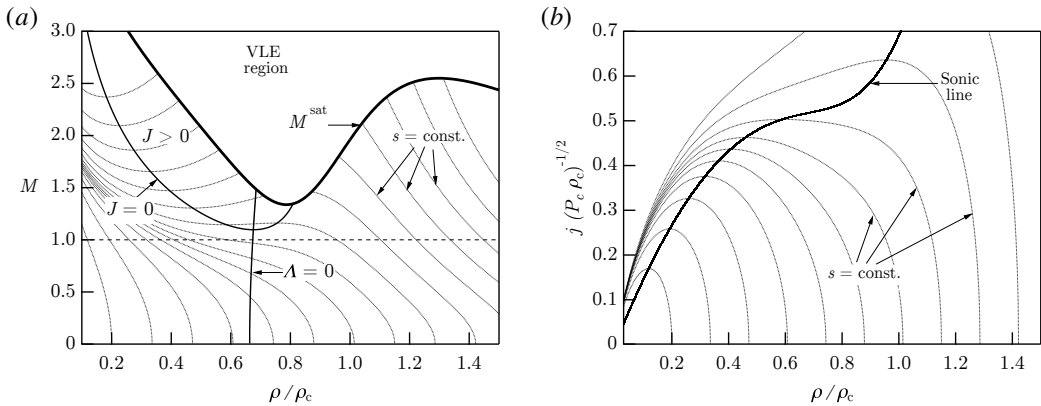
FIGURE 3.2. Variation of (a) Mach number and (b) mass flux function with the density along exemplary isentropes, as computed from the polytropic van der Waals model with $c_v/R = 15$. Variables have been made dimensionless using critical-point quantities (subscript c). The total enthalpy is constant, $h^t = h(1.0700 P_c, v_c)$.

Zel'dovich, 1946; Thompson & Lambrakis, 1973). On these isentropes, $\Gamma - 1$ has two zeros with a local minimum in between, where $\Lambda = \rho \, (\partial \Gamma / \partial \rho)_s$ vanishes. We differentiate (3.6) to obtain, after evaluation at $J = 0$,

$$\frac{\mathrm{d}^2 M}{\mathrm{d}\rho^2}\bigg|_{J=0} = -\frac{M}{\rho^2}\Lambda. \tag{3.7}$$

Thus, stationary points of the Mach number located at higher densities ($\Lambda > 0$) and at lower densities ($\Lambda < 0$) of the $\Lambda = 0$ locus are local maxima and minima, respectively.

It is evident from figure 3.2(a) that isentropes corresponding to sufficiently large stagnation densities must cross the $J > 0$ region. This is consistent with the fact that $J > 0$ if the region $\Gamma < 1$ is crossed at large values of the Mach number. We restrict the discussion to those curves that represent a single-phase expansion from stagnation conditions to vacuum. In this case, isentropes entering the $J > 0$ region exhibit both a local minimum and a local maximum of the Mach number. Since $\Gamma > 0$ in the single-phase vapour region of the van der Waals fluid considered here, the $J = 0$ locus is confined in the supersonic region $M > 1$. Thus, only supersonic flows will have extrema in the Mach number. Among the other things, this means that only one sonic point occurs along an isentropic expansion with constant total enthalpy. By decreasing the stagnation density, the two stationary points eventually merge in a stationary inflection point. If the stagnation density is further decreased, the Mach number ultimately becomes a monotone decreasing function of the density.

Next, we consider the variation of the mass flux function

$$j = \rho u = \rho \sqrt{2(h^t - h)} \tag{3.8}$$

with the density, in isentropic flows with constant total enthalpy. To determine whether j increases or decreases with ρ, the above relation is differentiated to obtain

$$\frac{1}{c}\frac{\mathrm{d}j}{\mathrm{d}\rho} = \frac{M^2 - 1}{M}. \tag{3.9}$$

Thus, the mass flux function increases (decreases) upon supersonic (subsonic) isentropic compression and sonic points are extrema. To determine the type of extrema, we differentiate (3.9) and

27

FIGURE 3.3. Phase plane illustrating density distributions for classical flows in converging-diverging nozzle, for different values of the mass flow rate. The value ρ_s denotes the sonic density.
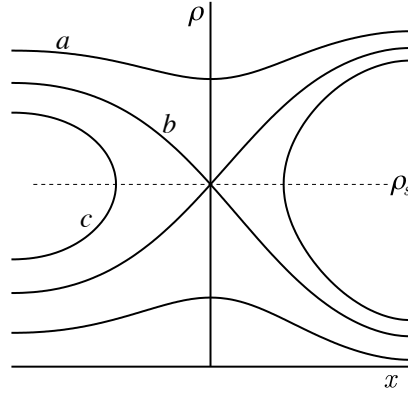
make use of relation (3.6), obtaining

$$\frac{\rho}{c} \frac{\mathrm{d}^2 j}{\mathrm{d}\rho^2}\bigg|_{M=1} = -2\Gamma, \tag{3.10}$$

which shows that a sonic point is a local maximum, minimum or stationary inflection point of the mass flux if Γ is positive, negative or null at that point, respectively. A similar analysis was performed by Kluwick (1993, 2004), albeit in the context of small perturbations in transonic flows. Figure 3.2(b) illustrates exemplary mass flux functions corresponding to different entropy values chosen along the isenthalpic locus $h = h^t$.

Strictly related to the flux function is the phase plane, i.e. the contour plot of the mass flow rate

$$\dot{m} = j(\rho; s, h^t) A(x) \tag{3.11}$$

in the (ρ, x)-diagram, for fixed entropy and total enthalpy. In the phase plane it is possible to predict the possible isentropic flows in a nozzle of given geometry, and, to a certain extent, it can anticipate the occurrence of non-isentropic flows. It is well-known that the density distribution in quasi-1D flows with constant entropy and total enthalpy satisfies the differential relation

$$\frac{1}{\rho} \frac{\mathrm{d}\rho}{\mathrm{d}x} = \frac{M^2}{1 - M^2} \frac{A'}{A}, \tag{3.12}$$

see Courant & Friedrichs (1948), and thus a subsonic flow expands upon area contraction and is compressed otherwise, while a supersonic flow is compressed upon area contraction and expanded otherwise. In the classical gasdynamic regime, phase planes are saddle shaped, as shown in figure 3.3. The value of the mass flow rate given by

$$\dot{m}_c = \max_{\rho} j(\rho; s, h^t) \min_{x} A(x), \tag{3.13}$$

corresponds to the saddle point and it is referred to as critical mass flow rate. In the present case $\dot{m}_c = j(\rho_s; s, h^t) A_{tr}$, where A_{tr} is the throat area and ρ_s denotes the density value at the sonic point. Given that we are interested in the expansion from a reservoir, we will naturally focus on subsonic inlet conditions. Curves such as a in figure 3.3 display $\dot{m} < \dot{m}_c$ and result in strictly subsonic flows. The curve labelled b in figure 3.3 corresponds to $\dot{m} = \dot{m}_c$. Subsonic-supersonic transition is possible, as well as completely subsonic flow with sonic throat. Along curves such as curve c, which display $\dot{m} > \dot{m}_c$, sonic conditions occur upstream of the throat and the flow cannot be continued beyond this point. These trajectories have no physical relevance in steady isentropic flows discharging from a still reservoir.

Isentropic pattern	Number of sonic points	$J\|_{M<1}$	$J\|_{M>1}$	$\max\limits_{\rho} j$
$\mathscr{S}^{I}$	1	$J<0$	$J<0$	ρ_s
$\mathscr{S}^{NI}$	1	$J<0$	$J \lesseqgtr 0$	ρ_s

TABLE 3.1. Description of isentropic patterns for non-ideal classical nozzle flows.
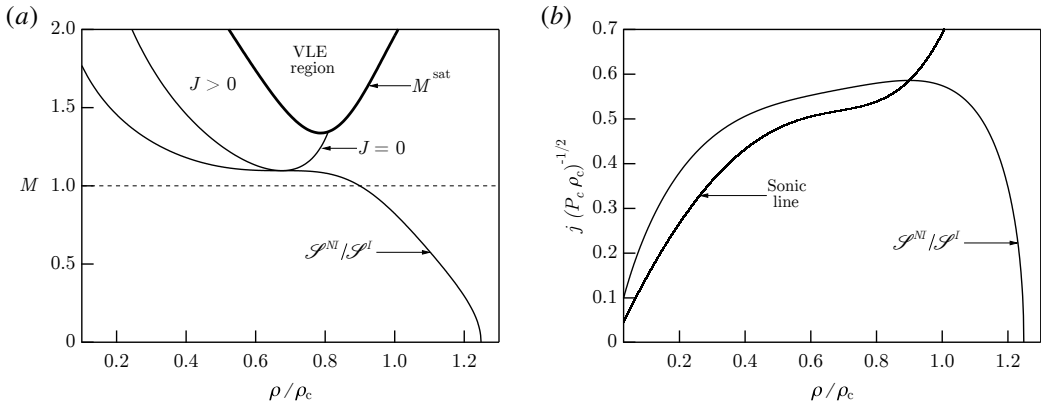
FIGURE 3.4. Variation of (a) Mach number and (b) mass flux function with the density for an exemplary transitional isentropic flow, computed from the polytropic van der Waals model with $c_v/R = 15$. The total enthalpy is constant and equal to the value used in the computation of figure 3.2.

3.3.2 Isentropic patterns

In order to examine piece-wise isentropic flows and determining functioning regimes in nozzles, it is useful to introduce the concept of *isentropic pattern*, in the following denoted with the symbol $\mathscr{S}$, as a way of classifying isentropic nozzle flows. In the classical gasdynamic regimes, two different isentropic patterns can be identified as follows. We regard any isentropic flow as ideal (i.e. ideal-gas like), and we denote the corresponding ideal isentropic pattern as $\mathscr{S}^{I}$, if the Mach number monotonically increases with decreasing density in a complete expansion from stagnation. Such flows will of course exhibit a single sonic point. The monotonicity of the Mach number may break down in the supersonic regime of flows evolving under non-ideal conditions, namely $0 < \Gamma < 1$. The corresponding non-ideal pattern is denoted as $\mathscr{S}^{NI}$. The outcome of this classification is summarized in table 3.1

The transition between isentropic patterns $\mathscr{S}^{NI}$ and $\mathscr{S}^{I}$ is marked by the limiting isentrope which exhibits a stationary inflection point in the Mach number distribution, as shown in figure 3.4. Thus, the isentrope corresponding to the transitional pattern $\mathscr{S}^{NI}/\mathscr{S}^{I}$ is tangent to the $J = 0$ curve at its minimum value of the Mach number, i.e. where $J = 0$ and $\Lambda = 0$ simultaneously, see equations (3.6) and (3.7).

By varying the total enthalpy and gathering the stagnation state corresponding to the transitional isentropic patterns, the thermodynamic map of figure 3.5 is ultimately obtained. This map allows one to determine the isentropic pattern resulting from a given pair of stagnation conditions. Due to the assumption of considering single-phase flows, the thermodynamic region of interest is bounded from below by the isentrope s_{vle} tangent to the saturation curve. If $s_{vle} < s < s_{\tau,1}$, where $s_{\tau,1}$ denotes the isentrope tangent to the locus $\Gamma = 1$, both $\mathscr{S}^{I}$ and $\mathscr{S}^{NI}$ can occur depending on the stagnation state. Consistently with the observed layout in figure 3.2, isentropic pattern $\mathscr{S}^{NI}$ occurs
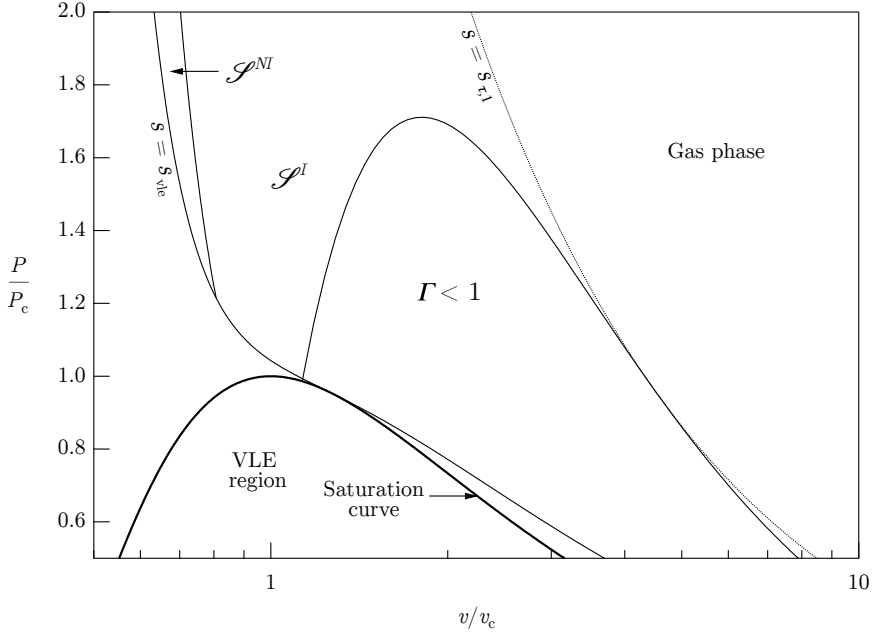
FIGURE 3.5. Thermodynamic map of stagnation states associated with each isentropic pattern, as computed from the van der Waals polytropic model with $c_v/R = 15$. Curves labelled $s = s_{vle}$ and $s = s_{\tau,1}$ represent the isentropes tangent to the vapour-liquid saturation curve and to the $\Gamma = 1$ locus, respectively.

for sufficiently large stagnation densities. If $\Gamma > 1$ everywhere along the reference isentrope, e.g. for $s > s_{\tau,1}$, the Mach number is a monotone decreasing function of the density and pattern $\mathscr{S}^I$ only can take place.

The identification of the different types of isentropic flow behaviour is essential prior to the construction of general solutions to nozzle flows, which possibly include shock waves. Indeed, smooth branches of any quasi-1D flow can be associated locally with an isentropic pattern. The entropy jump across shock waves results in a shift of the associated isentropic curve and can possibly result in the qualitative modification of the flow behaviour, i.e. in a transition of the isentropic pattern. The second law of thermodynamics dictates the direction in which this process can possibly occur. To show this, we first note that

$$\left(\frac{\partial \rho}{\partial s}\right)_h = -\frac{\rho T(1 + G)}{c^2} < 0, \tag{3.14}$$

where $G = v(\partial P/\partial e)_v$ is the Grüneisen parameter, which we assume to be positive here throughout. Menikoff & Plohr (1989) discussed the assumption of $G > 0$ for real materials, which is implied by a positive value of the coefficient of thermal expansion, a condition fulfilled by most fluids of interest (with the relevant exception of water at 0 °C and 1 bar, see Bethe 1942). Equation (3.14) implies that the stagnation density decreases with increasing entropy at constant total enthalpy. Therefore, with reference to figure 3.4(a), transitions of the isentropic pattern occur in the direction of increasing entropy as follows:

$$\mathscr{S}^{NI} \to \mathscr{S}^I. \tag{3.15}$$

Thus, in classical gasdynamics, the occurrence of shock waves can possibly drive the flow field to ideal-gas like behaviour; on the contrary, the opposite situation is not possible, i.e. an isentropic

flow having the qualitative features of ideal flows cannot turn into one presenting the non-ideal, non-monotonic Mach number profile.

3.3.3 Functioning regimes

We now derive exact solutions for steady flows in a converging-diverging nozzle, which is regarded as a discharging device between a reservoir and a stationary atmosphere. Thus, we will naturally focus on subsonic flow conditions at the nozzle inlet. The boundary condition in our problem are the reservoir conditions, i.e. a couple of thermodynamic variables describing the reservoir state, and the ambient pressure P_a in the downstream environment (which will be, in general, different from the pressure P_e observed at the exit section of the nozzle).

Specifically, the dependence of the flow field on P_a, or similarly on the ambient to reservoir pressure ratio $\varepsilon = P_a/P_r$, is examined for given reservoir conditions. When the range $0 < \varepsilon \leqslant 1$ is spanned, a specific sequence of solutions is observed, which together delineate the *functioning regime*, referred to as $\mathscr{R}$ in the following. Remarkably, each functioning regime can be represented by relatively few special solutions of the nozzle flow: the *limiting* solutions and selected *intermediate* solutions. A particular flow field is a limiting solution of the nozzle problem if an arbitrary small variation of the ambient pressure produces modifications to its qualitative structure, that is, limiting solutions are isolated solutions of the boundary value problem. Correspondingly, a set of limiting values of the ambient pressure is defined; each pressure value is associated with a limiting flow. On the contrary, an intermediate solution remains qualitatively unaltered under arbitrary small variations of the ambient pressure. Intermediate solutions are observed whenever the ambient pressure lies between two consecutive limiting ambient pressures. Generally speaking, the qualitative structure of a solution is characterized, among the others, by the presence of a sonic throat and by the existence and the possible sequence of shock waves. This will be made clear in the subsequent discussion.

3.3.3.1 Computation of exact solutions

The mass balance equation recast in the form

$$j(\rho; s, h^t)A(x) - \dot{m} = 0 \tag{3.16}$$

provides an implicit definition of the density distribution $\rho(x; s, h^t, \dot{m})$ in smooth regions of the flow field, which will be coupled with the application of the Rankine-Hugoniot relations (2.10)-(2.12) across shock waves, if any are present. For a general, non-ideal thermodynamic model, equations (2.10)-(2.12) and (3.16) are non-linear equations which can be solved using standard root-finding algorithms, up to arbitrary accuracy. Equation (3.16) will yield at least two different roots if $\dot{m} < \dot{m}_c$, one subsonic and one supersonic. Smooth transition from subsonic to supersonic flow can be attained only at the throat of the nozzle (if $M = 1$ and $A'(x) \neq 0$, the slope of the density distribution goes to infinity, see relation (3.12) and figure 3.3). Non-smooth supersonic to subsonic transition is of course possible across a shock wave.

In order to compute the roots of equation (3.16), three parameters need to be specified, namely the entropy, the total enthalpy and the mass flow rate. Of these parameters, only the total enthalpy is known a priori, since from governing equations it is uniform throughout the nozzle and equal to the reservoir enthalpy. The entropy, which changes across the nozzle only if shock waves are present, and the mass flow rate depend also on the value of the ambient pressure. The complex connection between the boundary conditions, the entropy and the mass flow rate is clarified with a practical example in the following section.
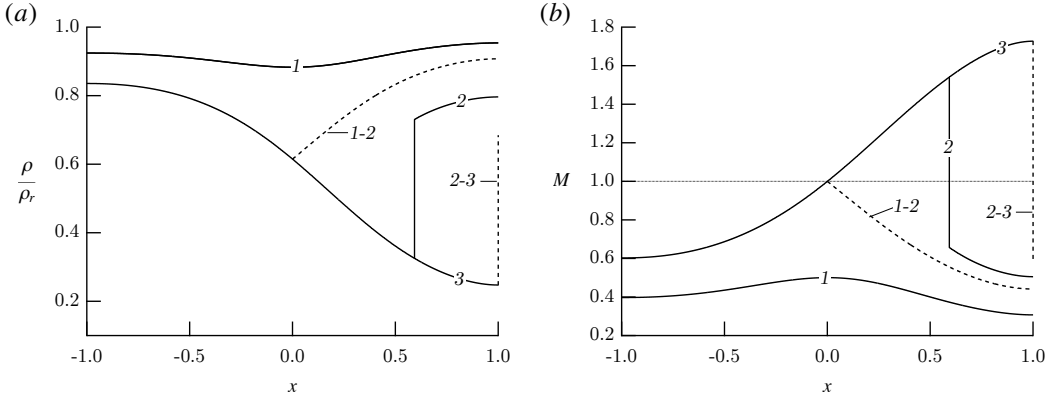
(a)

(b)

FIGURE 3.6. Exemplary limiting (- - - -) and intermediate (——) flows of type $\mathscr{R}^I$, computed from the van der Waals polytropic model with $c_v/R = 15$. (a) Density solutions, scaled to reservoir density ρ_r; (b) Mach number solutions. Reservoir conditions: $P_r = 10P_c$, $v_r = 10v_c$.

3.3.3.2   Functioning regime $\mathscr{R}^I$

The layout of the possible flow configurations produced by $\mathscr{S}^I$ reservoir conditions corresponds to the textbook case of an ideal gas with constant specific heats (see, e.g., Thompson, 1988) and is denoted here as $\mathscr{R}^I$. The main results are reported here for reference and are extended to a general, non-ideal thermodynamic description of the fluid. Limiting and intermediate flows are reported in figure 3.6. Flows of type $\mathscr{R}^I(1)$ are completely subsonic and are characterized by increasing mass flow rate with decreasing ambient pressure. Limiting solution $\mathscr{R}^I(1\text{-}2)$ determines the so-called *chocking* condition, because the throat is sonic and a further decrease of the ambient pressure has no influence on the mass flow rate. Let $\dot{m}_{max}$ denote the maximum mass flow rate dischargeable by the nozzle and $\dot{m}_s$ the mass flow rate in the choked condition; then

$$\dot{m}_{max} = \dot{m}_s = \dot{m}_c(s_r, h^t), \qquad (3.17)$$

where the critical mass flow rate $\dot{m}_c$ is defined by (3.13) and s_r is the reservoir entropy. If $\varepsilon < \varepsilon_{1\text{-}2}$, where $\varepsilon_{1\text{-}2}$ is the pressure ratio corresponding to limiting solution $\mathscr{R}^I(1\text{-}2)$, the flow is choked and subsonic to supersonic transition occurs at the throat.

Pressure ratios slightly lower than $\varepsilon_{1\text{-}2}$ cannot be attained in isentropic flows, as the phase plane analysis suggests. Matching with the imposed downstream boundary condition can be realised by inserting a shock wave in the diverging section of the nozzle, as in intermediate flows of type $\mathscr{R}^I(2)$. It can be shown that the entropy jump across the shock wave increases with decreasing ambient pressure. To this end, inserting $\rho = \rho(s, P)$ into the mass balance equation, we obtain an implicit definition of $s(P; \dot{m}, h^t, A)$. By evaluating this relation on the exit section, with $\dot{m} = \dot{m}_{max}$, $A = A_e$ and h^t fixed, we have

$$\frac{\mathrm{d}s_e}{\mathrm{d}P_e} = \frac{M_e^2 - 1}{\rho_e T_e (M_e^2 G_e + 1)}. \qquad (3.18)$$

Note that if the outflow is subsonic, as it is the case for solutions of type $\mathscr{R}^I(2)$, then $P_e = P_a$ and $ds_e/dP_e = ds_e/dP_a$ in the corresponding range of ε. In addition, by combining the jump relations and the differential relations for quasi-1D flows, the following relation between the shock wave
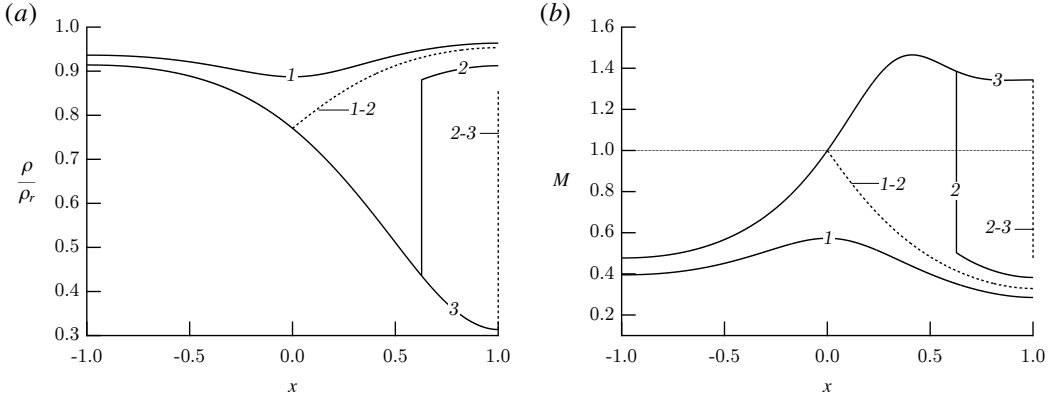
FIGURE 3.7. Exemplary limiting (- - - -) and intermediate (——) flows of type $\mathscr{R}^{NI}$, computed from the van der Waals polytropic model with $c_v/R = 15$. (a) Density solutions, scaled to reservoir density ρ_r; (b) Mach number solutions. Reservoir conditions: $P_r = 1.6P_c$, $v_r = 0.7v_c$.

location x_s and the entropy s_B downstream of a shock wave is obtained:

$$\frac{\mathrm{d}x_s}{\mathrm{d}s_B} = \frac{A}{A'}\frac{\rho_A T_B}{[P]}\left(\frac{1}{M_B^2} + \frac{[v]}{2v_B}B_B\right)\left[\left(\frac{1}{M_B^2} - 1\right)\frac{v_B}{v_A} + \frac{1}{2}\right]^{-1}. \tag{3.19}$$

Given that $M_B < 1$, the last two terms in the above expression are positive (ordinary shock adiabats satisfy $2v_B + [v]G_B \geqslant 0$, see §2.3.2). Hence, a compression shock in the diverging section of the nozzle moves downstream with increasing post-shock entropy, which, in turn, corresponds to decreasing values of the ambient pressure, as shown by (3.18) together with $s_e = s_B$ and $P_e = P_a$. Ultimately, the shock wave reaches the exit section, see limiting flow $\mathscr{R}^I(2\text{-}3)$. Flows of type $\mathscr{R}^I(3)$ are completely isentropic expansion with supersonic exit conditions. If $\varepsilon \neq \varepsilon_3$, where ε_3 corresponds to the exit pressure of solution $\mathscr{R}^I(3)$, in which the nozzle is said to be adapted, an over-expanded jet ($\varepsilon > \varepsilon_3$) or an under-expanded jet ($\varepsilon < \varepsilon_3$) develops outside of the nozzle.

3.3.3.3 Functioning regime $\mathscr{R}^{NI}$

A distinguished functioning regime, termed $\mathscr{R}^{NI}$, stems from reservoir conditions associated with isentropic pattern $\mathscr{S}^{NI}$, owing to the non-monotonic evolution of the Mach number in supersonic flows. Limiting solution $\mathscr{R}^{NI}(3)$ exhibits this feature, as shown in figure 3.7. Extrema in the Mach number may also occur in the supersonic expansion of solutions of type $\mathscr{R}^{NI}(2)$, provided that the shock wave is located sufficiently downstream the throat. On the other hand, the layout and the general properties of the density distributions and of the Mach solutions of type $\mathscr{R}^{NI}(1)$ and $\mathscr{R}^{NI}(3)$ is as described above for the case $\mathscr{R}^I$. Note that transition $\mathscr{S}^{NI} \rightarrow \mathscr{S}^I$ can possibly occur across the shock wave of flow $\mathscr{R}^{NI}(2)$. However, no change in the qualitative structure of the solution is detected, as patterns $\mathscr{S}^{NI}$ and $\mathscr{S}^I$ present similar features in subsonic flows.

3.3.4 Thermodynamic map of functioning regimes

With the same approach used to compute the map of the stagnation states associated with each isentropic pattern, a thermodynamic map of the reservoir states leading to each functioning regime has been generated and is shown in figure 3.8. The present map allows one to determine the functioning regime resulting from a given pair of stagnation conditions, and it should be compared
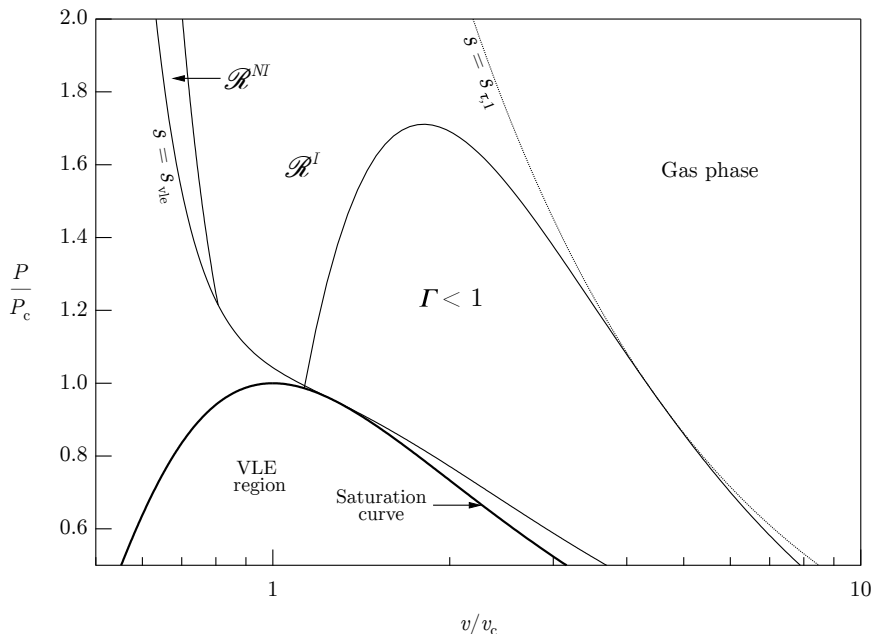
FIGURE 3.8. Thermodynamic map of reservoir states associated with each functioning regime, as computed from the van der Waals polytropic model with $c_v/R = 15$. Curves labelled $s = s_{vle}$ and $s = s_{\tau,1}$ represent the isentropes tangent to the vapour-liquid saturation curve and to the $\Gamma = 1$ locus, respectively.

with the map of the isentropic patterns in figure 3.5. Since there exists a one-to-one correspondence between functioning regime $\mathscr{R}^I$ and reservoir states featuring isentropic pattern $\mathscr{S}^I$, as well as between functioning regime $\mathscr{R}^{NI}$ and reservoir states featuring isentropic pattern $\mathscr{S}^{NI}$, the map of the functioning regimes in classical gasdynamics is formally identical to that of the isentropic patterns. Thus, under the assumption of considering single-phase flows, regime $\mathscr{R}^{NI}$ can be observed only from reservoir states along isentropes $s_{vle} < s < s_{\tau,1}$ and having sufficiently large density, i.e. larger than those corresponding to the transitional line $\mathscr{S}^{NI}/\mathscr{S}^I$.

3.3.4.1 Results of accurate models for selected substances

The polytropic van der Waals model has been used to illustrate nozzle flows of single-phase fluids in the non-ideal classical gasdynamic regime. From a qualitative standpoint, the current theoretical framework does not depend on the specific choice of the thermodynamic model. The existence of the non-ideal functioning regime $\mathscr{R}^{NI}$, in addition to the ideal-gas-like regime $\mathscr{R}^I$, is indeed found to result from the increase of the speed of sound along isentropic expansions, i.e. to the existence of a $\Gamma < 1$ region in the vapour phase. Thus, different thermodynamic models predicting $\Gamma < 1$ in the vapour phase will generate qualitatively similar maps of the functioning regimes. To support this claim, the simple van der Waals model is here abandoned in favour of more complex multi-parameter equations of state of the well-established library REFPROP (Lemmon *et al.*, 2013). These modern thermodynamic models allow computations of all relevant thermodynamic properties (except in the very close proximity of the critical point, where analytical models notoriously fail) with the accuracy required for design and analysis of advanced technical applications. The selected fluids to demonstrate the general validity of the theoretical framework delineated using the van der Waals model are MDM (octamethyltrisiloxane,
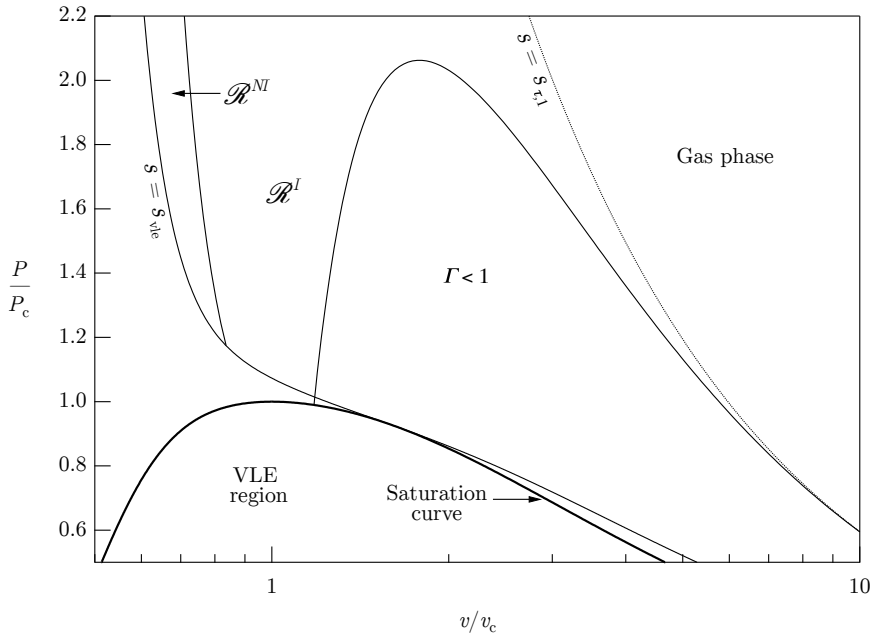
FIGURE 3.9. Thermodynamic map of reservoir states associated with each functioning regime, as computed from reference thermodynamic model of MDM (REFPROP library). See figure 3.8 for full caption.

$C_8H_2 4O_2Si_3$), modelled with the EoS of Thol *et al.* (2017) and toluene (C_7H_8), modelled with the EoS of Lemmon & Span (2006). These are multiparameter models in the Span-Wagner functional form (see Appendix A). The thermodynamic maps of the functioning regimes for MDM (figure 3.9) and toluene (figure 3.10) show excellent qualitative agreement with the picture given by the simple van der Waals model.

3.4 Non-classical nozzle flows

In this section, steady nozzle flows of BZT fluids are examined by adopting the analytical approach introduced in the previous section. The focus is on the non-classical gasdynamic regime, where the present approach is best suited and reveals its full capability. The discussion follows the same lines as the previous section. Firstly, the main properties of isentropic flows are investigated in §3.4.1 and non-classical isentropic patterns are singled out. Functioning regimes are presented in §3.4.3 and the related thermodynamic maps in §3.4.4.

3.4.1 Isentropic flow

The analysis presented here is intended to show the peculiarities associated with thermodynamic states featuring $\Gamma < 0$. To this end, the qualitative description of the flow will be performed using the polytropic van der Waals model of an exemplary BZT fluid with dimensionless isochoric specific heat equal to $c_v/R = 50$.

Figures 3.11(*a*) and 3.11(*b*) show the distribution of the Mach number and mass flux function, respectively, along exemplary isentropes crossing the negative-Γ domain. As before, the analysis presented here is based on the assumption of fixed total enthalpy, i.e. the stagnation states in figure
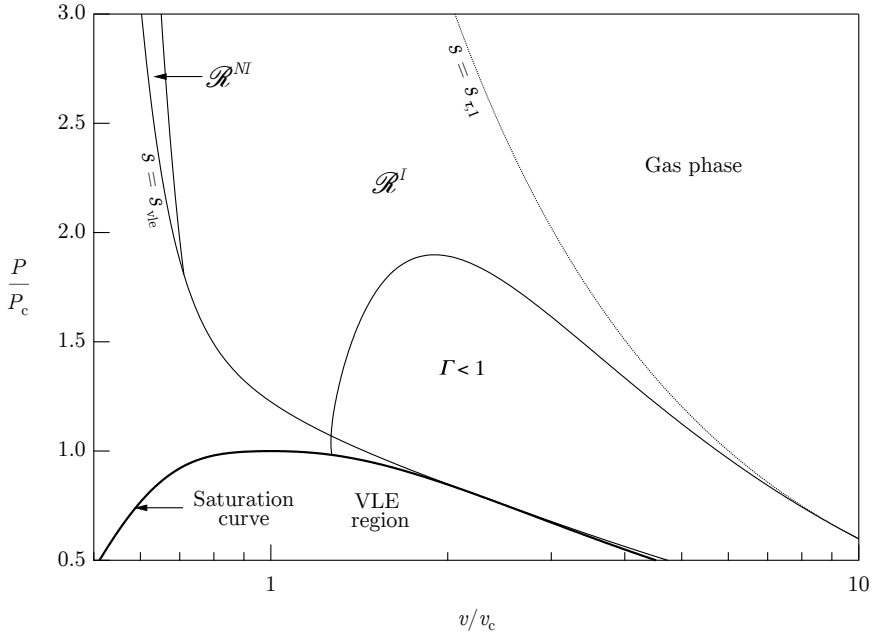
FIGURE 3.10. Thermodynamic map of reservoir states associated with each functioning regime, as computed from reference thermodynamic model of Toluene (REFPROP library). See figure 3.8 for full caption.

3.11(a) correspond to different entropy values on the same isenthalpic line $h = h^t$. With reference to figure 3.11(a), the main difference with respect to the classical gasdynamic regime is that the $J = 0$ locus now extends to the subsonic region $M < 1$. Focusing on curves in the single-phase region during a full expansion from stagnation conditions to vacuum, we note that isentropes corresponding to sufficiently large stagnation densities cross the $J > 0$ region, thus exhibiting extrema in the Mach number. If the local maximum occurs at sufficiently high Mach numbers, the flow remains supersonic upon further expansion. On the other hand, if the local maximum is only slightly supersonic, the flow becomes subsonic inside the $J > 0$ region. As a result, the selected isentrope exhibits three sonic points. By decreasing the stagnation density, the two stationary become subsonic and eventually merge in a stationary inflection point. If the stagnation density is further decreased, the Mach number ultimately becomes a monotone decreasing function of the density.

Phase plane representative of the different types of non-classical isentropic flows are sketched in figure 3.12. Isentropes containing a single sonic point generate saddle-shaped phase planes, as shown see figure 3.12(a). This layout is qualitatively identical to one previously described for classical nozzle flows; we'll thus omit the description of the related curves. The non-classical flows we are mainly interested in are those associated to isentropes including three sonic points. Phase planes related to such isentropes exhibit two saddle points with a local minimum in between. Given the following ordering for the sonic values of the density,

$$\rho_{s_3} < \rho_{s_2} < \rho_{s_1}, \tag{3.20}$$

two different categories of phase plane can be distinguished depending on the sonic density associated with the critical mass flow rate.

The case $\dot{m}_c = j(\rho_{s_3}; s, h^t) A_{tr}$, with $\dot{m}_c$ defined by equation (3.13), is depicted in figure 3.12(b). Note that this corresponds to having the sonic density ρ_{s_3} at the global maximum of
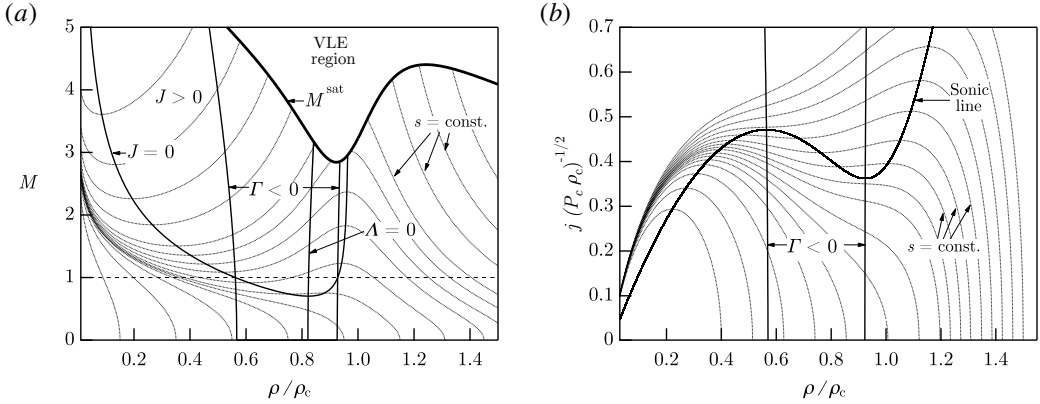
FIGURE 3.11. Variation of (*a*) Mach number and (*b*) mass flux function with the density along exemplary isentropes, as computed from the polytropic van der Waals model with $c_v/R = 50$. The total enthalpy is constant, $h^t = h(1.0182P_c, v_c)$.

the associated mass flux function. We follow Cramer & Fry (1993) in referring to this kind of non-classical phase plane as *Type-2* phase plane. Focusing on trajectories with subsonic inlet conditions, we not that in figure 3.12(*b*), in addition to the possible cases presented in figure 3.3(*a*), there exist curves connecting the inlet and exit sections in which sonic conditions are encountered either upstream or downstream of the throat. For example, if $\dot{m} = j(\rho_{s_1}; s, h^t)A_{tr}$, curve labelled *b* is generated which corresponds to a flow that is sonic both at the throat ($\rho = \rho_{s_1}$) and in the diverging section ($\rho = \rho_{s_2}$). However, at $\rho = \rho_{s_2}$ the slope $d\rho/dx$ goes to infinity (see equation 3.12) and the trajectory has a turning point. Therefore, the flow cannot be continued isentropically beyond this sonic point. Curves labelled *c* ($\dot{m} < \dot{m}_c$) and *d* ($\dot{m} = \dot{m}_c$) also include multiple sonic points and, such as case *b*, these paths cannot be accomplished in a steady-state isentropic flow.

Figure 3.12(*c*) describes the case $\dot{m}_c = j(\rho_{s_1}; s, h^t)A_{tr}$, which is referred to as *Type-1* phase plane in accordance with the nomenclature proposed by Cramer & Fry (1993). In this case, sonic density ρ_{s_1} corresponds to the global maximum of the associated mass flux function. Significant trajectories with subsonic inlet are those of type *a* ($\dot{m} < \dot{m}_c$) and *b* ($\dot{m} = \dot{m}_c$). The latter cannot be continued beyond sonic point ρ_{s_2}, which occurs downstream of the throat.

3.4.2 Isentropic patterns

In view of the different types of isentropic flow observed in the non-classical gasdynamic regime of BZT fluids, we propose a classification of isentropic flows into five different isentropic patterns, as detailed in table 3.2. In addition to the ideal pattern $\mathscr{S}^I$ and the non-ideal pattern $\mathscr{S}^{NI}$, attainable also in the classical gasdynamic regime, three different non-classical isentropic patterns can be distinguished. Firstly, if Γ becomes negative, the Mach number may increase with increasing density also in the subsonic regime. Pattern $\mathscr{S}_3^{NC}$ refers to isentropes having a single sonic point and featuring $J > 0$ for in subsonic flow. Following Cramer & Fry (1993), isentropic flows including three sonic point are classified according to the layout of the related phase plane. We formally define patterns of type $\mathscr{S}_2^{NC}$ as those exhibiting a phase plane qualitatively similar to that of figure 3.12(*b*), i.e. when the critical mass flow rate is attained with ρ_{s_3} at the throat. Isentropic pattern $\mathscr{S}_1^{NC}$ is associated to the phase plane of figure 3.12(*c*), for which the critical mass flow rate is attained with ρ_{s_1} at the throat.

Transitional isentropic patterns in the (M, ρ)–diagram and in the (j, ρ)–diagram are depicted
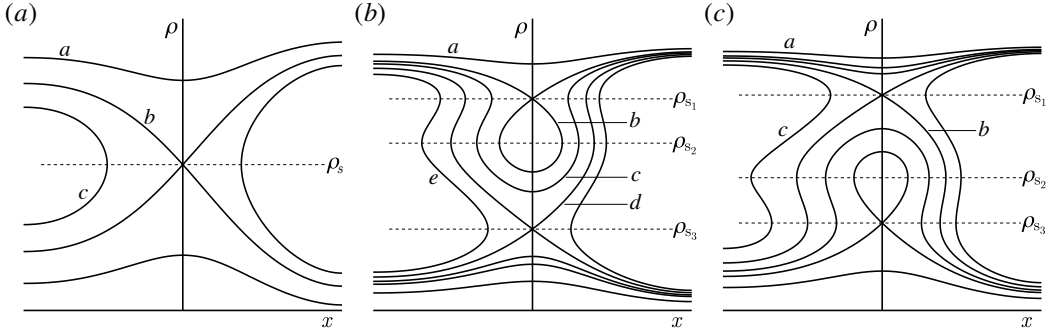
FIGURE 3.12. Phase planes for selected isentropes featuring (*a*) one sonic points and (*b*), (*c*) three sonic points along an isentropic expansion with constant total enthalpy. Dashed segments denote sonic values of the density, ordered as $\rho_{s_3} < \rho_{s_2} < \rho_{s_1}$. If one sonic point only is present, it is specified as ρ_s. (*b*) Sonic density ρ_{s_3} is the global maximum of the related mass flux function. (*c*) Sonic density ρ_{s_1} is the global maximum of the related mass flux function.

Isentropic pattern	Number of sonic points	$J\|_{M<1}$	$J\|_{M>1}$	$\max_{\rho} j$
$\mathscr{S}^I$	1	$J < 0$	$J < 0$	ρ_s
$\mathscr{S}^{NI}$	1	$J < 0$	$J \lessgtr 0$	ρ_s
$\mathscr{S}^{NC}_3$	1	$J \lessgtr 0$	$J < 0$	ρ_s
$\mathscr{S}^{NC}_2$	3	$J \lessgtr 0$	$J \lessgtr 0$	ρ_{s_3}
$\mathscr{S}^{NC}_1$	3	$J \lessgtr 0$	$J \lessgtr 0$	ρ_{s_1}

TABLE 3.2. Description of isentropic patterns for non-ideal, possibly non-classical nozzle flows. In the presence of multiple sonic points, the corresponding densities are ordered as $\rho_{s_3} < \rho_{s_2} < \rho_{s_1}$. If one sonic point only is present, it is specified as ρ_s.

in figures 3.13(*a*) and 3.13(*b*), respectively. These figures are computed for a constant value of the total enthalpy (the same used in the computation of figure 3.11). The limiting flows $\mathscr{S}^{NI}/\mathscr{S}^{NC}_1$ and $\mathscr{S}^{NC}_2/\mathscr{S}^{NC}_3$ are distinguished based on the presence of non-simple sonic points, at which $M = 1$ and $J = 0$ simultaneously, i.e. the Mach number profile is locally tangent to the sonic line. These transitional patterns thus include two distinct sonic points. In the limiting curve for $\mathscr{S}^{NI}/\mathscr{S}^{NC}_1$ transition the non-simple sonic point is the low-density sonic point, while in the transitional curve $\mathscr{S}^{NC}_2/\mathscr{S}^{NC}_3$ the non-simple sonic point is the high-density sonic point. For stagnation densities included between the values associated with transitions $\mathscr{S}^{NI}/\mathscr{S}^{NC}_1$ and $\mathscr{S}^{NC}_2/\mathscr{S}^{NC}_3$, three sonic point occur. For a particular value of the stagnation density, the mass flux function exhibits two global maxima, i.e. $\rho_{s_3} c(\rho_{s_3}, s) = \rho_{s_1} c(\rho_{s_1}, s)$; this condition identifies transition $\mathscr{S}^{NC}_1/\mathscr{S}^{NC}_2$. Finally, the limiting curve for $\mathscr{S}^{NC}_3/\mathscr{S}^I$ transition exhibits a stationary inflection point in the Mach number distribution, i.e. it intersects the locus $J = 0$ at its minimum ($J = 0$ and $\Lambda = 0$ simultaneously).

By varying the total enthalpy and gathering the stagnation state corresponding to the transitional isentropic patterns, the thermodynamic map of figure 3.14 is ultimately obtained. The value of the total enthalpy that was used for the computation of figures 3.11 and 3.13 is such that all different isentropic patterns possibly arise.

If $s_{vle} < s < s_{\tau,0}$, where $s_{\tau,0}$ denotes the isentrope tangent to the locus $\Gamma = 0$, each class of isentropic flow can be observed depending on the stagnation state. In the direction of increasing
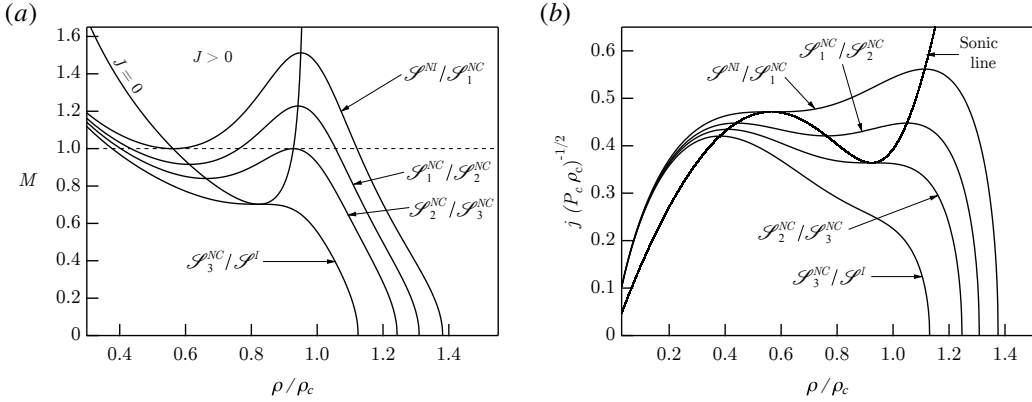
FIGURE 3.13.   Variation of (*a*) Mach number and (*b*) mass flux function with density for transitional isentropic flows, computed from the polytropic van der Waals model with $c_v/R = 50$. The total enthalpy is constant and equal to the value employed in the computation of figure 3.11.

density, patterns $\mathscr{S}^I$, $\mathscr{S}_3^{NC}$, $\mathscr{S}_2^{NC}$, $\mathscr{S}_1^{NC}$, $\mathscr{S}^{NI}$ are encountered. With increasing values of s, the region of stagnation states leading to non-classical isentropic patterns shrink and the corresponding transitional curves ultimately coincide in a single thermodynamic state when $s = s_{\tau,0}$. Similarly to the classical gasdynamic case, along isentropes featuring $0 < \Gamma < 1$, the Mach number may exhibit a non-monotone profile in the supersonic regime. Accordingly, either $\mathscr{S}^{NI}$ or $\mathscr{S}^I$ is possible depending on the stagnation state. Note that the transitional curves $\mathscr{S}^{NI}/\mathscr{S}^I$ for isentropes featuring $0 < \Gamma < 1$ and $\mathscr{S}_3^{NC}/\mathscr{S}^I$ for isentropes featuring $\Gamma < 0$ are constructed in the same way and form a single continuous locus, which comprises the stagnation states associated with stationary inflection points in the Mach number distribution. The inflection point is subsonic for transition $\mathscr{S}_3^{NC}/\mathscr{S}^I$ and supersonic for transition $\mathscr{S}^{NI}/\mathscr{S}^I$. If $\Gamma > 1$ everywhere along the reference isentrope, the Mach number is a monotone decreasing function of the density and pattern $\mathscr{S}^I$ only can take place.

Application of the second law of thermodynamic together with relation (3.14) shows the direction in which transitions of the isentropic patterns can possibly occur:

$$\mathscr{S}^{NI} \to \mathscr{S}_1^{NC} \to \mathscr{S}_2^{NC} \to \mathscr{S}_3^{NC} \to \mathscr{S}^I. \tag{3.21}$$

Evidently, the transition does not necessarily occur between two adjacent isentropic patterns (e.g. $\mathscr{S}^{NI} \to \mathscr{S}_2^{NC}$ or $\mathscr{S}_3^{NC} \to \mathscr{S}^I$ are admissible transitions). One of the most relevant consequences of the entropy rise across a shock wave is the possible change in the number of sonic points, for the phase planes featuring one only and three sonic points are topologically different. The number of sonic points may either decrease (following, e.g., a transition $\mathscr{S}_1^{NC} \to \mathscr{S}_3^{NC}$), or increase (e.g. $\mathscr{S}^{NI} \to \mathscr{S}_2^{NC}$). In addition, from previous investigations it was inferred that non-classical flow fields are associated to reservoir conditions of type $\mathscr{S}_1^{NC}$ and $\mathscr{S}_2^{NC}$. The present analysis suggests that non-classical flow configurations are expected also from reservoir conditions featuring a single sonic point, namely $\mathscr{S}^{NI}$, because of the possible transition $\mathscr{S}^{NI} \to \mathscr{S}_1^{NC}$ or $\mathscr{S}^{NI} \to \mathscr{S}_2^{NC}$. The latter claim is confirmed in the following section.

3.4.3   Functioning regimes

The analytical approach introduced in §3.3.3 to compute exact solutions of classical nozzle flows is extended in this section, where we describe functioning regimes for single-phase flows of BZT fluids in converging-diverging nozzles. It is anticipated here, to the understanding of the
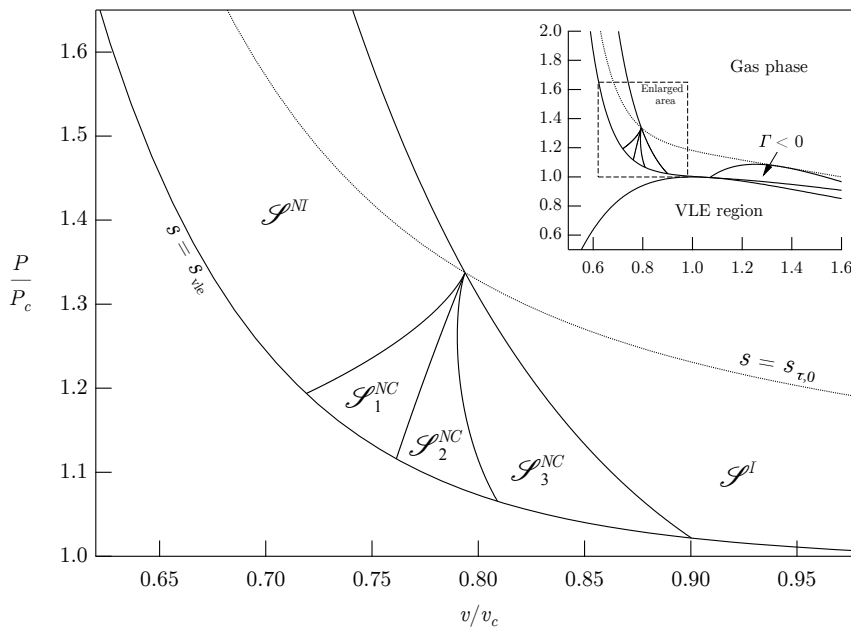
FIGURE 3.14. Thermodynamic map of stagnation states associated with each isentropic pattern, as computed from the van der Waals polytropic model with $c_v/R = 50$. Curves labelled $s = s_{vle}$ and $s = s_{\tau,0}$ represent the isentropes tangent to the vapour-liquid saturation curve and to the $\Gamma = 0$ locus, respectively.

following treatment, that starting from five different isentropic patterns associated to the reservoir conditions, as many as ten different functioning regimes have been singled out. These can be grouped in the six classes reported in table 3.3. Two classical functioning regimes are introduced, namely the ideal regime $\mathscr{R}^I$ and the non-ideal regime $\mathscr{R}^{NI}$, correspond to those illustrated in §3.3.3. Reservoir conditions featuring pattern $\mathscr{S}_3^{NC}$ produce the non-classical regime $\mathscr{R}_3^{NC}$, which features non-monotonic Mach number expansion in the subsonic regime, in both the converging and diverging sections. Two classes of functioning regimes, namely $\mathscr{R}_1^{NC}$ and $\mathscr{R}_2^{NC}$, are associated with reservoir conditions of type $\mathscr{S}_1^{NC}$ and $\mathscr{S}_2^{NC}$. In these flows, expansion to arbitrarily large exit Mach numbers requires that a rarefaction shock is formed. The distinction between regimes $\mathscr{R}_1^{NC}$ and $\mathscr{R}_2^{NC}$ is based on the location of this rarefaction shock, downstream of the throat in expanding flows of type $\mathscr{R}_1^{NC}$ and upstream of the throat section in $\mathscr{R}_2^{NC}$ expansions. A further grouping is also outlined, namely sub-classes a, b and c of regimes $\mathscr{R}_1^{NC}$ and $\mathscr{R}_2^{NC}$, which are defined according to the mechanism of formation of split shocks. Finally, it is shown that non-classical functioning regime $\mathscr{R}_0^{NC}$ is produced by reservoir conditions of type $\mathscr{S}^{NI}$, which are characterised by the occurrence of a single sonic point.

Functioning regimes will be discussed in the order of increasing number of possible transition of the isentropic pattern (see the ordering in 3.21), starting from $\mathscr{S}^I$ reservoir conditions, where no transition can take place, up to $\mathscr{S}^{NI}$ reservoir conditions, from where all transitions are possible.

3.4.3.1 Functioning regime $\mathscr{R}^I$

Limiting and intermediate flows of type $\mathscr{R}^I$ are reported in figure 3.15, which is qualitative identical to its counterpart in classical gasdynamics (figure 3.6). For the description of each solution, the reader is referred to §3.3.3. In spite of the possibility that the expansion partially takes place within

Isentropic pattern of the reservoir conditions	Possible functioning regimes
$\mathscr{S}^{I}$	$\mathscr{R}^{I}$
$\mathscr{S}^{NC}_{3}$	$\mathscr{R}^{NC}_{3}$
$\mathscr{S}^{NC}_{2}$	$\mathscr{R}^{NC}_{2}, \mathscr{R}^{NC}_{1}$
$\mathscr{S}^{NC}_{1}$	$\mathscr{R}^{NC}_{1}$
$\mathscr{S}^{NI}$	$\mathscr{R}^{NI}, \mathscr{R}^{NC}_{0}$

TABLE 3.3. Summary of the functioning regimes in a converging-diverging nozzle produced by different isentropic patterns of the reservoir conditions.
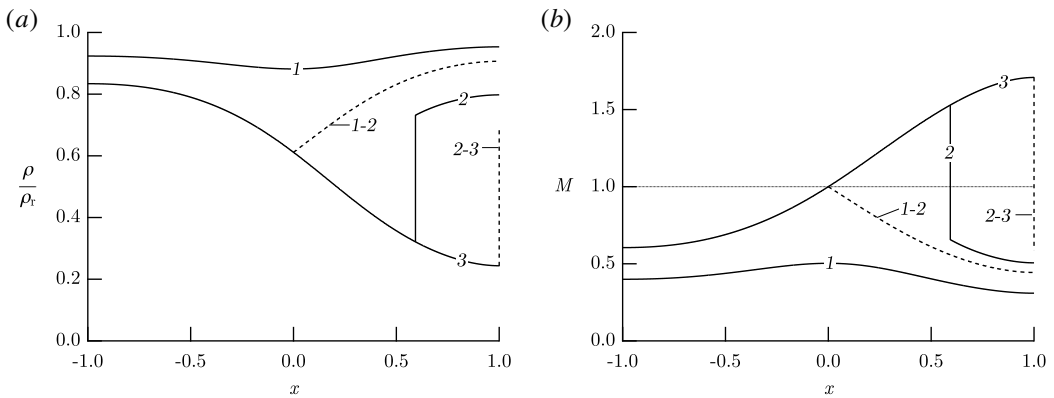

FIGURE 3.15. Exemplary limiting (- - - -) and intermediate (——) flows of type $\mathscr{R}^{I}$, computed from the van der Waals polytropic model with $c_v/R = 50$. (a) Density solutions, scaled to reservoir density ρ_r; (b) Mach number solutions. Reservoir conditions: $P_r = 10P_c$, $v_r = 10v_c$.

the negative-Γ region, reservoir conditions of type $\mathscr{S}^{I}$ result in functioning regime $\mathscr{R}^{I}$, because no isentropic-pattern transition is allowed from $\mathscr{S}^{I}$. Thus, at most one shock wave can occur within the nozzle (in the diverging section) and the isentropic flow upstream and downstream of the shock is of type $\mathscr{S}^{I}$. An ideal-gas-like situation is recovered, which is classified as $\mathscr{R}^{I}$.

3.4.3.2 Functioning regime $\mathscr{R}^{NC}_{3}$

If the reservoir conditions correspond to isentropic pattern $\mathscr{S}^{NC}_{3}$, the Mach number does not increase monotonically through a subsonic expansion. The associated functioning regime is denoted as $\mathscr{R}^{NC}_{3}$. This is our first example of non-classical regime, since the Mach number decrease/increase in subsonic expansions/compressions requires that $\Gamma < 0$. Limiting and intermediate flows of regime $\mathscr{R}^{NC}_{3}$ are sketched in figure 3.16. The layout and the general properties of the solutions is as described for regime $\mathscr{R}^{I}$, except for a pronounced subsonic peak in the Mach number. This appears as a steeper expansion or compression in the density solutions. In addition, contrary to the ideal case, in flows of type $\mathscr{R}^{NC}_{3}(2)$ the Mach number may also increase downstream of the shock wave in the divergent section. If, however, transition $\mathscr{S}^{NI}_{2} \to \mathscr{S}^{I}$ occurs in passing through the shock wave, the Mach number will necessary decrease up to the exit section, as in the exemplary solution $\mathscr{R}^{NC}_{3}(2)$ reported in figure 3.16.
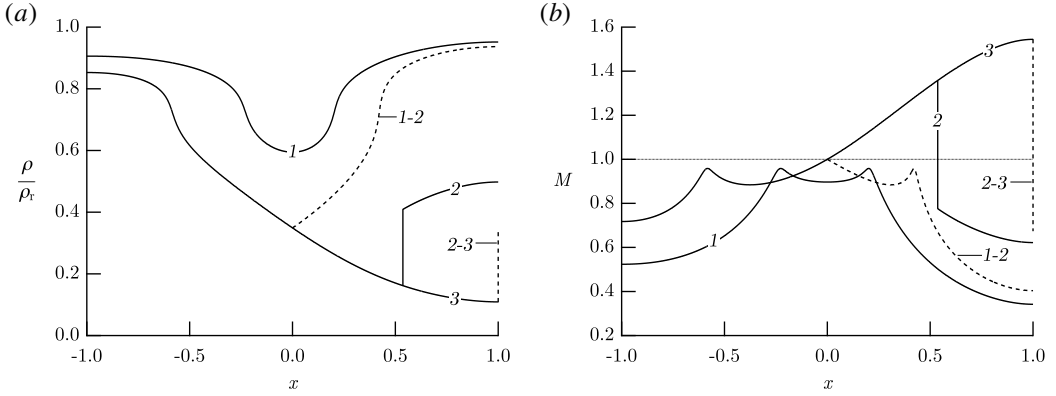
FIGURE 3.16. Exemplary limiting (- - - -) and intermediate (——) flows of type $\mathscr{R}_3^{NC}$, computed from the van der Waals polytropic model with $c_v/R = 50$. (a) Density solutions, scaled to reservoir density ρ_r; (b) Mach number solutions. Reservoir conditions: $P_r = 1.1427 P_c$, $P_r = 1.1427 P_c$.

3.4.3.3 Functioning regime $\mathscr{R}_2^{NC}$

The nozzle flows of central interest in non-classical gasdynamic are those where the isentropic pattern of the reservoir conditions exhibits three sonic points. In this section we discuss regimes of type $\mathscr{R}_2^{NC}$, which can originate from reservoir conditions of type $\mathscr{S}_2^{NC}$, see Table 3.3. Three possible configurations are admissible and detailed in §3.4.3.5: $\mathscr{R}_{2a}^{NC}$, $\mathscr{R}_{2b}^{NC}$ and $\mathscr{R}_{2c}^{NC}$. Here, regime $\mathscr{R}_{2a}^{NC}$, corresponding to *Type-2* flows of Cramer & Fry (1993), is presented to describe common features to the functioning regimes for the $\mathscr{R}_2^{NC}$ class.

Inspection of figure 3.17 reveals that flows such as $\mathscr{R}_{2a}^{NC}(2)$, that include a single compression shock in the diverging section of nozzle, exist for a very limited range of ambient pressures. This shock, owing to the non-monotone dependence of the Mach number on the density, ultimately has sonic upstream state ($\rho = \rho_{s_2}$), see limiting solution $\mathscr{R}_{2a}^{NC}(2\text{-}3)$, and cannot exist further downstream. Shocks with upstream sonic state are referred to as pre-sonic shocks.

If the ambient pressure is slightly reduced below $\varepsilon = \varepsilon_{2\text{-}3}$, the entropy rise needed to match the outlet boundary condition is carried by a double-shock configuration, in which the leading wave is a rarefaction shock and the trailing wave is a pre-sonic compression shock. The trailing shock is formed because the flow downstream of the rarefaction shock becomes sonic when $\rho = \rho_{s_2}$ in the local isentropic pattern, which remains of type $\mathscr{S}_2^{NC}$ (i.e., no transition occurs across the leading shock). Intermediate flows of type $\mathscr{R}_{2a}^{NC}(2)$ and $\mathscr{R}_{2a}^{NC}(3)$ are sonic at the throat (sonic condition ρ_{s_1}). Therefore, the nozzle is choked in the corresponding range of ambient pressures, with a constant value of the mass flow rate denoted as $\dot{m}_{s_1}$. The simultaneous shift upstream of the rarefaction shock and downstream of the pre-sonic compression shock, in accordance with relation (3.19), allows to satisfy the overall increasing entropy jump in a chocked flow as the ambient pressure is decreased, see relation (3.18). Eventually, the leading shock wave has sonic upstream state and it is located exactly at the throat section, see limiting solution $\mathscr{R}_{2a}^{NC}(3\text{-}4)$.

A rarefaction shock with sonic upstream state can also exist ahead of the throat. If $\varepsilon_{4\text{-}5} < \varepsilon < \varepsilon_{3\text{-}4}$, the mass flow rate increases with decreasing ambient pressure and sonic condition ρ_{s_1} occurs upstream of the throat. Trajectories such as $\mathscr{R}_{2a}^{NC}(4)$ can be continued provided a sonic rarefaction shock is inserted at the sonic point. Notably, this shock has the same upstream and downstream states as the leading shock in limiting flow $\mathscr{R}_{2a}^{NC}(3\text{-}4)$, though it occurs in a different location within the nozzle. Downstream of the rarefaction shock, the flow expands up to the throat because of the converging area. Flows of type $\mathscr{R}_{2a}^{NC}(4)$ are subsonic at the throat and therefore the pressure and
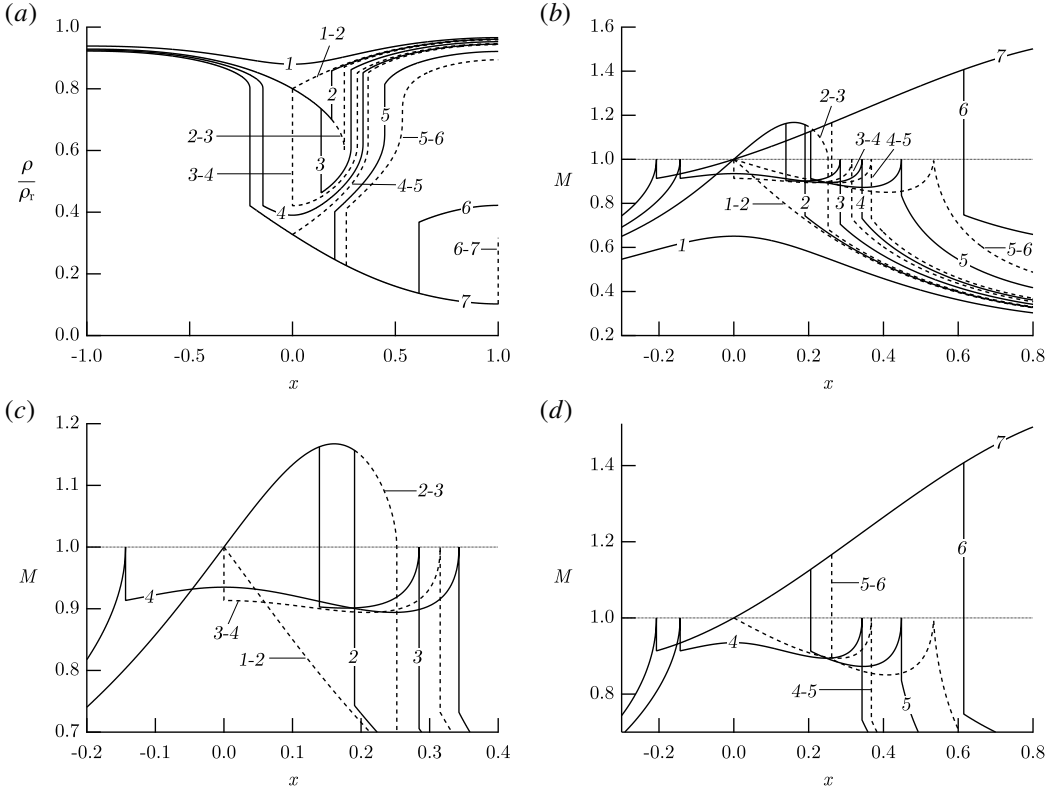
FIGURE 3.17. Exemplary limiting (- - - -) and intermediate (——) flows of type $\mathscr{R}_{2a}^{NC}$, computed from the van der Waals polytropic model with $c_v/R = 50$. (a) Density solutions, scaled to reservoir density ρ_r; (b) Mach number solutions; (c) enlargement of (b) including only flows from 2 to 4; (d) enlargement of (b) including only flows from 4 to 7. Reservoir conditions: $P_r = 1.1300 P_c$, $v_r = 0.7710 v_c$.

density increase in the diverging section of the nozzle. Because the local isentropic pattern is $\mathscr{S}_2^{NC}$, a pre-sonic compression shock must be inserted to continue the flow beyond sonic point ρ_{s_2} (this shock is identical to that of limiting solution $\mathscr{R}_{2a}^{NC}$(3-4)). The mass flow rate can be increased by decreasing ε until $M = 1$ at the throat, whereby the sonic condition corresponds to the low-density sonic point ρ_{s_3} in the isentrope downstream of the rarefaction shock. This condition determines limiting flow $\mathscr{R}_{2a}^{NC}$(4-5), in which the pre-sonic rarefaction shock is in its rearmost position. Let s_t denote the entropy value downstream of the limiting rarefaction shock wave and let $\dot{m}_{s_2}$ be the mass flow rate corresponding to $\varepsilon = \varepsilon_{4\text{-}5}$. Then

$$\dot{m}_{max} = \dot{m}_{s_2} = \dot{m}_c(s_t, h^t) < \dot{m}_c(s_r, h^t),\tag{3.22}$$

where for the last inequality we used

$$\left(\frac{\partial j}{\partial s}\right)_{\rho,h^t} = -\frac{\rho^2 T}{j}(1 + G),\tag{3.23}$$

which gives in turn $(\partial \dot{m}_c/\partial s)_{h^t} < 0$ and from the admissibility requirement $s_t > s_r$. It follows that there exist two different choking conditions in functioning regime $\mathscr{R}_{2a}^{NC}$, namely $\varepsilon_{3\text{-}4} < \varepsilon < \varepsilon_{1\text{-}2}$ ($\dot{m} = \dot{m}_{s_1}$) and $\varepsilon < \varepsilon_{4\text{-}5}$ ($\dot{m} = \dot{m}_{s_2}$).

Flows $\mathscr{R}_{2a}^{NC}(5)$ or $\mathscr{R}_{2a}^{NC}(6)$ admit ordinary compression shock waves in the diverging section of the nozzle. If the shock wave occurs sufficiently close to the throat section, such as in case $\mathscr{R}_{2a}^{NC}(5)$, the resultant subsonic compression eventually attains a sonic point and a further shock, with sonic upstream state, must be formed to continue the flow. This is in contrast with the shock configurations observed in the classical functioning regimes, where it is always possible to connect two states (the downstream one having larger entropy) by means of a single compression shock wave, without the need for an intermediate isentropic compression. Following Kluwick (1993) and Cramer & Fry (1993), we will refer to this double compression-shock configuration as a split shock, owing to the similarity with the shock-splitting phenomenon in unsteady flows[2] (see Cramer, 1989b, 1991). According to relation (3.19), if the leading compression shock moves downstream the corresponding entropy jump increases. Indeed, a reduction of the ambient pressure results in a stronger leading shock and in a weaker terminating shock. Ultimately, the entropy rise across the first compression shock is such that, in the downstream flow, the isentropic pattern corresponds to the transitional type $\mathscr{S}_2^{NC}/\mathscr{S}_3^{NC}$. Thus, in the limiting flow $\mathscr{R}_{2a}^{NC}(5\text{-}6)$ the trailing sonic shock wave has vanishing strength.

If $\varepsilon < \varepsilon_{5\text{-}6}$, a single non-sonic compression shock occurs, because the entropy jump generates either transition $\mathscr{S}_2^{NC} \to \mathscr{S}_3^{NC}$ or transition $\mathscr{S}_2^{NC} \to \mathscr{S}^{I}$. Hence, if a compression shock forms sufficiently far downstream of the throat, the post-shock isentrope no longer contains the additional sonic point required for the existence of the sonic compression shock. As in previous regimes, with decreasing ambient pressure the shock wave moves downstream in the diverging section of the nozzle and eventually attains the exit section in limiting flow $\mathscr{R}_{2a}^{NC}(6\text{-}7)$. If $\varepsilon < \varepsilon_{6\text{-}7}$, no shock waves exist downstream of the throat and the outflow is supersonic. The major difference with respect to flows evolving along isentropes including a single sonic point is that full expansion to arbitrarily large Mach numbers cannot be achieved isentropically, yet a pre-sonic rarefaction shock is required to occur upstream of the throat.

3.4.3.4 Functioning regime $\mathscr{R}_{1}^{NC}$

Regimes of class $\mathscr{R}_1^{NC}$, which includes regimes $\mathscr{R}_{1a}^{NC}$, $\mathscr{R}_{1b}^{NC}$ and $\mathscr{R}_{1c}^{NC}$ described in §3.4.3.5, can originate from reservoir conditions of type $\mathscr{S}_1^{NC}$ or $\mathscr{S}_2^{NC}$, see Table 3.3. Regime $\mathscr{R}_{1a}^{NC}$ in figure 3.18, which corresponds to *Type-1* flows of Cramer & Fry (1993), is now presented to outline all common features to regimes of type $\mathscr{R}_1^{NC}$.

With reference to figure 3.18, flows $\mathscr{R}_{1a}^{NC}(1)$, $\mathscr{R}_{1a}^{NC}(2)$ and $\mathscr{R}_{1a}^{NC}(3)$ are qualitatively similar to flows $\mathscr{R}_{2a}^{NC}(1)$, $\mathscr{R}_{2a}^{NC}(2)$ and $\mathscr{R}_{2a}^{NC}(3)$, respectively, discussed in the previous section. However, differently from flows of type $\mathscr{R}_{2a}^{NC}(3)$, the rarefaction shock of intermediate flows $\mathscr{R}_{1a}^{NC}(3)$ becomes sonic on the downstream side (post-sonic shock) when $\varepsilon = \varepsilon_{3\text{-}4}$. Rarefaction shocks cannot exist ahead of this limiting sonic shock. Thus, in contrast to $\mathscr{R}_{2a}^{NC}$ flows, functioning regime $\mathscr{R}_{1a}^{NC}$ exhibits a unique sonic condition at the throat, corresponding to the high-density sonic point ρ_{s1}, and in turn a unique chocking condition. Accordingly,

$$\dot{m}_{max} = \dot{m}_s = \dot{m}_c(s_r, h^t), \qquad (3.24)$$

where $\dot{m}_s$ is the mass flow rate discharged when $\varepsilon < \varepsilon_{1\text{-}2}$.

---

[2]Care must be taken. The shock splitting in single-phase gases described by Cramer (1989b) refers to the phenomenon by which an initial compression discontinuity which is inadmissible (see, e.g., case A_2-B_5 in figure 2.2) will split, as time evolves, in two weaker shocks with a smooth compression fan in between. In fact, the essence of this shock splitting is the formation of a composite wave. A truly split shock, according to Menikoff & Plohr (1989), is characterized by a constant state in between. A similar configuration requires that the speed of sound is discontinuous in the middle state, i.e. isentropes in the (P, v)–plane must have a kink in their slope (e.g. at a saturation boundary). To maintain continuity with the previous studies on non-classical nozzle flows, the nomenclature of Cramer & Fry (1993) is used and the analogy between the double compression-shock configuration in the nozzle and unsteady shock splitting is meant in the sense of Cramer (1989b).
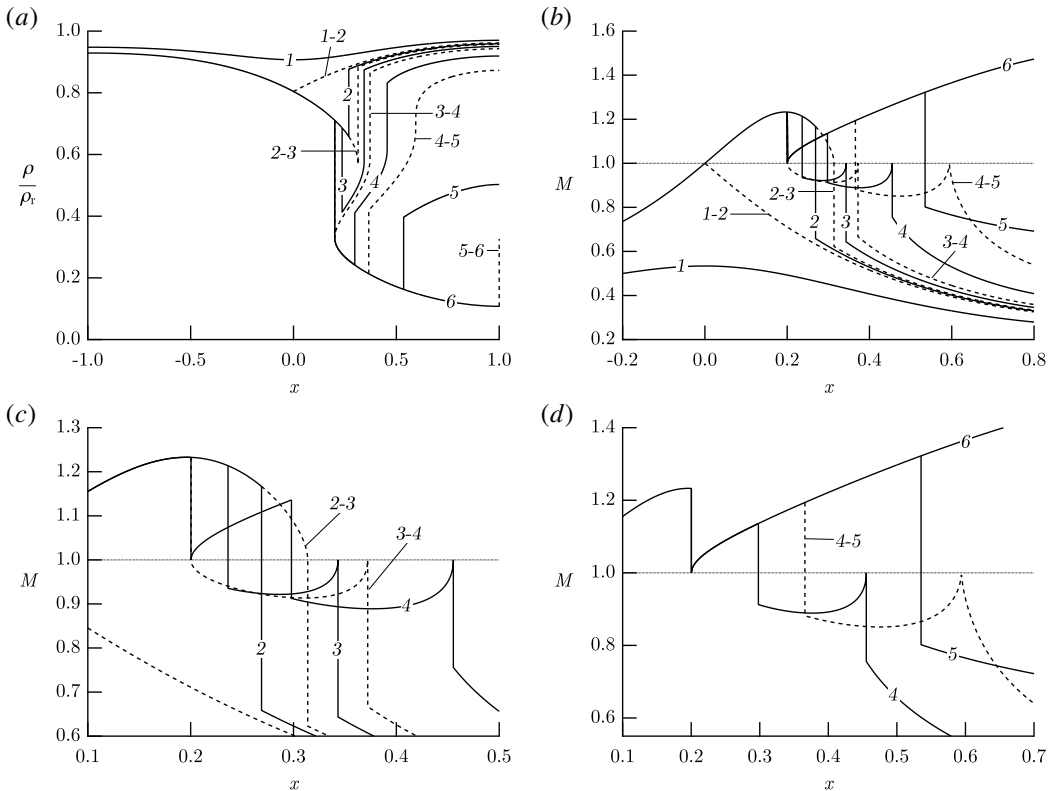
FIGURE 3.18. Exemplary limiting (- - - -) and intermediate (——) flows of type $\mathscr{R}_{1a}^{NC}$, computed from the van der Waals polytropic model with $c_v/R = 50$. (*a*) Density solutions, scaled to reservoir density ρ_r; (*b*) Mach number solutions; (*c*) enlargement of (*b*) including only flows from 2 to 4; (*d*) enlargement of (*b*) including only flows from 4 to 6. Reservoir conditions: $P_r = 1.1453 P_c$, $v_r = 0.7600 v_c$.

If $\varepsilon < \varepsilon_{3\text{-}4}$, the flow expands downstream of the limiting rarefaction shock and two different shock configurations are possible, similarly to functioning regime $\mathscr{R}_{2a}^{NC}$. Compression waves in the neighbourhood of the limiting rarefaction shock occur in the form of a split shock, see intermediate flow $\mathscr{R}_{1a}^{NC}(4)$. The split-shock configuration ultimately vanishes because of the disintegration of the sonic compression shock, as a result of the shift in the isentrope across the leading compression shock. If $\varepsilon_{5\text{-}6} < \varepsilon < \varepsilon_{4\text{-}5}$, a single non-sonic shock is formed downstream of the limiting rarefaction shock, as the entropy rise across the trailing shock is such that the post-shock isentrope no longer contains multiple sonic points (i.e. transition to isentropic pattern $\mathscr{S}_3^{NC}$ or $\mathscr{S}^I$ occurs). Finally, flows such as $\mathscr{R}_{1a}^{NC}(6)$, expanding to arbitrarily low densities and arbitrarily large Mach numbers, are realizable provided that a rarefaction shock with sonic downstream state is inserted in the diverging section of the nozzle.

Non-classical functioning regimes $\mathscr{R}_{1a}^{NC}$ and $\mathscr{R}_{2a}^{NC}$ are in fact the *Type-1* and *Type-2* flows introduced by Cramer & Fry (1993), respectively. In the following section we show that a further classification can be formulated according to the mechanism by which the split shock turns into the single-shock configuration.
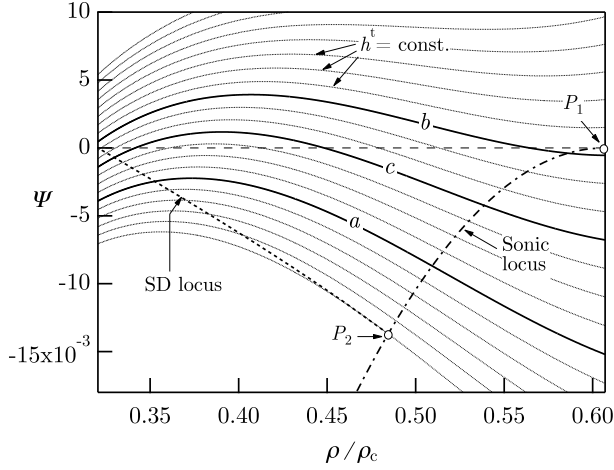
FIGURE 3.19. Contours of h^t in the (Ψ, ρ)-diagram, corresponding to the exemplary isentrope $s = s(1.0923P_C, v_c)$, as computed from the van der Waals polytropic model with $c_v/R = 50$. The range of densities coincides with the interval where j^* is defined, i.e. where a post-sonic compression shock can possibly originate. Two additional curves are plotted: the sonic locus $M = 1$ and the sonic shock disintegration (SD) locus, gathering the pre-shock states corresponding to a shock wave with downstream isentropic pattern $\mathscr{S}_2^{NC}/\mathscr{S}_3^{NC}$. The SD locus intersects the sonic locus at point P_2. The curve passing through point P_2 corresponds to the transitional isentropic pattern $\mathscr{S}_2^{NC}/\mathscr{S}_3^{NC}$. On the other hand, the curve passing through point P_1 ($M = 1$ and $\Psi = 0$) corresponds to the transitional isentropic pattern $\mathscr{S}^{NI}/\mathscr{S}_1^{NC}$.

3.4.3.5 On the split-shock formation: sub-classes $\mathscr{R}_a^{NC}$, $\mathscr{R}_b^{NC}$ and $\mathscr{R}_c^{NC}$

In order to investigate the different scenarios for the split-shock formation and eventual disintegration, it is instructive to examine the quantity

$$\Psi = j(\rho; s, h^t) - j^*(\rho; s), \tag{3.25}$$

where j^* is the mass flux corresponding to a post-sonic compression shock. The parameter Ψ is related to the difference between the slope $-j^2$ of the Rayleigh line of a shock wave with total enthalpy h^t and the slope $-j^{*2}$ of the Rayleigh line of a post-sonic compression shock, both centred on the thermodynamic state identified by ρ and s. Note that j^* and in turn Ψ are defined only if a post-sonic compression shock can originate from the given pre-shock state. If a post-sonic compression shock centred on a given pre-shock state exists and is admissible, then it is unique. To show this, we notice that the sign of Γ alternates at successive sonic points along the shock adiabat (see §2.3.2) and that the thermodynamic state in the sonic side of an admissible compression shock exhibits[3] $\Gamma < 0$ (see Menikoff & Plohr, 1989; Kluwick, 2001). According to the topology of Γ in the single-phase gases (Γ changing sign at most twice along isentropes, $\Gamma > 0$ asymptotically for infinitely-large and infinitely-small pressures), only one such sonic point is compatible with the topology of Γ, thus completing the proof.

   Figure 3.19 shows exemplary contours of h^t in the (Ψ, ρ)-plane of a given isentrope. In this diagram, the abscissa spans the range of densities where a post-sonic compression shock is admissible. Two relevant curves are plotted, namely the sonic locus and the sonic-shock disintegration (SD) locus. States located on the left-hand side (lower densities) of the sonic locus represent supersonic, and therefore candidate pre-shock states of admissible shock waves. By

---

[3]The first sonic point along the shock adiabat is a local maximum in the post-shock entropy. It follows from equation (2.37) that $\Gamma < 0$ at the first sonic point on the compression branch of the shock adiabat.
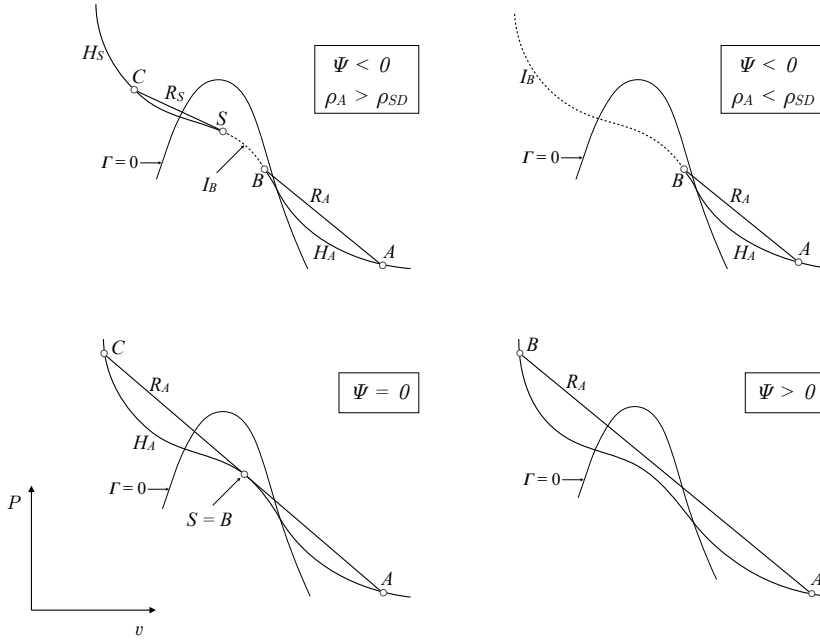
FIGURE 3.20. Qualitative chart illustrating compression waves that bridge the negative-Γ region: H_A and H_S shock adiabats from points A and S, respectively; R_A and R_S Rayleigh lines; I_B isentrope. Case $\Psi < 0$, $\rho_A > \rho_{SD}$: split-shock composed of shock A-B, isentropic compression along I_B up to sonic point S and sonic shock S-C. Case $\Psi < 0$, $\rho_A < \rho_{SD}$: shock A-B followed by isentropic compression along I_B. Case $\Psi = 0$: the Rayleigh line R_A of shock A-C is tangent to the shock adiabat H_A at the intermediate sonic step S; this shock can be seen as a unique non-sonic shock or as the composition of post-sonic shock A-S and pre-sonic shock S-C. Case $\Psi > 0$: single shock A-B; the Rayleigh line R_A bridges the concave-down region of H_A.

combining equation (3.19) with the well-known differential relations for quasi-1D isentropic flows, it is easy to show that the entropy jump increases with decreasing density of the candidate pre-shock state, provided that the shock wave is compressive. Ultimately, when the pre-shock state occurs on the SD locus, the post-shock isentropic pattern corresponds to the transitional type $\mathscr{S}_2^{NC}/\mathscr{S}_3^{NC}$.

To aid understanding of the following analysis, the possible compression-waves configurations in the thermodynamic region of interest in this work have been sketched in the (P, v)-plane, see figure 3.20. Here ρ_A denotes the density at the selected pre-shock state A and ρ_{SD} represents the density corresponding to the intersection between $\Psi(\rho; s, h^t)$ and the SD locus. Split shocks occur if $\Psi < 0$ and $\rho_A > \rho_{SD}$: along the isentropic compression resulting from shock A-B, sonic point S is encountered and a further shock wave is required to continue the flow. Note that state S is necessarily embedded in the region $\Gamma < 0$, for the curvatures of the shock adiabat and of the isentrope have the same sign in the (P, v)-plane at a sonic point (see, e.g., Menikoff & Plohr, 1989).

There exist two different mechanisms by which the split shock turns into an ordinary non-sonic shock. In the first case, the transition takes place when state A crosses the SD locus and the sonic shock disintegrates. As a result, if $\Psi < 0$ and $\rho_A < \rho_{SD}$, sonic point S is no longer encountered in the isentropic compression downstream of shock A-B. The split-shock/single-shock transition is also accomplished when Ψ changes sign. As Ψ goes to zero from below, a weaker isentropic compression and a stronger terminating shock are generated. When $\Psi = 0$, state B and sonic point S coincide, i.e. the intermediate isentropic compression vanishes. In this case, the leading
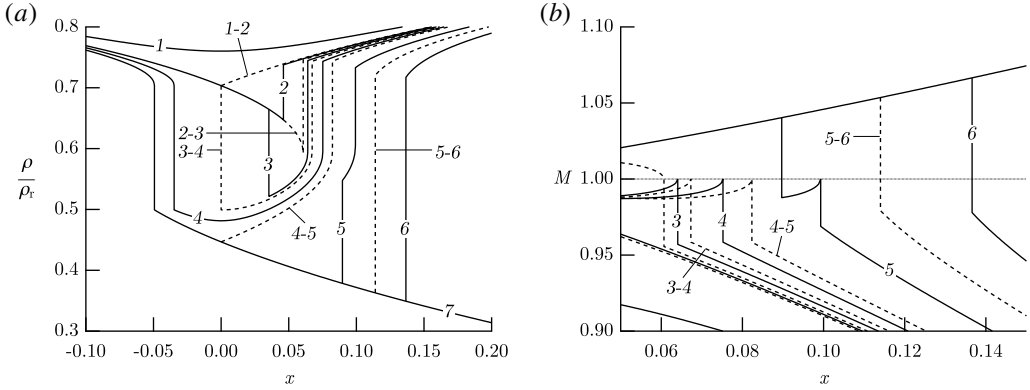
(a)

(b)

FIGURE 3.21. Exemplary limiting (- - - -) and intermediate (——) flows of type $\mathscr{R}_{2b}^{NC}$, computed from the van der Waals polytropic model with $c_v/R = 50$. (a) Density solutions, scaled to reservoir density ρ_r; (b) Mach number solutions. Reservoir conditions: $P_r = 1.2824P_c$, $v_r = 0.7863v_c$.
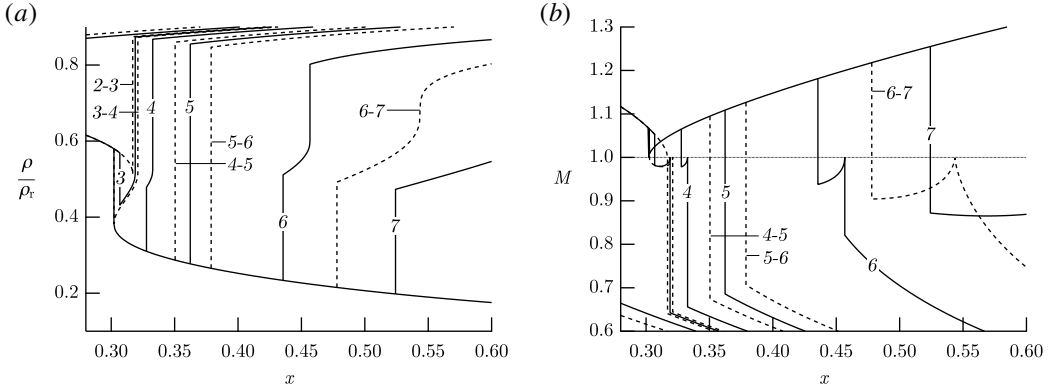
(a)

(b)

FIGURE 3.22. Exemplary limiting (- - - -) and intermediate (——) flows of type $\mathscr{R}_{1c}^{NC}$, computed from the van der Waals polytropic model with $c_v/R = 50$. (a) Density solutions, scaled to reservoir density ρ_r; (b) Mach number solutions. Reservoir conditions: $P_r = 1.2102P_c$, $v_r = 0.7542v_c$.

shock A-B and the trailing shock S-C merge into the single large-amplitude shock A-C. If $\Psi > 0$ an ordinary shock occurs, because the Rayleigh line completely bridges, without touching, the region where the shock adiabat H_A is concave down (inflection points of the shock adiabat nearly coincide with the intersections between the shock adiabat and the $\Gamma = 0$ locus, see for instance Kluwick 2001).

We now examine the different configuration reported in figure 3.19. Curves such as a display $\Psi < 0$; the split-shock configuration is formed and eventually vanishes when the pre-shock state crosses the SD locus. We refer to functioning regimes featuring this kind of split-shock/single-shock transition as the sub-class $\mathscr{R}_a^{NC}$, which includes regimes $\mathscr{R}_{1a}^{NC}$ and $\mathscr{R}_{2a}^{NC}$ described above. Curve labelled b in figure 3.19 exhibits a zero at which $d\Psi/d\rho < 0$. In this case, by decreasing the pre-shock density, the two compression shocks in the split-shock configuration merge into a single large-amplitude shock. We refer to functioning regimes featuring this kind of split-shock/single-shock transition as the sub-class $\mathscr{R}_b^{NC}$ ($\mathscr{R}_{1b}^{NC}$ and $\mathscr{R}_{2b}^{NC}$). Figure 3.21 reports the layout of limiting and intermediate flows corresponding the the exemplary case $\mathscr{R}_{2b}^{NC}$. The limiting flow corresponding to
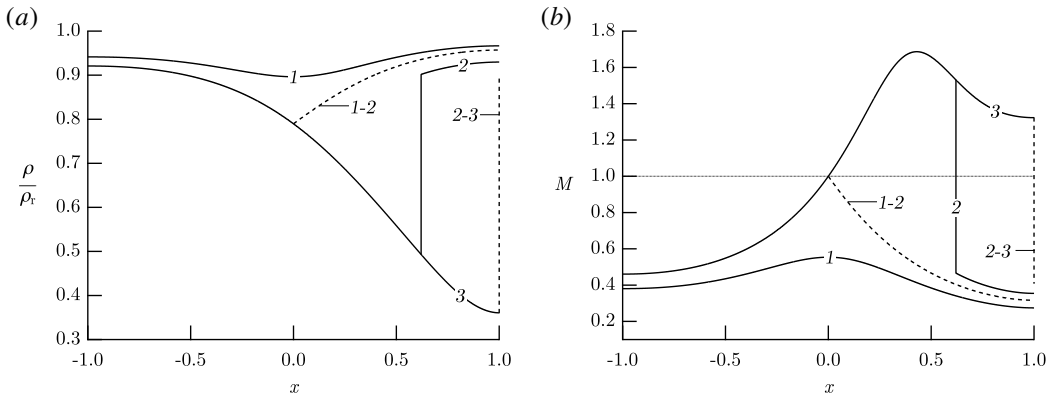
FIGURE 3.23. Exemplary limiting (- - - -) and intermediate (——) flows of type $\mathscr{R}^{NI}$, computed from the van der Waals polytropic model with $c_v/R = 50$. (a) Density solutions, scaled to reservoir density ρ_r; (b) Mach number solutions. Reservoir conditions: $P_r = 1.7355P_c$, $v_r = 0.6532v_c$.

the overlapping of the compression shocks is $\mathscr{R}^{NC}_{2b}(5\text{-}6)$. It is noticeable that the split-shock/single-shock transition of $\mathscr{R}^{NC}_b$ regimes is qualitatively similar to the transition predicted by the isentropic theory, i.e. if we were to neglect the entropy rise across shock waves (see Kluwick, 1993; Cramer & Fry, 1993).

In addition to $\mathscr{R}^{NC}_a$ and $\mathscr{R}^{NC}_b$ sub-classes, we introduce the sub-class $\mathscr{R}^{NC}_c$ ($\mathscr{R}^{NC}_{1c}$ and $\mathscr{R}^{NC}_{2c}$) of the functioning regimes in which a double split-shock/single-shock transition occurs. This is expected when the stagnation conditions are such that Ψ has two zeros, as it is the case in curves of type c in figure 3.19. The layout of the limiting and intermediate flows for the exemplary case $\mathscr{R}^{NC}_{1c}$ is sketched in figure 3.22. When the high-density zero of Ψ ($\mathrm{d}\Psi/\mathrm{d}\rho < 0$) is encountered, the two compression shocks merge, see limiting flow $\mathscr{R}^{NC}_{1c}(4\text{-}5)$. The reverse process occurs in limiting solution $\mathscr{R}^{NC}_{1c}(5\text{-}6)$, because the pre-shock density corresponds to the low-density zero of Ψ, where $\mathrm{d}\Psi/\mathrm{d}\rho > 0$. By further decreasing the pre-shock density, the split shock ultimately vanishes as in $\mathscr{R}^{NC}_a$ regimes, i.e. the sonic shock disintegrates.

3.4.3.6 Functioning regime $\mathscr{R}^{NI}$

If the reservoir conditions correspond to pattern $\mathscr{S}^{NI}$, the Mach number is non-monotone along supersonic branches of isentropic expansions. In the non-classical gasdynamic regime, the layout of the possible flows corresponding to reservoir conditions of type $\mathscr{S}^{NI}$ depends on the possible shock-induced transitions of the isentropic pattern. First of all, we note that rarefaction shocks cannot occur in these flows or other functioning regimes produced by reservoir conditions featuring a unique sonic point. This is easily seen by analysing the related mass flux functions or phase planes. However, compression waves near the negative-Γ region may occur either as ordinary non-sonic shocks or in the form of split shocks, according to the slope of the Rayleigh line. The same argument concerning the (Ψ, ρ)-diagram could be repeated for this type of nozzle flows. The functioning regime arising from reservoir conditions of type $\mathscr{S}^{NI}$ and corresponding to the case $\Psi > 0$, which implies that compression shocks occurring in the diverging section of the nozzle are ordinary non-sonic shocks, is denoted as $\mathscr{R}^{NI}$. In other words, the possible shock-induced transition of the isentropic pattern do not determine any limiting solutions, so that the layout of limiting and intermediate flows is as shown in figure 3.23, which presents the same qualitative features of its counterpart in classical gasdynamics (figure 3.7). For the description of each solution, the reader is referred to §3.3.3.
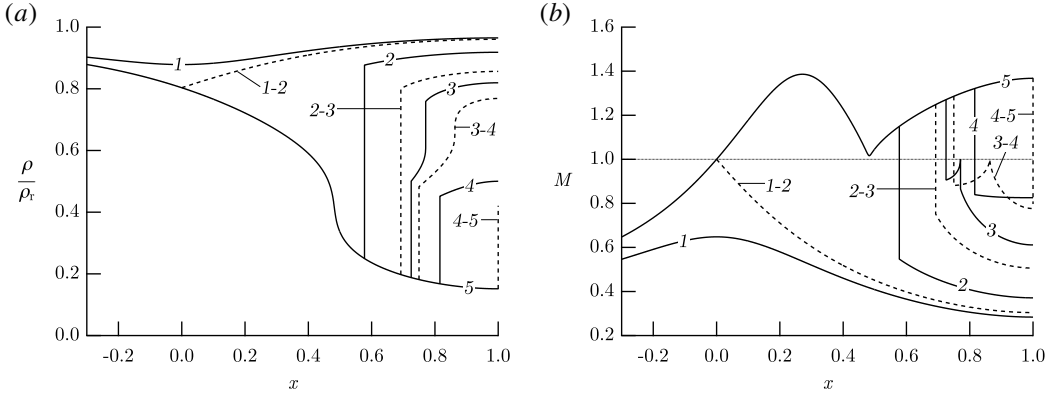
FIGURE 3.24. Exemplary limiting (- - - -) and intermediate (——) flows of type $\mathscr{R}_0^{NC}$, computed from the van der Waals polytropic model with $c_v/R = 50$. (*a*) Density solutions, scaled to reservoir density ρ_r; (*b*) Mach number solutions. Reservoir conditions: $P_r = 1.2315 P_c$, $v_r = 0.7287 v_c$.

3.4.3.7 Functioning regime $\mathscr{R}_0^{NC}$

Past investigations of non-classical nozzle flows (Cramer & Fry, 1993; Kluwick, 1993), mostly based on the simplifying assumption of isentropic flow, i.e. neglecting the entropy rise and the resultant shift in the isentropes across shock waves, might lead to the conclusion that non-classical nozzle flows develop exclusively from reservoir states featuring three sonic points.

To conclude we therefore present one additional non-classical functioning regime, named $\mathscr{R}_0^{NC}$, which develops from reservoir states associated to the isentropic pattern $\mathscr{S}^{NI}$. Following previous discussion, shocks that bridge the negative-Γ region are expected to split if the isentropic pattern downstream of a generic non-sonic shock exhibits three sonic points and the post-shock state lies between sonic points ρ_{s3} and ρ_{s2}. In this case, the resultant subsonic compression eventually encounters sonic point ρ_{s2} and a further shock is required. The layout of limiting and intermediate flows of the type $\mathscr{R}_0^{NC}$ is depicted in figure 3.24. The splitting mechanism in limiting solution $\mathscr{R}_0^{NC}$(2-3) is the same occurring in regimes of type $\mathscr{R}_c^{NC}$ when the low-density zero of Ψ ($\mathrm{d}\Psi/\mathrm{d}\rho < 0$) is crossed. Similarly to regimes of type $\mathscr{R}_a^{NC}$, a decrease in ambient pressure results in a weaker sonic shock, which ultimately vanishes when $\varepsilon = \varepsilon_{3\text{-}4}$.

3.4.4 Thermodynamic map of functioning regimes

In this section, we formalize the connection between the functioning regimes and the reservoir conditions (or stagnation condition at the nozzle inlet), which was anticipated in §3.4.3. Figure 3.25 illustrates the thermodynamic map of the reservoir states leading to each functioning regime described in the previous section.

In the region $s > s_{\tau,0}$, the scenario is formally identical to that observed in §3.3.4 for the classical gasdynamic regime. For reservoir conditions along these isentropes, the possible functioning regimes are $\mathscr{R}^I$ and $\mathscr{R}^{NI}$, which differ in terms of Mach number behaviour, inherited by the reservoir isentropic pattern. Thus, the transition between these functioning regimes corresponds to the transition between the associated isentropic patterns of the reservoir conditions.

In the region $s_{vle} < s < s_{\tau,0}$, the situation is quite different. Each functioning regime can possibly occur from reservoir conditions along these isentropes. Similarly to case $\mathscr{R}^{NI}/\mathscr{R}^I$, a set of transitional curves for functioning regimes coincides with its isentropic pattern counterpart. These transitions include $\mathscr{R}_3^{NC}/\mathscr{R}^I$, $\mathscr{R}_2^{NC}/\mathscr{R}_3^{NC}$, $\mathscr{R}^{NI}/\mathscr{R}_{1b}^{NC}$ and $\mathscr{R}_0^{NC}/\mathscr{R}_{1c}^{NC}$. Transition $\mathscr{R}_3^{NC}/\mathscr{R}^I$ corresponds to
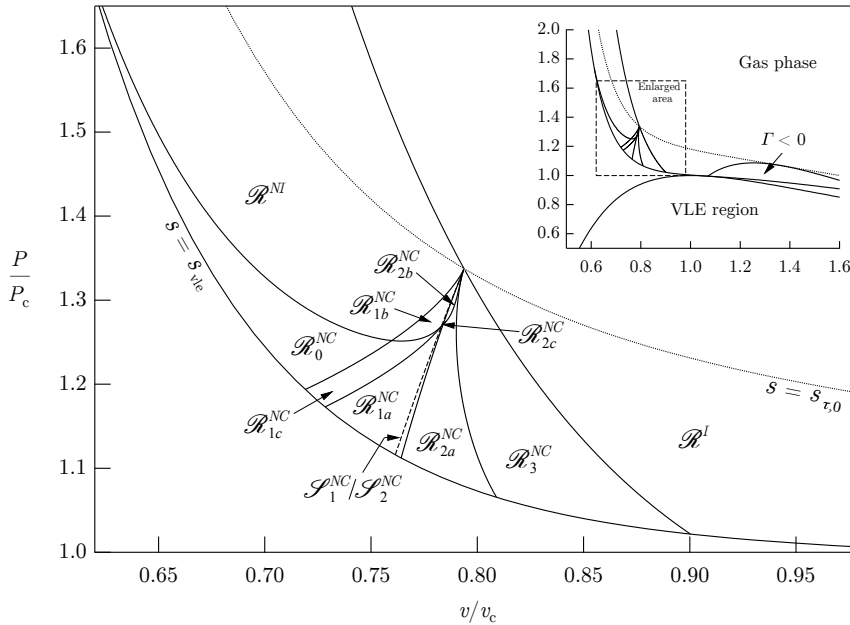
FIGURE 3.25. Thermodynamic map of reservoir states associated with each functioning regime, computed from the van der Waals polytropic model with $c_v/R = 50$. Curves labelled $s = s_{vle}$ and $s = s_{\tau,0}$ represent the isentropes tangent to the vapour-liquid saturation curve and to the $\Gamma = 0$ locus, respectively.

$\mathscr{S}_3^{NC}/\mathscr{S}^I$ because a one-to-one correspondence between the functioning regime and the isentropic pattern of the reservoir conditions exist between $\mathscr{R}_3^{NC}$ and $\mathscr{S}_3^{NC}$ and between $\mathscr{R}^I$ and $\mathscr{S}^I$. Functioning regimes of classes $\mathscr{R}_1^{NC}$ and $\mathscr{R}_2^{NC}$ require that the reservoir isentropic pattern includes three sonic points. Therefore, the transition between these flows and those including a single sonic point in the reservoir isentropic pattern is realised when the reservoir conditions exhibit either transitional pattern $\mathscr{S}_2^{NC}/\mathscr{S}_3^{NC}$ or $\mathscr{S}^{NI}/\mathscr{S}_1^{NC}$. In the first case, transition $\mathscr{R}_2^{NC}/\mathscr{R}_3^{NC}$ occurs; the second case corresponds to transitions $\mathscr{R}^{NI}/\mathscr{R}_{1b}^{NC}$ and $\mathscr{R}_0^{NC}/\mathscr{R}_{1c}^{NC}$.

The remaining transitions are related to some specific non-isentropic features of the flow. We first consider the transition between functioning regimes of classes $\mathscr{R}_1^{NC}$ and $\mathscr{R}_2^{NC}$. Flows expanding from reservoir conditions corresponding to three sonic points must include a rarefaction shock in order to attain arbitrarily large exit Mach numbers. In the case of $\mathscr{R}_2^{NC}$ flows, the rarefaction shock is a pre-sonic shock located in the converging section of the nozzle. In flows of type $\mathscr{R}_1^{NC}$, the rarefaction shock is a post-sonic shock located in the diverging section of the nozzle. The transitional regime between these two classes exhibits a double-sonic shock, i.e. a shock which has both pre-shock and post-shock sonic states (see Thompson & Lambrakis, 1973; Kluwick, 2001; Zamfirescu *et al.*, 2008), exactly located at the throat section. In this respect, the transitional locus $\mathscr{R}_1^{NC}/\mathscr{R}_2^{NC}$ gathers all such reservoir states from which a double-sonic shock may possibly occur. It is seen in figure 3.25 that curves $\mathscr{R}_1^{NC}/\mathscr{R}_2^{NC}$ and $\mathscr{S}_1^{NC}/\mathscr{S}_2^{NC}$ are not coincident. As a consequence, reservoir states corresponding to $\mathscr{S}_2^{NC}$ pattern may in fact result in functioning regimes of the $\mathscr{R}_1^{NC}$ class. Admittedly, the latter condition occurs in a very limited range of pressure and density values; nonetheless it is a further evidence of the fact that isentropic analysis alone is not sufficient for the correct prediction of such non-classical flows. Two additional transitional loci are sketched in figure 3.25. One is the curve associated with transition $\mathscr{R}_c^{NC}/\mathscr{R}_a^{NC}$, which requires that a shock wave featuring $\Psi = 0$ and $d\Psi/d\rho = 0$ is formed, see figure 3.26(*a*), namely this shock has downstream
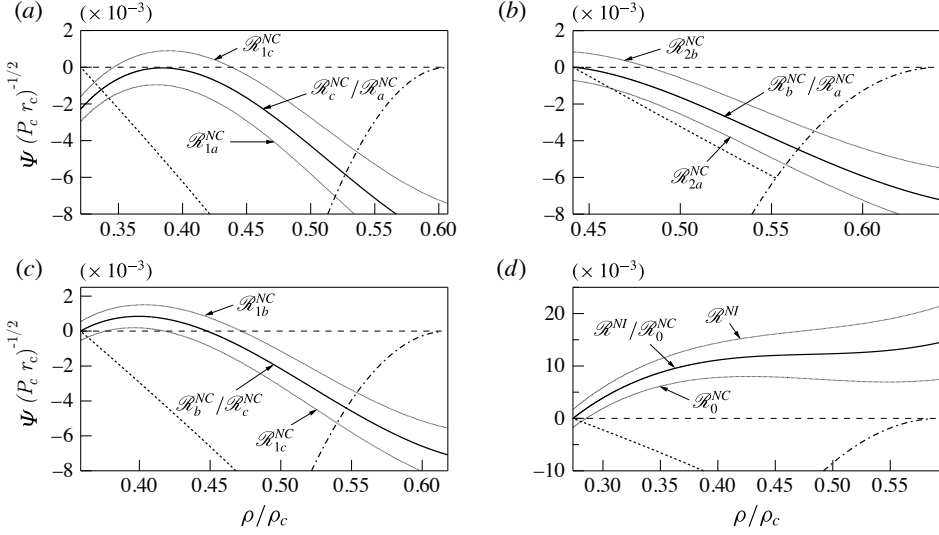
FIGURE 3.26. Exemplary transitional curves in the (Ψ, ρ)–diagram: (*a*) $\mathscr{R}_c^{NC}/\mathscr{R}_a^{NC}$; (*b*) $\mathscr{R}_b^{NC}/\mathscr{R}_a^{NC}$; (*c*) $\mathscr{R}_b^{NC}/\mathscr{R}_c^{NC}$; (*d*) $\mathscr{R}^{NI}/\mathscr{R}_0^{NC}$. Also shown are the sonic locus (–·–·) and the sonic shock disintegration (SD) locus (·········).

sonic state and it is also a stationary point of Ψ. The last transitional curve involves $\mathscr{R}_{2b}^{NC}/\mathscr{R}_{2a}^{NC}$, $\mathscr{R}_{2b}^{NC}/\mathscr{R}_{2c}^{NC}$, $\mathscr{R}_{1b}^{NC}/\mathscr{R}_{1c}^{NC}$ and $\mathscr{R}^{NI}/\mathscr{R}_0^{NC}$. These transitions all have in common the occurrence of a post-sonic compression shock featuring $\Gamma = 0$ at the post-shock state, which is verified if $\Psi = 0$ at the lower endpoint of the density interval where Ψ is defined, see figures 3.26(*b-d*) for exemplary cases.

3.4.4.1 Influence of the molecular complexity

The analysis presented in this section and in the following one addresses an open question in the investigation of Guardone & Vimercati (2016), regarding the general validity of the conclusions drawn using a specific van der Waals fluid (with $c_v/R = 50$, the same used here to illustrate non-classical functioning regimes).

Different van der Waals fluids are considered to study the influence of the molecular complexity on the layout of the thermodynamic map of the functioning regimes in non-classical gasdynamics. Figure 3.27 illustrates the maps of different polytropic van der Waals fluids, for selected values of the molecular complexity. The only parameter which characterizes the molecular complexity in polytropic van der Waals fluids is the dimensionless isochoric specific heat c_v/R. The higher the value of c_v/R, the higher the molecular complexity of the fluid (Colonna & Guardone, 2006). The extension of the region associated with thermodynamic conditions leading to non-classical functioning regimes increases with increasing molecular complexity, as does the negative-Γ region. Most importantly, however, the layout of the map of the functioning regimes depends on the level of molecular complexity. At large values of c_v/R, no qualitative difference is found with the map defined in the previous section for $c_v/R = 50$. For $c_v/R = 35$, the same layout is maintained, though the size of region associated with regime $\mathscr{R}_0^{NC}$ is comparatively smaller. In the exemplary case $c_v/R = 25$, regime $\mathscr{R}_0^{NC}$ is no longer possible. By further decreasing the molecular complexity, the situation is obtained in which regimes of type $\mathscr{R}_c^{NC}$ disappear along with regime $\mathscr{R}_{1a}^{NC}$, as shown in figure 3.27 for $c_v/R = 20$.
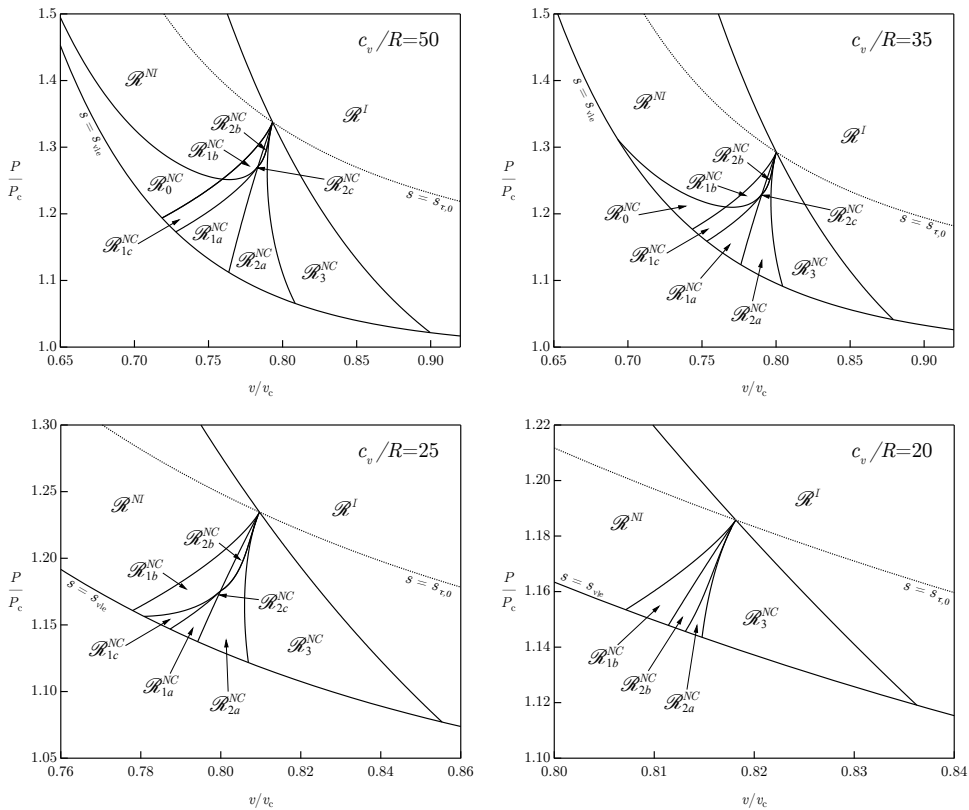
FIGURE 3.27. Thermodynamic maps of reservoir states associated with each functioning regime, computed from different polytropic van der Waals fluids. See figure 3.25 for full caption.

The differences in the observed layout of the maps are somewhat related to the shock-splitting phenomenon, which is indeed responsible for the existence of regime $\mathscr{R}_0^{NC}$ and for the distinction between classes $\mathscr{R}_a^{NC}$, $\mathscr{R}_b^{NC}$ and $\mathscr{R}_c^{NC}$. Therefore, from this analysis a strong connection appears to exist between the molecular complexity of the polytropic van der Waals fluid and the mechanism of shock splitting.

3.4.4.2 Results of accurate models for selected substances

The simple van der Waals model used in the previous sections is abandoned here in favour of more accurate thermodynamic models. Since the size of the negative-Γ region and related non-classical effects are strongly dependent on the thermodynamic model employed (Guardone *et al.*, 2004), and considering also the influence of the map on the molecular complexity suggested by the van der Waals model, here we consider several thermodynamic models capable of taking into account BZT effects. The relevant relations for the considered thermodynamic models are given in the Appendix A.

Figure 3.28 shows the thermodynamic map of the functioning regimes for fluid PP10 (perfluoroperhydrofluorene, $C_{13}F_{22}$), modelled using the Martin-Hou thermodynamic model (Martin & Hou, 1955; Martin *et al.*, 1959) implemented in the library FluidProp (Colonna *et al.*, 2012). With this fluid and model specifications, the layout of the map is qualitatively similar to obtained from the polytropic van der Waals gas with $c_v/R = 25$. Next, we consider the improved Peng-
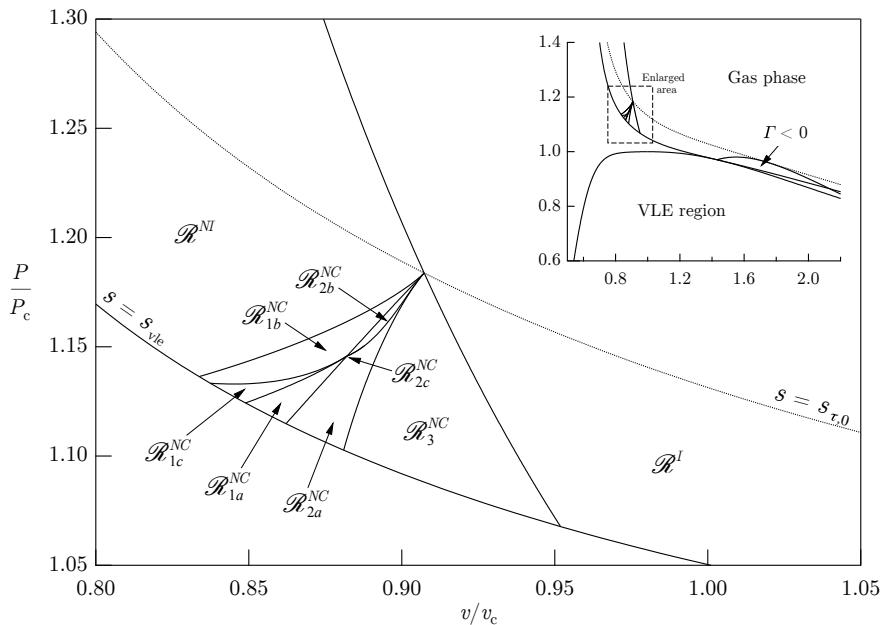
FIGURE 3.28. Thermodynamic map of reservoir states associated with each functioning regime, computed from Martin-Hou thermodynamic model of PP10 (FluidProp library). See figure 3.25 for full caption.

Robinson Stryiek-Vera thermodynamic model (iPRSV, Van der Stelt *et al.*, 2012) of fluid D_6 (dodecamethylcyclohexasiloxane, $C_{12}H_{36}O_6Si_6$), implemented in FluidProp. The thermodynamic map of the functioning regimes for this fluid is reported in figure 3.29 and shows similarities with the map obtained from the polytropic van der Waals model with $c_v/R = 20$, even though for D_6 regime $\mathscr{R}_{1a}^{NC}$ is still possible. Finally, figure 3.30 shows the thermodynamic map of the functioning regimes for fluid MD_4M (tetradecamethylhexasiloxane, $C_{14}H_{42}O_5Si_6$), modelled using the reference thermodynamic model in Span-Wagner form of (Thol *et al.*, 2018), implemented in the REFPROP library. The map of MD_4M is similar to that of PP10 and of the van der Waals fluid with $c_v/R = 25$.

If the parameter c_v/R is used to classify the different layouts of the thermodynamic map of the functioning regimes, then qualitative agreement between the predictions of van der Waals model and those from more accurate models, such as those adopted in this section, is actually not found. In fact, $c_{v,\infty}(T_c)/R = 78.4$ for PP10, $c_{v,\infty}(T_c)/R = 102.5$ for D_6 and $c_{v,\infty}(T_c)/R = 117.2$ for MD_4M, where $c_{v,\infty}(T)$ is the ideal-gas isochoric heat capacity. This discrepancy reflects the known drawback that the polytropic van der Waals model overpredicts the minimum value of Γ and the size of the $\Gamma < 0$ region, if compared to accurate thermodynamic models, as discussed for example by Cramer (1989a) and Guardone & Argrow (2005).

A better matching is instead obtained if Γ_{min}, the minimum value of the fundamental derivative in the vapour region, is used as the comparison criterion. For the polytropic van der Waals model, it is found that $\Gamma_{min} = -1.50, -0.91, -0.45, -0.19$ for $c_v/R = 50, 35, 25, 20$, respectively, while $\Gamma_{min} = -0.30$ for PP10, $\Gamma_{min} = -0.22$ for D_6 and $\Gamma_{min} = -0.37$ for MD_4M.
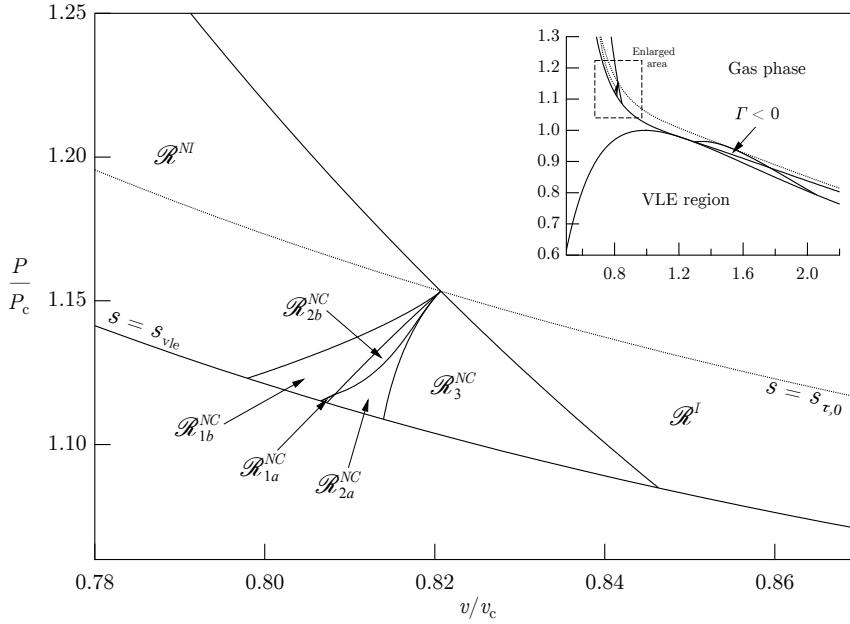
FIGURE 3.29. Thermodynamic map of reservoir states associated with each functioning regime, computed from iPRSV thermodynamic model of D_6 (FluidProp library). See figure 3.25 for full caption.
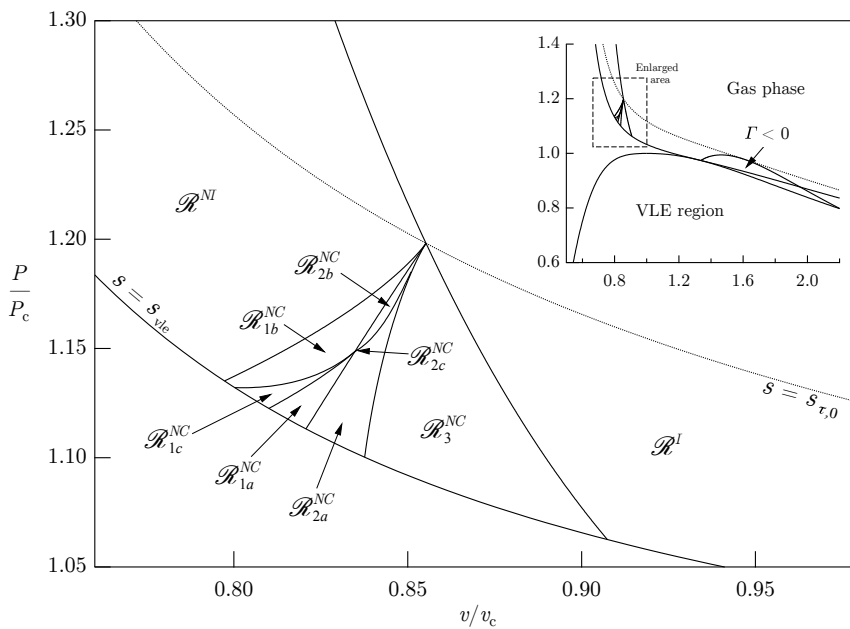

FIGURE 3.30. Thermodynamic map of reservoir states associated with each functioning regime, computed from reference thermodynamic model of MD_4M (REFPROP library). See figure 3.25 for full caption.

3.5   Concluding remarks

Steady flows of single-phase fluids in a converging-diverging nozzle were investigated within the quasi-one-dimensional approximation.

Isentropic flow analysis provided the starting point and a solid base for the study of more general piece-wise isentropic flows including shock waves. To this end, isentropic patterns were introduced to recognize and classify specific isentropic flow properties. Fluids of moderate molecular complexity in their non-ideal gasdynamic regime are found to exhibit non-monotone evolution of the Mach number in supersonic flows. If the molecular complexity is large enough to generate a thermodynamic region where Γ is negative, as many as three sonic points possibly occur along isentropic expansions in the non-classical gasdynamic regime. Isentropic analysis resulted in the definition of two isentropic patterns ($\mathscr{S}^{I}$, $\mathscr{S}^{NI}$) in the classical gasdynamic regime and five isentropic patterns ($\mathscr{S}^{I}$, $\mathscr{S}^{NI}$, $\mathscr{S}^{NC}_{1}$, $\mathscr{S}^{NC}_{2}$, $\mathscr{S}^{NC}_{3}$) in the non-classical gasdynamic regime.

Exact flows were computed by solving an implicit equation for the density distribution along smooth isentropic branches of the solutions and by connecting these with the Rankine-Hugoniot jump relations. The central point in this study is the classification of nozzle flows according the layout of the exact solutions associated with expansions from a reservoir with fixed thermodynamic state into a stationary atmosphere. Starting from reservoir conditions corresponding to the five different isentropic patterns, as many as ten different functioning regimes were identified: the ideal functioning regime $\mathscr{R}^{I}$ which reflects the ideal-gas scenario, the non-ideal functioning regime $\mathscr{R}^{NI}$ and the non-classical regimes $\mathscr{R}^{NC}_{3}$, $\mathscr{R}^{NC}_{2a}$, $\mathscr{R}^{NC}_{2b}$, $\mathscr{R}^{NC}_{2c}$, $\mathscr{R}^{NC}_{1a}$, $\mathscr{R}^{NC}_{1b}$, $\mathscr{R}^{NC}_{1c}$, $\mathscr{R}^{NC}_{0}$. Key features of non-classical flows are the presence of rarefaction shocks, of shock waves that are sonic either on the upstream or downstream side and of compression shocks splitting in two distinct entities (split-shock configuration).

A thermodynamic map of the reservoir conditions resulting in each functioning regime was produced, in order to identify the thermodynamic region of interest for the observation of non-ideal nozzle flows. The complexity of the map is due to the occurrence of shock-induced transitions of the isentropic pattern. It was shown that these transitions, in order to occur in the direction of increasing entropy, must follow a specific sequence. Notably, admissible transitions of the isentropic pattern may either increase or decrease the number of sonic points, leading to significant modification of the flow behaviour. As an example, reservoir states in the region associated with isentropic pattern $\mathscr{S}^{NI}$ can generate a non-classical split-shock configuration (functioning regime $\mathscr{R}^{NC}_{0}$), although the phase plane corresponding to reservoir conditions is of the classical type (one sonic point).

Classical and non-classical nozzle flows were illustrated with the simple polytropic van der Waals model (with $c_v/R = 15$ and $c_v/R = 50$, respectively). By considering different levels of molecular complexity, it was found that each of the above-mentioned functioning regimes can be observed in van der Waals fluids with sufficiently large c_v/R values (and in turn large negative values of Γ_{min}), while some non-classical functioning regimes may in fact disappear if the molecular complexity is reduced (of course only the classical regimes $\mathscr{R}^{I}$ and $\mathscr{R}^{NI}$ are possible if $\Gamma_{min} > 0$). This discrepancy was traced back to the a different response of the flow to the shock-splitting phenomenon, as the molecular complexity of the van der Waals fluid is varied. Addressing an open question by Guardone & Vimercati (2016), the predictions of the simple van der Waals model were verified against accurate thermodynamic models of selected fluids (including state-of-the-art multi-parameters models). Comparison between the different fluids considered indicates that good qualitative agreement, in terms of layout of the thermodynamic map of the functioning regimes, is found between fluids with similar values of Γ_{min}.

Non-classical nozzle flows represent a challenge not only for theory, but also for numerics. In Appendix D, non-classical nozzle flows are computed using finite volume methods, specifically

Roe-type upwind schemes. Numerical experiments show difficulties connected with the numerical representation of sonic shocks: either an incorrect steady-state transonic expansion neighbouring the sonic shock is computed or the discrete steady state is not attained. Lack of convergence is due to numerical unbalancing of the flux difference and source term integral across the transonic expansion which occurs in the close proximity of sonic shocks approaching their steady-state position. An improved method is proposed which is able to produce the desired steady-state balance and allows for substantial improvement in the resolution of sonic shocks.

Some comments concerning the presented results are as follows:

(i) A necessary condition for the existence of regime $\mathscr{R}^{NI}$ in fluids with a retrograde saturated vapour boundary is that $s_{\tau,1} > s_{vle}$. It appears that most retrograde fluids satisfy $s_{\tau,1} > s_{vle}$. To the best of the author's knowledge, retrograde fluids for which $s_{\tau,1} < s_{vle}$ are not available. A necessary condition for the existence of non-classical functioning regimes is that $s_{\tau,0} > s_{vle}$. However, $s_{\tau,0} < s_{vle}$ if the negative-Γ region is sufficiently small or equivalently $|\Gamma_{min}| \ll 1$. This is the case, for example, of polytropic van der Waals gases with molecular complexity c_v/R slightly larger than the limiting value $c_v/R \approx 16.66$ for the existence of the BZT region.

(ii) Extension of the above discussion to the single-phase portions of isentropes $s < s_{vle}$ requires that the crossing of the phase boundary be taken into account. We suggest an approach for future investigation of this problem, in which the procedure described above is partially applicable. Specifically, it applies to reservoir states for which the extrema in the Mach number, along the associated isentropic expansion, occur in the single-phase region before (i.e. at larger densities) crossing the phase boundary. A further transitional criterion is required for the cases where $J > 0$ in crossing the saturation curve. This additional criterion could be defined by looking for the intersections between the $J = 0$ locus and the saturation curve (for a given value of the total enthalpy as in figure 3.2). We observe that the thermodynamic region associated with non-ideal regimes is located at supercritical densities and pressures. It is therefore likely that expansion from a reservoir state located on the saturated vapour boundary, or on its right-hand side in the (P,v)–plane, will be associated with regime $\mathscr{R}^I$.

(iii) There exist fluids with non-retrograde phase boundaries but possessing a $\Gamma < 1$ region; an example is sulfur hexafluoride (as predicted by the reference thermodynamic model from REFPROP). The suggested approach in remark (ii) can be applied to this class of fluids.

(iv) The computed reservoir conditions leading to non-ideal and non-classical functioning regimes lie in a range of pressures and temperatures corresponding to supercritical fluid conditions. For molecularly complex fluid (especially for candidates BZT fluids), thermal stability is a major issue (see Calderazzi & Colonna, 1997; Colonna & Silva, 2003; Colonna et al., 2007; Pasetti et al., 2014). In a future attempt to observe non-classical nozzle flows, an experimental setup realizing an adiabatic blow-down process might be impracticable due to the high temperatures required in the reservoir. In order to avoid thermal decomposition, a potential alternative would be to insert, between the reservoir and the nozzle, a converging duct where the fluid can be heated gradually while expanding, thus increasing the stagnation enthalpy. In this way, it is possible in principle to keep the static temperature below the thermal decomposition limit, although care must be exerted in avoiding stagnation points.

CHAPTER 4

OBLIQUE WAVES IN NON-IDEAL STEADY SUPERSONIC FLOWS

The present chapter covers the theory of oblique waves in steady supersonic flows of single-phase fluids in the non-ideal gasdynamic regime, with reference to the canonical problem of two-dimensional flow past compressive/rarefactive ramps. Oblique waves in classical gasdynamics are either compressive oblique shocks or rarefactive Prandtl-Meyer fans. Of particular interest in non-ideal compressible flows is the possibility of realising oblique shocks that increase the flow Mach number. These special shock waves, named non-ideal oblique shocks, are systematically studied and their admissibility, in terms of pre-shock thermodynamic conditions and Mach number, is also determined. Moreover, a unified description of classical oblique waves is presented to extend the validity of the common shock angle-deflection angle diagram for oblique shocks into the realm of isentropic expansions. In the non-classical gasdynamic regime of BZT fluids, where isentropes and shock adiabats are non-convex in the pressure-specific volume diagram, four additional wave configurations may possibly occur; these are composite waves in which a Prandtl-Meyer fan is adjacent up to two oblique shock waves. Wave curves consisting of states connected to a given initial state (namely, the uniform state upstream of the ramp) by an oblique wave are constructed. In addition to the classical case, as many as six non-classical wave curve configurations are singled out. The necessary conditions leading to each type of wave curves are analysed and a map of the upstream states leading to each configuration is determined.

Selected contents from:

Gori, G., Vimercati, D. & Guardone, A. 2017 Non-ideal compressible-fluid effects in oblique shock waves. *Journal of Physics: Conference Series*, Vol. 821, No. 1, p. 012003. IOP Publishing.

Vimercati, D., Gori, G. & Guardone, A. 2018 Non-ideal oblique shock waves. *J. Fluid Mech*, 847, 266-285.

D'Angelo, S., Vimercati, D. & Guardone, A. 2018 A unified description of oblique waves in ideal and non-ideal steady supersonic flows around compressive and rarefactive corners. *Acta Mechanica*, 229(6), 2585-2595.

Vimercati, D., Kluwick, A. & Guardone, A. 2018 Oblique waves in steady supersonic flows of Bethe-Zel'dovich-Thompson fluids. *J. Fluid Mech*, 855, 445-468.

4.1   Introduction and theoretical background

In the supersonic ramp problem, a supersonic uniform stream is deflected onto a sharp corner by means of oblique waves. The term "oblique" reflects the distinguishing geometrical property of the wave of being oblique with respect to the local flow direction. The steady-state solution configurations of the ramp problem are fundamental in gasdynamics, as they provide both global and local structures in diverse flow fields: supersonic intakes and discharges, turbine flows, steady regular and Mach reflections, two-dimensional Riemann problems, just to mention a few.

Oblique waves originating at the corner of a ramp/wedge exposed to a supersonic stream exhibit no length scale provided that the ramp angle does not exceed a so-called detachment angle which depends on the upstream state. In this case, it is possible to study oblique waves moving from the one-dimensional Riemann problem, as suggested by Menikoff & Plohr (1989). If a scale-invariant solution of the Euler equations is sought, a set of ordinary differential equations is obtained which produces three distinct waves families, for both two-dimensional steady supersonic flows and unsteady one-dimensional flows (see, e.g., Godlewski & Raviart, 2013). One wave family is linearly degenerate (in two dimensions with a multiplicity of two) and corresponds to contact discontinuities, while the other two families are non-degenerate (except at isolated points in non-classical flows) and are associated with acoustic and shock waves. Oblique shocks in two dimensions satisfy the one-dimensional Rankine-Hugoniot relations in the direction normal to the shock front. Smooth solutions consist of wave fans, spreading either in the two-dimensional space or in one dimension as time progresses. Thus, unsteady normal shocks translate into steady oblique shocks and unsteady wave fans become Prandtl-Mayer waves. The qualitative equivalence between these wave patterns is key to extend the tools and concept developed for the one-dimensional Riemann problem to the study of oblique waves in steady supersonic flows. Following the same line of Menikoff & Plohr (1989), in this chapter the analysis of the ramp problem is traced back to the construction of steady two-dimensional wave curves, which consist of all the states connected to a given supersonic upstream state by means of an oblique wave. Similarities and differences with the wave curves of the one-dimensional Riemann problem are discussed.

In the classical theory of gasdynamics, a compressive ramp can produce two types of oblique wave — the weak and the strong oblique shock configurations — provided the wedge angle doesn't exceed the detachment angle, whereas a rarefactive ramp gives rise to a centred Prandtl-Meyer fan (see, e.g., Thompson, 1988). In dilute-gas flows to which the theory of perfect gases can be reasonably applied, the variation of the thermodynamic and kinematic quantities across the shock wave is determined by the Mach number of the flow ahead of the shock, relative to the shock front itself. If instead the thermodynamic states of the fluid cannot be accurately described by means of the perfect-gas model, a more or less noticeable dependence on the pre-shock thermodynamic state, say the values of the pre-shock temperature and pressure, is also observed. Similar considerations apply to Prandtl-Meyer waves, for which the Mach number of the upstream state entirely determines the properties of the wave.

Depending on the upstream state, in the non-ideal gasdynamic regime a number of atypical effects can be observed in oblique waves. Of particular interest in practical applications is the variation of the flow Mach number across the wave. Cramer & Crickenberger (1992) demonstrated that the Mach number can possibly decrease, rather than increase as in the dilute-gas limit, across Prandtl-Meyer waves. More recently, the oblique-shock counterpart of this phenomenon has been documented by Gori *et al.* (2017*a*). In their investigation, Gori *et al.* (2017*a*) reported conditions under which oblique shocks in van der Waals gases increase the Mach number and named this peculiar kind of oblique shocks as non-ideal oblique shocks (in contrast to oblique shocks in the ideal gasdynamic regime where the Mach number is always smaller in the post-shock state than in the pre-shock state). The non-ideal increase of the flow Mach number across oblique

shocks is definitely relevant to applications where oblique shock waves are either intentionally formed (e.g. engine intake ramps) or a by-product of the supersonic flow expansion (e.g. fish-tail shocks in turbine nozzle vanes, over/under-expanded jet from a nozzle exit). In this chapter, a step towards the precise characterization of non-ideal oblique shocks is performed. Specifically, the conditions leading to the formation of non-ideal oblique shocks in single-phase fluids are examined. A convenient procedure is detailed which allows to determine the existence domain, in terms of pre-shock state properties, of non-ideal oblique shock waves. Results are then presented using accurate state-of-the-art thermodynamic models for several fluids of practical interest.

An additional theme that the present chapter deals with, in the context of classical gasdynamics, is related to the geometrical properties of oblique waves. These are typically embedded in the shock angle–deflection angle diagram for oblique shocks, while the geometrical information regarding the fan configuration is retrieved by the Prandtl-Meyer function. It is remarkable that the geometrical properties of oblique waves can be seen under a unifying perspective. To this end, the shock angle–deflection angle diagram is extended into the realm of Prandtl-Meyer waves by defining an equivalent-fan angle. Guided by the bisector rule for oblique shocks, which states that in the isentropic approximation the shock angle equals the average between the pre-shock and the post-shock characteristic slope (Kluwick 1971 for ideal gases, extension below to non-ideal gases), the choice of the simple arithmetic mean between the two extreme angles of the fan is shown to yield the desired matching with the oblique shock curve. Results are presented for both perfect gases, for which the newly introduced diagram depends exclusively on the value of the upstream flow Mach number, and for non-ideal gases modelled using accurate thermodynamic models, where a marked dependence on the upstream thermodynamic state is also observed and discussed.

In the theory of non-classical gasdynamics, the steady supersonic flow past solid wedges was only partially examined in the scientific literature. In his pioneering work, Thompson (1971) studied the formation of the two elementary wave configurations in the ramp problem for negative-Γ fluids: the oblique rarefaction shock and the compressive Prandtl-Meyer fan, which represent the non-classical counterparts of the classical compression shock and rarefaction fan. Although oblique waves were not explicitly dealt with, Menikoff & Plohr (1989) suggested the important analogy with the one-dimensional Riemann problem (for an arbitrary equation of state, thus including BZT behaviour) mentioned above. Recently, the ramp problem for BZT fluids was investigated by Kluwick & Cox (2018a) in the transonic approximation, with the further assumption that $|\Gamma| \ll 1$, namely in the vicinity of the transition line $\Gamma = 0$. In this framework, the parameter space determining the solution configuration includes the wedge angle, the upstream Mach number, the upstream fundamental derivative and its isentropic derivative with respect to the density. The authors showed that, through the scaling originally introduced by Cramer & Tarkenton (1992), the parameter space can be reduced to dimension two. Five different ranges of these similarities parameters were identified, which correspond to qualitative different flow scenarios. The resulting picture is considerably rich, due to the possibility of observing, in addition to inverted gasdynamic behaviour (viz. rarefaction oblique shocks and compression Prandtl-Meyer fans), also composite waves configurations, in which a Prandtl-Meyer fan is adjacent to an oblique shock wave.

In order to put the following analysis in the correct perspective, it is important to note that the flow past ramps/wedges is a particular case of the more general gasdynamic problem of the abrupt turning of a supersonic stream, which is accomplished by scale-invariant oblique waves. The ramp problem is considered here as an exemplifying gasdynamic problem, arguably the simplest, to which the theoretical framework established below can possibly apply. It is simple because it involves one single oblique wave. More complex problems (e.g., wave interactions) can be addressed building on the concepts developed for the ramp problem.

In the present chapter, oblique waves in the non-classical gasdynamic regime of BZT fluids are

systematically investigated by identifying each possible wave-curve configuration. The proposed analytical approach — undertaken here in a fully non-linear perspective, differently from the asymptotic theory developed by Kluwick & Cox (2018a) — leads to the identification of seven different wave-curve types, six of which are of purely non-classical type. The latter cases all include branches where the solution of the ramp problem consists of a composite wave (e.g. combination of Prandtl-Meyer fan and oblique shock). As the wave-curve configuration is determined by the properties of the uniform supersonic state upstream of the wedge, the corresponding parameter space (e.g. the upstream pressure, density and Mach number) is explored. Eventually, the necessary conditions for the occurrence of each of the identified wave-curve types are singled out and a map of the upstream states leading the different configurations is delineated. The van der Waals model of a BZT fluid is used for explanatory purposes, but results are confirmed by accurate thermodynamic models.

The structure of this chapter is as follows. In §4.2, the mathematical description of the fluid flow is recalled for the special case of two-dimensional steady scale-invariant flows that are compatible with a prescribed supersonic conditions at upstream infinity. The elementary waves that can possibly occur in these flows are defined. In §4.3, we describe how the established concepts for the one-dimensional Riemann problem can be suitably translated into the present two-dimensional steady context, thus leading to the definition of the wave curves for the ramp problem. The construction of these curves from one-parameter families of elementary waves is treated. Sections 4.4 and 4.5 present the results for classical and non-classical gasdynamic regime, respectively. In §4.4, the focus is on non-ideal oblique shocks and on the unified description of oblique waves, while in §4.5 is primarily aimed at classifying non-classical oblique waves and the related wave curves. Section 4.7 presents the concluding remarks.

4.2 Formulation

We restrict our attention to the steady two-dimensional flow equations that model equilibrium fluid dynamics in the limit of vanishing viscosity and heat conductivity, namely the steady two-dimensional Euler equations (see 2.2) reported here in conservative form for a cartesian (x, y) coordinate system as

$$\frac{\partial}{\partial x} F_x(q) + \frac{\partial}{\partial y} F_y(q) = 0 \tag{4.1}$$

where the unknown vector of conservative variables $q(x, y)$ is

$$q = (\rho,\ \rho u_x,\ \rho u_y,\ \rho e^t)^T \tag{4.2}$$

in which u_x and u_y are the velocity x-component and y-component, respectively, and the fluxes F_x and F_y are given by

$$F_x(q) = (\rho u_x,\ \rho u_x^2 + P,\ \rho u_x u_y,\ \rho h^t u_x)^T, \tag{4.3}$$

$$F_y(q) = (\rho u_y,\ \rho u_x u_y,\ \rho u_y^2 + P,\ \rho h^t u_y)^T, \tag{4.4}$$

where the pressure is computed, e.g., from the equation of state $P(e, \rho) = P(q_4 - (q_2^2 + q_3^2)/(2q_1), q_1)$ and similarly for other thermodynamic quantities encountered in the following (being q_i, $i = 1, \ldots, 4$ the i-th element of q).

The steady two-dimensional Euler equations are classified as elliptic, parabolic or hyperbolic depending on the value of the flow Mach number (see, e.g., Godlewski & Raviart, 2013). System (4.1) is of the elliptic type if $M < 1$ and of the parabolic type if $M = 1$. If $M > 1$, system (4.1) is hyperbolic in every direction (i.e. timelike direction) that is not perpendicular to characteristic lines (Dafermos, 2010).
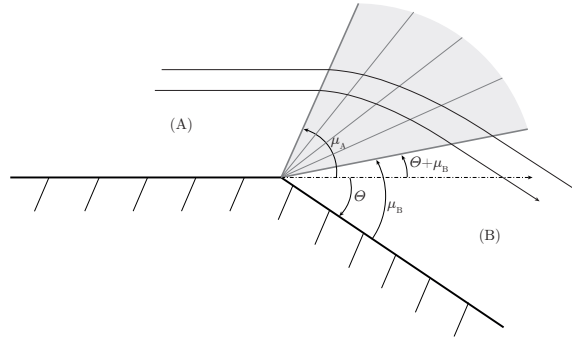
FIGURE 4.1. Sketch of centred fan of left-running waves over a rarefactive corner. Subscripts A and B denote the states upstream and downstream of the fan, respectively.

We consider, with reference to the ramp problem, a solid boundary described by the the equations

$$y = 0, \qquad\qquad x \leqslant 0, \tag{4.5}$$

$$y = (\tan \Theta)\, x, \qquad x > 0, \tag{4.6}$$

where Θ is the ramp angle. The corner of the ramp is thus located at $x = 0$, $y = 0$. Along the solid wall, slip boundary condition is enforced. A uniform flow state is prescribed at infinite upstream $x = -\infty$, which is aligned with the wall ($u_y = 0$) and supersonic.

In this study, scale-invariant solutions of the steady supersonic ramp problem are examined. These are functions of the form $q(x, y) = w(y/x)$ that satisfy the integral form of the conservation law associated with (4.1) in the domain (circular sector) delimited by the solid wall, along with the boundary conditions imposed on the wall itself and at upstream infinity. On physical grounds, we shall also limit ourself to consider scale-invariant solutions that are piecewise C^1. Introducing $\xi = y/x$, this means that $w(\xi)$ is continuously differentiable except for a finite number of points at which w has a jump discontinuity or is continuous but not differentiable. As a consequence, we examine solutions that are constant along rays emanating from the corner of the ramp; in the solution flow field, a finite number of rays, carrying jump discontinuities in w or its gradient, separate circular sectors where w is continuously differentiable. In the following, the building blocks for the construction of scale-invariant solutions of the steady supersonic ramp problem are described. These are the continuously differentiable simple waves, the discontinuous waves (shocks and contacts) and the composite waves, which are combination of the previous ones.

4.2.1 Simple waves

The flow pattern corresponding to a non-trivial, continuously differentiable function $w(\xi)$ is called a centred simple wave and in the physical plane it takes the form of a fan, commonly denoted as Prandtl-Meyer fan, converging at a single point. An example of a Prandtl-Meyer fan is shown in figure 4.1. At points where $w(\xi)$ is continuous and differentiable, equation (4.1) is equivalent to the generalized eigenvalue problem

$$\big(\mathcal{A}_y(w(\xi)) - \xi \mathcal{A}_x(w(\xi))\big) w'(\xi) = 0, \tag{4.7}$$

where $\mathcal{A}_x(q) = \nabla_q F_x(q)$ and $\mathcal{A}_y(q) = \nabla_q F_y(q)$ are the Jacobians of the fluxes (see appendix B). It follows that either $w'(\xi) = 0$ or

$$\xi = \lambda_k(w(\xi)), \qquad \text{for some } k \in \{1, ..., 4\} \tag{4.8}$$

and

$$w'(\xi) = r_k(w(\xi))/\alpha_k(w(\xi)), \qquad \text{for some } k \in \{1, ..., 4\}, \tag{4.9}$$

where λ_k and r_k denote the k-th eigenvalue and right eigenvector, respectively, in the generalized eigenvalue problem (4.7) and $\alpha_k = \nabla_q \lambda_k(q) \cdot r_k(q) \neq 0$ is the nonlinearity factor (see appendix B). Note also that the ray marking the transition between a simple-wave region and a uniform flow region is a point of jump discontinuity for $w'(\xi)$.

Since $\xi = x/y$ is a real number, relation (4.8) implies that the eigenvalue λ_k is also real. It is well-known (see, e.g., Thompson, 1988) that the characteristic equation of the eigenvalue problem (4.7) always gives a real root $\lambda = \tan \vartheta$ of multiplicity two, where $\vartheta = \tan^{-1}(u_y/u_x)$ is the angle formed by the particle path with the x-axis (positive if counter-clockwise), whereas the remaining roots are real if and only if the flow is supersonic ($M > 1$). For supersonic flow, the eigenvalues of the steady planar Euler equations can be written as

$$\lambda_1 = \tan(\vartheta - \mu), \quad \lambda_{2,3} = \tan \vartheta, \quad \lambda_4 = \tan(\vartheta + \mu), \tag{4.10}$$

in which the angle $\mu = \sin^{-1}(1/M)$ is called the Mach angle. The characteristic curves, having slope $dy/dx = \lambda_k$ in the physical (x, y)–plane, are thus the particle paths and the curves that locally form an angle $\pm \mu$ with the particle paths. Because of this, the characteristics of the 1–field and 4–field (the k–field is the characteristic field associated with λ_k and r_k) are also referred to as right-running and left-running acoustic waves, respectively. Equation (4.8) implies that the rays in a centred simple wave correspond to characteristic lines.

Relation (4.9) asserts that the states within a centred simple wave all lie along an integral curve of $r_k(q)$. However, in order that $w'(\xi)$ stays finite, the nonlinearity factor appearing in (4.9) must not be zero. With a proper scaling of the eigenvectors, the nonlinearity factors read (appendix B)

$$\alpha_{1,4} = \Gamma, \quad \alpha_{2,3} = 0, \tag{4.11}$$

thus showing, together with relation (4.9), that continuously differentiable waves are not possible in the 2–field and 3–field (which are linearly degenerate and give rise to contact discontinuities, see §4.2.2) and in the 1–field and 4–field at degenerate points $\Gamma = 0$. In other words, centred simple waves can only take place in the acoustic wave families (1–field or 4–field) if $\Gamma \neq 0$.

For each characteristic field of an n-dimensional system of conservation laws (in our case $n = 4$) is defined a set of $n - 1$ Riemann invariants (Dafermos, 2010). A Riemann invariant of the k-th field is a scalar-valued function that is constant along the integral curve of $r_k(q)$. The Riemann invariants of the 1–field and 4–field are the triplets

$$\begin{cases} s, \; h^t, \; \vartheta - v & \text{(1–field)}, \\ s, \; h^t, \; \vartheta + v & \text{(4–field)}, \end{cases} \tag{4.12}$$

where

$$v = v_0 + \int_{u_0}^{u} \sqrt{M^2 - 1} \frac{du}{u} = v_0 - \int_{P_0}^{P} \frac{\sqrt{M^2 - 1}}{\rho u^2} dP \tag{4.13}$$

is the Prandtl-Meyer function, in which subscript 0 refers to a reference state (in fluids exhibiting $\Gamma < 1$, the above forms of the Prandtl-Meyer function are valid at all velocities and pressures, contrarily to the more common form parametrized using the Mach number, see Cramer & Crickenberger 1992). Therefore, the flow field within a centred simple wave has constant entropy and
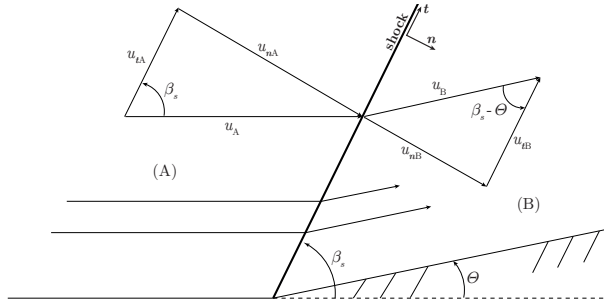
FIGURE 4.2. Sketch of left-running oblique shock over a compressive corner. Subscripts A and B indicate the pre-shock and post-shock quantities, respectively; $\boldsymbol{n}$ and $\boldsymbol{t}$ are the unit vector normal and tangent to the shock front, respectively, $u_n = \boldsymbol{u} \cdot \boldsymbol{n}$ is the normal velocity ($\boldsymbol{n}$ is selected such that $u_n > 0$) and $u_t = \boldsymbol{u} \cdot \boldsymbol{t}$ is the tangential velocity.

total enthalpy. By examining the eigenvectors r_1 and r_4 (see appendix B), it is readily seen that $P'(\xi) \gtrless 0$, $u'(\xi) \lessgtr 0$ and $\vartheta'(\xi) \gtrless 0$ if $\Gamma \gtrless 0$ within left-running simple waves, while $P'(\xi) \lessgtr 0$, $u'(\xi) \gtrless 0$ and $\vartheta'(\xi) \gtrless 0$ if $\Gamma \gtrless 0$ in right-running simple waves. Among the other things, these inequalities imply that simple waves through states $\Gamma > 0/\Gamma < 0$ are rarefactive/compressive.

4.2.2 Shock waves

The turning of a supersonic stream can also be accomplished by means of shock waves. If w has a jump discontinuity along the ray ξ, the balance laws of mass, momentum and energy assume the form

$$[F_y - \xi F_x] = 0, \tag{4.14}$$

where $[\cdot]$ denotes the jump across the discontinuity. Equations (4.14) mirror the Rankine-Hugoniot relations (2.10)-(2.12). As discussed in §2.3, the Rankine-Hugoniot relations include both contact discontinuities and shock waves, which are distinguished according to the value of the mass flux $m = \rho u_n$ across the discontinuity front.

The states that can be connected by means of contact discontinuities lie on the integral curves of $r_2(q)$ and $r_3(q)$, see Godlewski & Raviart (2013). The corresponding Riemann invariants are

$$\begin{cases} P, \ \vartheta, \ s & \text{(2–field)}, \\ P, \ \vartheta, \ u & \text{(3–field)}, \end{cases} \tag{4.15}$$

thus indicating that the discontinuous waves of the 2–field are vorticity waves (or slip lines, i.e. jumps in the velocity magnitude at the same pressure, entropy and flow direction) and those of the 3–field are entropy waves (i.e. entropy jumps at constant pressure and velocity). Note that ϑ is constant across contact discontinuities, which therefore cannot produce any flow deflection.

Shock waves are discontinuities in the acoustic wave families (1–field and 4–field) and thanks to the conservation of the tangential velocity they can be represented as normal shocks to which a uniform velocity field, parallel to the shock front, is superposed. An oblique produced by a ramp is sketched in figure 4.2. It is easily checked that if the normal velocity decreases when the shock front is crossed (from the mass and normal momentum relations, the shock is compressive), the shock wave turns the flow towards the front itself; the opposite occurs if the normal velocity increases (rarefaction shock). This means that $[\vartheta] \gtrless 0$ if $[P] \gtrless 0$ for left-running shock waves (4–field) and $[\vartheta] \lessgtr 0$ if $[P] \gtrless 0$ for right-running shocks (1–field).
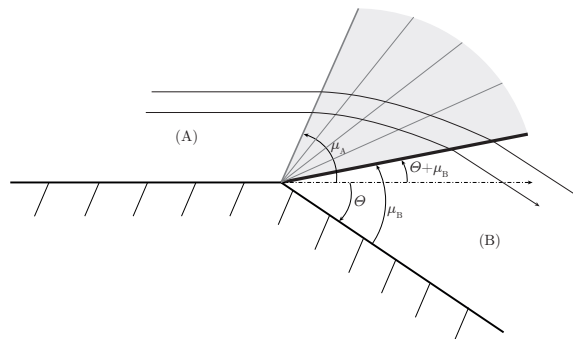
FIGURE 4.3. Sketch of left-running composite wave over a rarefactive corner: the rarefaction fan terminates in a rarefaction shock. Subscripts A and B denote the states upstream and downstream of the composite wave, respectively.

4.2.3 Composite waves

Following the loss of genuine nonlinearity due to crossing of the $\Gamma = 0$ locus, in addition to the elementary waves described above, composite waves in which two or more elementary waves propagate as a single entity can possibly occur (Menikoff & Plohr, 1989; Kluwick, 2001). Figure 4.3 illustrates an exemplary composite wave formed by a Prandtl-Meyer fan and a rarefaction shock. In order that a composite wave exists, the propagation rays of its elementary waves must be compatible, i.e. they must neither collide nor split. This rules out the case that composite waves be formed by elementary waves of different families. Composite waves can be obtained by stitching together simple waves and shock waves of a given acoustic wave family (of course, two or more adjacent simple waves can be regarded as forming a single simple wave and two or more adjacent discontinuities can be seen as a single discontinuity). In order that a shock wave is adjacent to a simple waves fan, the shock must propagate on the same ray as the edge of the fan, which in turn implies that $M_n = 1$ on the side of the shock wave neighbouring the fan (Cramer *et al.*, 1986). Thus, a composite wave includes at least one sonic shock (see §2.3.2).

From the arguments of sections 4.2.1 and 4.2.2 on the variation of the flow angle and the pressure across simple waves and shock waves, it is readily obtained that both the flow angle and the pressure are monotonic within a composite wave. It will be shown below that the topology of Γ in typical BZT fluids imposes a constraint on the maximum number of simple wave fans or shock waves that can possibly appear in a composite wave.

4.3 Wave curves

We now investigate the wave configurations that can possibly deliver the turning of an upstream supersonic stream in a steady flow. Across entropy and shear waves there is neither mass flux nor deviation of the particle paths, see the Riemann invariants (4.15). Therefore the uniform supersonic flow can be turned only across acoustic or shock waves (or combination of these), i.e. *oblique waves* with respect to the flow direction, thanks to their geometrical properties in the physical plane. With reference to the ramp problem, we note that the presence of both left-running and right-running waves emanating from the ramp corner is not compatible with the boundary conditions imposed by the solid boundary, since the disturbance generated by the change in the wall slope must propagate away from the wall itself. It is assumed here that the ramp angle Θ

appearing in (4.5) coincides with the flow deviation across oblique waves, namely $\Theta = \vartheta_{\mathrm{B}} - \vartheta_{\mathrm{A}}$, where subscripts A and B indicate the upstream and downstream states, respectively (in our case, $\vartheta_{\mathrm{A}} = 0$ as the upstream flow is aligned with the x–axis). Contrary configurations that do no satisfy this requirement include contact discontinuities downstream of the oblique wave[1]; these cases are not relevant to our purposes.

In terms of scale-invariant wave patterns, the two-dimensional steady supersonic flow involves several analogies with the one-dimensional unsteady case. As is well-known (see, e.g., Godlewski & Raviart, 2013), the unsteady one-dimensional Euler equations possess two acoustic characteristic fields corresponding to left-facing and right-facing waves (propagating with speed $u - c$ and $u + c$, respectively), with a linearly degenerate field corresponding to contact discontinuities (propagating with speed u) in between. In both two-dimensional steady supersonic flows and one-dimensional unsteady flows, the acoustic fields have a similar structure thanks to the following facts. Smooth wave patterns occur, in both cases, in the form of centred fans of acoustic waves. The nonlinearity factor of the acoustic fields, in both cases, are proportional to Γ, which means that the breakdown of simple waves coincides with the condition $\Gamma = 0$ both in two-dimensional steady supersonic flows and in one-dimensional unsteady flows (in turn, this implies that the mechanism of formation of composite waves is the same). Moreover, oblique shocks in two dimensions satisfy the one-dimensional Rankine-Hugoniot relations in the direction normal to the shock front. Thus, steady Prandtl-Meyer fans and oblique shocks are the counterparts of unsteady wave fans and normal shocks, respectively. The correspondence between the elementary wave patterns makes it possible to extend many of the concepts developed for the one-dimensional unsteady case to the steady two-dimensional one. On the other hand, two differences between these frameworks are as follows. In two-dimensional steady flows, scale-invariant waves can separate hyperbolic and elliptic regions of the flow fields. This change can possibly occur across strong oblique shocks, which drive the Mach number below unity. Secondly, in two-dimensional steady flows, there exists a maximum pressure jump across shock waves, due to the fact that the total enthalpy is constant (cf. 4.12 and 2.12) along streamlines. In contrast, in one-dimensional unsteady flows, any value of the pressure jump can be attained depending on the shock speed.

To formalise the similarity between one-dimensional unsteady flows and two-dimensional steady flows, we introduce here the idea of wave curves for steady two-dimensional flows. In the one-dimensional unsteady flows, the wave curve represents the set of states connected to a given initial state by a scale-invariant wave of the left-facing or right-facing field (Menikoff & Plohr, 1989). In two-dimensional steady flows, the wave curve consists of all the states connected to a given supersonic state by means of a steady scale-invariant planar wave of the left-running or right-running field. Thus, the wave curve is made of branches corresponding to centred simple waves, shock waves and composite waves. In the context of the supersonic ramp problem, the wave curve computed from the state associated with the uniform supersonic stream embeds all the scale-invariant waves that can possibly deliver the deflection imposed by the ramp.

Similarly to the one-dimensional case, the construction of wave curves can be simplified by first considering the projection onto the thermodynamic variables; the kinematic quantities are retrieved afterwards (this will prove particularly useful in the non-classical context). Three important observations lay the groundwork for the following treatment:

(i) the projection of the set of states within a Prandtl-Meyer fan, onto the thermodynamic variables, is a branch of the isentrope passing through the upstream thermodynamic state (cf. the Riemann invariants 4.12). Given, e.g., the downstream pressure, all the thermodynamic quantities downstream of the fan are readily determined. The kinematic quantities (e.g. u_{B} and ϑ_{B}) are computed by imposing the conservation of the total enthalpy h^t and of the

---

[1]The solid ramp/wedge can be replaced by a slip line beyond which the fluid is at rest, without changing the overall deflection of the supersonic stream produced by the oblique wave.

Riemann invariant $\vartheta \mp \nu$ of opposite sign;

(ii) the projection of a shock curve (see §2.3.2), onto the thermodynamic variables, is a branch of the Hugoniot locus passing through the upstream thermodynamic state (cf. equation 2.15). Given, e.g., the downstream pressure, the downstream density is computed from (2.15) and, from those, each downstream thermodynamic quantity and the mass flux $m = (-[P]/[v])^{1/2}$. The shock angle β_s and flow deflection angle Θ (with respect to the upstream flow direction) are computed from $m = \rho_A u_A \sin \beta_s$ and $\rho_A \tan \beta_s = \rho_B \tan(\beta_s - \Theta)$, respectively.

(iii) Prandtl-Meyer fans cannot be continued at states of linear degeneracy $\Gamma = 0$, because there the characteristic lines fold. If a further pressure variation is imposed, this is accomplished by means of a composite wave in which the fan terminates in a pre-sonic oblique shock (Menikoff & Plohr, 1989). The shock-wave branch of the wave curve cannot be continued at entropy extrema, where the Rayleigh line is tangent to the shock adiabat, because a further variation in the post-shock pressure would lead to violation of the speed ordering relation (2.18). The wave curve beyond an entropy extremum in the Hugoniot locus is continued as a composite shock/fan wave. By collecting the states downstream of the composite wave, a composite locus is obtained (see also Kluwick, 2001).

4.4 Classical oblique waves

The concepts outlined in the previous sections are specialised here to the case of molecularly complex fluids in the non-ideal yet classical gasdynamic regime. Classical waves curves are computed in §4.4.1 and peculiarities related to non-ideal thermodynamics are discussed. In particular, the focus is on non-ideal oblique shocks allowing for a discontinuous increase of the flow Mach number (§4.4.2). Also presented is a unified description of geometrical properties of the wave pattern around compressive and rarefactive corner (§4.4.3).

4.4.1 Wave curves structure

Let us consider the structure of the wave curve projection onto the thermodynamic variables, say the (P, v)–plane. Remarks (i) and (ii) in the previous section imply that for a given upstream state, the projected wave curve is a subset of the one-dimensional unsteady counterpart. The kinematic state of the upstream flow, through the value of the total enthalpy which remains constant throughout the flow field and limits the maximum pressure jump across oblique shocks, determines endpoints of the wave curve. This suggests that one can use the well-established results for the one-dimensional unsteady case (replacing, of course, unsteady wave fans with Prandtl-Meyer waves and unsteady normal shocks with steady oblique shocks) to determine the underlying structure of the wave curve in the thermodynamic plane, namely the extended (i.e. drawn up to vacuum and infinite pressure) wave curves. The upstream kinematic is then taken into account (in the following section) to determine endpoints of the waves curves.

An exemplary wave curve is shown in figure 4.4(a) and is computed from the reference thermodynamic model (Span-Wagner EoS, see appendix A) of MDM (Thol *et al.*, 2017) implemented in REFPROP (Lemmon *et al.*, 2013). Based on the arguments of §4.2.1 and §4.2.2, figure 4.4(a) can be commented on as follows. The rarefaction branch of the extended wave curve through state A is the isentrope containing A, associated with elementary Prandtl-Meyer waves connected to A. On the other hand, the compressive branch of the wave curve coincides with the shock adiabat centred on A, associated with oblique shock waves. The fact that $\Gamma > 0$ in classical gasdynamics precludes the possibility that simple waves fold, the existence of entropy extrema along shock
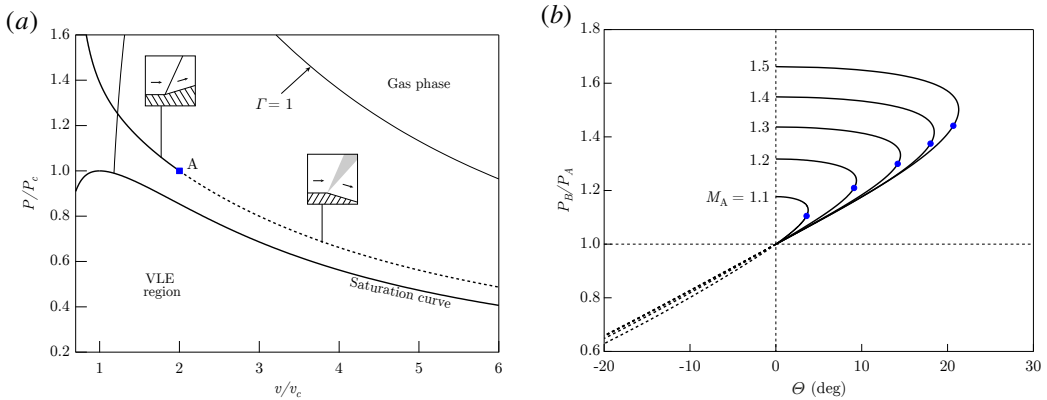
FIGURE 4.4. Wave curves for MDM, computed from the reference thermodynamic model available in REFPROP. Upstream thermodynamic conditions: $P_A = P_c$, $v_A = 2v_c$. (a) Extended wave curve in the pressure–specific volume diagram, attached to each branch is a sketch of the corresponding wave in the physical plane, for an exemplary flow past a ramp; (b) left-running wave curves in the pressure–deflection diagram for selected upstream Mach numbers. Wave configurations: —— shock, - - - fan. Symbol • denotes downstream sonic points ($M_B = 1$).

adiabats and therefore the existence of composite waves[2]. It follows that the local structure on both sides of the upstream thermodynamic state is maintained for arbitrary downstream pressure changes.

A complementary description of the wave curve is obtained from common pressure–deflection diagram, where the downstream pressure P_B is plotted against the downstream deflection angle Θ that the wave generates. The representation of the wave curve in these variables is necessary connected with the kinematic quantities along the wave curves. Here it is possible to evaluate the effect of the kinematic state of the upstream flow, in particular how this determines the endpoints of the wave curve (which are associated with the maximum pressure jump across oblique shocks). The upstream kinematic state is accounted for in terms of upstream Mach number M_A. Without loss of generality, only left-running wave curves are considered, as the right-running wave is just the reflection, through the $\Theta = 0$ axis, of the left-running counterpart. Figure 4.4(b) illustrates selected (P_B, Θ)–polars corresponding to the same upstream thermodynamic state of figure 4.4(a) and different values of the upstream Mach number. The rarefaction branch (Prandtl-Meyer waves) extends to vacuum conditions (eventually the saturated phase boundary is crossed), where the deflection angle attains a finite limit value. The pressure rise along the compression branch is limited by the normal shock wave ($\beta_s = 90°, \Theta = 0$) from the upstream state. By increasing the upstream Mach number, and therefore the total enthalpy of the stream, the maximum pressure jump increases. As is well-known (see, e.g., Thompson, 1988), for a given $\Theta > 0$ two oblique shocks can possibly occur, which are named the weak and the strong (based on the pressure jump) solutions.

The wave-curve configuration shown here using MDM is common to all single-phase fluids in their classical gasdynamic regime. Nevertheless, important effects of practical interest are associated with the variation of the flow Mach number across oblique waves in the non-ideal regime. The flow field corresponding to a simple wave is isentropic with constant total enthalpy, similarly to flows treated in §3.3.1. It follows that the variation of the flow Mach number with

---

[2]If $\Gamma > 0$, ξ is monotonic along integral curves of the acoustic fields because the related nonlinearity factor is always positive, see equations (4.8) and (4.11). Sonic points and therefore entropy extrema along the shock adiabat are not allowed from the Bethe-Weyl theorem, see relations (2.27) and (2.36).

the density, within Prandtl-Meyer fans, is ruled by the quantity J defined by relation (3.6). Thus, as first noticed by (Cramer & Crickenberger, 1992), in the non-ideal regime $\Gamma < 1$ it is possible that the expansion around a corner decreases the Mach number of a supersonic stream, rather than increasing it as is the case if $\Gamma > 1$. The non-ideal Mach number decrease in the simple wave is then associated with $J > 0$. Interestingly, analogous considerations apply for the Mach number variation across oblique shocks generated at compressive corners. Indeed, in the corresponding flow field the total enthalpy is uniform and entropy jumps can be made arbitrary small by controlling the shock strength through the ramp angle. This suggests that the flow Mach number may possibly increase across oblique shocks of small amplitude with pre-shock state in the $\Gamma < 1$ region and such that $J > 0$. Surprisingly enough, the discontinuous increase of the Mach number across oblique shocks has not been studied in the scientific literature until the recent studies by Gori *et al.* (2017*a*) and Vimercati *et al.* (2018*a*).

4.4.2   Non-ideal oblique shocks

Analysis of the isentropic limit of weak compression shock waves demonstrates that oblique shock waves in which the post-shock Mach number is larger than the pre-shock Mach number, named *non-ideal oblique shocks*, are admissible in the non-ideal regime $\Gamma < 1$ of substances characterized by moderate molecular complexity. In this section, non-ideal oblique shocks of finite amplitude are systematically analysed, clarifying the roles of the pre-shock thermodynamic state and Mach number. In §4.4.2.1, specific properties of the shock curves are recalled and discussed in view of their relevance to subsequent prove of existence of non-ideal oblique shocks in §4.4.2.2. Section 4.4.2.3 describes the computation of the existence domain, in terms of pre-shock thermodynamic quantities and Mach number, leading to non-ideal oblique shocks. In §4.4.2.4, results for different substances of practical interest are presented.

4.4.2.1   Properties of shock curves in classical gasdynamics

The Rankine-Hugoniot relations for planar flow involve 8 parameters: the 2 velocity components (normal and tangent to the shocks) and 2 thermodynamic quantities (e.g., pressure and density), for both the pre-shock and post-shock states. In these coordinates, the Rankine-Hugoniot relations consist of 4 functional relations (the equation of the tangential velocity (2.14) reduces to a scalar one), so that 4 remaining parameters are needed to parametrize the solution. The choice of this set of parameters is typically based on the specific context. In many occasions, for instance, one knows the evolution of the flow up to the point where a shock wave occurs. In this respect, it is customary to specify the thermodynamic and kinematic state upstream of the shock, which together correspond to a triplet such as, e.g., $\mathbf{A} = (P_A, v_A, \boldsymbol{u}_A)$ or $\mathbf{A} = (v_A, s_A, M_A \boldsymbol{t}_A)$ with $\boldsymbol{t}_A$ upstream velocity unit vector. Any other equivalent triplet can be obtained by simple manipulation. Given a triplet $\mathbf{A}$, the Rankine-Hugoniot relations determine the state downstream of an oblique shock from the considered pre-shock state, as a function of β_s, the angle between the shock front and the pre-shock flow direction (see figure 2.1). By analogy with one-dimensional unsteady flows (given a pre-shock state, one obtains the post-shock state as a function of the shock speed), the resulting locus is called the shock curve.

In the following, some properties of the shock curves of oblique shocks are recalled from §2.3 and adapted the present context. If $\Gamma > 0$, only compression shocks satisfy the law of entropy increase (2.17) and the speed ordering relation (2.18), and therefore can be admissible. The shock curve can be parametrized by any of the post-shock quantities v_B, P_B, s_B, or also by m or $\beta_s \in [\mu_A, \pi/2]$. In particular, the β_s-parametrization follows from monotonicity of β_s with v_B when condition (2.23) holds as we assume in this study.

We therefore comment on the dependence of selected thermodynamic and kinematic quantities of interest on the shock strength, which we conveniently identify with the shock angle β_s. The same notation of §2.3 will be used, namely a quantity X evaluated on the shock curve of the pre-shock state **A** is denoted as $X^{\mathcal{H}}(\beta_s; \mathbf{A})$; it follows that $X_B = X^{\mathcal{H}}(\beta_{sB}; \mathbf{A})$ for the shock angle β_{sB} producing a particular post-shock state B. The shorthand $dX_B/d\beta_s$ is used for the derivative $dX^{\mathcal{H}}(\beta_s; \mathbf{A})/d\beta_s\big|_{\beta_s=\beta_{sB}}$.

With fixed pre-shock state **A**, combination of (2.32) and (2.33) gives

$$\frac{du_B}{d\beta_s} = \frac{u_B}{\tan\beta_s}\frac{M_{nB}^2}{1-M_{nB}^2}\frac{[v]}{v_B}\left\{\left(2+\frac{[v]}{v_B}G_B\right)+\left(1+\frac{v_A}{v_B}\right)\left(\frac{1}{M_{nB}^2}-1\right)\right\}, \qquad (4.16)$$

which is always negative for compression shocks. A thermodynamic quantity of particular interest in this work is the speed of sound, since it is directly related to the occurrence of non-ideal effects across oblique shocks. The variation of the post-shock speed of sound along the shock curve is given by

$$\frac{dc_B}{d\beta_s} = \frac{c_B}{\tan\beta_s}\frac{M_{nB}^2}{1-M_{nB}^2}\frac{[v]}{v_B}\left\{(1-\Gamma_B)\left(2+\frac{[v]}{v_B}G_B\right)-\mathcal{K}_B\frac{[P]}{\rho_B c_B^2}\left(\frac{1}{M_{nB}^2}-1\right)\right\}, \qquad (4.17)$$

which has been obtained by combing (2.31) and (2.33). Besides Γ, the above expression involves the dimensionless isochoric derivative of the speed of sound with the entropy $\mathcal{K} = (c/T)(\partial c/\partial s)_v$. Assuming $\mathcal{K}_B > 0$ and that (2.23) is satisfied, the post-shock speed of sound increases with the shock strength along the compression branch of the shock curve if $\Gamma_B > 1$, but can possibly decrease if $\Gamma_B < 1$. Finally, we report the variation of the post-shock Mach number along the shock curve, By combining the variations of the velocity magnitude and speed of sound (or directly from relations 2.34 and 2.33), one obtains

$$\frac{dM_B}{d\beta_s} = -\frac{M_B}{\tan\beta_s}\frac{M_{nB}^2}{1-M_{nB}^2}\frac{[v]}{v_B}\left\{J_B\left(2+\frac{[v]}{v_B}G_B\right)+\frac{[v]}{v_B}\left(1-M_{nB}^2\right)\left(\mathcal{K}_B+\frac{1+G_B}{M_B^2}\right)\right\} \qquad (4.18)$$

where J is defined in (2.35). Assuming that $\mathcal{K}_B > 0$, $G_B > -1$ and (2.23) is satisfied, the post-shock Mach number decreases with increasing shock angle along the compression branch of the shock curve if $J_B < 0$. If instead the values of the post-shock Mach number and fundamental derivative are such that $J_B > 0$, the post-shock Mach number can possibly increase.

4.4.2.2 Existence of non-ideal oblique shocks: isentropic limit of weak shocks

Within the context of classical gasdynamics, diverse qualitative differences can be found between shock waves in the ideal-gas and non-ideal regime. Anomalies that are related to violation of condition (2.23) and to fluid states exhibiting $G < 0$ or $\mathcal{K} < 0$ are discussed by Menikoff & Plohr (1989). Here we restrict attention to compressibility-related effects that are caused by fluid states exhibiting $0 < \Gamma < 1$, that are therefore not possible in the ideal-gas limit. The parameter Γ directly controls the sound speed variation in isentropic processes as well as adiabatic, possibly non-isentropic, processes (assuming $\mathcal{K}$ does not change its sign). For the case of oblique shock waves, the well-known formulas for ideal gases (see, e.g., Thompson, 1988) indicate that the speed of sound necessarily increases across the shock (a consequence of the temperature rise). On the contrary, in the non-ideal gasdynamic regime, the speed of sound can possibly decrease following the adiabatic compression across an oblique shock, as suggested by relation (4.17).

Because the flow velocity magnitude is required to decrease across a compressive shock (the normal component decreases by mass conservation while the tangential one is conserved

by momentum balance), the peculiar behaviour of the speed of sound ultimately determines the variation of the Mach number across an oblique shock. In particular, we ask, Under which conditions is it possible to realize a discontinuous increase in the Mach number? Thus, the question is whether

$$M_B^2 = M_{nB}^2 + \|\boldsymbol{u}_t\|^2/c_B^2 \geqslant M_{nA}^2 + \|\boldsymbol{u}_t\|^2/c_A^2 = M_A^2 \tag{4.19}$$

can be satisfied. The speed ordering condition (2.18) requires that the normal Mach number is larger in the pre-shock state than in the post-shock state. On the contrary, no constraint is imposed on the tangential Mach number $\|\boldsymbol{u}_t\|/c$, whose variation across the shock is inversely proportional to the sound speed. It follows that whenever $c_B > c_A$, as in the ideal-gas limit, the Mach number necessarily decreases across any admissible shock waves. If instead $c_B < c_A$, which is possible in the non-ideal regime, the Mach number can either decrease or increase across an oblique shock; the Mach number increase will occur if the sound speed decrease is sufficiently large that the increase in the tangential Mach number compensates the necessary decrease in the normal Mach number.

Because the Mach number is a parameter of primary interest in many applications, the Mach number increase across oblique shock waves is undoubtedly among the most significant shock-related non-ideal effects. In this sense, hereinafter we will refer to oblique shock waves featuring $M_B > M_A$ as non-ideal oblique shock waves. The analysis of the weak shock limit $|\beta_s - \mu_A| \ll 1$ provides a condition of existence of non-ideal oblique shocks in terms of pre-shock quantities, since Taylor series expansion of the post-shock Mach number in the neighbourhood of the acoustic angle reads

$$\frac{[M]}{M_A} = 2\frac{J_A}{\Gamma_A}\sqrt{M_A^2 - 1}\,(\beta_s - \mu_A) + \mathcal{O}((\beta_s - \mu_A)^2), \qquad \beta_s \to \mu_A^+. \tag{4.20}$$

For weak oblique shock waves in the above limit (for convenience, in the remainder of §4.5 we refer to them as weak shocks simply, to not be confused with the more general definition of weak shock given in §4.4.1, which includes also shocks of large amplitude), the sign of the Mach number variation is related to the values of the pre-shock fundamental derivative Γ_A and Mach number M_A only. If the combination of these values is such that $J_A > 0$, the Mach number increases across a weak oblique shock. It is readily seen that if $\Gamma_A < 1$ non-ideal oblique shocks necessarily occur when M_A is sufficiently large. The role of the fundamental parameter J will be further clarified in the following.

4.4.2.3 Existence domain of non-ideal oblique shocks

This section addresses the flow conditions, in terms of pre-shock thermodynamic quantities and Mach number, resulting in the non-ideal Mach number increase across oblique shocks. The choice of pre-shock Mach number as the parameter accounting for the kinematic state of the fluid ahead of the shock waves is twofold. Firstly, it is the quantity that directly enters into the definition of the parameter J, whose sign determines the direction of the Mach number variation across weak oblique shocks. Secondly, in the perfect-gas limit, several quantities of interest such as Θ (deflection angle of the flow across the shock, see figure 2.1), M_B, P_B/P_A, $[s]$, etc. (see, e.g. Thompson, 1988), depend uniquely on M_A and β_s. This also legitimises the use of β_s for the shock-curve parametrization in the perspective of evaluating the differences between ideal-gas and non-ideal regime.

After identifying the different scenarios for the observation of non-ideal oblique shocks, the domain of pre-shock states that possibly lead to non-ideal oblique shocks is computed. The mentioned domain includes all the pre-shock states for which $M^{\mathcal{H}}(\beta_s; \mathbf{A}) > M_A$ for some values of the shock angle. Results are given for each of the fluids listed in table 4.1.

Name	M (g mol^{-1})	T_c (K)	P_c (kPa)	EoS	Γ_{min}
MDM	236.531	565.36	1437.5	Thol *et al.* (2017)	0.1646
MM	162.378	518.75	1939.0	Colonna *et al.* (2006)	0.3389
Octane	114.229	569.32	2497.0	Span & Wagner (2003*b*)	0.3625
Cyclopentane	70.1629	511.72	4571.2	Gedanitz *et al.* (2015)	0.6433
Toluene	92.1384	591.75	4126.3	Lemmon & Span (2006)	0.5637
Benzene	78.1118	562.02	4907.3	Thol *et al.* (2012)	0.6155
Sulfur Hexafluoride	146.055	318.78	3755.0	Guder & Wagner (2009)	0.8050
R245fa	134.048	427.16	3651.0	Lemmon & Span (2006)	0.7089

TABLE 4.1. Molecular weight M, critical temperature T_c, critical pressure P_c for selected substances. The fluid properties are computed from the equation of state indicated in the fifth column of the table; Γ_{min} is the minimum value of the fundamental derivative in the vapour phase, as predicted by the EoS (Γ_{min} occurs along the vapour-liquid saturation curve). Properties and thermodynamic models are taken from the well-established REFPROP library (Lemmon *et al.* 2013).

Influence of the pre-shock state

A parametric study is carried out to evaluate the dependence of $M^{\mathcal{H}}(\beta_s; \mathbf{A})$ on the pre-shock state, in the parameter space of pre-shock thermodynamic states and Mach number. To do this, we consider the projection of the shock curve on the (M_B, β_s)–plane for exemplary pre-shock states that allow to illustrate the different scenarios for the occurrence of non-ideal oblique shock waves.

The fluid employed here throughout for explanatory purposes is siloxane MDM (ocatmethyl-trisiloxane, $C_8H_{24}O_2Si_3$), which is modelled via the multi-parameter EoS reported in Table 4.1 together with relevant thermophysical properties of this and other substances considered in the following. MDM exhibits $\Gamma_{min} < 1$, where Γ_{min} is the minimum value of the fundamental derivative in the vapour phase, indicating that the selected fluid is endowed with a finite vapour-phase $\Gamma < 1$ region. Therefore, according to the arguments of the previous section, MDM is expected to allow for the occurrence of non-ideal oblique shock waves, provided the pre-shock state is carefully chosen. As for the other non-dimensional quantities that enter into the definition of the Mach number variation (4.18), MDM exhibits $G > 0$ and $\mathcal{K} > 0$ in the single phase vapour region to which this discussion is restricted. Moreover, G is small enough that condition (2.23) is always satisfied along shock curves originating from pre-shock thermodynamic states in the vapour region.

In contrast to the case of perfect gases, for which the post-shock to pre-shock ratios of most quantities interest can be expressed as functions of the pre-shock normal Mach number only, the full pre-shock state plays a major role in determining the properties of oblique shock waves for arbitrary equations of state. In order to facilitate the following analysis, two parametric studies are conducted. Firstly, a parametric analysis is carried out for a fixed pre-shock Mach number and for different pre-shock thermodynamic states. Secondly, the pre-shock thermodynamic state is fixed and the pre-shock Mach number is varied.

Figure 4.5 shows the variation of the post-shock Mach number with the shock angle for a fixed pre-shock Mach number $M_A = 2$ and different pre-shock thermodynamic states selected along the same isentrope $s_A < s_\tau$, where s_τ denotes the isentrope tangent to the locus $J_A = 0$. Under the assumption that the pre-shock Mach number M_A is fixed, the locus $J_A = 0$ shown in figure 4.5 coincides with the Γ-isoline $\Gamma = 1 - 1/M_A^2$, see relation (3.6). The thermodynamic region between the $J_A = 0$ locus and the saturated vapour curve embeds all the possible pre-shock states exhibiting $J_A > 0$. Note that, according to (4.20), the function $M^{\mathcal{H}}(\beta; \mathbf{A})$ corresponding to pre-shock thermodynamic states having $J_A > 0$ will exhibit positive initial slope, thus indicating that the flow
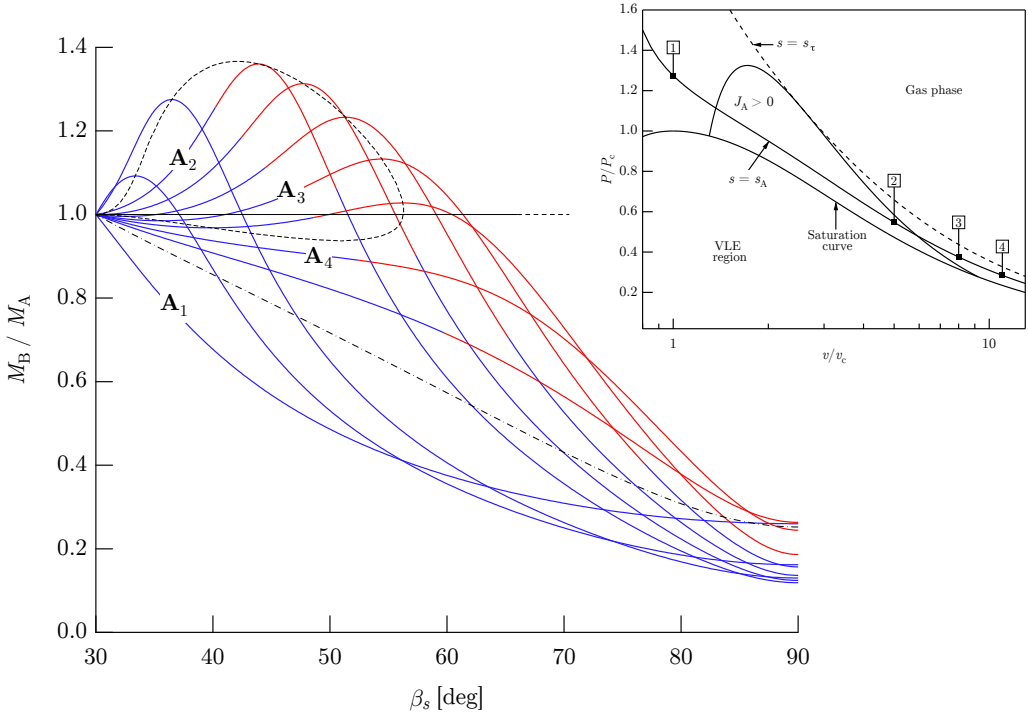
FIGURE 4.5. Shock curves for MDM in the post-shock Mach number–shock angle plane (thermodynamic properties from REFPROP). The pre-shock Mach number is fixed to $M_A = 2$. The pre-shock thermodynamic states are selected along the same isentrope $s_A = s(1.2743P_c, v_c) < s_\tau$, with s_τ denoting the isentrope tangent to the locus $J_A = 0$ (corresponding to the Γ-isoline $\Gamma = 1 - 1/M_A^2$). Marked configurations: $v_1 = v_c$, $v_2 = 5v_c$, $v_3 = 8v_c$, $v_3 = 11v_c$. The red portions of the shock curves correspond to neutral stability of the shock front against transverse perturbations (acoustic emission). Also shown is the ideal gas limit (dash-dotted curve) and the locus of the stationary points of $M^{\mathcal{H}}(\beta_s; \mathbf{A})$ for pre-shock thermodynamic states along the isentrope considered (dashed curve).

Mach number increases across weak oblique shock waves. Four pre-shock thermodynamic states are now considered, as representative of the possible qualitative evolution of the post-shock Mach number along the shock curve. The triplets corresponding to the marked configurations are given by $\mathbf{A}_i = (P(s_A, v_i), v_i, M_A t_A)$, $i = 1, \ldots, 4$.

State $\mathbf{A}_1$ is considered first, which is located on the left-hand side (higher densities) of the region $J_A > 0$. As shown in figure 4.5, along the shock curve originating from state $\mathbf{A}_1$, the post-shock Mach number monotonically decreases with increasing shock angle. Exemplary non-monotonic Mach number variations are those corresponding to pre-shock states $\mathbf{A}_2$ and $\mathbf{A}_3$ in figure 4.5. State $\mathbf{A}_2$ is taken as representative of the Mach number evolution for pre-shock states featuring $J_A > 0$. Thus, for increasing shock angles starting from $\beta_s = \mu_A$, the post-shock Mach number initially increases. As the magnitude of the tangential velocity decreases (i.e. with increasing shock angle), $M^{\mathcal{H}}(\beta_s; \mathbf{A}_2)$ reaches a local maximum and subsequently decreases towards the subsonic values characterizing strong oblique shocks. For shock curves qualitatively similar to the present case $\mathbf{A}_2$, there exists a shock angle value $\tilde{\beta}_s = \tilde{\beta}_s(\mathbf{A})$, $\tilde{\beta}_s \neq \mu_A$, such that $M^{\mathcal{H}}(\tilde{\beta}_s; \mathbf{A}) = M_A$. It must be noticed, however, that the computed shock curve exhibits a fairly large interval of shock angles for which the conditions of spontaneous acoustic emission are satisfied, and thus the shock front is neutrally stable.
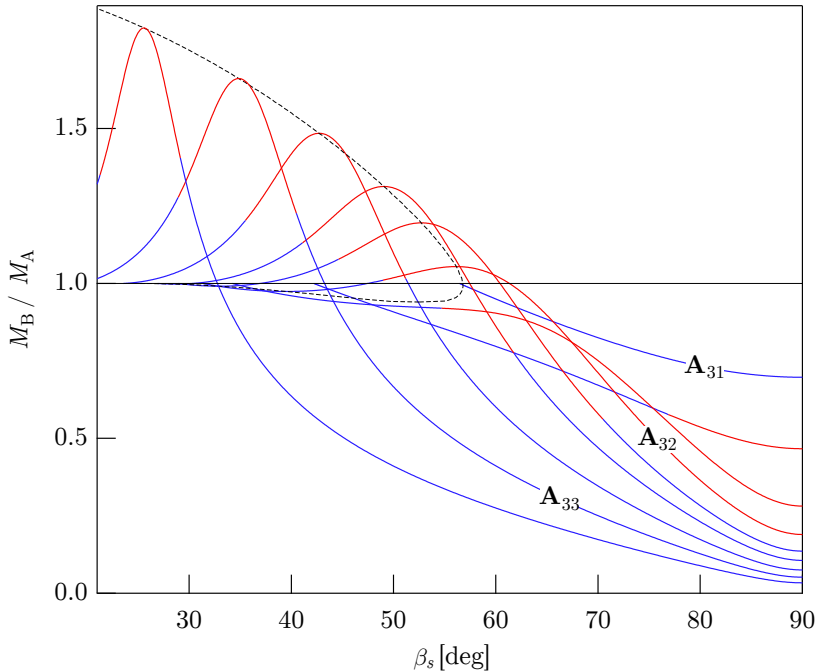
FIGURE 4.6. Shock curves for MDM in the post-shock Mach number–shock angle plane (thermodynamic properties form REFPROP). The pre-shock thermodynamic state is fixed and corresponds to case 3 of figure 4.5, namely $s_A = s(1.2743 P_c, v_c)$, $v_A = 8v_c$. Each curve corresponds to a different pre-shock Mach number. Marked configurations: $M_{31} = 1.2$, $M_{32} = 1.9$, $M_{33} = 3$. See figure 4.5 for full caption.

If the pre-shock state exhibits $J_A < 0$, yet the thermodynamic state is selected in the close proximity of the region $J_A > 0$, as for case A_3 in figure 4.5, the post-shock Mach number features an interesting non-monotonic profile comprising two stationary points, with the local minimum (maximum) occurring at $M_B < M_A$ ($M_B > M_A$). Configurations qualitatively similar to A_3 thus exhibit two different shock angles $\tilde{\beta}_{s1} = \tilde{\beta}_{s1}(A)$ and $\tilde{\beta}_{s2} = \tilde{\beta}_{s2}(A)$, other than the acoustic angle, such that $M^{\mathcal{H}}(\tilde{\beta}_{s1}; A) = M^{\mathcal{H}}(\tilde{\beta}_{s2}; A) = M_A$; these angles delimit the β_s–interval of Mach number–increasing oblique shocks. It must be noticed, however, that a significantly larger portion of the shock curve of case A_3 (in particular, of the portion corresponding to non-ideal oblique shocks) is predicted to satisfy the conditions for acoustic emission.

By increasing the pre-shock specific volume along the reference isentrope, the two stationary points found in A_3-like configurations occur at $M_B < M_A$ and ultimately become coincident. Therefore, any further increase in v_A such that the post-shock Mach number monotonically decreases with increasing shock angle. Not surprisingly, $M^{\mathcal{H}}(\beta_s; A)$ profiles originating from pre-shock thermodynamic states relatively close to the region $J_A > 0$ can still exhibit a somewhat anomalous, non-ideal curvature (due to the sound speed decrease) as shown in the exemplary case A_4 of figure 4.5.

Next, a complementary parametric study is presented, which is carried out by fixing the pre-shock thermodynamic state and considering different pre-shock Mach numbers. Figure 4.6 shows examples of variations of the post-shock Mach number with the shock angle obtained from the same pre-shock thermodynamic state, which corresponds to case 3 of figure 4.5, and different values of the pre-shock Mach number. Selected configurations are now detailed, as representative of the shock curve dependence on the pre-shock Mach number. The triplets corresponding to

the marked configurations are given by $\mathbf{A}_i = (P(s_A, v_3), v_3, M_{3i}\mathbf{t}_A)$, $i = 1, \ldots, 3$. For sufficiently low values of the pre-shock Mach number, $M^{\mathcal{H}}(\beta_s; \mathbf{A})$ is monotonically decreasing (case $\mathbf{A}_{31}$). By increasing the pre-shock Mach number, $M^{\mathcal{H}}(\beta_s; \mathbf{A})$ eventually develops an inflection point; any further increase leads to a non-monotonic configuration. As in the previous parametric study, two different configurations can possibly occur. For pre-shock Mach numbers slightly larger than the limiting value for the formation of an inflection point, the profile of post-shock Mach number is qualitatively similar to that of case $\mathbf{A}_{32}$, which exhibits both a local minimum and a local maximum. If the pre-shock Mach number is sufficiently large, instead, the initial slope of $M^{\mathcal{H}}(\beta_s; \mathbf{A})$ is necessarily positive (cf. equations3.6 and 4.20, with $\Gamma_A < 1$), and the shock curve becomes qualitatively similar to case $\mathbf{A}_{33}$. Again, acoustic emission is predicted to occur over large portions of the shock curves.

Computing the existence domain

Based upon the results of the previous section, the flow conditions resulting in the non-ideal Mach number increases across oblique shocks are collectively considered to single out each possible pre-shock state, in terms of pre-shock thermodynamic quantities and Mach number, for which $M^{\mathcal{H}}(\beta_s; \mathbf{A}) > M_A$ for some values of the shock angle. The result is the definition of the domain of existence of non-ideal oblique shocks in the parameter space of pre-shock thermodynamic states and Mach number. For pre-shock states in this domain, there exists at least one value of the shock angle leading to $M_B > M_A$.

A convenient procedure for the computation of the existence domain of non-ideal oblique shocks is presented here. In order to reduce the complexity associated with the dependence of the shock properties on each of the pre-shock variables, we consider a fixed pre-shock Mach number, thus isolating the contribution of the pre-shock thermodynamic state. For a given pre-shock Mach number M_A, the proposed method consists in determining, for each value of the pre-shock entropy, the limit values of the pre-shock pressure or density that bound the range where the shock curve possibly exhibits $M^{\mathcal{H}}(\beta_s; \mathbf{A}) > M_A$ for some values of the shock angle. These limiting thermodynamic states define a locus delimiting the region in which the pre-shock thermodynamic state must be selected (together with the given M_A) in order to observe a non-ideal oblique shock. As the pre-shock Mach number is varied, this procedure determines a one-parameter family of thermodynamic regions embedding all the pre-shock states from which non-ideal oblique shock can possibly occur.

The proposed approach is first illustrated for MDM and one value of M_A and then it is applied in the next section to the fluids listed in table 4.1 for different values of M_A, confirming the general validity and applicability of the concept outlined here.

In §4.4.2.2, the shock curves considered were entirely enclosed in the single-phase vapour region. Here we consider also the cases in which the shock curves enter the two-phase region, limiting the discussion to their single-phase vapour portion. The shock angle leading to post-shock saturated conditions will be denoted by $\beta_{s,\mathrm{sat}} = \beta_{s,\mathrm{sat}}(\mathbf{A})$. Crossing the liquid-vapour saturation curve possibly occurs if a portion of the saturated vapour boundary is retrograde, which means that certain isentropes (and in turn, some shock adiabats) cross the phase boundary from the single towards the two-phase region, in the direction of increasing density. Siloxane fluid MDM is one such case of fluid with retrograde behaviour. Note, in this respect, that substances featuring $\Gamma < 1$ regions in the vapour phase typically have heat capacities large enough that a portion of the saturated vapour boundary is retrograde (see Thompson *et al.*, 1986).

With reference to the parametric studies carried out above, three different types of $M^{\mathcal{H}}(\beta_s; \mathbf{A})$ profiles were identified. These include the ideal-gas like (Mach–number decreasing) case and two non-ideal cases (possibly Mach–number increasing); the latter were distinguished depending on the
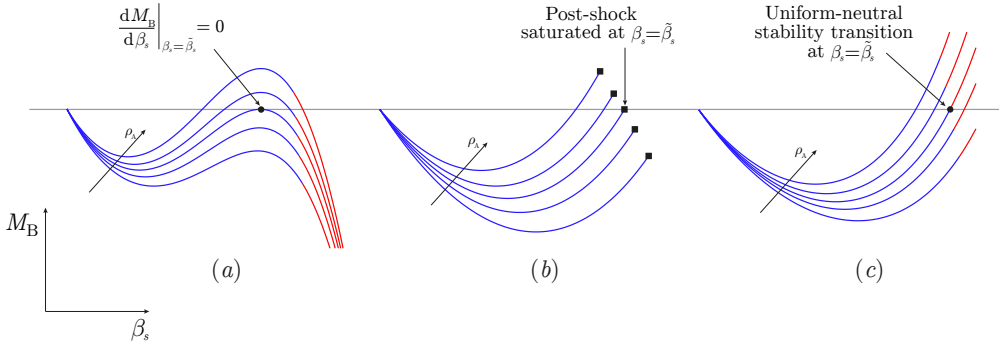
FIGURE 4.7. Illustration of the limit shock curves in the (M_B, β_s)–diagram. Solid squares: post-shock saturated conditions; red line: acoustic emission is predicted to occur. The shock angle $\tilde{\beta}_s \neq \mu_A$ indicates that the Mach number is preserved across the shock, namely $M^{\mathcal{H}}(\tilde{\beta}_s; \mathbf{A}) = M_A$. (a) The limit curve exhibits $dM_B/d\beta_s = 0$ at $\beta_s = \tilde{\beta}_s$; (b) on the limit curve, the post-shock thermodynamic state associated to $\beta_s = \tilde{\beta}_s$ lies on saturated phase boundary; (c) transition from uniform to neutral stability occurs at $\beta_s = \tilde{\beta}_s$ on the limit curve.

positive/negative slope in the weak shock limit. For the ideal configuration, it can be noticed that when the shock adiabat is entirely enclosed within the thermodynamic region $\Gamma > 1 - 1/M_A^2$, the function $M^{\mathcal{H}}(\beta_s; \mathbf{A})$ is monotonically decreasing. This follows from the fact that $M_B < M_A$ for weak shocks, being $J_A < 0$, and from $\Gamma_B > 1 - M_A^2$, which therefore gives $J_B < 0$ along the shock curve. Substituting this into relation (4.18) yields the monotonicity of the post-shock Mach number with the shock angle ($\mathcal{K} > 0$, $G > 0$ and relation 2.23 holds from earlier assumption). Examples of shock adiabats that satisfy the aforementioned condition are those originating from pre-shock states exhibiting $s_A > s_\tau$ or from pre-shock states $s_A < s_\tau$ that are either on the left-hand side of the $J_A > 0$ region (case $\mathbf{A}_1$ in figure 4.5) or entering the two-phase region at a point where $\Gamma > 1 - 1/M_A^2$.

On the other hand, shock curve originating from pre-shock states featuring $J_A > 0$ necessarily lead to $M^{\mathcal{H}}(\beta_s; \mathbf{A})$ profiles embedding a non-ideal portion $M_B \geqslant M_A$. This range is of the type $\beta_s \in [\mu_A, \tilde{\beta}_s]$, see case $\mathbf{A}_2$ in figure 4.5, or of the type $\beta_s \in [\mu_A, \beta_{s,\text{sat}}]$ if the shock curve enters the two-phase region within the Mach number–increasing portion, that is $M^{\mathcal{H}}(\beta_{s,\text{sat}}; \mathbf{A}) > M_A$.

Finally, it was shown that pre-shock states satisfying $s_A < s_\tau$ and $J_A < 0$, yet in the close proximity of the low-density zero of J_A along the selected isentrope, possibly lead to $M^{\mathcal{H}}(\beta_s; \mathbf{A})$ functions of the non-ideal type. In this case, the interval of shock angles corresponding to $M_B \geqslant M_A$ is of the form $\beta_s \in [\tilde{\beta}_{s1}, \tilde{\beta}_{s2}]$, see case $\mathbf{A}_3$ in figure 4.5, or of the form $\beta_s \in [\tilde{\beta}_{s1}, \beta_{s,\text{sat}}]$ if $M^{\mathcal{H}}(\beta_{s,\text{sat}}; \mathbf{A}) > M_A$.

Following the above considerations, the upper and lower pre-shock density limits for non-ideal post-shock Mach number profiles, along any given isentrope $s_A < s_\tau$, can be determined as follows:

(i) the upper pre-shock density limit is either the high-density zero of J_A along the selected isentrope or the saturation curve, if the selected isentrope enters the two-phase region and $J_A > 0$ at the saturated vapour boundary;

(ii) with reference to figure 4.7, the lower pre-shock density limit corresponds to the pre-shock state leading either to the shock curve depicted in figure 4.7(a), which is characterized by $dM_B/d\beta_s = 0$ at $\beta_s = \tilde{\beta}_s$ ($M_B = M_A$), or to the shock curve in figure 4.7(b), where the post-shock state corresponding to $M_B = M_A$ occurs on the saturation curve, namely

$\tilde{\beta}_s = \beta_{s,\text{sat}}$ on the limit curve;

(iii) the conditions for acoustic emission may be satisfied within the complete non-ideal region $M_B > M_A$ of a shock curve, thus resulting in a narrower domain of pre-shock states for non-ideal oblique shocks that are uniformly stable against multidimensional perturbations. In the related limit shock curve, the transition from uniform to neutral stability occurs at $\beta_s = \tilde{\beta}_s$ ($M_B = M_A$), as shown in figure 4.7(c).

By varying the reference isentrope, the existence domain of non-ideal oblique shocks as computed from the proposed procedure is shown in figure 4.8 for $M_A = 2$. The newly defined thermodynamic region is bounded by three different curves, which together define the so-called Pre-Shock Limit Locus (PSLL). Firstly, the portion of PSLL between point $A^J_{V,1}$, the high-density zero of J along the VLE line, and point A^J_τ, for which the isentrope is tangent to the $J = 0$ locus, is indeed coincident with the the $J = 0$ locus. The branch included between A^J_τ and $A^V_{dM,0}$ represents the locus of the limit pre-shock states resulting in shock curves featuring $\mathrm{d}M_B/\mathrm{d}\beta_s = 0$ when $M_B = M_A$ (figure 4.7(a)). At point $A^V_{dM,0}$, the shock curve simultaneously exhibits $\mathrm{d}M_B/\mathrm{d}\beta_s = 0$ at $\beta_s = \tilde{\beta}_s$ ($M_B = M_A$) and $\tilde{\beta}_s = \beta_{s,\text{sat}}$. The portion of the PSLL between point $A^V_{dM,0}$ and $A^J_{V,2}$, the low-density zero of J along the VLE line, is obtained by collecting the limit pre-shock states for which $\tilde{\beta}_s = \beta_{s,\text{sat}}$, that is, post-shock saturated conditions occur when $M_B = M_A$ (figure 4.7(b)). Furthermore, the locus denoted as DKLL (D'yakov–Kontorovich Limit Locus) bounds a relatively small region (on its right-hand side) of pre-shock states leading to shock curves in which acoustic emission occurs over the entire β_s-range associated with $M^{\mathcal{H}}(\beta_s; A) > M_A$. For pre-shock states in the right-hand side region of the DKLL, there do not exist uniformly stable non-ideal oblique shocks.

In the next section, the procedure outlined above is applied to the different fluids listed in table 4.1 to show its validity. Among the fluids considered, MDM, MM, octane, cyclopentane, toluene, benzene and R245fa all exhibit retrograde vapour boundaries; sulfur hexafluoride only exhibits non-retrograde vapour boundary. The procedure for the computation of the existence domain of non-ideal oblique shocks in fluids having non-retrograde vapour boundaries is almost identical to that described above. When the saturated vapour boundary is non-retrograde, the shock curves centred on pre-shock states in the vapour phase cannot cross the two-phase region, thus remaining single-phase. This implies that transitional shock curves of the type shown in figure 4.7(b) cannot occur. Therefore, with reference to the procedure outlined in the previous paragraph, the lower pre-shock density limit, along any given isentrope crossing the $J_A > 0$ locus, is either the saturation curve or the pre-shock state leading to the transition depicted in figure 4.7(a).

4.4.2.4 Results for selected substances

The procedure described in the previous section for MDM and one particular value of M_A is applied here to the fluids listed in table 4.1 and the influence of M_A is also evaluated. Similarly to MDM, the other fluids considered here are modelled with state-of-the-art EoS of the Span-Wagner type (appendix A). The Pre-Shock Limit Loci and the D'yakov–Kontorovich Limit Loci in the selected fluids are reported, for different pre-shock Mach numbers, in figures 4.9(a-h). All the substances considered are endowed with $\Gamma < 1$ thermodynamic region. Moreover, for each of these fluids, $\mathcal{K} > 0$, $G > 0$ and condition (2.23) is satisfied in the single-phase vapour region to which the present discussion is restricted. The selected siloxanes (cases a-b), hydrocarbons (cases b-f) and R234fa (case h) exhibit a retrograde portion of the saturated vapour boundary; accordingly, the corresponding pre-shock limit curves are qualitatively similar to those obtained in the previous section for MDM with $M_A = 2$. On the other hand, sulfur hexafluoride (case g) exhibits a fairly simpler configuration as a result of its saturated vapour boundary being non-retrograde. In this
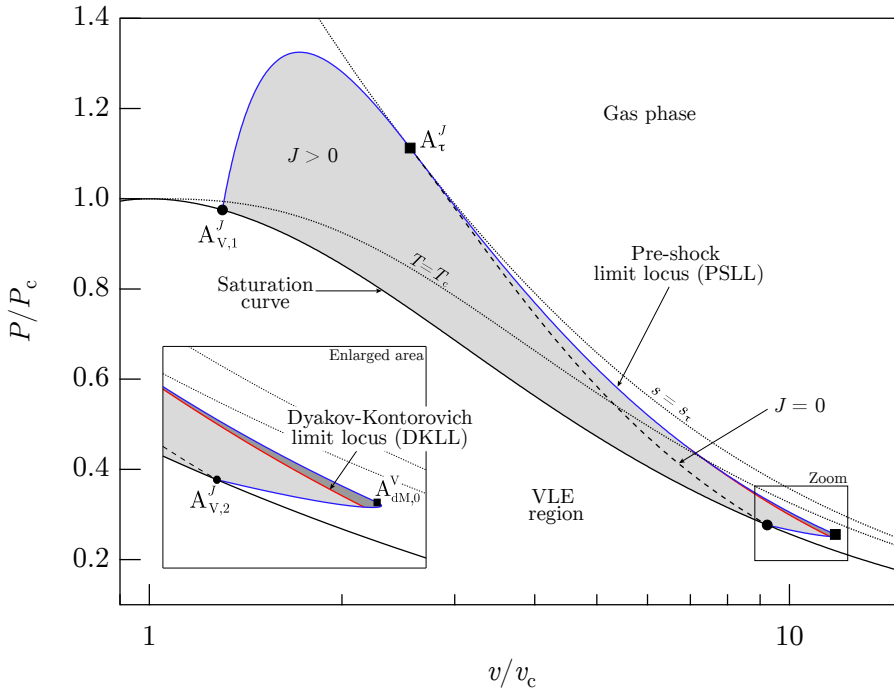
FIGURE 4.8. Pre-shock-state domain (shaded area) for non-ideal oblique shock waves in MDM with fixed pre-shock Mach number $M_A = 2$. Thermodynamic properties from REFPROP. The domain is bounded by the Pre-Shock Limit Locus (PSLL, blue line) and by the vapour-liquid saturation curve. Points $A_{V,1}^J$ and $A_{V,2}^J$ indicate the high- and low-density intersection, respectively, of the $J_A = 0$ locus with the VLE line. The isentrope passing through A_τ^J is tangent to the $J_A = 0$ locus. The shock curve centred on $A_{dM,0}^V$ features $dM_B/d\beta_s = 0$ at $\beta_s = \tilde{\beta}_s = \beta_{sat}$. From pre-shock states in the dark-shaded region (enlarged area), uniformly stable non-ideal oblique shocks cannot occur. This region is bounded by the PSLL and the D'yakov–Kontorovich Limit Locus (DKLL).

case, according to the nomenclature used in figure 4.8, the portion of PSLL on the right-hand side of point A_τ^J (comprising pre-shock states for shock curves featuring $dM_B/d\beta_s = 0$ when $M_B = M_A$) extends to a point on the VLE line.

It must be noticed that, among the configurations depicted in figures 4.9(*a-h*), only MDM, MM and octane exhibit limit curves for acoustic emission (DKLL), possibly owing to the lower values of Γ_{min} and the larger extension of the region $\Gamma < 1$ with respect to the other fluids considered here.

The influence of the pre-shock Mach number on the shape and extension of the pre-shock-state region for non-ideal oblique shock waves, which can be appreciated from figures 4.9(*a-h*), can be commented as follows. Firstly, there exists a minimum threshold of the pre-shock Mach number $M_{A,min} = (1 - \Gamma_{min})^{-1/2}$, below which non-ideal oblique shocks cannot occur. This amounts to requiring that $\Gamma < 1 - 1/M_A^2$ somewhere in the single-phase vapour region. The condition $\Gamma < 1 - 1/M_A^2$ is necessary for the existence of non-ideal oblique shocks having pre-shock Mach number M_A. Indeed, assuming $G > 0$, $\mathcal{K} > 0$ and that (2.23) holds, $J_B > 0$ must be satisfied somewhere along the shock curve in order that the post-shock Mach number is non-decreasing, see equation (4.18). Unless $J_B > 0$ holds in the acoustic limit (namely $J_A > 0$ and $M_B > M_A$ for weak oblique shocks), $J_B > 0$ must be satisfied when $M_B < M_A$. Both cases clearly imply that

(a) MDM (octamethyltrisiloxane)

(b) MM (hexamethyldisiloxane)
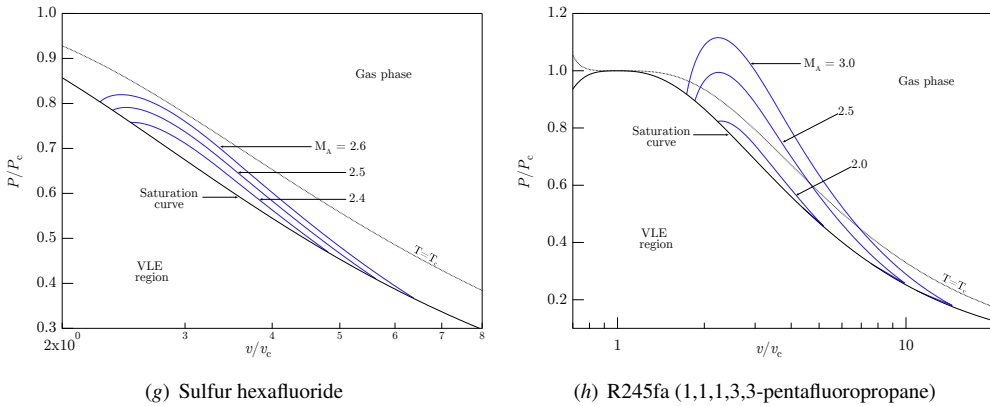
(c) Octane

(d) Cyclopentane

(e) Toluene

(f) Benzene
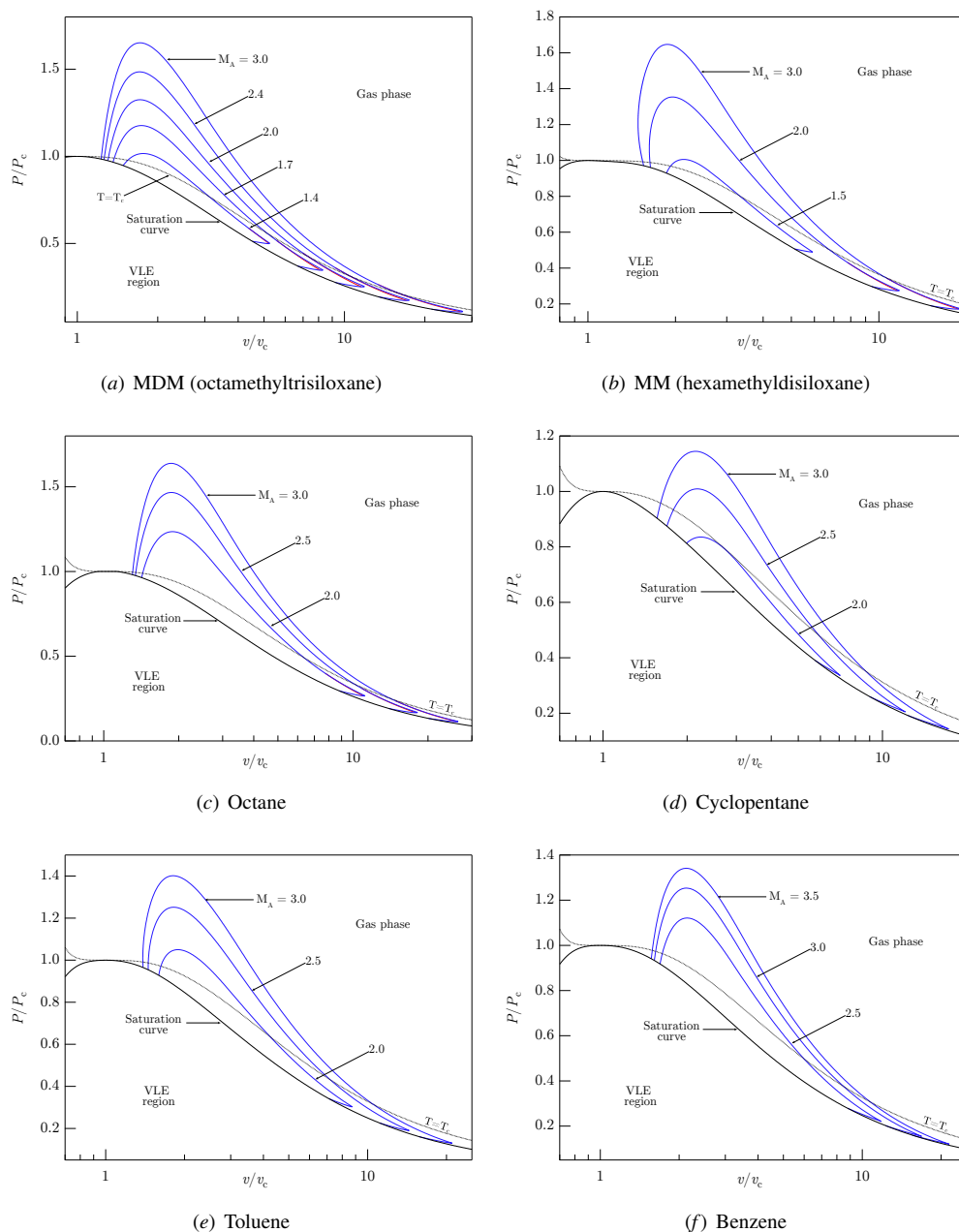
FIGURE 4.9. PSLL (blue line) and DKLL (red line) for different pre-shock Mach numbers, in each of the substances listed in table 4.1. Thermodynamic properties from REFPROP.

$\Gamma < 1 - 1/M_A^2$ somewhere in the thermodynamic state space. With increasing values of the pre-shock Mach number, the size of the pre-shock-state domain for non-ideal oblique shocks increases (as the size of the $J_A > 0$ region does), whereas its shape remains qualitatively unchanged. In this respect, the size of Γ–isolines (and thus of $J = 0$ loci for fixed M_A, which roughly coincides with the newly defined thermodynamic domain) of most pure fluids increases with Γ (see, e.g., Colonna

(g) Sulfur hexafluoride

(h) R245fa (1,1,1,3,3-pentafluoropropane)

FIGURE 4.9 (Cont.). PSLL (blue line) and DKLL (red line) for different pre-shock Mach numbers, in each of the substances listed in table 4.1. Thermodynamic properties from REFPROP.

et al., 2007, for siloxanes). More in general, the qualitative trend of the fundamental derivative in the single-phase vapour region of all fluids having regions $\Gamma < 1$ agrees with the predictions of the simple van der Waals model (see, e.g. Thompson & Lambrakis, 1973), which in turn are consistent with the results obtained in the present section. The latter claim leads us expect that the present findings are arguably valid for most single-phase fluids exhibiting $\Gamma < 1$ in the vapour region.

4.4.3 Unified description of classical oblique waves

Due to their peculiar nature, in the scientific literature oblique shocks and rarefaction fans are often dealt with separately and therefore it is difficult to identify possible similarities between the diagrams depicting these two different phenomena. It is well-known that if the flow deflection is small and likewise is the pressure jump, the entropy jump across shock waves is negligible, see equation (2.28). In this isentropic limit, the link between oblique shocks and rarefaction fans can be appreciated from the diagrams reporting the value of a thermodynamic quantity downstream of the wave as a function of the deflection angle, for the shock and the fan branches smoothly match, as shown in figure 4.4(*b*). However, the geometrical properties of the wave pattern around compressive and rarefactive corners have always been treated separately. On one side, the (β_s, Θ)–diagram for oblique shock waves provides the slope of an oblique shock β_s as a function of the deflection angle Θ. On the other side, the geometrical information regarding the fan configuration is retrieved by the Prandtl-Meyer function (4.13). In this section, an extension of the common (β_s, Θ)–diagram for oblique shock waves to rarefaction fans is presented, which exemplifies the fundamental similarity between shock and fan waves in the isentropic limit.

The geometrical properties of the oblique shock waves and of the flow through it are commonly presented in the form of diagrams reporting the oblique shocks angle as a function of the flow deflection angle, namely the (β_s, Θ)–diagrams, for a number of upstream flow conditions. For the general features of the (β_s, Θ)–diagram, see, e.g., (Thompson, 1988). For a given deflection angle, up to the detachment value Θ_d, two solutions can possibly occur, namely the weak and strong oblique shocks. Therefore, the multivalued function $\beta_s(\Theta; \mathbf{A})$, in which the dependence on the upstream state is again indicated using the parameter vector $\mathbf{A}$, is composed by the two branches $\beta_{ws}(\Theta; \mathbf{A})$ and $\beta_{ss}(\Theta; \mathbf{A})$ representing the weak and the strong oblique shock solutions, respectively. Each of these branches is obtained by inverting the relation $\Theta = \Theta(\beta_s; \mathbf{A})$, implicitly defined by system (2.10)-(2.12), in the appropriate range of shock angles, namely in the interval
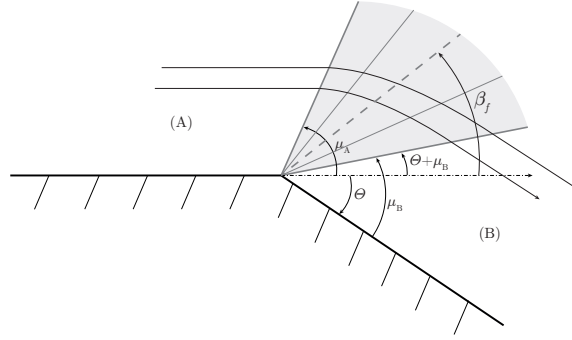
FIGURE 4.10. Centered fan for streaming flow over a rarefactive corner. Graphical illustration of the equivalent-fan angle β_f, defined in equation (4.21) as the average between the characteristic slopes at the beginning and at the end of the fan.

$\beta_s \in [\mu_A, \beta_{s,d}]$ for the weak shock branch and in $\beta_s \in [\beta_{s,d}, \pi/2]$ for the strong shock branch, where $\beta_{s,d}$ is the shock angle corresponding to the detachment condition.

In the following, a corresponding half-plane for rarefaction waves is constructed. The possibility of describing also the rarefaction half-plane would allow for an easier, more versatile and complete diagram than existing ones. To this purpose, we need to define a symmetry between the two governing relations. Thus, an angle β_f which is the counterpart of the β_s angle of oblique shocks, must be introduced for the rarefaction fan. Similarly to the case of oblique shocks, the angle β_f indicates the direction of the fan with respect to the upstream flow.

The natural choice for β_f, justified below by resorting to the bisector rule, is to average the leading characteristic slope $\pm\mu_A$ and the terminating characteristic slope $\Theta \pm \mu_B$, both computed with respect to the upstream flow direction (see figure 4.10), namely

$$\beta_f = \frac{\Theta \pm (\mu_A + \mu_B)}{2}, \tag{4.21}$$

where the plus/minus sign holds for oblique shocks and rarefaction fans in the left-running/right-running characteristic field, respectively. It is therefore possible to draw a rarefaction fan branch starting at $(0, \pm\mu_A)$ up to the limit condition associated with vacuum. We define a generalized wave angle β_g, representing either the oblique shock angle or the equivalent fan angle, by introducing the piecewise defined function

$$\beta_g(\Theta; \mathbf{A}) = \begin{cases} \beta_s(\Theta; \mathbf{A}), & \text{if } \pm\Theta \geqslant 0, \\ \beta_f(\Theta; \mathbf{A}), & \text{if } \pm\Theta \leqslant 0, \end{cases} \tag{4.22}$$

whose graph provides the extended (β_g, Θ)–diagram of left-running/right-running waves around a corner, for a given upstream state (note that the right-running wave curve is simply obtained by 180° rotation of the corresponding left-wave curve). As pointed out previously, the shock portion $\beta_s(\Theta; \mathbf{A})$ is multivalued and comprises the branches $\beta_{ws}(\Theta; \mathbf{A})$ and $\beta_{ss}(\Theta; \mathbf{A})$ of weak and strong oblique shocks, respectively.

The definition (4.21) of the equivalent-fan angle allows to smoothly match (to first order in Θ) the weak oblique shock branch with the newly defined rarefaction fan branch. Indeed, it is shown in appendix C, the piecewise function (4.22) is continuously differentiable at $\Theta = 0$, where

$$\left. \frac{\mathrm{d}\beta_f}{\mathrm{d}\Theta} \right|_{\Theta=0} = \frac{\Gamma_A}{2} \frac{M_A^2}{M_A^2 - 1} = \left. \frac{\mathrm{d}\beta_{ws}}{\mathrm{d}\Theta} \right|_{\Theta=0}, \tag{4.23}$$
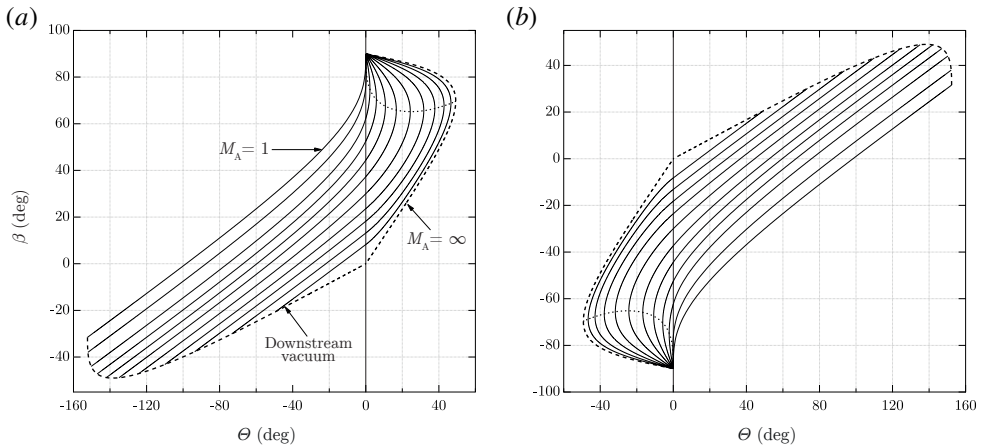
FIGURE 4.11. Extended (β_g, Θ)–diagram for (a) left-running and (b) right-running oblique shock waves and rarefaction fans in perfect gas methane. Each curve corresponds to a different upstream Mach number. The limit curve (dashed) is obtained for $M_A = \infty$ on the shock branch and for downstream vacuum conditions on the rarefactive branch. Also shown is the locus (dotted line) of the maximum deviation angles that the fluid can sustain across an attached oblique shock.

The C^1 continuity of the function defined by (4.22) can be conveniently interpreted in view of the bisector rule for oblique shock waves (see Kluwick (1971) and §C.1), which states that in the isentropic shock limit ($\Theta \to 0$ and $[v] \to 0$) the shock angle equals the average between the pre-shock and the post-shock characteristic slopes. In passing through the $\Theta = 0$ axis from the rarefactive to the compressive side, the characteristics delimiting the rarefaction fan fold, thus forming an oblique shock wave. Accounting for the bisector rule, a symmetry is established between the roles of the characteristic waves in the upstream and downstream states and the corresponding "average" wave (either the equivalent fan wave or the shock wave). Condition (4.23) implies that, as $\Theta \to 0$, the rate at which the characteristic lines delimiting the Pradtl-Meyer fan shrink equals the rate at which the pre-shock and post-shock characteristic lines unfold. The C^2 continuity is instead demonstrated to be not guaranteed in appendix C.

The unified description of supersonic flows around compressive and rarefactive corners, embodied in the complete (β_g, Θ)–diagram for both positive and negative deflection angles, is illustrated in figure 4.11(a)-(b) for methane under the perfect-gas assumption ($\gamma = 1.32$). Here, the left and right figures correspond to left-running and right-running waves, respectively. As is well-known, for perfect gases both β_s and β_f are independent of the pre-shock thermodynamic state, leaving the upstream Mach number as the only parameter in the β_g–Θ relation. In other words, for a perfect gas, the β_g–Θ–M_A representation is independent from the upstream thermodynamic state and therefore it is unique. The dashed curves in figure 4.11(a)-(b) represent the limiting cases for both compression and rarefaction waves. In the shock portion, this is obtained for an infinitely large pre-shock Mach number, while, in the rarefaction branch, the limiting curve is the locus of the downstream states corresponding to vacuum conditions.

In contrast with the perfect-gas case, the β_g–Θ relation, as computed via any non-ideal equation of state, depends on the choice of the upstream state, as this influences both the shock and the rarefaction curves. Exemplary (β_g, Θ)–diagrams for gases in non-ideal thermodynamic conditions are shown in figure 4.12(a)-(b) for left-running waves in methane. The fluid is now modelled via the state-of-the-art equation of state described in Setzmann & Wagner (1991) available in REFPROP. In figure 4.12(a), the upstream thermodynamic state is fixed to $P_A = 0.4P_c$, $\rho_A = 0.1\rho_c$; each
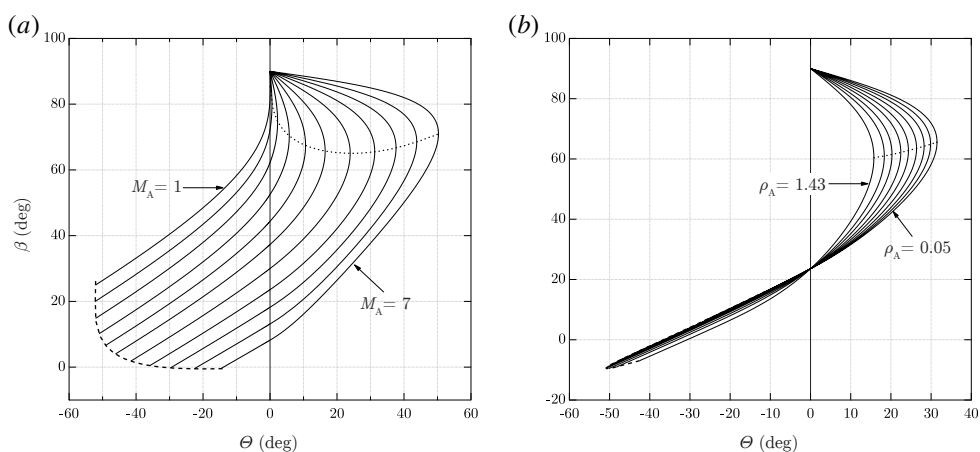
FIGURE 4.12. Extended (β_g, Θ)–diagram for oblique shock waves and rarefaction fans in gaseous methane, computed from REFPROP. (*a*) The upstream thermodynamic state is fixed to $P_A = 0.4P_c$, $\rho_A = 0.1\rho_c$; each curve corresponds to a different upstream Mach number. (*b*) The upstream Mach number is fixed to $M_A = 2.5$; each curve corresponds to a different density along the same isentrope $s_A = s(0.4P_c, 0.1\rho_c)$. For both figures, the rarefaction-fan branch is drawn up to the deviation angle corresponding to downstream saturated conditions (dashed curve). Also shown is the locus (dotted line) of the maximum deviation angles that the fluid can sustain across an attached oblique shock.

curve thus correspond to a different value of the upstream Mach number. For each case reported, the rarefaction branch extends to the downstream state where condensation occurs (dashed line). On the other hand, in figure 4.12(*a*), the upstream Mach number is fixed to $M_A = 2.5$ and each curve corresponds to a different upstream density value chosen along the same isentrope $s_A = s(0.4P_c, 0.1\rho_c)$. Because the upstream entropy is the same, the rarefaction portions are nearly coincident. It can be noticed that the shock curve is significantly influenced by the value of the pre-shock density. In particular, the maximum deflection angle that the flow can sustain across an attached oblique shock wave is seen to decrease with increasing pre-shock density.

Ease and versatility of the complete (β_g, Θ)–diagram is shown in this section for a typical steady supersonic flow in two dimensions, namely the textbook case of flow past a symmetric diamond-shaped airfoil. Such a case owes both oblique shocks and rarefaction fans for either left- and right-running waves, respectively for the suction and pressure sides. This exemplary configuration is shown in figure 4.13; the fluid considered is, again, methane (EoS from REFPROP). The diamond airfoil has a $10°$ half angle and it is put into a uniform supersonic freestream at an angle of attack of $15°$. The freestream conditions are $P_1 = 0.4P_c$, $\rho_1 = 0.1\rho_c$, $M_1 = 2.5$. On the suction surface, the flow is expanded across two rarefaction fans and finally compressed across an oblique shock to match the downstream pressure and flow direction at the slip line emerging from the trailing edge. On the pressure side the flow is initially compressed and subsequently expanded. For each of the wave patterns on the diamond airfoil (except, of course, the contact surface at the trailing edge), the β_g–Θ curves obtained from the corresponding upstream state is plotted in figure 4.13, where each wave is also marked. The fluid properties in the different uniform regions around the airfoil are reported in table 4.2, together with the flow deviation angles and the wave angles at each corner.

Flow region	P/P_c	ρ/ρ_c	M	$\Theta_{i-1,i}$ (deg)	$\beta_{g,i-1,i}$ (deg)
1	0.4	0.1	2.5	/	/
2	0.29	0.078	2.70	-5	20.15
3	0.062	0.024	3.67	20	8.78
4	0.39	0.083	2.12	26.4	40.45
5	1.56	0.26	1.45	-25	-48.94
6	0.57	0.12	2.12	20	-25.87
7	0.39	0.092	2.35	6.4	-23.45

TABLE 4.2. Fluid properties in each of the uniform states around the diamond-shaped airfoil of figure 4.13, together with the wave angles. Thermodynamic properties from REFPROP. The quantities $\Theta_{i-1,i}$ and $\beta_{g,i-1,i}$ are the flow deflection angle and the wave angle in passing from state $i-1$ to state i, respectively, as computed with respect to the upstream flow direction.
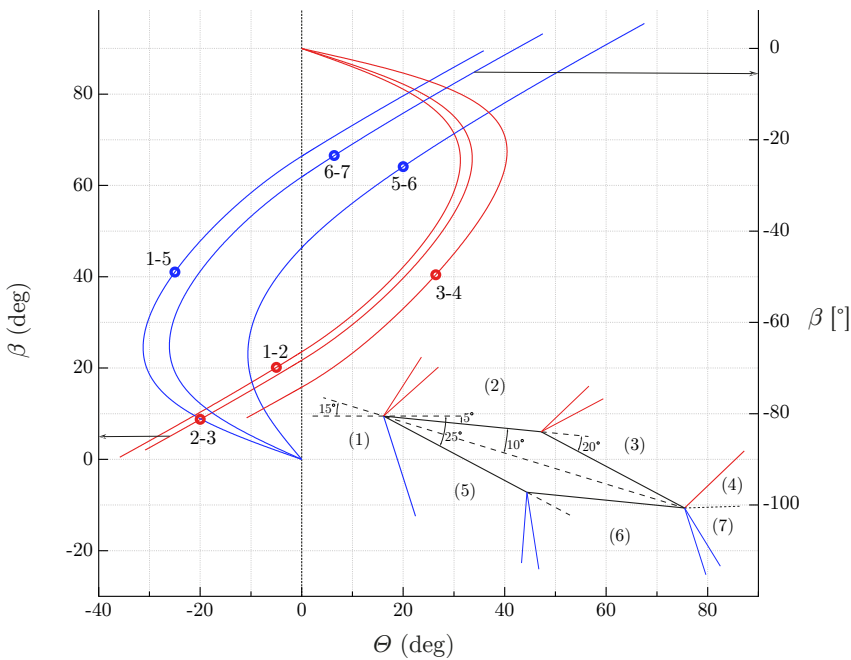
FIGURE 4.13. β_g–Θ curves for steady flow of gaseous methane past a diamond-shaped airfoil. The freestream conditions are $P_1 = 0.4P_c$, $\rho_1 = 0.1\rho_c$, $M_1 = 2.5$. The left and right axis are for left-running and right-running waves, respectively. For each of the states upstream of an oblique shock or rarefaction fan, the corresponding β_g–Θ curve is drawn and the wave configuration due to flow deflection is marked. Note that the Θ and β_g angles refer to the flow direction upstream of each wave pattern. The rarefaction-fan branch is drawn up to the deviation angle corresponding to downstream saturated conditions.

4.5 Non-classical oblique waves

Non-ideal thermodynamic properties offer a remarkable degree of freedom by which the expansion/compression of a supersonic stream at a corner can be accomplished. This degree of

freedom emerges in the non-classical gasdynamic regime of BZT fluids, which is analysed in the present section with the aim of identifying non-classical wave curves. In this context, the two-step procedure described in §4.3 for the computation of the wave curves proves to be particularly advantageous. The structure of the wave curves is analysed by first considering their projection in a thermodynamic plane (§4.5.1) and secondly those on common polar diagrams (§4.5.2). Section 4.6 presents the computation of the map of the upstream states that are associated to each type of wave curve.

4.5.1   Wave curves in the thermodynamic plane

In order to illustrate the different types of wave curves in a typical BZT fluid, the polytropic van der Waals model (appendix A) of a molecularly complex fluid is considered (the non-dimensional isochoric specific heat is set to $c_v/R = 57.69$). Five thermodynamic states $A_i = (P(s_A, v_i), v_i)$, $i = 1, \ldots, 5$, are chosen along the same isentrope s_A crossing the negative-Γ region while remaining in the single-phase, as shown in figure 4.14(a). The corresponding extended wave curves in the (P, v)–plane are shown in figure 4.14(b)-(f). These are now detailed.

Case 1 – figure 4.14(b). Thermodynamic state A_1 is located on the right-hand side of the negative-Γ region. Thus, the rarefaction branch of the extended wave curve through A_1 is the isentrope containing A_1, associated with elementary Prandtl-Meyer waves connected to A_1. On the other hand, the compressive branch of the wave curve coincides with the shock adiabat centred on A_1, associated with oblique shock waves. Note that, despite the shock adiabat crosses the negative-Γ region and it is non-convex, no entropy extrema occur. Graphically, this means the Rayleigh line (straight line connecting the pre-shock and post-shock states) is never tangent to the shock adiabat at the post-shock state. The same wave curve configuration (compression shock and rarefaction fan branches) is observed whenever the isentrope passing through the upstream state is convex (see, e.g., Kluwick, 2001).

Case 2 – figure 4.14(c). Similarly to case 1, thermodynamic state A_2 is on the right-hand side of the negative-Γ region. The rarefaction branch of the wave curve, therefore, is as in the previous case. On the contrary, the compression branch is significantly different. The wave curve is still, for moderate pressure rises, the locus of the oblique shocks connected to A_2. In contrast to case 1, however, there there exist a downstream pressure (point S^+) for which the entropy along the shock adiabat reaches a local maximum (i.e. the Rayleigh line is tangent to the shock adiabat at S^+); shock A_2-S^+ is indeed a post-sonic compression shock. As mentioned in §4.3, the wave curve is continued along the isentrope passing through S^+, for a composite oblique shock/Prandtl-Meyer fan combination. The fan in the composite wave cannot be continued beyond point I, where the isentrope through S^+ intersect the $\Gamma = 0$ locus, for the characteristic lines would fold. Beyond point S^+, the wave curve is continued by inserting a pre-sonic oblique shock adjacent to the fan. Thus, the corresponding wave configuration is a composite of the type oblique shock/Prandtl-Meyer fan/oblique shock. With increasing downstream pressure, the terminating shock becomes stronger and the wave fan weaker. Ultimately, at point S^- the fan disappears; shock A_2-S^- can be seen as the composition of the post-sonic shock A_2-S^+ and the pre-sonic shock S^+-S^-. For downstream pressures larger than the value at point S^-, a single oblique shock configuration is recovered.

Case 3 – figure 4.14(d). If the upstream thermodynamic state is selected in the negative-Γ region, such as point A_3, the rarefaction branch of the wave curve is the shock adiabat centred on the initial state (rarefaction oblique shock waves), up to the point S^+ where a post-sonic rarefaction shock occurs. Beyond this point, the wave curve is continued along the isentrope through S^+, for a composite oblique shock/Prandtl-Meyer fan combination. On the other hand, the compression branch of the wave curve is initially the isentrope through A_3 (compression Prandtl-Meyer waves), up to the point I where this isentrope intersects the $\Gamma = 0$ locus. The wave curve is continued by inserting a pre-sonic shock adjacent to the fan, for a Prandt-Meyer fan/oblique shock composite
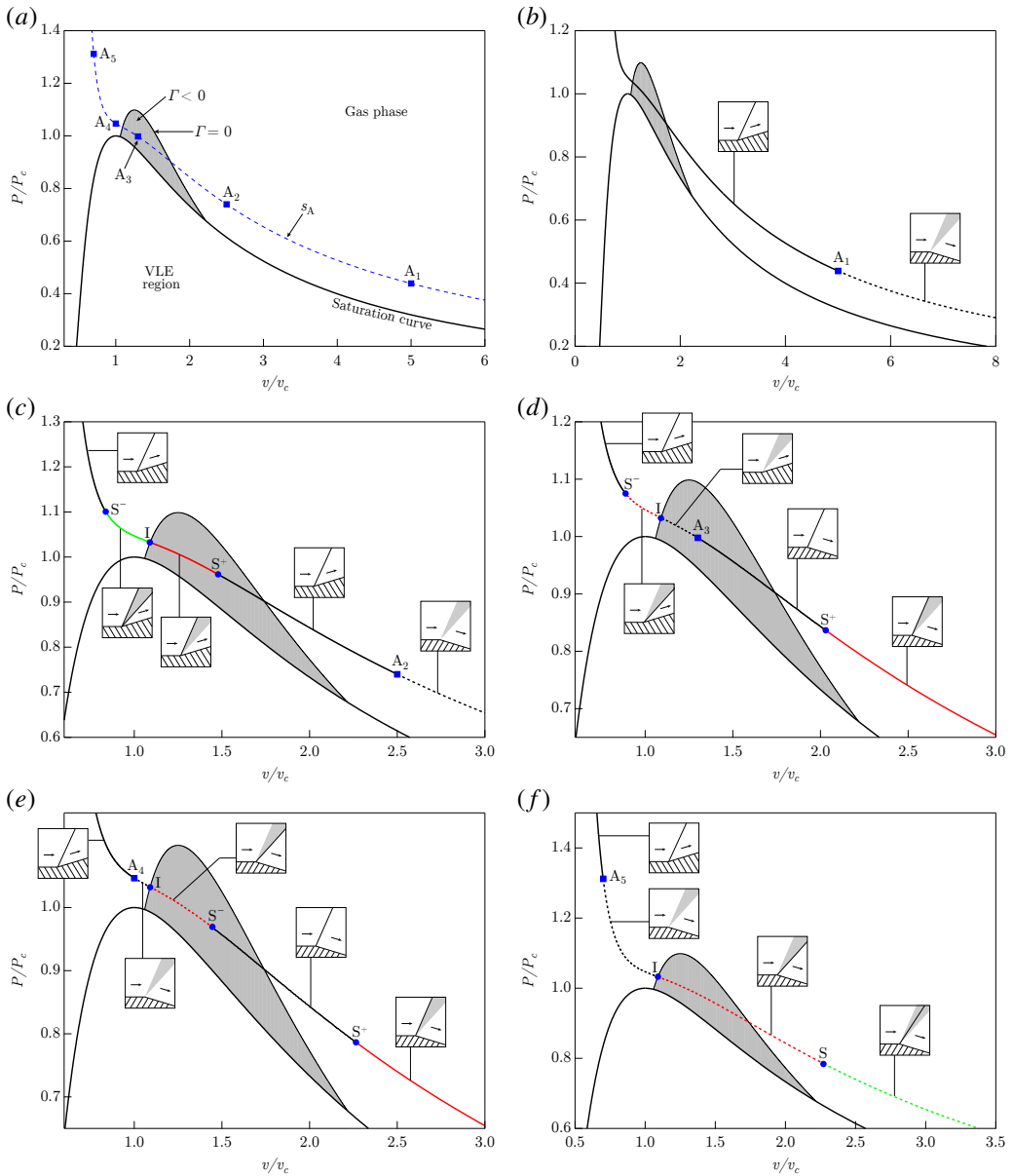
FIGURE 4.14. Extended wave curves in the pressure–specific volume diagram computed from the polytropic van der Waals model with $c_v/R = 57.69$. (a) The selected upstream states, chosen along an isentrope crossing the negative-Γ region (shaded area). (b)-(f) Extended wave curve for each upstream state. Wave configurations: —— shock, —— shock/fan, - - - shock/fan/shock, - - - fan, - - - fan/shock, - - - fan/shock/fan. Point S$^+$: downstream state of post-sonic oblique shock; point S$^-$: downstream state of pre-sonic oblique shock; point S: downstream state of double-sonic oblique shock; point I: intersection between the local isentrope and $\Gamma = 0$ locus. Attached to each branch is a sketch of the corresponding wave in the physical plane, for an exemplary flow past a ramp.

configuration in the physical plane. With increasing downstream pressure, the terminating oblique shock becomes stronger and the wave fan weaker; downstream pressures beyond point S^-, at which a pre-sonic compression shock occurs, are accomplished by a single oblique shock configuration.

Case 4 – figure 4.14(e). State A_4 lies on the left-hand side of the negative-Γ region. Therefore, the compression branch of the wave curve through state A_4 is the shock adiabat centred on A_4. The rarefaction branch is initially the isentrope through state P_4, up to the point where the $\Gamma = 0$ locus is encountered. The wave curve is continued by inserting a pre-sonic shock adjacent to the fan. For the downstream pressure corresponding to point S^- (pre-sonic rarefaction shock A_4-S^-), the Prandtl-Meyer fan disappears and a single oblique shock occurs. By decreasing the downstream pressure, the post-shock normal Mach number decreases and at point S^+ it is equal to unity (post-sonic oblique shock A_4-S^+). Smaller downstream pressures are achieved by means of a composite oblique shock/Prandtl-Meyer fan combination, for the wave curve beyond point S^+ is indeed the isentrope through S^+.

Case 5 – figure 4.14(f). The wave curve configuration is the same as in case 4, except that for the downstream pressure corresponding to point S, a composite fan/double-sonic shock configuration is observed (see also Zamfirescu *et al.*, 2008). The wave curve of point A_5 is continued, beyond point S, along the isentrope through S. The associated wave in the physical plane is the composite fan/shock/fan configuration.

4.5.2 Polar representation of the wave curves

Moving from the identification of the different types of extended wave curves in the space of thermodynamic variables, in this section we describe the wave curves in the common pressure–deflection diagram, thus enabling the effect of the kinematic state of the upstream flow to be considered. Consistent with the study of classical wave curves in §4.4.1, the upstream kinematic state is accounted for in terms of upstream Mach number M_A. In order to analyse the possible configurations of the wave curves along with the influence of M_A, we select the same upstream thermodynamic states considered in the previous section and we draw the wave curve projection in the (P_B, Θ)–diagram for different values of M_A, as shown in figure 4.15. Left-running wave curves are considered; the right-running wave is obtained by reflection of the left-running counterpart through the $\Theta = 0$ axis.

Case 1 – figure 4.15(b). On a qualitative basis, this is the classical case described in §4.4.1.

Case 2 – figure 4.15(c). While the rarefaction branch is qualitatively similar to case 1, there exists a limit value of the upstream Mach number, M_A^{tr}, marking the transition between two qualitatively different compression-branch configurations. If $1 < M_A < M_A^{tr}$, the ordinary shock polar, similar to case 1, occurs. For $M_A > M_A^{tr}$, along the compressive branch of the wave curve the following sequence is encountered, in the direction of increasing downstream pressure: oblique shock, oblique shock/Prandtl-Meyer fan, oblique shock/Prandtl-Meyer fan/oblique shock, oblique shock. The transitional wave curve is distinguished because the normal shock delimiting the first shock branch exhibits the sonic downstream state $M_{nB} = M_B = 1$, namely the post-shock thermodynamic state coincides with point S^+ in figure 4.14(c). By enforcing the Rankine-Hugoniot relations for a normal shock wave, the transitional Mach number is therefore computed as

$$M_A^{tr} = \frac{1}{\rho_A c_A} \sqrt{\frac{P_{S^+} - P_A}{v_A - v_{S^+}}}, \tag{4.24}$$

where P_{S^+} and v_{S^+} are the pressure and specific volume, respectively, at point S^+. For upstream Mach numbers slightly larger than the transitional value, Θ exhibits three stationary points along the wave curve (two local maxima with a minimum in between). Thus, up to four different wave configurations can provide the same flow deflection.
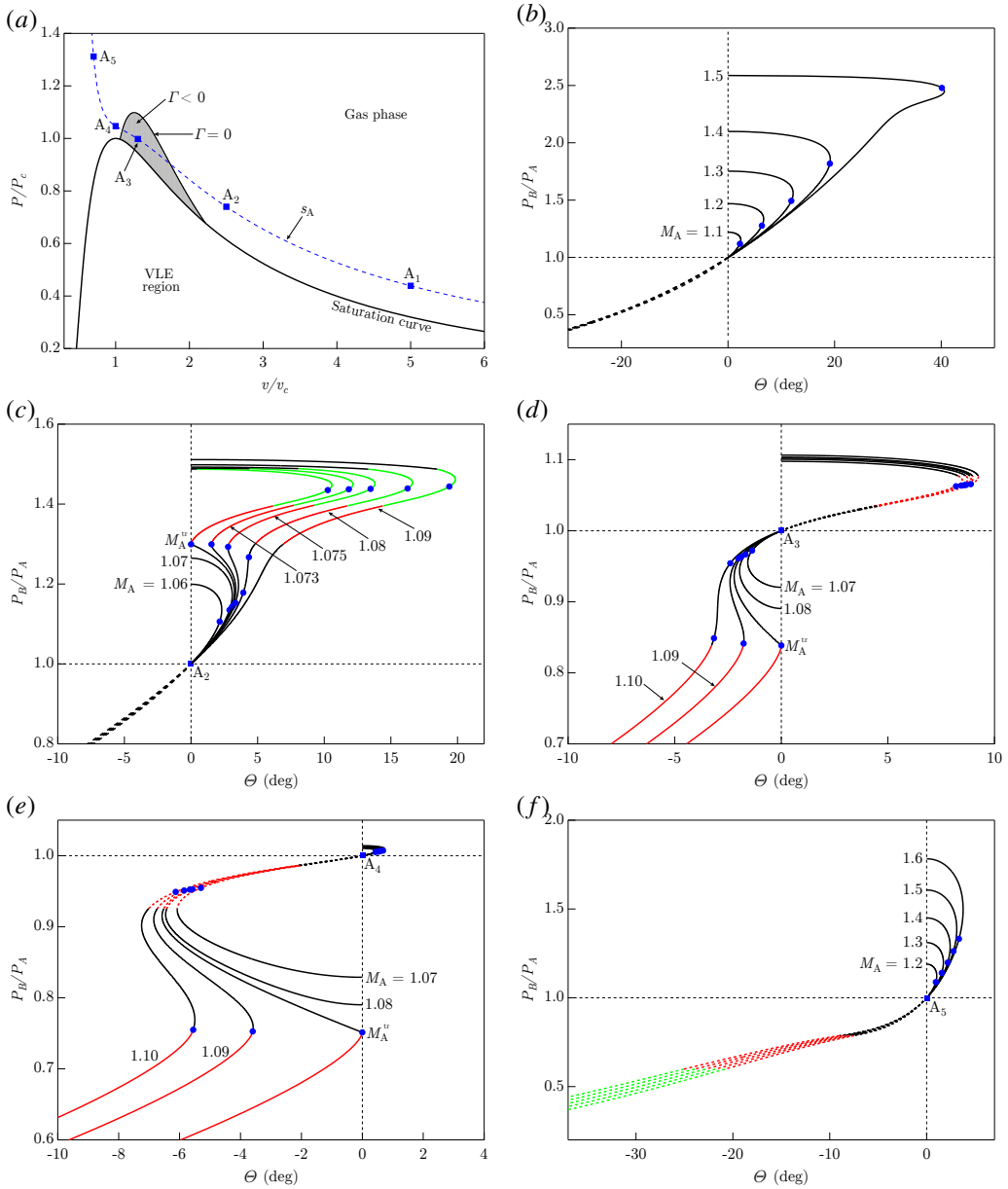
FIGURE 4.15. Left-running wave curves in the pressure–deflection diagram computed from the polytropic van der Waals model with $c_v/R = 57.69$. (a) The selected thermodynamic upstream states, chosen along an isentrope crossing the negative-Γ region (shaded area). (b)-(f) Wave curve for each upstream thermodynamic state and different upstream Mach numbers. For each case, the downstream pressure P_B is scaled using the corresponding upstream pressure P_A. Wave configurations: —— shock, —— shock/fan, - - - shock/fan/shock, - - - fan, - - - fan/shock, - - - fan/shock/fan. Symbol • denotes downstream sonic points ($M_B = 1$).

Case 3 – figure 4.15(d). A single qualitative configuration is observed for the compression side of the wave curve, which is composed by three branches: Prandtl-Meyer fan, Prandtl-Meyer fan/oblique shock, oblique shock (increasing downstream pressure). Two qualitatively different configurations are possible for the rarefaction branch, based on the value of the upstream Mach number. As in the previous case, a threshold Mach number M_A^{tr} exists, such that the ordinary shock polar (though for rarefaction shocks) occurs if $M_A < M_A^{tr}$. Note that, for $M_A < M_A^{tr}$, the largest pressure drop is attained across the normal rarefaction shock from the upstream state, i.e. the rarefaction branch does not extend to vacuum. The transitional curve is again determined by the occurrence of a post-sonic normal shock wave (downstream thermodynamic state S^+ in figure 4.14(d)). Therefore, formula (4.24) applies for the computation of M_A^{tr}.

Case 4 – figure 4.15(e). The compression branch is the classical polar of oblique shocks. Two qualitatively different configurations of the rarefaction branch can possibly occur, again depending on M_A. If $M_A < M_A^{tr}$, the configurations are, in the direction of decreasing downstream pressure: Prandtl-Meyer fan, Prandtl-Meyer fan/oblique shock, oblique shock. If $M_A > M_A^{tr}$, the wave curve extends to vacuum via an additional oblique shock/Prandtl-Meyer fan configuration. Similarly to cases 2 and 3, the transitional wave curve is distinguished by the occurrence of a post-sonic normal shock wave (downstream thermodynamic state S^+ in figure 4.14(e)), so that M_A^{tr} is again computed from relation (4.24).

Case 5 – figure 4.15(f). For case 5 a single wave curve configuration is possible. The compression branch comprises the ordinary shock polar. For decreasing downstream pressures, the rarefaction branch consists of: Prandtl-Meyer fan, Prandtl-Meyer fan/oblique shock, Prandtl-Meyer fan/oblique shock/Prandtl-Meyer fan.

4.6 Upstream-state map of the wave-curve types

Having described the different configurations for the compression and rarefaction branches of the waves curves for steady, two-dimensional and supersonic (possibly mixed supersonic/subsonic across strong oblique shocks) flows, we can now investigate the necessary conditions that the upstream state must satisfy in order to produce a specific wave-curve configuration. Ultimately, the purpose of this section is to determine a map of the upstream states leading to the different types of wave curve identified in the previous section.

For future convenience, the wave curve types are classified according to their qualitative structure, as shown in table 4.3. Seven different wave-curve configurations are singled out, which include the classical configuration $\mathcal{C}$ and six different non-classical configurations $\mathcal{N}_i, i = 1, \ldots, 6$. The classical wave curve $\mathcal{C}$ is the one depicted in figure 4.15(b) and in figure 4.15(c) for $M_A < M_A^{tr}$; $\mathcal{N}_1$ is found in 4.15(c) if $M_A > M_A^{tr}$; $\mathcal{N}_2$ and $\mathcal{N}_3$ occur in figure 4.15(d) for $M_A < M_A^{tr}$ and $M_A > M_A^{tr}$, respectively; $\mathcal{N}_4$ and $\mathcal{N}_5$ in figure 4.15(e) for $M_A < M_A^{tr}$ and $M_A > M_A^{tr}$, respectively; finally $\mathcal{N}_6$ is the configuration shown in figure 4.15(f).

In order to reduce the complexity associated with the dependence of the wave curves on three upstream quantities (two thermodynamic quantities, e.g. P_A, v_A and a kinematic or mixed one, e.g. M_A), we first consider upstream thermodynamic states along exemplary isentropes, as shown in figure 4.16, and we analyse the conditions that determine the transition between different wave curve configurations.

Isentrope a in figure 4.16 is representative of the scenario observed for convex isentropes. As such, only classical wave curves can originate from upstream thermodynamic states along these curves and any given upstream Mach number $M_A > 1$.

Isentrope b is the same used for the parametric studies of the previous sections. It is representative of the scenario arising from isentropes that cross the negative-Γ region while remaining in the single-phase. At sufficiently low upstream pressure, only the classical configuration shown in

Wave-curve type	Compression branch	Rarefaction branch
$\mathcal{C}$	S	F
$\mathcal{N}_1$	S–SF–SFS–S	F
$\mathcal{N}_2$	F–FS–S	S
$\mathcal{N}_3$	F–FS–S	S–SF
$\mathcal{N}_4$	S	F–FS–S
$\mathcal{N}_5$	S	F–FS–S–SF
$\mathcal{N}_6$	S	F–FS–FSF

TABLE 4.3. Classification of the wave curves. S: oblique shock; F: Prandtl-Meyer fan; SF: composite oblique shock/Prandtl-Meyer fan; SFS: composite oblique shock/Prandtl-Meyer fan/oblique shock; FS: composite Prandtl-Meyer fan/oblique shock; FSF: composite Prandtl-Meyer fan/oblique shock/Prandtl-Meyer fan. In the compression branch, the configurations encountered are listed in the order of increasing downstream pressure, while in the rarefaction branch they are in the order of decreasing downstream pressure.

figure 4.14(b) and 4.15(b) can occur. By increasing the pressure along the selected isentrope, point $\mathrm{PS}_{\mathrm{max}}$ is encountered at which the wave curve first includes a post-sonic compression shock. It can be shown (Menikoff & Plohr, 1989) that the post-sonic compression shock arising from $\mathrm{PS}_{\mathrm{max}}$ exhibits $\Gamma_{\mathrm{B}} = 0$. Also, it is the post-sonic compression shock of largest intensity (e.g., pressure or entropy jump) among those originating from the selected isentrope. For pressures included between $\mathrm{PS}_{\mathrm{max}}$ and I'_b (low-density intersection with the $\Gamma = 0$ locus), the extended wave curve in the thermodynamic plane is qualitatively similar to that of figure 4.14(c). As shown in §4.5.2, two different types of wave curve ($\mathcal{C}$ and $\mathcal{N}_1$) can occur based on the value of the upstream Mach number. The threshold Mach number between these two configurations, as computed from relation (4.24), is graphically highlighted in figure 4.16 using the colormap. For upstream states exhibiting $\Gamma_{\mathrm{A}} < 0$, wave curves of type $\mathcal{N}_2$ or $\mathcal{N}_3$ can be observed. The same transitional criterion based on M_{A} applies and is again represented on the isentrope itself in figure 4.16. The branch of isentrope b on the left-hand side of point I''_b (high-density intersection with the $\Gamma = 0$ locus), is two sections by point DS, which denotes the occurrence of a double-sonic shock (Zamfirescu *et al.*, 2008). Between I''_b and DS, double-sonic shocks from upstream states along the chosen isentrope are not possible. Therefore, configurations $\mathcal{N}_2$ or $\mathcal{N}_3$ can occur based on M_{A}. Beyond point DS, the wave curve is of type $\mathcal{N}_6$ only.

In the present discussion, we also consider the single-phase portions of isentropes crossing the saturation curve. The case of isentropes crossing both the negative-Γ region and the saturation curve is the one labelled c in figure 4.16. Non-classical configurations can possibly exist only in the neighbourhood of point I'_c. The branch $\mathcal{C}/\mathcal{N}_1$, in this case, is bounded below by point $\mathrm{PS}_{\mathrm{sat}}$, where the post-sonic shock required for the existence of $\mathcal{N}_1$ configurations features post-shock saturated conditions (namely, the post-shock thermodynamic state lies on the vapour-liquid saturation curve). Finally, for isentropes such as case d in figure 4.16, which cross the phase boundary but do not cross the negative-Γ region, only the classical wave curve configuration is predicted to occur.

By applying the above procedure to each possible isentrope, a map, in terms of thermodynamic quantities and Mach number, of the upstream states leading to each wave curve configuration is obtained, see figure 4.17. In the (P, v)–plane, the thermodynamic region associated with non-classical wave curves is bounded above by the isentrope $s_{\tau,0}$ tangent to the $\Gamma = 0$ locus and by the curve $\mathrm{PSL}_{\mathrm{max}}$. The latter is obtained by collecting all the upstream states $\mathrm{PS}_{\mathrm{max}}$ leading to post-sonic shocks of maximal intensity along a given pre-shock isentrope (as defined above). In a similar fashion, the curve $\mathrm{PSL}_{\mathrm{sat}}$ is computed as the locus of thermodynamic states $\mathrm{PS}_{\mathrm{sat}}$, for each isentrope crossing both the negative-Γ region and the saturation curve. The $\mathrm{PSL}_{\mathrm{sat}}$ bounds
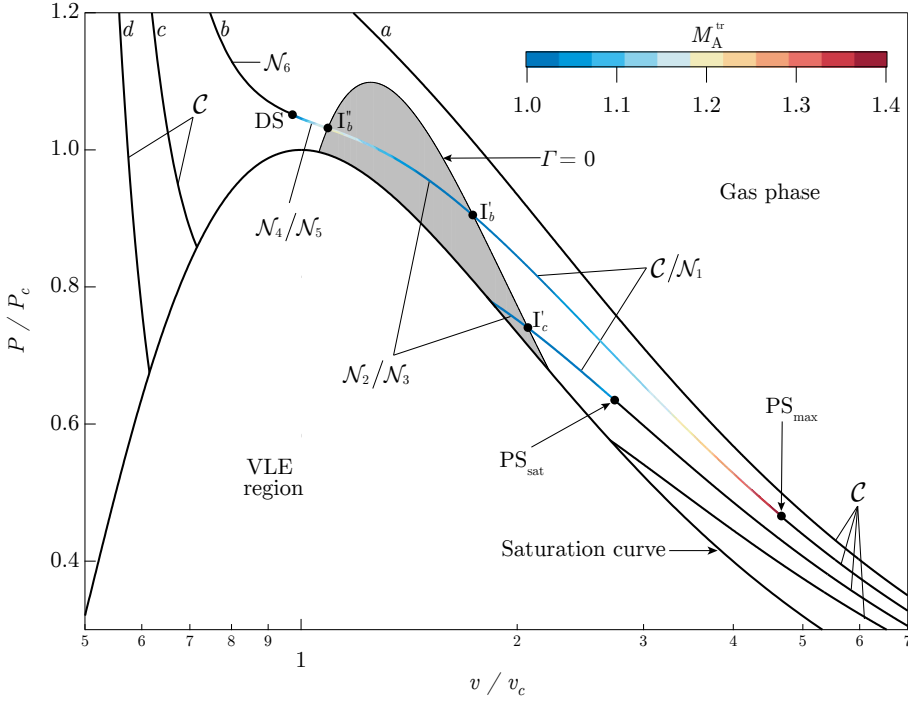
FIGURE 4.16. Wave curve configurations for upstream thermodynamic states along selected isentropes, as computed from the polytropic van der Waals model with $c_v/R = 57.69$. The colormap indicates the transitional upstream Mach number (cf. relation 4.24) for the branches where two different configurations are possible.

from below the region for non-classical wave curves, along with the saturation curve itself and the isentrope $s_{v\text{le}}$ tangent to the latter. The locus $\Gamma = 0$ marks the transition between the regions $\mathcal{C}/\mathcal{N}_1$ and $\mathcal{N}_2/\mathcal{N}_3$ and between the regions $\mathcal{N}_2/\mathcal{N}_3$ and $\mathcal{N}_4/\mathcal{N}_5$. The DSL, which separates the regions $\mathcal{N}_4/\mathcal{N}_5$ and $\mathcal{N}_6$, is obtained by collecting the pre-shock states of double sonic shocks (DS). The DSL shown in figure 4.17 is indeed a portion of the Double-Sonic Locus defined by Zamfirescu *et al.* (2008). Outside the above-described bounds, only classical wave curves can take place.

We assert that the present findings do not depend on the specific choice of the thermodynamic model, insofar as they result from the existence of a finite negative-Γ region in the vapour phase. To support this claim, the upstream-state map of the wave curves for fluid MD_4M (tetradecamethyl-hexasiloxane, $C_{14}H_{42}O_5Si_6$), as computed from the state-of-the-art Span-Wagner EoS of Thol *et al.* 2018 (see also appendix A) available via the REFPROP library, is reported in figure 4.18 and shows excellent qualitative agreement with the picture given by the simple van der Waals model.

4.7 Concluding remarks

The general properties of oblique waves in steady supersonic flows of single-phase fluids were studied. The developed theoretical framework concentrates on compressive and rarefactive ramps/wedges in both the classical and non-classical gasdynamic context, which are the building blocks of more general planar supersonic flows. The supersonic ramp problem was described moving from the one-dimensional Riemann problem, thus allowing us to exploit most of the techniques
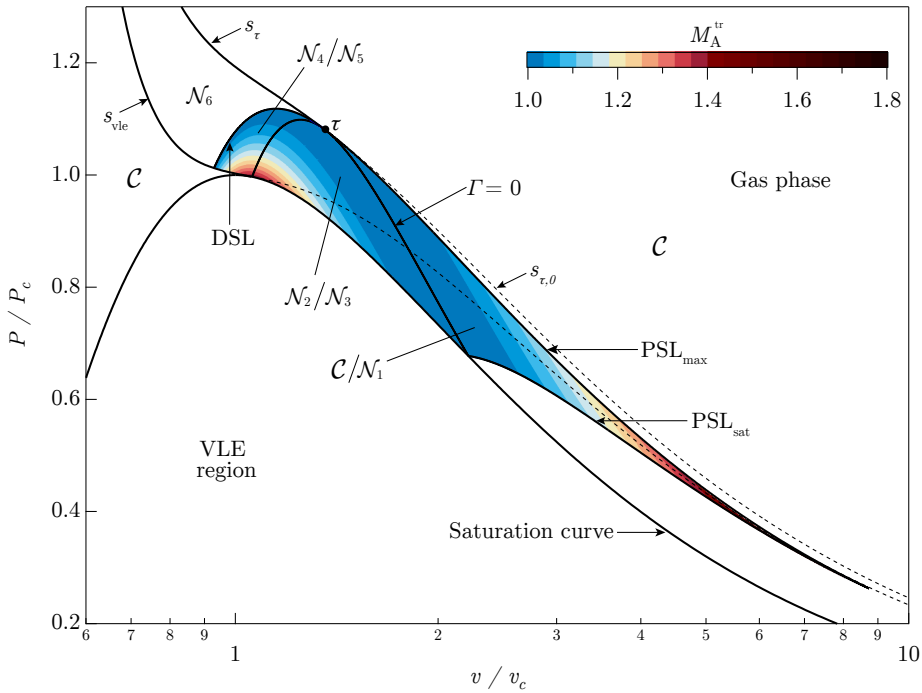
FIGURE 4.17. Upstream-state map of the wave curves in the (P, v)–plane, as computed from the polytropic van der Waals model with $c_v/R = 59.67$. Superposed is the value of transitional upstream Mach number (cf. relation 4.24) for the regions where two different configurations are possible.

developed for scale-invariant flow in one dimension. Accordingly, the concept of wave curve for steady two-dimensional flow, which is the counterpart the wave curve in the one-dimensional Riemann problem, was introduced. Within the present context, the wave curve consists of all the states (in terms of thermodynamic and kinematic quantities) that can possibly be connected to a given supersonic state by means of a steady, two-dimensional and scale-invariant wave. A two-step procedure was adopted to compute the wave curve: the projection onto the thermodynamic variables was first considered, since it represents a subset of the unsteady one-dimensional counterpart, and afterwards all the kinematic quantities were retrieved.

In the classical gasdynamic regime, the wave curve is composed of the well-known oblique-shock branch (compressive side) and simple-wave or Prandtl-Meyer branch (rarefaction side). Among the non-ideal effects pertaining to oblique waves, of particular importance is the discontinuous Mach number increase across oblique shocks (non-ideal oblique shocks) which, surprisingly, has not been detailed in the scientific literature until recently. Non-ideal oblique shocks were investigated here in the context of classical gasdynamics. The increase of the Mach number results from the decrease of the speed of sound across the shock wave, which is possible in the non-ideal gasdynamic regime of fluids characterized by moderate-to-high molecular complexity. By examining oblique shocks in the (M_B, β_s)–plane, the different scenarios for the observation of Mach number–increasing configurations were identified, pointing out the roles of the pre-shock thermodynamic quantities and Mach number. Considerations of multi-dimensional shock stability, in terms of D'yakov–Kontorovich conditions for acoustic emission or neutral stability to transverse perturbations of the shock front, were also given. In the parameter space associated to the pre-shock state variables (thermodynamic quantities and Mach number), the flow conditions
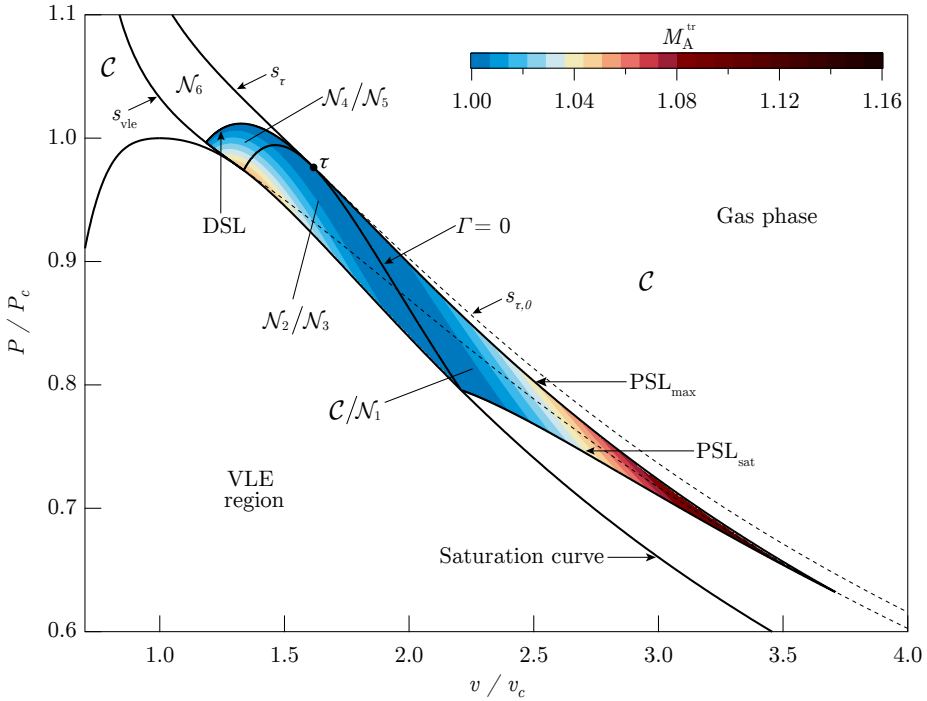
FIGURE 4.18. Upstream-state map of the wave curves in the (P, v)–plane, as computed from the reference thermodynamic model of fluid MD_4M (REFPROP library). Superposed is the value of transitional upstream Mach number (cf. relation 4.24) for the regions where two different configurations are possible.

leading to the occurrence of non-ideal oblique shocks were singled out. As a result, a family of thermodynamic regions, parametrized by the pre-shock Mach number M_A, was introduced. For a given value of M_A, the newly defined regions embed all the pre-shock thermodynamic states from which non-ideal oblique shocks can possibly occur. The computational procedure for determining the admissibility domain of non-ideal oblique shocks was first illustrated using siloxane MDM and subsequently applied to other fluids of practical interest, yielding consistent results (state-of-the-art thermodynamic modelling for each fluid considered). Remarkably, for any given M_A, it is sufficient that $\Gamma < 1 - 1/M_A^2$ somewhere in the thermodynamic state space in order to observe a non-ideal oblique shock. Therefore, the present findings apply to any fluid exhibiting $\Gamma < 1$ in the single-phase vapour region.

A unified approach for the description of the geometrical properties of steady supersonic corner flows in the classical gas dynamic context was presented, which applies to thermally and calorically ideal gases as well as non-ideal fluids. The proposed method takes advantage of the definition of an angle β_f for Prandtl-Meyer fans, which is equivalent to the angle β_s describing the slope of oblique shocks with respect to the upstream flow direction. Using the newly defined fan angle, the common shock angle–deflection angle diagram for oblique shock waves was extended to deal with rarefaction waves. The fan angle was chosen to equal the average of the leading and terminating characteristic slopes in the rarefaction fan. This choice was dictated by the analogy between the role of the fan angle thus defined and that of the oblique shock angle in the isentropic limit, whereby the bisector rule states that the oblique shock is the bisector of the characteristic lines delimiting the folded fan. The interplay between the two angles discloses in the C^1 continuity of β_g–Θ relation in passing through the no-deviation angle $\Theta = 0$. Examples of the complete

(β_g, Θ)–diagram were shown for the perfect-gas case, in which the graph itself is dependent on the value of the upstream Mach number only, and for non-ideal gases, where a marked dependence on the upstream thermodynamic state is also observed. The new diagram was finally applied to the steady supersonic flow of a non-ideal gas past a diamond-shaped airfoil.

In the non-classical gasdynamic regime of BZT fluids, due to the possibly non-convex character of isentropes and shock adiabats in the pressure–specific volume diagram, several oblique-wave patterns are identified which are not admissible in the classical theory of gasdynamics: the composite shock/fan, fan/shock, shock/fan/shock and fan/shock/fan combinations. Moreover, the elementary oblique waves originating from thermodynamic states in the negative-Γ exhibit inverse gasdynamic behaviour, namely oblique shocks carry an expansion while Prandtl-Meyer fans are compressive. The different types of wave curves were illustrated my means of a parametric study in the space of the upstream thermodynamic quantities (e.g., pressure and specific volume) and Mach number, using the van der Waals gas model (with constant isochoric specific heat) of a molecularly complex fluid. Seven different wave curve configurations were singled out, which include the classical case ($\mathcal{C}$) and six non-classical cases ($\mathcal{N}_1$, $\mathcal{N}_2$, $\mathcal{N}_3$, $\mathcal{N}_4$, $\mathcal{N}_5$, $\mathcal{N}_6$). The conditions leading to the transition between the different types of wave curve were analysed. This led to the definition of a map, in the parameter space of the thermodynamic quantities and Mach number, of the upstream states leading to each type of wave curve. Most important, it was shown that the domain of the thermodynamic states leading to wave curves of non-classical type is significantly larger than the negative-Γ region in which inverse gasdynamic behaviour is expected to occur. As the peculiar oblique-wave properties stem from the occurrence of a negative-Γ region in the vapour phase, we expect that the results obtained from the simple van der Waals model apply to diverse thermodynamic models of BZT fluids. The computation of the upstream-state map of the wave curves using the state-of-the-art thermodynamic model of fluid MD$_4$M corroborates this statement.

Remarks concerning the presented results are as follows:

(i) In contrast with the classical case, if the non-classical configuration $\mathcal{N}_1$ is generated, up to four different wave patterns corresponding to the same ramp angle can possibly occur. Moreover, for the non-classical configurations $\mathcal{N}_2$, $\mathcal{N}_3$, $\mathcal{N}_4$ and $\mathcal{N}_5$, the deviation angle does not vary monotonically with the downstream pressure along the expansion branch, where up to three different wave patterns can possibly occurs which correspond to the same ramp angle. Among others, an important problem for further study is the stability of oblique waves in the ramp configuration, which is required for the experimental observation of these non-classical phenomena, see Kluwick & Cox (2018a) for a survey on this topic.

(ii) Violation of condition (2.21) has not been considered in the discussion of non-classical wave curves, being the focus on the structure of wave curve itself. The occurrence of neutral stability can be graphically recognized from the fact that relations (2.22) are satisfied if the sonic point in the pressure-deflection diagram is at larger pressures then the maximum turning angle; one such case is the oblique shock polar marked by $M_A = 1.5$ in figure 4.15(b). A more thorough investigation of this phenomena is left for future investigations.

(iii) As it has been noted by Kluwick & Cox (2018b), the experimental investigation of non-classical phenomena under steady flow conditions overcomes some of the critical weaknesses associated with shock-tube experiments (see Mathijssen et al., 2015), in particular the high sensitivity of the flow to disturbances caused by opening devices. By contrast, the flow conditions leading to steady-state non-classic effects correspond, in general, to larger total enthalpies then those required in unsteady flows. As mentioned in §3, the thermal stability of the working fluid may represent a limiting factor, especially if a blow-down facility is employed. Care must also be exerted in avoiding that the channel (viz. test chamber) undergoes chocking due to an excessive contraction of the cross section (for the case of

incident compression shocks), which would lead to a detachment of the oblique shock from the generating ramp.

In closing, we note that the current theoretical framework can be conveniently applied to the study of shock reflections and shock interactions, to be addressed in the next chapter.

SHOCK REFLECTIONS AND INTERACTIONS IN NON-IDEAL STEADY FLOWS

This chapter describes the theory for reconstructing the steady flow field in the vicinity of the singularity point (node) formed by the intersection of oblique waves in shock-reflection and shock-interaction patterns, with special emphasis on the non-ideal gasdynamic regime. In the classical gasdynamic regime, a limited number of outcomes is expected due to the possibility of deviating a supersonic stream by means of two types of oblique wave, the Prandtl-Meyer rarefaction fan and the oblique compression shock wave. Nevertheless, the admissible patterns are commented in light of the non-ideal increase of the Mach number across oblique shock waves. In the non-classical gasdynamic regime of BZT fluids, the turning of a supersonic stream can be accomplished in a variety of ways other than the conventional oblique shock and Prandtl-Meyer fan. Besides the occurrence of inverted gasdynamic behaviour (rarefaction shocks and compression fans), four additional wave configurations can exist which are of the composite type, namely combination of shocks and fans propagating as a single entity. Consequently, the incoming and outgoing waves at the node in shock reflections and shock interactions in BZT fluids may be non-classical waves. The shock-reflection and shock-interaction theories pertaining classical gasdynamics are extended and adapted to the non-classical framework by allowing outgoing waves to be any sort of oblique wave, and the case of incoming rarefaction shocks is also discussed.

5.1   Introduction and theoretical background

In confined supersonic flows, shock waves are most likely to interact with a solid boundary or other shocks. These processes configure either a shock reflection or a shock-shock interaction, examples of which are sketched in figure 5.1(*a-c*). Shock reflection and interactions are characterized by the presence of a point of singularity called node, where two or more oblique waves intersect. Shock reflections were first reported by Mach (1878), who discovered in his experiments two types of reflection: a regular reflection and an irregular reflection later named after him (Mach reflection). von Neumann (1943, 1945) recognized that the flow field in the neighbourhood of the node consists of uniform states separated by shock waves and possibly by a slip line. On this basis, von Neumann introduced the celebrated two-shock and three-shock theories that model regular and Mach reflections, respectively. Experiments (Ben-Dor, 2007) suggested that a reflection pattern similar to the Mach reflection persists in the range of parameters where no solutions should exist according to the theories of von Neumann. This discrepancy has been termed the von Neumann paradox. In the attempt to solve the von Neumann paradox, Colella & Henderson (1990) discovered a non-standard solution of the three-shock theory and named it von Neumann reflection. It is only at the end of the last century that the von Neumann paradox was successfully solved (Vasil'ev & Kraiko, 1999), by discovering the existence of a fourth wave (wave fan) centred at the node with a local supersonic zone downstream (as suggested long ago by Guderley 1962).

Two basic types of shock interactions can be recognized: the cross node (crossing of two shocks propagating in opposite directions, see figure 5.1(*b*)) and the overtake node (overtake of one shock by another moving in the same direction, see figure 5.1(*c*)). When the flow downstream of the incident shocks is supersonic, a supersonic steady-state Riemann problem is established, in which the data is provided by the states behind the incident waves (Glimm *et al.*, 1985; Glimm & Majda, 2012). Thus, three outgoing waves are expected at the node, namely two oblique waves with a slip line in between. An outgoing oblique wave can disappear (degenerate node) for special deflection angles of the incident shocks, or more commonly if the flow downstream of an incident shock is subsonic.

A common feature between shock reflections and shock interactions is the scale-invariance of the flow pattern in the neighbourhood of the node (uniform states separated by oblique waves and a slip line). For this reason, the wave curves of oblique waves computed in the previous chapter play a central role. Since the boundary conditions in shock reflection and interactions are expressed in terms of flow deflection and pressure, it is advantageous to determine the possible outcomes with a graphical analysis of the wave curve in the pressure-deflection diagram (see, e.g., Ben-Dor, 2007).

This chapter is aimed at extending the established framework of shock reflections and interactions of ideal gases to the non-ideal domain. Two main topics are dealt with, in line with discussion of chapter 4: the presence of non-ideal oblique shocks (§5.2) and the occurrence of non-classical oblique waves which generate new configurations not possible in classical gasdynamics (§5.3).

Few preconditions concerning the present analysis are as follows. At the node, each wave can be classified as incoming or outgoing. The definition of incoming/outgoing waves is based on the tangential velocity along its front or each of its rays in the case of wave fan: if this points toward the node, the wave is incoming, otherwise the wave is outgoing (Henderson & Menikoff, 1998). This criterion for the orientation of oblique waves is illustrated in figure 5.1(*d*). On the ground of the physical meaning of the wave interaction, configurations containing a total of more than two incoming rays are disregarded. Contrary configurations are indeed geometrically irregular (Sanderson, 2004), in the sense that a slight geometrical perturbation of one of the incoming rays would break the single-node interaction pattern into multiple nodes. As an example, a node with three incoming shocks, see figure 5.1(*e*), will split into a pair of regular nodes (each having two incoming shocks) if one of the three shocks undergoes an arbitrary displacement of its front. This
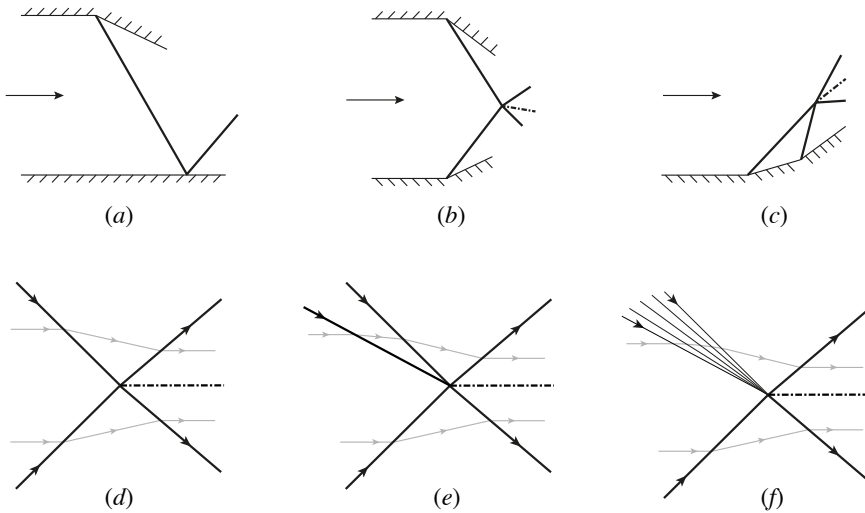
FIGURE 5.1. Examples of (*a*) shock reflection, (*b*) cross node and (*c*) overtake node; (*d*) illustration of the oblique wave orientation: an arrow pointing toward (away from) the node indicates an incoming (outgoing) wave; (*e*),(*f*) excluded configurations with more than two incoming rays. Thick lines denote shock waves, thin lines denote simple waves and dash-dotted lines denote contact discontinuities.

requirement also excludes the case of incoming wave fans centred on the node itself (figure 5.1(*f*)).

The discussion is limited to the case of incident weak oblique shock waves, namely those lying on the branch of the wave curve up to the first detachment point (for both compression and rarefaction sides if these include oblique shocks). In the non-ideal gasdynamic regime, strong oblique shocks having downstream supersonic states may also be constructed. Although not explicitly dealt with, on occasions some remarks on the consequences of considering incident strong shocks will be provided. The occurrence of such shocks is connected with the violation of the uniform stability criterion (2.21) and the potential appearance of acoustic emission from shock waves along the considered wave curve (Menikoff & Plohr, 1989). In this chapter, considerations of multidimensional stability will be omitted, as the focus is primarily on the structure and mechanism of the wave interaction (in other words, we do not take into account the multidimensional stability analysis performed for non-ideal oblique shocks).

5.2 Classical shock reflections and interactions

The general concepts behind steady shock reflections and interactions in classical gasdynamics are recalled to set the ground for the subsequent analysis of non-classical wave interactions. In §5.2.1, regular shock reflections are studied by means of the two-shock theory of von Neumann. When dealing with irregular reflections (§5.2.2), either the three-shock theory of von Neumann or the four-wave model are needed. Classical shock interactions are reviewed in §5.2.3 for the cross-node configuration and in §5.2.4 for the overtake-node configuration. The non-ideal effect of primary interest in the following discussion is the non-ideal increase/decrease of the Mach number across oblique shocks/Prandlt-Meyer fans, which has been detailed previously in §4.4.1 and §4.4.2. Shock reflection and interactions are illustrated using the polytropic van der Waals model with dimensionless isochoric specific heat set to $c_v/R = 15$.
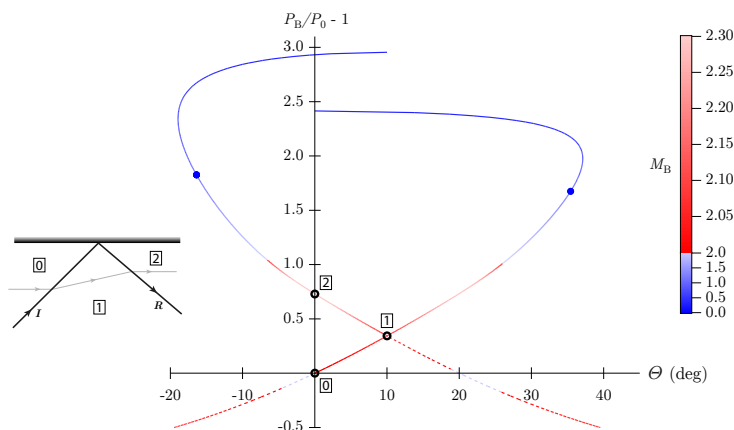
FIGURE 5.2. Pressure–deflection diagram for the regular reflection in a polytropic van der Waals gas with $c_v/R = 15$. Upstream state: $s_0 = s(0.74P_C, 2.5v_C)$, $v_0 = 3v_C$, $M_0 = 2$. Shock-wave branch represented by the solid line, rarefaction fan branch dashed. The colormap indicates the value of the Mach number downstream of each oblique wave. Sketch of the reflection pattern: **I** incident shock, **R** reflected shock.

5.2.1 Regular reflection

When the angle between the shock front and the reflecting surface is small enough, a regular reflection takes place. In a regular-reflection pattern, an incident oblique shock wave is reflected as a wave of the opposite family. In classical gasdynamics, the incident shock is of course compressive; likewise, the reflected wave is a compression shock producing an opposite flow deflection, with respect to that of the incident shock, and therefore satisfying the boundary condition imposed by the reflecting surface. This is the two-shock theory of von Neumann (1943).

The problem of regular shock reflection consists in determining the properties of the reflected shock and its downstream state, once the incident shock (together with the flow states across itself) and the geometry of the reflecting surface are known. Since we are dealing with the description of the flow field near to the node where the reflection occurs, the incident shock, as well as the reflected wave and the reflecting surface, are considered as straight.

As is well-known, the shock-reflection pattern can be determined from the analysis of the pressure-deflection diagrams. An example is provided in figure 5.2 for the case of an incident left-running shock. The left-running wave curve (incident) from state 0 is drawn from the origin of the (P_B, Θ)–plane, while the right-running wave curve (reflected) from state 1, which occurs along the incident wave curve. The state 2 downstream of the reflected shock is found at the intersection of the reflected wave curve and the $\Theta = 0$ axis. Among the two possible intersections, the high-pressure one yields a subsonic downstream state and is discarded because unstable to small perturbations and thus it would not occur in a steady-state flow (Teshukov, 1989).

The upstream state 0 and the incident-shock angle are such that both shocks in the reflection pattern are non-ideal oblique shocks. We expect this situation to occur whenever the incident shock is non-ideal and sufficiently weak. A sequence of similar reflections would configure an almost isentropic compression in the region of thermodynamic states associated with $J > 0$, leading to an overall increase of the flow Mach number.

5.2.2 Irregular reflection

If the strength of the incident shock is large enough, an irregular reflection takes place. This involves the detachment of both the incident and reflected shock from the surface and the generation of a third shock, which is the one actually colliding with the reflecting surface. The node where the three shocks intersect is called the triple point. Henderson & Menikoff (1998) demonstrated that for a convex EoS (thus, in the classical gasdynamic regime), a sequence of two shocks has a lower entropy than a single shock to the same final pressure. This implies that a pure three-shock configurations cannot exist, namely a contact discontinuity is required to sustain the entropy jump generated by fluid particles crossing either one of the shocks in the three-shock pattern, or the remaining two. More recently, Serre (2007) presented a proof if the impossibility of triple shock structures that is based on kinematic arguments only, i.e. independently of any assumption on the EoS.

In the reference textbook of Ben-Dor (2007), several irregular-reflection patterns are described theoretically and verified against numerical simulations and experiments. In this work it is hypothesized that irregular reflections can uniquely occur in the form of Mach reflections (see below). However, recent studies (Defina *et al.*, 2008; Ivanov *et al.*, 2012; Vasil'ev, 2016) indicate that additional irregular-reflection configurations can occur in steady flows, namely the von Neumann reflection, the Guderley reflection and the Vasil'ev reflection. These are recalled in the following sections.

5.2.2.1 Mach reflection

The Mach-reflection pattern in classical gasdynamics is schematically shown in figure 5.3. It consists of three shock waves and one slip line, all meeting at the triple point. At this node, one shock wave is incoming (the incident shock), while the reflected shock (pointing away from the wall), the Mach stem (pointing towards the wall) and the slip line (between the reflected shock and the Mach stem) are outgoing.

A Mach reflection involves subsonic flow downstream of the Mach stem, thus the complete description of the flow field requires that the downstream boundary conditions are properly accounted for. Nevertheless, if the interest is on the flow field in the close neighbourhood of the triple point, the three-shock theory by von Neumann (1945) can be used to determine the reflection pattern. In the three-shock theory, the incoming shock as well as the outgoing waves are all considered straight (which is a fairly good approximation close to the node). Thus, the analysis of the pressure-deflection diagram allows us to determine the properties of the outgoing waves, once the incident-shock properties are known.

In figure 5.3, the left-running wave curve (incident) from state 0 is drawn from the origin, while the left-running wave curve (reflected) from state 1, which occurs along the incident wave curve. The pair of outgoing shocks, namely the reflected shock and the Mach stem, are determined by imposing that their downstream pressures and flow directions (states 2 and 2', respectively) are equal, since they are separated by the outgoing slip line. The resulting value of the flow direction is therefore the slope of the slip line.

In the present example, the reflected wave curve does not intersect the $\Theta = 0$ axis, so that the Mach reflection is indeed the only admissible reflection pattern. However, it is also possible that the reflected wave curve intersects both the incident one (Mach reflection) and the $\Theta = 0$ axis (regular reflection). A dual solution is therefore possible; which solution should be preferred is still a topic of debate (see, e.g., Ben-Dor, 2007). In experiments and numerical studies on quasi-steady flows, hysteresis effects have been found to occur (Chpoun *et al.*, 1995; Ivanov *et al.*, 1995, 1998). Thus, in the dual-solution domain, both the regular and the Mach reflections can be compatible with the applied boundary conditions. Here we limit the description to cases in which a Mach
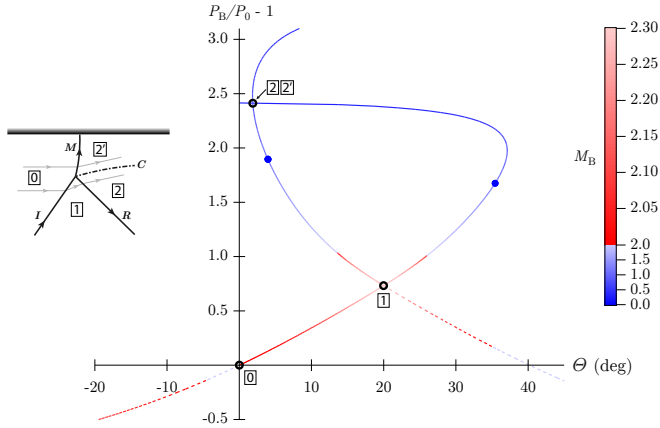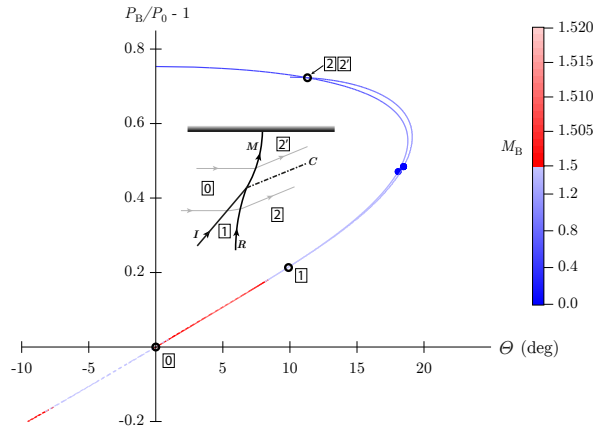
FIGURE 5.3. Pressure–deflection diagram for the Mach reflection in a polytropic van der Waals gas with $c_v/R = 15$. Upstream state: $s_0 = s(0.74 P_c, 2.5 v_c)$, $v_0 = 3 v_c$, $M_0 = 2$. Sketch of the reflection pattern: *I* incident shock, *R* reflected shock, *M* Mach stem, *C* contact discontinuity. Same conventions of figure 5.2.

reflection is admissible from the (P_B, Θ)–diagram analysis (thus, even when this occurs in the dual-solution domain).

In the Mach reflection depicted in figure 5.3, the incident shock produces an increase of the Mach number. However, because of the large shock angles characterizing the reflected shock and the Mach stem, it is unlikely that Mach reflections involve non-ideal oblique shocks other than the incident one. We expect this to be true even if the incident shock angle is quite large, so that the reflected shock is in fact relatively weak as we are reducing the difference in the pressure jumps across the incident shock and the Mach stem. In doing so, state 1 would occur in the neighbourhood of the sonic point along the incident shock polar. In this case, indeed, not only the incident shock would be Mach number-decreasing, but the smaller Mach number upstream of the reflected shock would lead to a narrow range of reflected shock angles in which the Mach number can increase. Computations not shown here seem to confirm this claim.

5.2.2.2 von Neumann reflection

When the opposite-family reflected wave curve intersects neither the $\Theta = 0$ axis nor the incident wave curve (excluding of course the state ahead of the reflected wave), a solution within the three-shock theory is still possible and it is known as the von Neumann reflection (Ben-Dor, 2007). In a von Neumann reflection, see figure 5.4, the reflected shock is of the same family as the incident shock (and of the Mach stem), therefore it is an incoming wave into the triple point (Viero *et al.*, 2013). In order that the local pattern at the node be compatible with the global flow, i.e. for the further incoming shock to originate from the shock reflection, rather than from some specific upstream boundary conditions (e.g. the same producing the incident shock) which is evidently not the case here, the reflected shock must be a curved shock with a vertex (at which the front is normal to the incoming flow) at some distance away from the triple point. From the vertex, two curved shocks originate: an inner branch, of the same family as the incident shock, which is oriented towards the triple point, and an outer branch, of the opposite family, directed away from it. A similar configuration is physically admissible only if the flow downstream of the curved shock is not supersonic (Vasil'ev *et al.*, 2008; Ivanov *et al.*, 2010).

In the close proximity of the node, the approximation of straight shocks is again reasonable
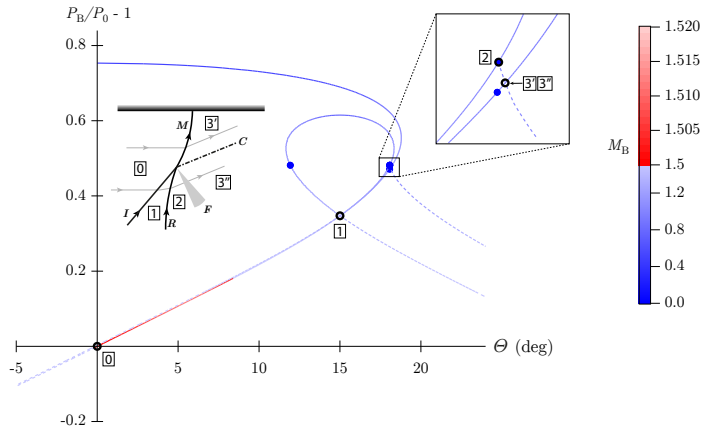
FIGURE 5.4. Pressure–deflection diagram for the von Neumann reflection in a polytropic van der Waals gas with $c_v/R = 15$. Upstream state: $s_0 = s(0.74 P_c, 2.5 v_c)$, $v_0 = 1.75 v_c$, $M_0 = 1.5$. Sketch of the reflection pattern: *I* incident shock, *R* reflected shock, *M* Mach stem, *C* contact discontinuity. Same conventions of figure 5.2.

and the three-shock theory can be applied, this time, however, considering shock waves of the same family as the incident one. An exemplary pressure-deflection diagram corresponding to the three-shock interaction in a von Neumann reflection is shown in figure 5.4.

Remarks similar to those given for the Mach reflection apply to the present case. Even though the incident wave is a non-ideal oblique shock, the intersection between the incident and reflected shock curves typically occurs on their strong shock branch (it being understood that the state downstream of the reflected wave is subsonic or at most sonic). This suggests that von Neumann reflection patterns that increase the Mach number are unlikely circumstances.

5.2.2.3 Vasil'ev and Guderley reflections

If the reflected wave curves (of both families) cross neither the $\Theta = 0$ axis nor the incident wave curve, the three-wave theory does not yield any solution. This particular situation is referred to as the von Neumann paradox. In order to overcome the von Neumann paradox, Guderley (1962) proposed a four-wave model which has recently been confirmed by theoretical, numerical and experimental investigations (Vasil'ev & Kraiko, 1999; Tesdall & Hunter, 2002; Skews & Ashworth, 2005; Vasil'ev *et al.*, 2008).

The structure of the four-wave reflection pattern is illustrated in figures 5.5 and 5.6. The incident and reflected shocks, together with the Mach stem are all of the same wave family, similarly to the von Neumann reflection. The slope of the reflected shock in the neighbourhood of the node is such that its downstream flow is uniformly sonic ($M_B = 1$ in region 2). Behind the reflected shock, a fourth wave is generated, namely an outgoing expansion fan centred at the node itself (recall that incoming wave fans are disallowed). Because the fan originates in a sonic flow, the leading acoustic wave of the fan is normal to the flow direction in region 2. The fan terminates when the same pressure and direction as those behind the stem are attained.

The possible reflection patterns under conditions corresponding to the von Neumann paradox are the Vasil'ev reflection and the Guderley reflection. In the Vasil'ev reflection, see figure 5.5, the flow behind the Mach stem is subsonic. On the contrary, in the Guderley reflection (figure 5.6) the flow downstream of the Mach stem is still supersonic and it is further deflected towards the
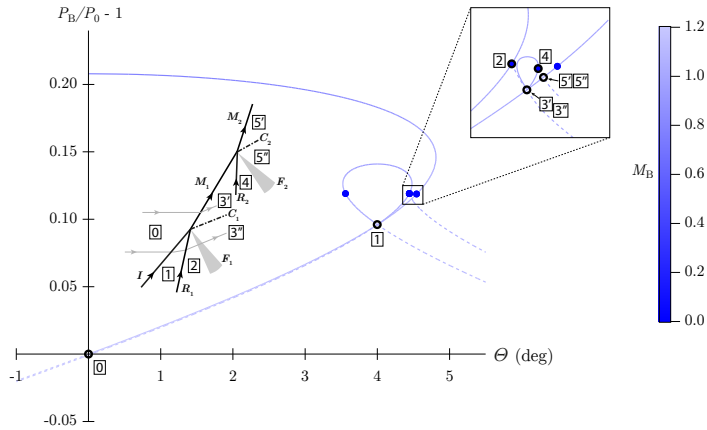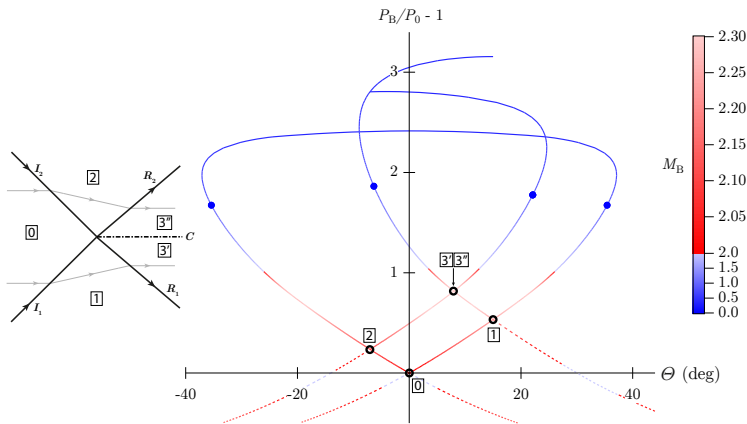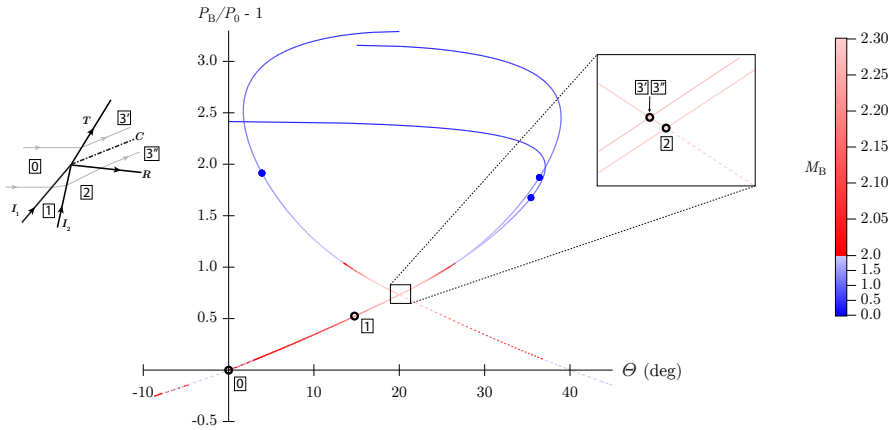
FIGURE 5.5. Pressure–deflection diagram for the Vasil'ev reflection in a polytropic van der Waals gas with $c_v/R = 15$. Upstream state: $s_0 = s(0.74P_c, 2.5v_c)$, $v_0 = 1.75v_c$, $M_0 = 1.5$. Sketch of the reflection pattern: $\boldsymbol{I}$ incident shock, $\boldsymbol{R}$ reflected shock, $\boldsymbol{M}$ Mach stem, $\boldsymbol{F}$ rarefaction fan, $\boldsymbol{C}$ contact discontinuity. Same conventions of figure 5.2.

wall. The Mach stem embedded in a supersonic flow can be regarded as the incident shock in a new reflection problem, thus generating an additional node with the same structure as the previous one, as shown in figure 5.6. Under unsteady flow conditions, a cascade of four-wave nodes, joined by tiny stems, is formed (Vasil'ev *et al.*, 2008; Tesdall *et al.*, 2015). Still it is unclear whether the sequence is finite or infinite; in the latter case the cascade continues until the flow behind the last stem is sonic. Conversely, in steady flows, both finite-cascade configurations (Vasil'ev, 2016) and single-node configurations with a single, weakly curved Mach stem has been observed (Defina *et al.*, 2008).

With respect to the presence of non-ideal oblique shocks in the reflection pattern, we notice that the conditions under which Vasil'ev or Guderley reflections can possibly develop are characterized by the largest incident-shock deflections (in the proximity of the sonic point of the incident shock polar) among the other types of reflection (see, e.g., the reflection domain computed by Vasil'ev *et al.* 2008; Defina *et al.* 2008). As a result, we do not expect the possibility of non-ideal Mach number variation across the waves involved in Vasil'ev or Guderley reflections.

5.2.3 Cross node

The collision point between two oblique shocks of opposite families is called a cross-node. If the strength of the incident shocks is sufficiently small, the flow immediately downstream is supersonic. Thus the interactions gives rise three outgoing waves, two oblique waves (shock or fan) separated by a slip line. An outgoing oblique wave can disappear if a transition to subsonic conditions occurs across one of the incident shocks (degenerate cross-node). It should be noted that, for a perfectly symmetric incident-shock configuration, the outgoing wave pattern is also symmetric and the jumps across the slip line vanish. It is evident that the flow configuration in each of the half planes about the symmetry axis is identical to that of a regular reflection.

The cross-node flow pattern can of course be studied using the (P, Θ)–diagram analysis. A typical cross-node configuration is shown in figure 5.7. The two incoming shocks produce as many outgoing shocks with a contact discontinuity in between. By examining the shape of the wave curves in the (P, Θ)–plane, it is clear that the collision of two weak oblique shocks in a

FIGURE 5.6. Pressure–deflection diagram for the Guderley reflection in a polytropic van der Waals gas with $c_v/R = 15$. Upstream state: $s_0 = s(0.74 P_c, 2.5 v_c)$, $v_0 = 1.3 v_c$, $M_0 = 1.2$. Sketch of the reflection pattern: I incident shock, R_1, R_2 reflected shocks, M_1, M_2 Mach stems, F_1, F_2 rarefaction fans, C_1, C_2 contact discontinuities. Same conventions of figure 5.2.
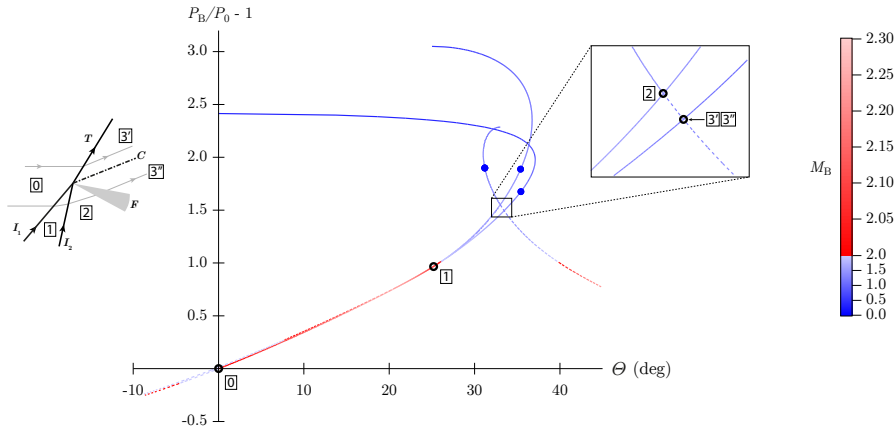

FIGURE 5.7. Pressure–deflection diagram for the cross-node interaction in a polytropic van der Waals gas with $c_v/R = 15$. Upstream state: $s_0 = s(0.74 P_c, 2.5 v_c)$, $v_0 = 3 v_c$, $M_0 = 2$. Sketch of the cross-node pattern: I_1, I_2 incident shocks, R_1, R_2 reflected shocks, C contact discontinuity. Same conventions of figure 5.2.

cross node can generate outgoing oblique shocks only. Menikoff & Plohr (1989) observed that an alternative scenario is possible if one of the incoming shock is a strong oblique shock with supersonic downstream state: the strong shock is reflected as a rarefaction fan.

Non-ideal oblique shocks can be easily observed in cross-node configurations if the upstream state is properly chosen. This is especially true for small-amplitude incident shocks, as in the example of figure 5.7, which involves incoming and outgoing non-ideal oblique shocks.

FIGURE 5.8. Pressure–deflection diagram for the overtake-node interaction in a polytropic van der Waals gas with $c_v/R = 15$. Upstream state: $s_0 = s(0.74P_c, 2.5v_c)$, $v_0 = 3v_c$, $M_0 = 2$. Sketch of the overtake-node pattern: I_1, I_2 incident shocks, T transmitted shock, R, reflected shock, C contact discontinuity. Same conventions of figure 5.2.

5.2.4 Overtake node

Two shocks of the same family meet generating an overtake node. This interaction produces a transmitted shock of the same family as the incident ones, a slip line and a reflected wave of the opposite family if the flow passing through both incoming shocks remains supersonic. The reflected wave can be either a shock wave or a rarefaction fan (see also Glimm *et al.*, 1985). These two possibilities are shown in figures 5.8 and 5.9, respectively.

Examples of overtake node were already encountered in the previous sections as the Guderley and Vasil'ev reflections are, in all respects, overtake nodes with an outgoing shock and an outgoing fan separated by a slip line, whereas the von Neumann reflection pattern is a degenerate overtake-node with a single outgoing shock in addition to the slip line.

With reference to figures 5.8 and 5.9, we notice that in general the reflected rarefaction wave is generated for incident shocks of relatively large amplitude. This, in turn, is likely to preclude the possibility of outgoing non-ideal oblique shocks in the overtake-node pattern (see figure 5.9). Conversely, with incident shocks that are sufficiently weak and of the non-ideal type (as in the exemplary configuration of figure 5.8), overtake nodes with outgoing non-ideal oblique shocks can be obtained.

5.3 Non-classical shock reflections and interactions

Maintaining the same structure of the previous section, shock reflections and interactions in the non-classical gasdynamic regime of BZT fluids are investigated using the polytropic van der Waals model with dimensionless isochoric specific heat set to $c_v/R = 57.69$. Several combinations of incoming shocks and outgoing waves at a node are expected due to the fact that the incoming shocks can be not only pressure-increasing but also pressure-decreasing, and that the outgoing waves can be shocks, fans or composite waves, both compressive and expansive. In order to account for the wider variety of outgoing waves, a two-wave theory and a three-wave theory — non-classical counterparts of the two-shock and three-shock theories — are introduced. Moreover, the four-wave model of the Guderley and Vasil'ev reflections is adapted to the non-classical context.

FIGURE 5.9. Pressure–deflection diagram for the cross-node interaction in a polytropic van der Waals gas with $c_v/R = 15$. Upstream state: $s_0 = s(0.74P_c, 2.5v_c)$, $v_0 = 3v_c$, $M_0 = 2$. Sketch of the overtake-node pattern: I_1, I_2 incident shocks, T transmitted shock, F reflected rarefaction fan, C contact discontinuity. Same conventions of figure 5.2.

Differently from the previous section, the focus here is on the structure of the shock reflection or interaction, namely on the possible types of wave expected at the node.

5.3.1 Regular reflection

In a regular reflection, the reflected wave is required to produce a flow deflection which is opposite in direction and equal in magnitude, with respect to that of the incident shock. From the arguments of 4.5.2, it follows that the reflected wave is of the same compression/rarefaction type as the incident shock. The aim of this section is to show that in the non-classical gasdynamic regime, a number of regular-reflection configurations exist in which the reflected wave is not an oblique shock, rather a wave fan or a composite wave. The two-wave theory presented below to model the reflection of oblique shocks in non-classical gasdynamics can be regarded as an extension of the classical two-shock theory.

A first example of the new scenarios is depicted in figure 5.10. According to the nomenclature defined in table 4.3, the incident wave curve is of type $\mathcal{N}_1$. Here we focus on the first branch of oblique shock waves (approximately up to $12°$). Various reflected wave curves are plotted; these correspond to different incident-shock conditions which are now examined. For the oblique shocks of smallest pressure jump, the reflected wave curve is qualitatively similar to the incident one, and the $\Theta = 0$ axis is crossed on the reflected oblique-shock branch (case a in figure 5.10). Thus, the shock-reflection pattern is qualitatively similar to the classical one.

However, as the deflection angle of the incident shock is increased, the reflected wave curve crosses the $\Theta = 0$ axis at its composite shock/fan branch. This implies that the reflection of the incident oblique shock is accomplished by a composite shock/fan wave, see case b of figure 5.10. It is also possible, by further increasing the incident shock strength, that the flow deflection needed to return the flow parallel to the wall is provided by a composite shock/fan/shock wave, see case c in figure 5.10.

The reflected wave curve can also change its configuration. In figure 5.10, this transition occurs for the largest values of the incident-shock strength, as the flow state downstream of the incident shock lies within the negative-Γ region. Thus, the configuration of the compression branch of
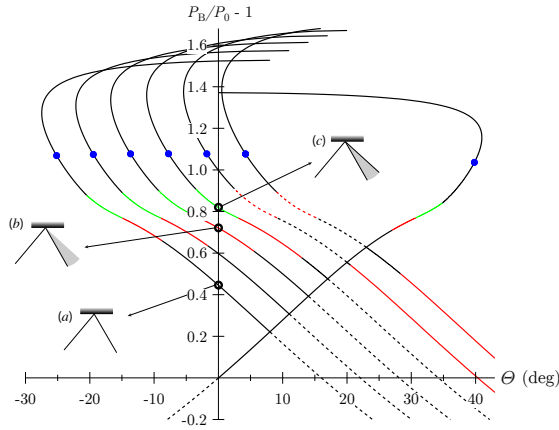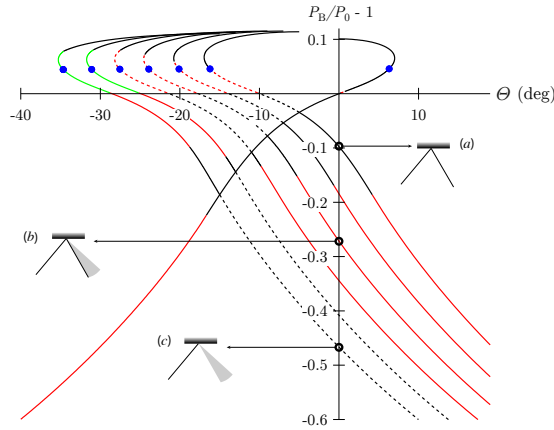
FIGURE 5.10. Pressure–deflection diagram for the regular reflection in a polytropic van der Waals gas with $c_v/R = 57.69$ and simplified sketches of the reflection pattern. Upstream state: $s_0 = s(0.74P_c, 2.5v_c)$, $v_0 = 3.5v_c$, $M_0 = 1.5$. Legend: —— shock, —— shock/fan, - - - shock/fan/shock, - - - fan, - - - fan/shock, • downstream sonic point.
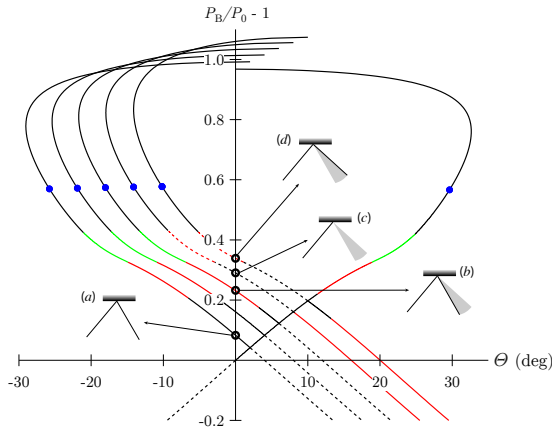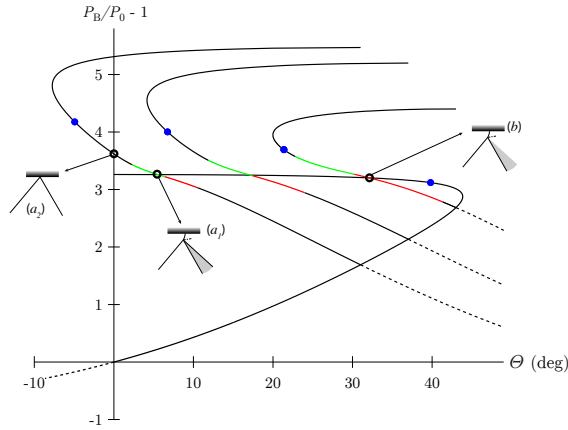

FIGURE 5.11. Pressure–deflection diagram for the regular reflection in a polytropic van der Waals gas with $c_v/R = 57.69$ and simplified sketches of the reflection pattern. Upstream state: $s_0 = s(0.74P_c, 2.5v_c)$, $v_0 = 2.3v_c$, $M_0 = 1.5$. Legend: —— shock, —— shock/fan, - - - shock/fan/shock, - - - fan, - - - fan/shock, • downstream sonic point.

the wave curve changes from the type $\mathcal{N}_1$ to $\mathcal{N}_3$. The reflected wave curves exhibiting the $\mathcal{N}_3$ configuration, however, cross the $\Theta = 0$ in figure 5.10 at the oblique shock branch, thus resulting in a classical oblique-shock reflection.

    An additional example is shown in figure 5.11. In this case, patterns in which the incident shock reflects as a compressive Prandtl-Meyer fan (case c) or as a composite fan/shock wave (case d) are in fact observed.

    In the non-classical gasdynamic regime of a BZT-fluid flow, rarefaction shock waves are also admissible. Possible reflection patterns for an incident rarefaction shock are shown in figure 5.12. The incident wave curve is of the type $\mathcal{N}_3$. As previously noted for the case of incident
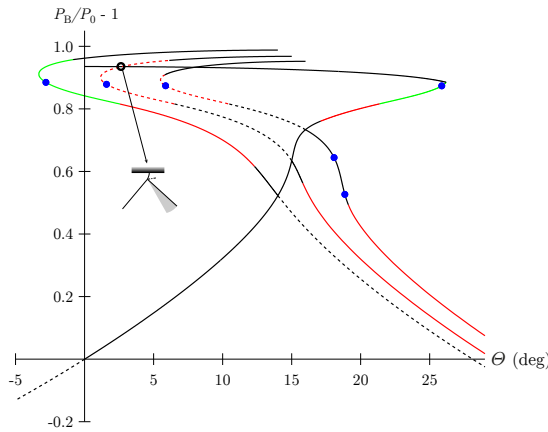
FIGURE 5.12. Pressure–deflection diagram for the regular reflection in a polytropic van der Waals gas with $c_v/R = 57.69$ and simplified sketches of the reflection pattern. Upstream state: $s_0 = s(0.74P_c, 2.5v_c)$, $v_0 = 1.1v_c$, $M_0 = 1.5$. Legend: —— shock, —— shock/fan, - - - shock/fan/shock, - - - fan, - - - fan/shock, • downstream sonic point.

compression shocks, the reflected wave curve can intersect the $\Theta = 0$ axis at different branches, in addition to change it's qualitative configuration because of the pressure and entropy jump (at constant total enthalpy). In figure 5.12, the incident rarefaction shock is seen to reflect as another rarefaction shock (case a), as a rarefaction shock/fan composite waves (case b) or also as a pure rarefaction fan (case c).

5.3.2 Irregular reflection

As in the classical gasdynamic regime, regular reflections in non-classical gasdynamic turn into irregular reflections as the strength of the incident shock is increased. It is important to notice that Serre's proof of the impossibility of triple shock structures (Serre, 2007) is completely general and thus applies to the non-classical framework. Irregular reflection patterns similar to those encountered in §5.2.2 are investigated, with a special attention to the presence of wave fans or composite waves whereby the classical theory predicts oblique shocks.

5.3.2.1 Mach reflection

In the following examples we show how the Mach-reflection pattern emerging in the classical gasdynamic context can change due to the appearance of non-classical waves. In doing so we introduce a three-wave theory, extension of the classical three-shock theory, to model Mach reflections in the non-classical gasdynamic context.

Figure 5.13 shows selected Mach-reflection configurations in which the reflected wave is no longer an oblique shock. Case a_1 represents a Mach reflection in which the reflected wave is a composite shock/fan/shock wave. Note that the (P_B, Θ)–diagram of the present configuration indicates a dual solution (a_1 Mach reflection, a_2 regular reflection). In case b of figure 5.13, a shock/fan composite wave originates at the triple point in order to accomplish the incident-shock reflection. A reflected fan/shock wave can also occur in a Mach reflection, as shown in figure 5.14.

On the basis of numerical evidence, it appears that Mach-reflection patterns are not possible for incident rarefaction shocks, at least with the current thermodynamic model. Within the range of the parameters corresponding to an incident rarefaction shock, the reflected wave curve is seen

FIGURE 5.13. Pressure–deflection diagram for the Mach reflection in a polytropic van der Waals gas with $c_v/R = 57.69$ and simplified sketches of the reflection pattern. Upstream state: $s_0 = s(0.74P_c, 2.5v_c)$, $v_0 = 9.55v_c$, $M_0 = 2.0$. Legend: —— shock, —— shock/fan, - - - shock/fan/shock, - - - fan, • downstream sonic point.
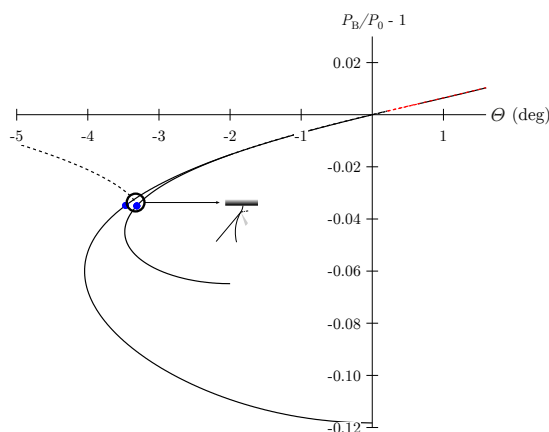

FIGURE 5.14. Pressure–deflection diagram for the Mach reflection in a polytropic van der Waals gas with $c_v/R = 57.69$ and simplified sketches of the reflection pattern. Upstream state: $s_0 = s(0.74P_c, 2.5v_c)$, $v_0 = 3.62v_c$, $M_0 = 1.26$. Legend: —— shock, —— shock/fan, - - - shock/fan/shock, - - - fan, - - - fan/shock, • downstream sonic point.

to either cross the $\Theta = 0$ axis (as shown, e.g., in figure 5.12) or to not cross the incident wave curve at all. The latter situation is sketched in figure 5.15 (left).

The lack of Mach-reflection configurations for incident rarefaction shocks is possibly connected to the following fact. Let state 0 and state 1 indicate the flow states upstream and downstream of the incident shock, respectively. The mass balance across the shock then reads

$$\rho_0 u_0 \sin \beta_s = \rho_1 u_1 \sin(\beta_s - \Theta). \tag{5.1}$$

The quantity $\rho_0 u_0$ is the mass flux for an incident normal shock (point N_0 in figure 5.15). The mass-flux value $\rho_1 u_1$, instead, is associated with the maximum pressure decrease along the reflected

112
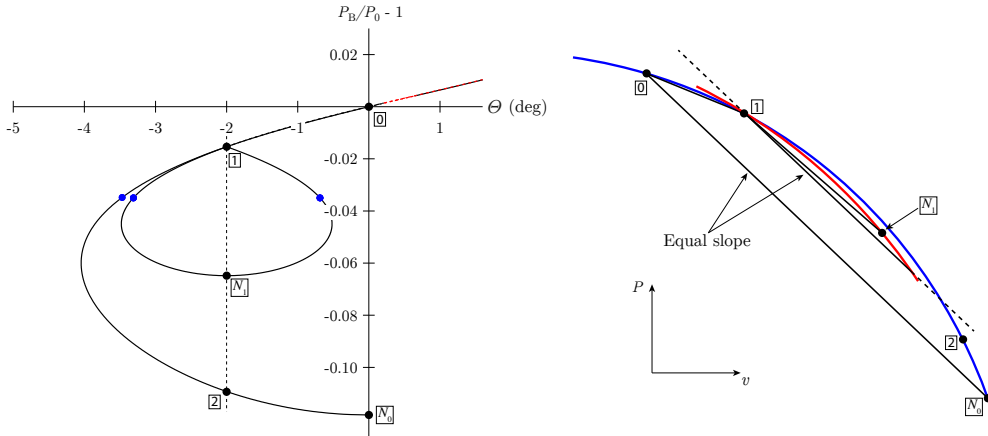
FIGURE 5.15. (Left) Pressure–deflection diagram computed from the polytropic van der Waals model with $c_v/R = 57.69$ and upstream state $s_0 = s(0.74P_c, 2.5v_c)$, $v_0 = 1.1v_c$, $M_0 = 1.15$. Legend: —— shock, - - - fan, - - - fan/shock, • downstream sonic point. (Right) Qualitative illustration of the shock curves in the (P,v)–plane corresponding to the layout of the left figure. Blue line: wave curve (shock adiabat) centred on point 0; red line: wave curve centred on point 1.

wave curve (namely, the normal shock from state 1, point N_1). A compression shock deviates the flow towards the front itself ($|\beta_s - \Theta| < |\beta_s|$), whereas a rarefaction shock away from it ($|\beta_s - \Theta| > |\beta_s|$). Thus we obtain that $\rho_1 u_1 < \rho_0 u_0$ for an incident rarefaction shock.

Now consider the construction of figure 5.15 (right). The quantity ρu is strictly related to the slope of the chord between the pre-shock and the post-shock states (which is given by $-\rho^2 u^2$). The shock adiabat from state 1, for $v > v_1$, is located below the shock adiabat from state 0 (see Kluwick, 2001). Combining these two results, we obtain that the pressure at point N_1 is larger than the pressure at N_0. This condition is necessary, but not sufficient, for the non-existence of Mach reflections of rarefaction shocks, for the pressure value at N_1 should be larger than the pressure at point 2, the strong oblique shock with the same flow deflection as point 1. Nevertheless, the present finding explains the observed rarefaction-shock configurations in the polar diagram (in clear contrast with compression waves) and may arguably suggest a possible mechanism by which Mach reflections would not occur for incident rarefaction shocks.

5.3.2.2 von Neumann reflection

Our polar-diagram analysis suggests that von Neumann reflections of incident rarefaction shocks do not occur (just like Mach reflections), as the incident and the reflected wave curves do not intersect at all. In other words, together with the result of the previous section, triple-point patterns with three rarefactions waves appear to be disallowed.

Limiting to incident compression shocks for which von Neumann reflections are possible, the question can be raised if intersections between the incident and the reflected wave curves exist such that reflected wave is not an oblique shock, as a result of non-classical phenomena. Our numerical study indicates that this kind of non-classical von Neumann reflection does not occur. Note, however, that even if a similar configuration would be mathematically admissible, it should be disregarded for the following reason. In addition to being geometrically irregular (in the above sense), the extra incoming wave, namely a pure wave fan or a composite wave, would imply supersonic flow within or downstream of the wave itself, thus it would require the presence of a
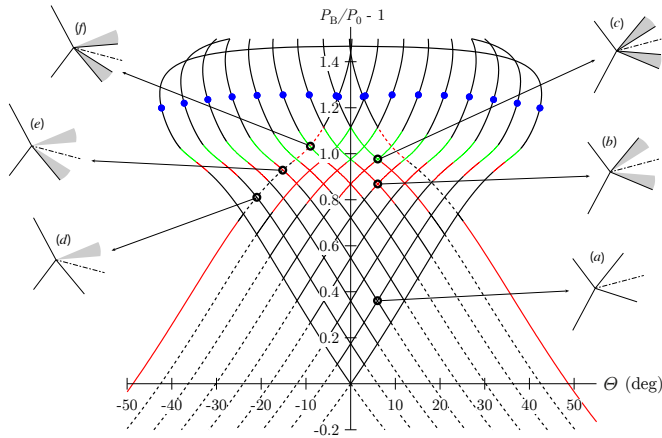
FIGURE 5.16. Pressure–deflection diagram for the Guderley reflection in a polytropic van der Waals gas with $c_v/R = 57.69$ and simplified sketches of the reflection pattern. Upstream state: $s_0 = s(0.74P_c, 2.5v_c)$, $v_0 = 1.1v_c$, $M_0 = 1.15$. Legend: —— shock, - - - fan, - - - fan/shock, • downstream sonic point.

suitable upstream boundary condition that can generate and maintain the wave, which is apparently not the case here.

5.3.2.3 Vasil'ev and Guderley reflections

By the same arguments of the previous section, we exclude the case of incoming fans from our discussion. It is possible, in principle, that the additional outgoing wave (F in figures 5.5 and 5.6) is not a pure fan, but rather a shock wave or a composite wave. However, after an extensive research in the parameter space of the incident shock, non-classical Guderley or Vasil'ev reflection patterns with outgoing composite waves were not found to occur.

It is remarkable that in the case of incident rarefaction shocks, the Guderley reflection appears to be the only alternative to the regular reflection, see figure 5.16. Our analysis indicates that the sonic points on the incident and reflected shock polars occur approximately at the same pressure, so that the additional wave curve drawn from the sonic point of the reflected curve intersects the incident curve along its supersonic branch, yielding a Guderley pattern. Note that each acoustic wave involved in the flow pattern at the node of a rarefaction Guderley reflection carries an opposite pressure jump with respect to its classical counterpart, namely each oblique shock is rarefactive rather than compressive and the additional wave fan is compressive rather than rarefactive.

5.3.3 Cross node

Some of the most relevant configurations of non-degenerate cross nodes in the non-classical gasdynamic regime are shown below. Figure 5.17 illustrates possible scenarios corresponding to incident compression shocks. The "network" of wave curves shown in figure 5.17 is obtained in the following way. First the left-running and right-running incident curves are drawn. For each of these curves, at specified incident-shock conditions (e.g., deflection angles) we plot the opposite-family wave curve from the corresponding downstream states. It is therefore possible to analyse several cross-node patterns originating from a given upstream flow state.

We first note, by examining the general shape of the wave curves, that only compression waves can be generated at the node with incident compression shocks (unless one of the incident shocks is a strong shock with supersonic downstream state).
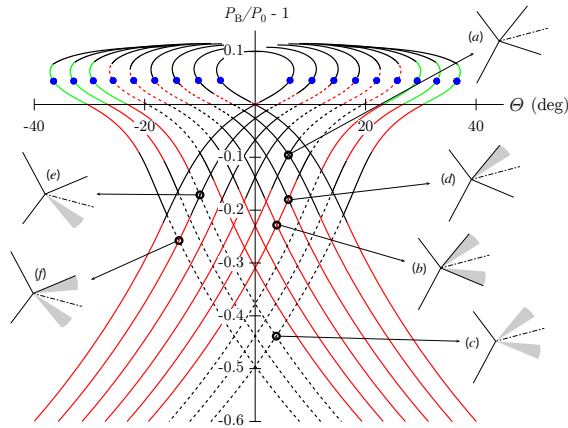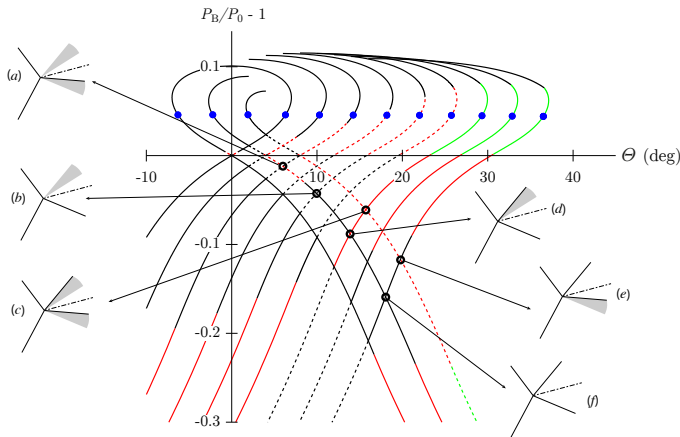
114

FIGURE 5.17. Pressure–deflection diagram for the cross-node interaction in a polytropic van der Waals gas with $c_v/R = 57.69$ and simplified sketches of the cross-node pattern. Upstream state: $s_0 = s(0.74P_c, 2.5v_c)$, $v_0 = 4.0v_c$, $M_0 = 1.5$. Legend: —— shock, —— shock/fan, - - - shock/fan/shock, - - - fan, - - - fan/shock, • downstream sonic point.

Case a yields the qualitative pattern found in classical gasdynamics. Cases b and c are non-classical examples in which the outgoing waves are composite waves of the same kind. This occurs when the flow deflection (or the pressure jump) across the incident shocks is similar (in this sense, the resulting pattern, on each side of the slip line, resembles that of a regular reflection with similar incident-shock conditions). In a wide range of incident-shock conditions, the two outgoing acoustic wave can be of different types. In case d, for instance, one oblique shock and one fan are generated. Case e corresponds to a combination of compression fan and composite shock/fan wave and finally, for case f, a fan/shock wave together with a shock/fan/shock wave are observed.

In the non-classical framework, it is also possible that a pair of oblique rarefaction shocks interact forming a cross-node. Exemplary scenarios are shown in the example of figure 5.18. From the polar-diagram analysis it appears that only rarefaction waves can be generated at the node with incident rarefaction shocks. Configurations that are symmetrical, in terms of outgoing wave types, are those labelled a, b and c; these correspond to couples of outgoing rarefaction shocks, shock/fan waves and fans, respectively. Further possible configurations of the outgoing waves are the rarefaction shock–shock/fan (d), the shock–fan (e) and the fan–shock/fan (f) combinations.

The last cross-node scenario is that of a compression shock interacting with a rarefaction shock, see figure 5.19. By examining the shape of the wave curves, it is seen that the fluid particles passing though the incident compression shock must successively go through a rarefaction wave; the opposite holds if the incident rarefaction shock is crossed. With reference to figure 5.19, possible combinations of outgoing waves at the cross node are (each couple is of the form rarefaction wave–compression wave): fan/shock–fan (a), shock–fan (b), fan/shock–shock/fan (c), shock–shock/fan (d), fan/shock–shock (e), shock–shock (f).

5.3.4 Overtake node

In the classical gasdynamic context, an overtake-node formed by two incoming compression shocks can give rise to either two outgoing shock waves or to an oblique shock and a Prandtl-Meyer fan. In theory, in the non-classical framework many different outcomes can be expected, owing to the comparatively higher degree of freedom in the choice of the incoming waves curves. In practice,
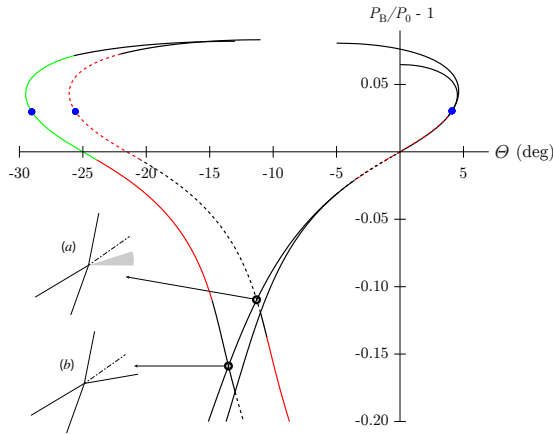
FIGURE 5.18. Pressure–deflection diagram for the cross-node interaction in a polytropic van der Waals gas with $c_v/R = 57.69$ and simplified sketches of the cross-node pattern. Upstream state: $s_0 = s(0.74P_c, 2.5v_c)$, $v_0 = 1.1v_c$, $M_0 = 1.5$. Legend: —— shock, —— shock/fan, - - - shock/fan/shock, - - - fan, - - - fan/shock, ● downstream sonic point.

FIGURE 5.19. Pressure–deflection diagram for the cross-node interaction in a polytropic van der Waals gas with $c_v/R = 57.69$ and simplified sketches of the cross-node pattern. Upstream state: $s_0 = s(0.74P_c, 2.5v_c)$, $v_0 = 1.1v_c$, $M_0 = 1.5$. Legend: —— shock, —— shock/fan, - - - shock/fan/shock, - - - fan, - - - fan/shock, - - - fan/shock/fan, ● downstream sonic point.

however, the requirement that the two incoming shocks are of the same wave family (in contrast to the cross-node) is seen to significantly decrease the possible outgoing-wave patterns.

Our investigation in the parameter space of the upstream state (ahead of the forerunner shock) and flow deflections across the two incoming shocks yielded the following combinations of outgoing oblique waves: two oblique shocks (transmitted and reflected), a transmitted oblique shock along with a reflected a Prandtl-Meyer fan, two Prandtl-Meyer fans (transmitted and reflected). Apart from the latter configuration, the admissible scenarios (in term of wave structure, without considering the pressure variation) coincide with the classical ones. Of course a new feature is the possibility of considering rarefaction shocks in the overtake-node configuration.
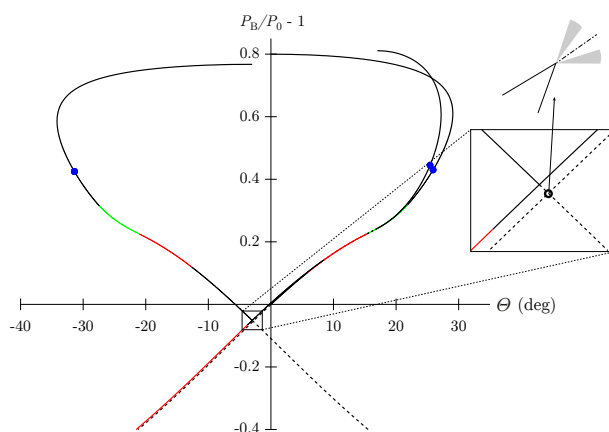
FIGURE 5.20. Pressure–deflection diagram for the overtake-node interaction in a polytropic van der Waals gas with $c_v/R = 57.69$ and simplified sketches of the overtake-node pattern. Upstream state: $s_0 = s(0.74P_c, 2.5v_c)$, $v_0 = 1.05v_c$, $M_0 = 1.4$. Legend: —— shock, —— shock/fan, - - - shock/fan/shock, - - - fan, - - - fan/shock, • downstream sonic point.

Figure 5.20 shows an exemplary pressure-deflection diagram corresponding to the overtake of two rarefaction shocks. Case a features a transmitted rarefaction shock and a reflected compression fan, whereas case b both outgoing oblique waves are rarefaction shocks. In this sense, the two configurations just described are the opposite, in terms of pressure variation across the oblique waves, of the classical overtake-node configurations.

The transmitted wave need not necessarily be of the same compression/rarefaction type as the forerunner shock. This situation is depicted in figure 5.21, where a compression shock (forerunner) overtakes a rarefaction shock. The overall deflection across the incident shocks is chosen such that the outgoing waves are rarefaction fans.

We did not determine theoretically whether it is possible that two shocks overtake forming an outgoing composite wave, but based on the polar-diagram analysis it appears that these configurations are not possible.

5.4 Concluding remarks

Steady shock reflections and interactions in the non-ideal gasdynamic regime were investigated, focusing on the inviscid flow pattern about the point of intersection of oblique waves. The local solution in the neighbourhood of the node is constant along each ray emanating from the node itself, namely it exhibits no length scale. In other words, about the node a set of uniform states is separated by centred oblique waves or slip lines. The configurations analysed include all sort of steady shock reflections (regular, Mach, von Neumann, Guderley, Vasil'ev) and two primary shock-interaction patterns, namely the cross node and overtake node (both in their non-degenerate form). The presented results complement, to a certain extent, the theoretical framework established in §4 and together provide a more accurate description of confined flows, where oblique shocks generated by ramps interact with each other or with an opposing solid wall.

Shock reflection and interactions in the classical and non-classical gasdynamic regime were treated separately. In the classical case, for which the theory is well-established, the attention was drawn to the occurrence of non-ideal oblique shocks in the reflection or interaction pattern. It

FIGURE 5.21. Pressure–deflection diagram for the overtake-node interaction in a polytropic van der Waals gas with $c_v/R = 57.69$ and simplified sketches of the overtake-node pattern. Upstream state: $s_0 = s(0.74P_c, 2.5v_c)$, $v_0 = 2v_c$, $M_0 = 1.5$. Legend: —— shock, —— shock/fan, - - - shock/fan/shock, - - - fan, - - - fan/shock, • downstream sonic point.

was shown that flow fields that locally involve only non-ideal oblique shocks, and thus provide an overall increase of the flow Mach number, are possible in the case of regular reflection, cross node or overtake node. Other configurations seemed to preclude this possibility based on the fact that they involve shock waves characterized by large flow deflections.

In the non-classical gasdynamic regime, the primary interest was on the structure of the shock reflection or interaction at the node. The admissibility of pressure-decreasing shocks, pressure-increasing Prandtl-Meyer fans and of composite waves (either compressive or rarefactive) suggested the existence of a variety of wave-interaction patterns that has no counterpart in the classical gasdynamic regime. An overview of the possible outcomes was given. For a wide range of incident-shock conditions, the regular reflection of compression as well as rarefaction shocks was shown to the achieved by means of reflected wave fans or composite waves. Similarly, in the Mach reflection of compression shocks, the necessary matching of the pressure and flow direction across the outgoing slip line may require a reflected composite wave. For example, conditions were reported under which an oblique shock reflects as a centred fan or shock/fan wave (regular reflection) or also as fan/shock or shock/fan/shock wave (both regular and Mach reflections).

In analogy with the two-shock and three-shock theories by von Neumann, the theories describing these non-classical flow patterns were named as two-wave and three-wave theories, respectively. Four-wave patterns (Guderey or Vasil'ev reflections) were also considered, but in this case no composite wave was found to occur, so that the non-classical theory is formally identical to the classical one if one replaces compression waves with rarefaction waves and vice versa.

Our investigation pointed out an asymmetry between the reflection of compression and rarefaction shocks (in contrast with the transonic theory, see recent results by Kluwick & Cox 2018b). Firstly, it appears that Mach reflections are not possible when the incident shock is pressure-decreasing. As a partial explanation of the observed configurations, it was demonstrated that the pressure jump across two successive rarefaction shocks cannot exceed the pressure jump corresponding to the normal rarefaction shock from the same initial state. The present suggestion may be of help in the proof or disproof of the existence of Mach reflections for incident rarefaction shocks. More in general, triple-point patterns containing three rarefaction waves were not observed, as the reflected wave curves do not intersect the incident one in the pressure-deflection
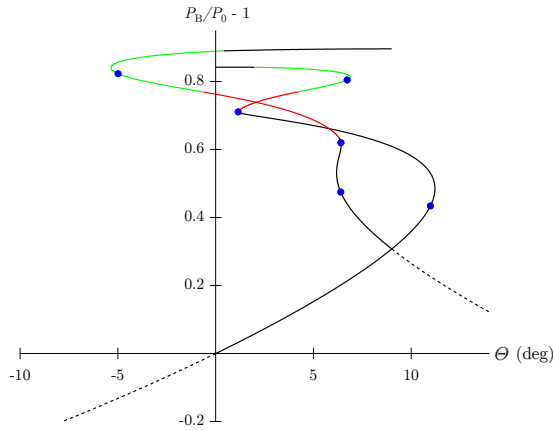
FIGURE 5.22. Pressure–deflection diagram for the Mach reflection in a polytropic van der Waals gas with $c_v/R = 57.69$. Upstream state: $s_0 = s(0.74P_c, 2.5v_c)$, $v_0 = 3.5v_c$, $M_0 = 1.221$. Legend: —— shock, —— shock/fan, - - - shock/fan/shock, - - - fan, • downstream sonic point.

plane (i.e., von Neumann reflections of rarefaction shocks are not possible as well). As a result, four-wave reflections appear then to be the only alternative to the regular reflection of rarefaction shocks. Numerical analysis indicates that only Guderley reflections occur as the sonic points on the incident and reflected wave curves have approximately the same pressure. This contrasts with the compression-shock case, where both Guderley and Vasil'ev reflections are possible. The flow pattern in a rarefaction Guderley reflection is qualitatively similar to the one observed in ideal gases, except that each wave carries an opposite pressure jump.

In the shock-interaction framework, a wide variety of non-classical cross-node patterns was described, as representative of the possible scenarios for the interaction of a pair of compression shocks, a pair of rarefaction shocks and one compression along with a rarefaction shock. For the overtake-node configuration, our analysis revealed a restricted amount of possible patterns, none of which include composite waves.

Some remarks concerning the presented results are as follows:

(i) this work is intended to provide an overview of the theory of shock reflections and interactions in non-ideal flows, in particular on the modifications to the classical theory that follow from the appearance of non-classical waves. This justifies the choice of presenting selected wave patterns, rather than performing a rigorous analysis on each of the admissible configurations.

(ii) The outgoing-wave configurations presented in this work are a subset of those realizable at a sharp trailing edge (e.g. of an airfoil or turbine blade) where two different supersonic streams interact. When the thermodynamic and kinematic state of two streams can be independently chosen, there is no constraint on the configuration of the outgoing waves. Thus, in principle, every combination among the ten possible types of acoustic wave (compression or rarefaction shock, fan, shock/fan and fan/shock, compression shock/fan/shock and rarefaction fan/shock/fan) can be generated.

(iii) Results were obtained using the van der Waals model with non-dimensional isochoric specific heat set to $c_v/R = 15$ for the classical regime and to $c_v/R = 57.69$ for the non-classical one. The analysis of §4 confirms, on the one hand, that non-ideal oblique shocks may occur in fluids exhibiting $\Gamma < 1$ following the same mechanism and, on the other hand, that fluids

exhibiting a negative-Γ region in the vapour phase display the same qualitative behaviour in terms of wave-curve configurations, regardless of the specific choice of the thermodynamic model. Thus, we believe that the present findings have a more general validity and that the same results, namely the same intersections of wave curves in the pressure-deflection diagram, can be reproduced by diverse thermodynamic models (in particular reference EoS in Span-Wagner form).

(iv) Wave curves in the (P_B, Θ)–plane are bounded and non-monotonic, therefore they may have multiple intersections or no intersection at all. In the context of shock reflections, the case of no intersections between the incident and the reflected wave curves leads to Guderley/Vasil'ev patterns, in which the reflected wave, in the neighbourhood of the node, is in fact an incoming shock with sonic downstream state and an additional wave fan is present. The problem of multiple intersections is well-known in classical gasdynamics and it is further amplified by non-classical effects. If the wave curve branch is bounded and it intersects the $\Theta = 0$ axis, then at least two intersections are possible. A subsonic regular reflection is unstable to small perturbations (Teshukov, 1989). However, it is possible that multiple supersonic intersections occur, as the sonic point can occur at higher pressures than the detachment point (see, e.g., the incident wave curve in figure 5.13). Some of these patterns may not be admissible as the reflected wave includes oblique shocks that would be unstable to transverse perturbations of the their front (Fowles, 1981; Henderson & Menikoff, 1998). Another example of non-uniqueness is when the wave curves intersect yielding both a regular reflection and a Mach reflection (see, e.g., cases a_1 and a_2 in figure 5.13). In classical gasdynamics, experiments indicate that hysteresis can occur in this dual-solution domain (see, e.g., Ivanov *et al.*, 1995). In the non-classical gasdynamic framework, because of the peculiar shape of the wave curves, it is also possible to observe two distinguished Mach-intersections, as shown in figure 5.22. The problem of multiple intersections may be resolved by considering the local stability of the solution and the global boundary conditions.

APPLICATION: FLOW THROUGH ORC TURBINE VANES

This chapter presents a realistic application case of the theory of non-ideal supersonic flows developed in this thesis. Turbine cascades of high-temperature Organic Rankine Cycle power systems, which at present adopt moderately complex (non-BZT) working fluids, operate close to the saturation curve and critical point, where it is possible that $\Gamma < 1$. Potential advantages and drawbacks of turbine blades designed for operating conditions featuring a non-monotonic variation of the Mach number through the expansion process and non-ideal oblique waves downstream of the trailing edge are discussed. In contrast to ideal-gas flows, for a given pressure ratio across the cascade, the flow field and the turbine performance are found to be highly dependent on the thermodynamic state at the turbine inlet, in both design and off-design conditions. A potentially advantageous design is proposed, which is characterised by stationary points of the Mach number at the blade trailing edge, thus inducing a nearly uniform outlet Mach number distribution in the stator-rotor gap with a low sensitivity to slight variations in the outlet pressure.

Selected contents from:

Romei A. & Vimercati, D. & Persico, G. & Guardone, A. 2018 Non-ideal compressible flows in supersonic turbine cascades. Submitted to: *J. Fluid Mech*.

6.1 Introduction and theoretical background

In power system exploiting low-to-moderate temperature sources, the choice of complex organic fluids allows for an optimal design of the turbine and a better match of temperature profiles between the hot source and the corresponding cycle heating (Colonna *et al.*, 2015; Macchi & Astolfi, 2016; Meroni *et al.*, 2018). At present, the majority of ORC plants feature cycles with relatively mild maximum pressures and temperatures (subcritical cycles). In these conditions, even if the expansion through the turbine may partly occur in the non-ideal gasdynamic regime, non-ideal effects are, in fact, not observed (Hoffren *et al.*, 2002; Persico, 2017). Due to the combination of high expansion ratio and low enthalpy drop, ORC turbines are usually composed by a few supersonic or transonic blade rows, with the first-stage nozzle cascade carrying the largest pressure ratio and severe supersonic flow regime.

The typical flow field related to the expansion through the first stator of an ORC system is shown in figure 6.1. The blade is characterized by a large leading-edge region that acts as a converging section upstream of the section with minimum cross-sectional area (throat) and a diverging section downstream of the throat. The curved shape of the rear suction side imposes to the flow a significant unguided turning. The expansion corresponding to this turning process results in a severe over-speed, which ultimately generates a compression wave on the rear suction side of the blade, where the fish-tail shock originated at the trailing edge of the adjacent blade impinges. The two compression waves coalesce in a single strong shock at almost half axial chord downstream of the trailing edge generating a strong azimuthal pressure gradient, which results in massive entropy production.

Several studies (Schuster *et al.*, 2010; Lai *et al.*, 2011) indicate that a potential gain in efficiency may be achieved by employing high-temperature ORCs, in particular supercritical cycles. Within this framework, the occurrence of non-ideal effects cannot be excluded. An example can be found in the work of Colonna *et al.* (2008*b*), where some numerical simulations display a non-monotonic Mach number in the blade channel. This result, however, was not commented in light of its potential influence on the aerodynamic performance of the cascade. Whether non-ideal effects in the expansion process can affect the turbine performance and design is still unclear.

The present study contributes to the understanding of non-ideal flows evolving in supersonic nozzle cascades, by showing the role of non-ideal effects in the turbine performance and discussing their design implications. To this end, exemplary flows of siloxane MM (hexamethyldisiloxane, $C_6H_{18}OSi_2$) in nozzle cascades are considered and compared. MM is a molecularly complex fluid currently employed in ORC power plants (Colonna *et al.*, 2015). The results are shown to be of general validity and thus may be extended to most fluids relevant to ORC field. In the cases analysed here, the nozzle operates in the non-ideal gasdynamic regime. However, depending on the upstream stagnation conditions, two very different operating regimes can be established: one mirrors the ideal-gas scenario and is obtained with relatively dilute conditions at the cascade inlet; the other one, obtained for high-pressure inlet conditions, is characterised by non-ideal effects. For both operating regimes, a parametric study in which the boundary conditions of the turbine cascade are changed is performed with the aim of assessing the off-design behaviour.

The existence of two distinguished operating regimes of the nozzle cascade can be anticipated from the theoretical studies presented in chapters §3-§5. We offer a brief summary of the main results pertaining to expanding flows through a turbine cascade. These results are presented here in the form of parametric studies covering the theories of quasi-one-dimensional flows and oblique waves (Prandtl-Meyer waves and oblique shock waves); the thermodynamic location of the selected states is illustrated in the (T, s) and (P, v) diagrams reported in figure 6.2. The fluid considered throughout this chapter, namely the siloxane MM, is modelled using the state-of-the-art multi-parameter equation of state formulated by Thol *et al.* (2016).
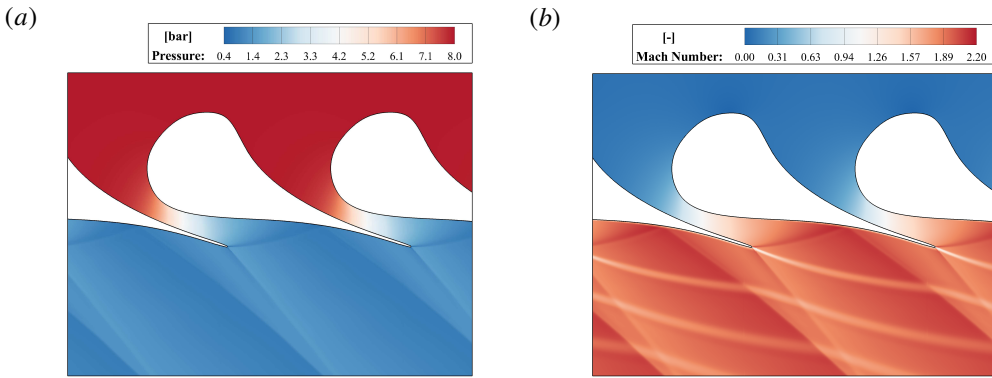
FIGURE 6.1. Pressure field (a) and Mach number field (b) for the expansion of fluid MM (thermodynamic model from the REFPROP library) in a representative turbine cascade. The upstream stagnation pressure and temperature are $P_0^t = 8$ bar and $T_0^t = 272\,°C$, respectively. The outlet static pressure is $P_1 = 1.08$ bar. Details on the numerical simulation in §6.2.1.
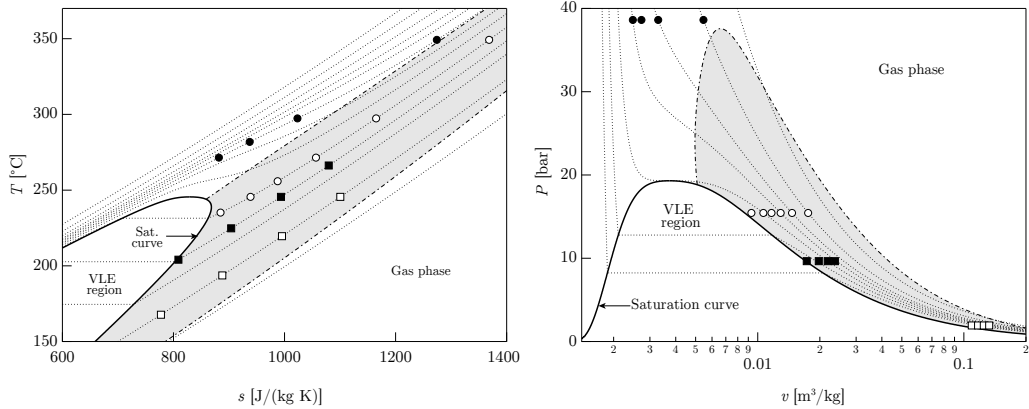

FIGURE 6.2. Thermodynamic diagrams for MM (properties from the REFPROP library) showing the states used in the parametric studies: ■ stagnation conditions for isentropic nozzle flows in figures 6.3(a) and 6.4(a); ● stagnation conditions for isentropic nozzle flows in figures 6.3(b) and 6.4(b); □ upstream thermodynamic state for Prandtl-Mayer waves of figure 6.5(a) and for oblique shock waves of figure 6.6(a); ○ upstream thermodynamic state for Prandtl-Mayer waves of figure 6.5(b) and for oblique shock waves of figure 6.6(b). Dotted lines ($\cdots$) represent different isobars (left figure) or isotherms (right figure). Dash-dotted lines ($\cdot - \cdot$) identify $\Gamma = 1$; shaded area $\Gamma < 1$.

Steady quasi-one-dimensional flow (see §3) is recalled as representative of the expansion process through a variable-area duct (inviscid and with constant total enthalpy). Figure 6.3 shows the distribution of the Mach number for different stagnation conditions chosen along the same isobaric line, which is $P^t = 0.5\,P_c$ in figure 6.3(a) and $P^t = 2\,P_c$ in figure 6.3(b), where P^t is the stagnation pressure and P_c is the critical pressure. Despite $\Gamma < 1$ at the selected stagnation states, at relatively low stagnation pressures and high temperatures (figure 6.3(a)), most of the expansion occurs in dilute-gas conditions. Thus, the distributions of the Mach number are qualitatively identical and also quantitatively very similar to those computed form the ideal-gas model, which depend on the pressure ratio P/P^t only. The ideal-gas limit curves hereafter are all obtained by setting $\gamma = c_{p,\infty}(T_c)/c_{v,\infty}(T_c)$, where $c_{p,\infty}$ and $c_{v,\infty}$ are the specific heats in the ideal-gas limit

125
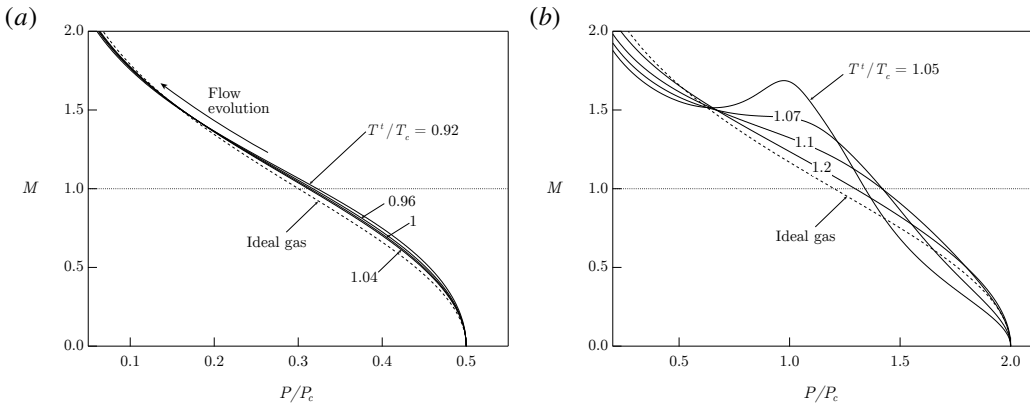
FIGURE 6.3. Mach number distribution for quasi-one-dimensional flow of fluid MM with stagnation pressure (a) $P^t = 0.5\,P_c$ and (b) $P^t = 2\,P_c$; each solid line corresponds to a different value of the stagnation temperature T^t (thermodynamic properties from REFPROP), while dotted lines are obtained from the ideal-gas model of MM.

and T_c is the critical temperature. Using the nomenclature established in §3, the isentropic pattern of each stagnation state in figure 6.3(a) is $\mathscr{S}^I$.

The effects of the non-ideal thermodynamic behaviour of the fluid can be appreciated by selecting thermodynamic states in the proximity of the critical point or in the supercritical region. The scenario observed in figure 6.3(b), representative of the flow evolution in the non-ideal gasdynamic regime, involves not only a marked quantitative difference with respect to its ideal-gas counterpart, but also important qualitative differences. At the selected stagnation pressure ($P^t = 2\,P_c$), isentropic expansion from near-to-critical isentropes may exhibit extrema in the Mach number, i.e. isentropic pattern $\mathscr{S}^{NI}$ (see case $T^t = 1.05\,T_c$). For such high-density stagnation states, a noticeable departure from the ideal-gas trend is observed also for isentropic expansions of type $\mathscr{S}^I$.

Figure 6.4 reports the distribution of the area ratio A/A^*, where A^* is the critical area (at which $M = 1$), for different stagnation conditions chosen along the same isobaric lines as above, namely $P^t = 0.5\,P_c$ in figure 6.4(a) and $P^t = 2P_c$ in figure 6.4(b). In both cases, the distribution of the area ratio is qualitatively similar to that of the ideal-gas limit. However, significant quantitative differences are seen in the exemplary non-ideal case depicted in figure 6.4(b). As an example, expansion from stagnation conditions up to $A/A^* = 2$ corresponds to an expansion ratio $\beta = P^t/P = 2.76$ from $T^t = 1.05\,T_c$ and to $\beta = 6.78$ in the ideal-gas limit ($T^t \rightarrow \infty$ at fixed P^t). This should be compared to the case $P^t = 0.5\,P_c$, for which the same area ratio $A/A^* = 2$ corresponds to $\beta = 6.15$ from $T^t = 1.05\,T_c$. An alternative interpretation is connected with the design of the diverging portion of a nozzle aimed at realizing a given exit pressure ratio. The same exit pressure ratio is attained with a considerably larger exit-to-throat area ratio if expanding from high stagnation-pressure states, thus involving severe non-ideal gasdynamic effects.

Next, oblique waves are examined, as representative of the turning processes of a supersonic stream that can possibly occur at the trailing-edge of the turbine blades and in the rear blade section. Figure 6.5(a) reports the downstream Mach number against the flow deflection angle ϑ across Prandtl-Meyer waves, computed for a fixed upstream pressure $P_A = 0.1\,P_c$ and Mach number $M_A = 2$, and different values of the upstream temperature T_A. At the selected upstream states, $\Gamma_A = 0.96 \div 0.98$. In this range, the impact of non-ideal conditions is small enough that the actual features of Pradtl-Meyer waves are qualitatively similar to those computed from the ideal-gas model, despite a slight quantitative difference is still observed. Note, also, that Prandtl-
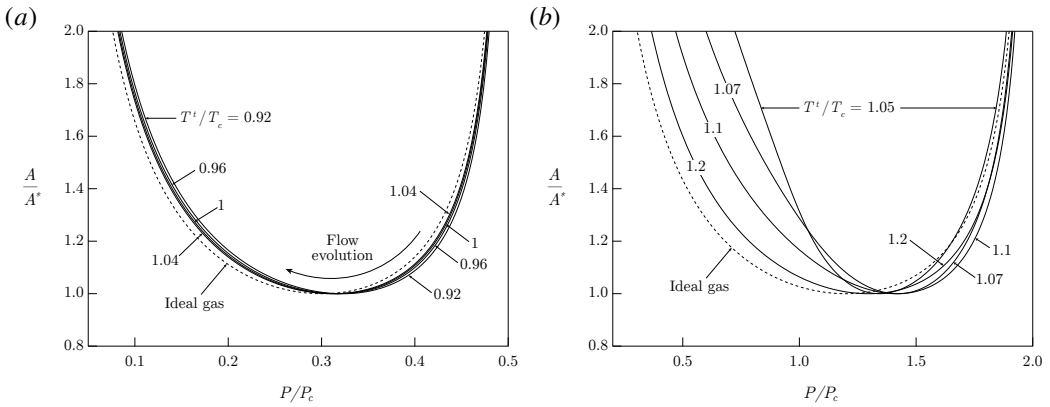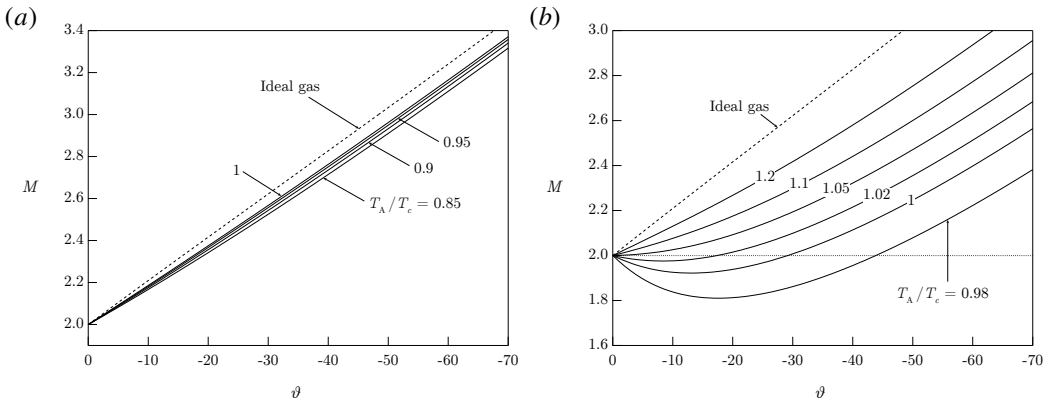
FIGURE 6.4. Area ratio distribution for quasi-one-dimensional flow of fluid MM with stagnation pressure (*a*) $P^t = 0.5\,P_c$ and (*b*) $P^t = 2\,P_c$; each solid line corresponds to a different value of the stagnation temperature T^t (thermodynamic properties from REFPROP), while dotted lines are obtained from the ideal-gas model of MM.
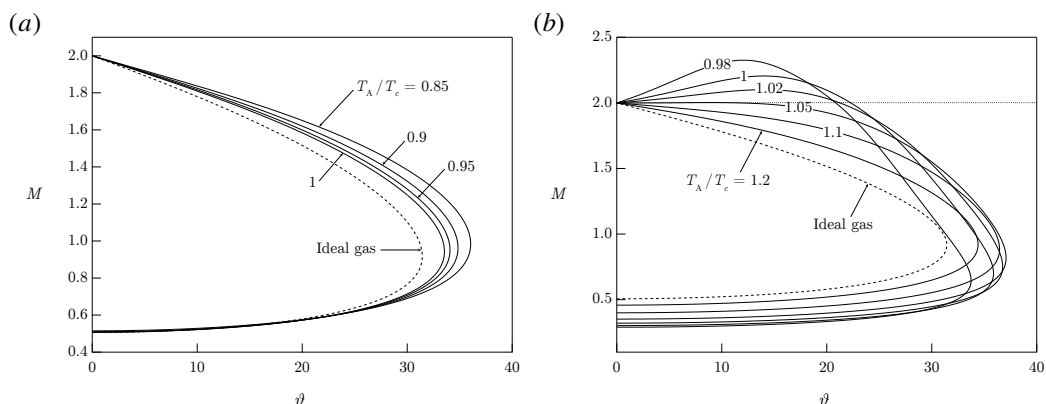

FIGURE 6.5. Variation of the Mach number with the wave deflection angle across Prandtl-Meyer waves in fluid MM with upstream Mach number $M_A = 2$ and pressure (*a*) $P_A = 0.1\,P_c$ and (*b*) $P_A = 0.8\,P_c$, each solid line corresponds to a different value of the upstream temperature T_A (thermodynamic properties from REFPROP), while dotted lines are obtained from the ideal-gas model of MM.

Meyer waves are expansion waves and therefore the process drives the flow towards more dilute thermodynamic conditions. The non-ideal turning of a supersonic stream across Prandtl-Meyer waves is depicted in figure 6.5(*b*), which is obtained by setting the state upstream of the wave to $P_A = 0.8\,P_c$ and $M_A = 2$, while different values of T_A are considered. Remarkable quantitative and qualitative differences can be observed, most importantly the possibility that the Mach number decreases across the rarefaction wave, which is in contrast with the ideal-gas behaviour. For later convenience, Prandtl-Meyer waves featuring a decrease of the Mach number are referred to as non-ideal Prandtl-Meyer waves. As discussed in §4.4.1, the non-monotonic variation of the Mach number within Prandtl-Meyer waves stems from thermodynamic states satisfying $J > 0$ during the expansion (see also Cramer & Crickenberger 1992).

An analogous study is performed for oblique shock waves, see figure 6.6. Figures 6.6(*a*) and 6.6(*b*) are generated using the same upstream states of figures 6.5(*a*) and 6.5(*b*), respectively. Although the compression across the shock may bring the flow towards more dense and therefore

(a)

(b)

FIGURE 6.6. Variation of the Mach number with the wave deflection angle across oblique shock waves in fluid MM with upstream Mach number $M_A = 2$ and pressure (a) $P_A = 0.1\,P_c$ and (b) $P_A = 0.8\,P_c$; each solid line corresponds to a different value of the upstream temperature T_A (thermodynamic properties from REFPROP), while dotted lines are obtained from the ideal-gas model of MM.

non-ideal thermodynamic conditions, at relatively low upstream pressures such as figure 6.6(a), non-ideal effects are in fact not observed, except at the quantitative level and to a limited extent. On the contrary, in figure 6.6(b) it is possible to observe shock curves encompassing non-ideal oblique shocks (see §4.4.2) that feature an increase of the flow Mach number. This phenomenon is the compression (and discontinuous) counterpart of the decrease of the Mach number in the non-ideal Prandtl-Meyer waves depicted in figure 6.5(b).

In the subsequent section, numerical simulations of supersonic nozzle cascades are presented. The core of the present chapter is the analysis presented in §6.2.4 and §6.2.5 for each operating regime occurring in the nozzle cascade.

6.2   Gasdynamics of nozzle cascades in the non-ideal regime

In this section, the flow field within a linear nozzle cascade operating in the non-ideal gasdynamic regime is examined by means of numerical simulations. The computational flow solver is described in §6.2.1. The blade configurations used in this study are presented in §6.2.2 and the grid-convergence assessment in §6.2.3. Expansion through states featuring $\Gamma < 1$ can possibly present very different behaviours, according to the occurrence of diverse non-ideal effects. Three exemplary operating conditions (each consisting of a design point and selected off-design cases) are presented in §6.2.4 and §6.2.5 to illustrate the larger variability and diversity of the flow evolution offered by the non-ideal thermodynamics.

6.2.1   Computational flow model

Numerical simulations are carried out with ANSYS-CFX 18.1®. Stagnation pressure and temperature (P_0^t, T_0^t) are set as inlet boundary conditions. Axial flow is prescribed at the inlet. At the outlet, an average static pressure P_1 is imposed. Local pressure differences of 5% are allowed at the exit. Moreover, the outlet domain is placed at four axial chords downstream of the trailing edge to avoid spurious pressure wave reflections. Since only blade-to-blade effects are of interest, quasi-three-dimensional simulations are carried out by considering a straight stream-tube around the midspan. The employed turbulence model is $k - \omega$ SST, whose boundary conditions are set

as Turbulence Intensity ($TI = 5\%$ for all simulations) and eddy viscosity ratio ($\mu_t/\mu = 100$ for all simulations). The cascade Reynolds number, $Re = \rho_1 u_1 c/\mu_1$, where ρ_1, μ_1 and u_1 are the massflow-averaged density, dynamic viscosity and velocity, respectively, evaluated at the blade outlet and c is the blade chord, is high enough ($Re = 10^7 \div 10^8$ in all simulations) to assume fully-turbulent boundary layer along the whole blade.

The implemented thermodynamic model is the Span-Wagner equation of state by Thol *et al.* (2016). A Look-up-Table (LuT) approach is used to speed up the evaluation of the thermodynamic properties (see, e.g., Pini *et al.*, 2015). Thermodynamic tables are built by referring to the NIST REFPROP® database (Lemmon *et al.*, 2013), which also provides dedicated correlations for transport properties (Meier *et al.*, 2004; Perkins *et al.*, 2013). High-resolution Total Variation Diminishing (TVD) schemes (Barth & Jespersen, 1989) are employed in the discretization of both flow and turbulence equations. A central difference scheme is instead adopted for the diffusive flux.

Computations are performed on structured hexahedral meshes. A proper cell clustering near blade walls is imposed to ensure $y^+ < 1$, thus avoiding the introduction of wall functions in the solution.

6.2.2 Blade configuration and operating conditions

The turbine cascades used in the following study result from an optimization procedure aimed at minimizing the entropy production, starting from the baseline blade shown in figure 6.1. The baseline blade geometry was initially conceived for a combined heat and power application, featuring MDM as working fluid (Colonna *et al.*, 2008*b*). As the shock pattern of figure 6.1 is strongly influenced by the peculiar shape of the blade, several exercises of shape-optimization were carried out in order to reduce as much as possible the intensity of the main compression shock (Rodriguez-Fernandez & Persico, 2015; Vitale *et al.*, 2017). However, the fish-tail shock is unavoidable due to the finite thickness of the trailing edge, which should be preserved to avoid issues in the blade manufacturing. The shape-optimization procedures proved to be successful in dealing with such cascade, all methods leading to qualitatively similar optimal shapes. Indeed, all optimal blades feature a higher curvature in the diverging channel and an almost straight profile in the rear part of the blade. In this way, the main compression shock wave is almost eliminated, adapting the nozzle cascade geometry to the expansion process on which the optimization is performed.

The optimization procedure used in this work is based on a global surrogate strategy coupled with evolutionary algorithms, augmented with an on-line training strategy of the surrogate model to increase locally its reliability. In the present work, the same computational flow model is employed both for the optimization and the following analyses. All optimizations were performed using the in-house design tool FORMA, see Persico (2017). The optimization is performed for three exemplary design conditions, namely I-DES, Ñ-DES and Ň-DES, reported in table 6.1 and depicted in the T–s diagram in figure 6.7.

The design case labelled I-DES recalls the same application, in terms of inlet and outlet thermodynamic conditions of the nozzle cascade, examined by Colonna *et al.* (2008*b*), but using MM as working fluid. The resulting optimal blade is qualitatively similar to the ones obtained with MDM by Rodriguez-Fernandez & Persico (2015) and Vitale *et al.* (2017). In these thermodynamic conditions, the flow evolution is similar to that of an ideal gas, thus the expansion inside the nozzle depends almost only on the expansion ratio and on the ratio between specific heats γ, which slightly differs between the two fluids. On this basis, I-DES and related off-design conditions I-OFF-i, $i = \{\beta_+, \beta_-, T_+^t, P_-^t\}$, are referred to as the ideal-like operating regime of the nozzle cascade.

Operating conditions Ñ-DES and Ň-DES are chosen to highlight non-ideal effects on the flow features arising in the proximity of the blade trailing edge, which are highly influential on the

Case Label	P_0^t [bar]	T_0^t [°C]	P_1 [bar]	β
I-DES	8.00	272	1.08	7.4
I-OFF-β_+	8.00	272	0.96	8.3
I-OFF-β_-	8.00	272	1.20	6.7
I-OFF-T_+^t	8.00	292	1.08	7.4
I-OFF-P_-^t	7.00	272	0.95	7.4
$\hat{\text{N}}$-DES	40.0	270	17.5	2.3
$\check{\text{N}}$-DES	40.0	270	12.5	3.2
$\hat{\text{N}}$-OFF-β_+	40.0	270	15.0	2.7
$\check{\text{N}}$-OFF-β_-	40.0	270	15.0	2.7
$\check{\text{N}}$-OFF-T_+^t	40.0	290	12.5	3.2
$\check{\text{N}}$-OFF-P_-^t	35.0	270	10.9	3.2

TABLE 6.1. Boundary conditions for the numerical simulations. P_0^t and T_0^t are the upstream stagnation pressure and temperature, respectively, P_1 is the downstream static pressure and $\beta = P_0^t/P_1$.
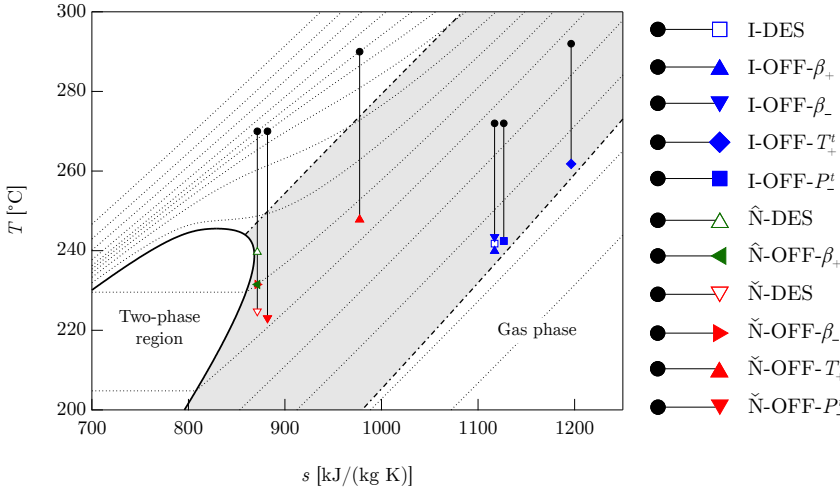
FIGURE 6.7. Temperature–specific entropy diagram showing the expansion processes considered in the present work. Thermodynamic properties from REFPROP. Dotted lines ($\cdots$) represent different isobars. Dash-dotted lines ($\cdot - \cdot$) identify $\Gamma = 1$.

overall cascade performance. Two peculiar operating conditions can be identified in which the Mach number at the trailing edge is close to a local maximum ($\hat{\text{N}}$-DES) or to a local minimum ($\check{\text{N}}$-DES). For convenience, these operating conditions along with the related off-design cases $\hat{\text{N}}$-OFF-β_+ and $\check{\text{N}}$-OFF-i, $i = \{\beta_-, T_+^t, P_-^t\}$, are referred to, in the following, as the non-ideal operating regime of the nozzle cascade.

The blades optimized for I-DES, $\hat{\text{N}}$-DES and $\check{\text{N}}$-DES are shown in figure 6.8. In the non-ideal gasdynamic regime, relatively small expansion ratios can generate large outlet Mach numbers, due to the low values of the speed of sound. As an example, operating condition $\hat{\text{N}}$-DES features $M \approx$ 1.8 at the nozzle exit with $\beta = 2.3$. Thus, converging-diverging shapes are mandatory to cope with the supersonic expansion. The resulting geometries are consistent with the quasi-one-dimensional theory. The selected design conditions are such that $A_e/A^* = 2.28$ for I-DES, $A_e/A^* = 1.57$ for
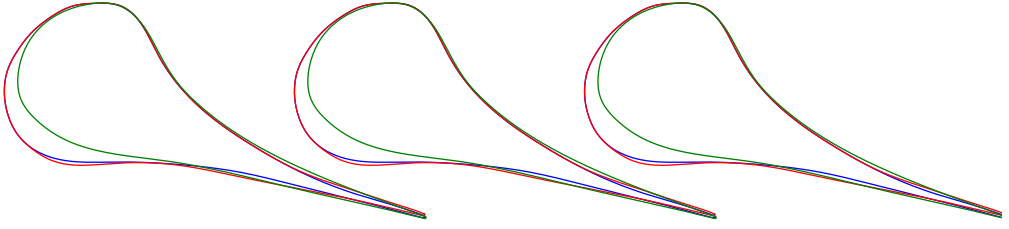
FIGURE 6.8. Optimized nozzle cascades for I-DES (——), Ñ-DES (- - -) and Ň-DES (——). The optimization is aimed at minimising the entropy production.
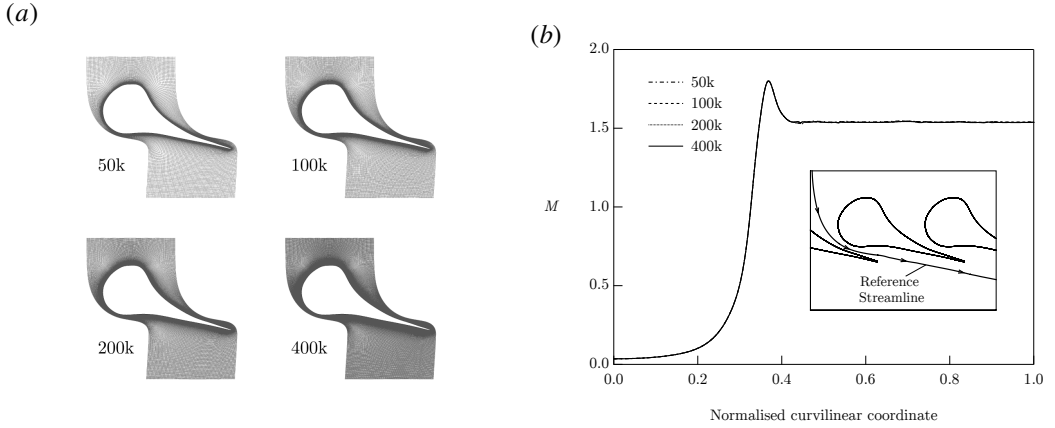
FIGURE 6.9. Mesh refinements (*a*) employed in the grid-convergence assessment and corresponding Mach number distributions (*b*) evaluated on a reference streamline. The assessment is performed with boundary conditions $P_0^t = 40\,\mathrm{bar}$, $T_0^t = 270\,^{\circ}\mathrm{C}$ and $P_1 = 12.5\,\mathrm{bar}$, corresponding to the exemplary expansion process of the non-ideal operating regime.

Ñ-DES and $A_e/A^* = 2.22$ for Ň-DES, where A_e is the equivalent-nozzle exit area. Note that the optimized blades for I-DES and Ň-DES are very similar, despite the significantly different expansion ratios. On the other hand, the optimal blade for Ñ-DES differs significantly from all the others due to the much smaller exit-to-throat area ratio.

6.2.3 Grid assessment

Mesh sensitivity analysis is carried out by resorting to four different grid refinements, consisting in 50k, 100k, 200k, 400k cells in the blade-to-blade plane, as shown in figure 6.9(a). Grid convergence is assessed on operating condition Ň-DES, detailed in §6.2.2. To evaluate the grid convergence, two criteria are considered. Firstly, the Mach number distribution along a reference streamline (approximately following the centreline of the blade channel), as shown in figure 6.9(b), is examined. No appreciable differences among the four meshes are detected. Secondly, we consider the kinetic energy loss coefficient, defined as

$$\zeta_S = \frac{h_{out} - h_{out,is}}{u_{out}^2/2}, \tag{6.1}$$

where h_{out} and $h_{out,is}$ are the mass flow averaged specific enthalpy and the isentropic specific enthalpy at the outlet of the domain, respectively, while $u_{out}^2/2$ is the mass flow averaged kinetic

(*a*)

(*b*)
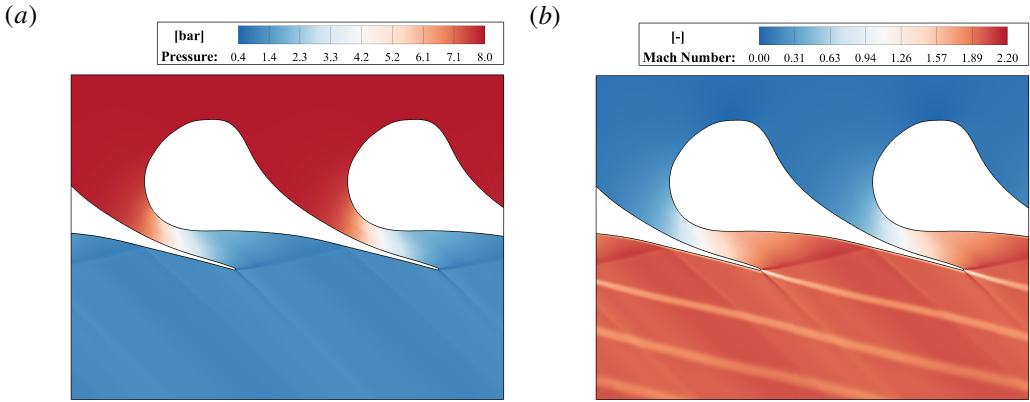
FIGURE 6.10. Pressure field (*a*) and Mach number field (*b*) for I-DES. The working fluid is MM.

energy at the outlet domain.

This coefficient accounts for all loss sources such as shock (and related shock-boundary layer interaction), mixing and viscous losses, thus giving an overall indication of cascade performance. The convergence of the kinetic loss coefficient towards the grid independent value allows establishing the convergence of the flow field from the integral perspective. It is found that the relative error with respect to the finest-grid value ($\zeta_S = 3.84\%$) is 0.32% for 50k cells, 0.20% for 100k cells and 0.03% for 200k cells. Therefore, grid convergence is achieved starting from the 200k mesh. For a better flow field resolution, numerical results presented in the following sections are obtained using the 400k mesh.

6.2.4 Ideal-like operating regime of nozzle cascades

We consider the converging-diverging nozzle optimized for the design condition I-DES. In addition to the design condition, cascade performance is also analysed by considering four different off-design expansions I-OFF-i, $i = \{\beta_+, \beta_-, T_+^t, P_-^t\}$. Each of these processes is detailed in table 6.1 and shown graphically in the (T, s)–plane of figure 6.7. Note that the stagnation temperature values used throughout this work lie within the thermal stability limit of the working fluid (Preissinger & Bruggemann, 2016; Keulen *et al.*, 2018).

Pressure and Mach number distributions for I-DES are reported in figure 6.10. The optimization, performed in such conditions, generates a nozzle cascade which features a smooth expansion process, characterized by a nearly uniform pressure field downstream of the cascade. A weak fish-tail shock stems from the trailing edge. Quantitatively, the nozzle cascade exhibits a kinetic energy loss coefficient $\zeta_S = 3.6\%$. This value is used as reference to quantify the impact of off-design conditions on the blade performance within the ideal-like operating regime. Furthermore, I-DES presents a massflow-averaged Mach number measured at half axial chord downstream of the trailing edge (representing a plausible stator-rotor gap) equal to $M_{05} = 1.95$.

Off-design cases I-OFF-β_+ and I-OFF-β_- expand from the design superheated conditions to lower and higher outlet pressures, respectively, with respect to the design one. These conditions are very common in power systems due to the seasonal variation of ambient temperature, which directly affects the temperature of condensation and hence the turbine outlet pressure.

I-OFF-β_+ imposes to the flow an expansion characterized by a higher pressure ratio. In the present study, the increased pressure ratio is derived by imposing a decrease of 20 °C of the condensation temperature; the resulting change in the turbine pressure ratio was propagated to that
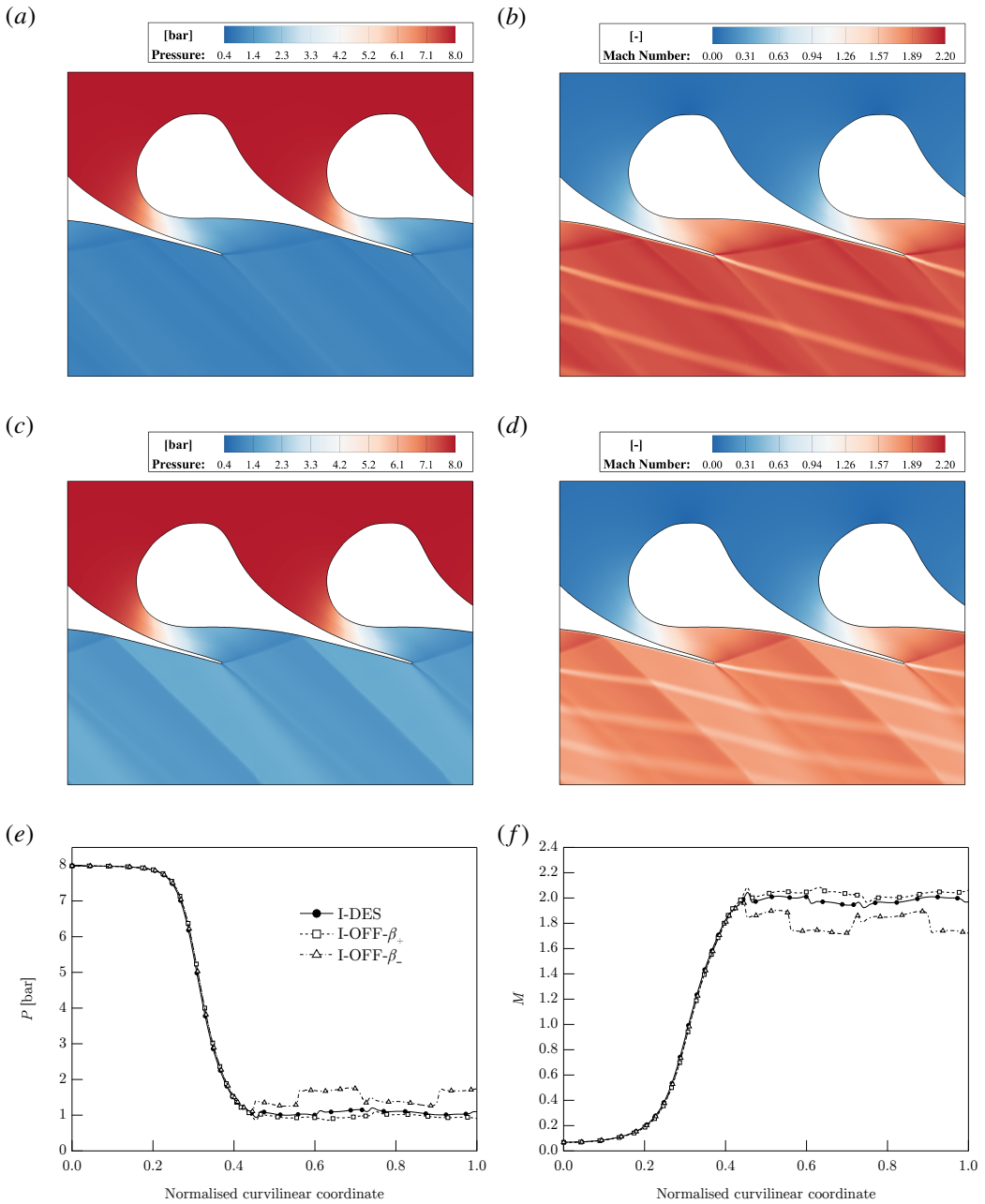
FIGURE 6.11. The effect of variations in the outlet static pressure for the ideal-like operating regime. (*a*), (*b*) pressure and Mach number fields for I-OFF-β_+; (*c*), (*d*) pressure and Mach number fields for I-OFF-β_-; (*e*), (*f*) pressure and Mach number distributions along a reference streamline, approximately following the centreline of the blade channel, see figure 6.9(b). The working fluid is MM.

of the first stator assuming that the turbine is composed by five stages, consistently with the latest trend in the ORC field (Bini & Colombo, 2017), and that the distribution of the enthalpy drops among each cascade remains unchanged. According to quasi-one-dimensional theory, in the blade

133

channel the flow expands as in the design condition and a post-expansion is required to match the lower outlet pressure. This behaviour can be qualitatively recognized in figures 6.11(a–b) and 6.11(e–f). Most differences with respect to I-DES are visible in the Mach number distribution of figures 6.11(b) and 6.11(f), where a higher Mach number ($M_{05} = 2.00$) can be observed at the outlet. The cascade loss coefficient ($\zeta_S = 3.5\%$) is comparable with the design value, consistently with the fact that the post-expansion process is nearly isentropic.

The effect of a reduced pressure ratio is illustrated by case I-OFF-β_-, shown in figures 6.11(c–f) and obtained by increasing the condensation temperature of 20 °C with the same approach used above for I-OFF-β_+ to compute the outlet pressure. The pressure distribution shown in figures 6.11(c) and 6.11(e) is strongly affected by the onset of a strong shock wave, especially where the fish-tail shock reflects. As a consequence, cascade losses increase showing a net increment of the kinetic energy loss coefficient to 7.50%. Moreover, the rotor will experience a higher aerodynamic forcing induced by the presence of shock waves. Stronger shock waves lead to a reduction of the Mach number downstream of the nozzle cascade ($M_{05} = 1.76$), as expected in ideal-like conditions.

The following off-design cases I-OFF-T_+^t and I-OFF-P_-^t feature design pressure ratio, but the fluid is expanded from different upstream stagnation temperatures and pressures, respectively, with respect to I-DES. These conditions are representative of part-load control strategies of the ORC power system.

I-OFF-T_+^t corresponds to an increase of the upstream stagnation temperature. In this case, quasi-one-dimensional theory of ideal gases predicts no differences with respect to the design flow evolution, as the expansion process is governed only by the expansion ratio and the specific heats ratio, which remains fairly constant by increasing the inlet temperature of 20 °C. The flow field distributions reported in figures 6.12(a–b) and 6.12(e–f) confirm qualitatively this behaviour, showing no appreciable differences with respect to the ones presented in figure 6.10 for the design condition. Quantitatively, both the outlet Mach number ($M_{05} = 1.95$) and the kinetic energy loss coefficient ($\zeta_S = 3.6\%$) are very close to the design values.

Finally, I-OFF-P_-^t features a lower upstream stagnation pressure. The outlet pressure is also reduced to maintain the design pressure ratio. Similarly to I-DES and I-OFF-T_+^t, the same pressure ratio entails qualitatively similar flow fields, see figures 6.12(c–f), and in turn analogous values of the outlet Mach number ($M_{05} = 1.95$) and of the loss coefficient ($\zeta_S = 3.7\%$).

To sum up, we have reported the performance of a supersonic converging-diverging cascade operating in the non-ideal gasdynamic regime ($\Gamma < 1$) but qualitatively showing ideal-gas behaviour. In the ideal-like operating regime, four off-design conditions were analysed: (i) an increase of the pressure ratio delivers a larger outlet Mach number without affecting cascade losses; (ii) reducing the pressure ratio, the nozzle cascade features lower performance due to the onset of a strong shock wave to match the higher outlet pressure; (iii) variation of the upstream stagnation state at the same pressure ratio has practically no effect on the cascade performance.

6.2.5   Non-ideal operating regime of nozzle cascades

In order to investigate the performance of the representative nozzle cascades working in the non-ideal operating regime, two different blades are considered, which are designed for expansions N̂-DES and Ň-DES. Off-design behaviour is assessed on four cases labelled N̂-OFF-β_+ and Ň-OFF-i, $i = \{\beta_-, T_+^t, P_-^t\}$. Each of these cases is detailed in table 6.1 and the corresponding expansion processes are reported in the (T, s)–plane of figure 6.7.

The present choice of the upstream stagnation state for both design conditions offers the possibility to observe and examine effects associated with the non-ideal evolution of the Mach number. According to quasi-one-dimensional theory, the isentropic expansion from $P_0^t = 40$ bar
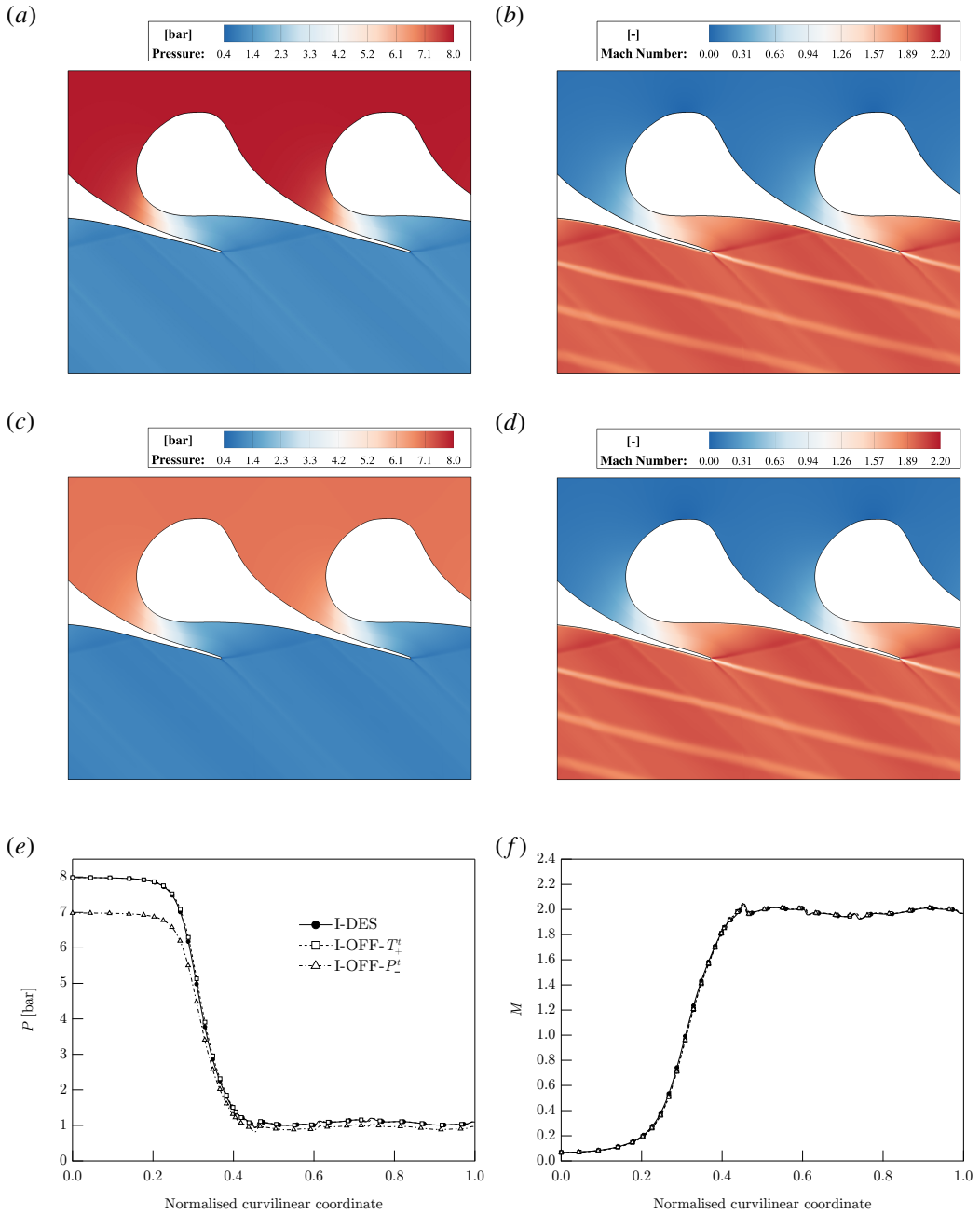
FIGURE 6.12. The effect of variations in the upstream stagnation conditions for the ideal-like operating regime. (*a*), (*b*) pressure and Mach number fields for I-OFF-T_+^t; (*c*), (*d*) pressure and Mach number fields for I-OFF-P_-^t; (*e*), (*f*) pressure and Mach number distributions along a reference streamline, approximately following the centreline of the blade channel, see figure 6.9(*b*). The working fluid is MM.
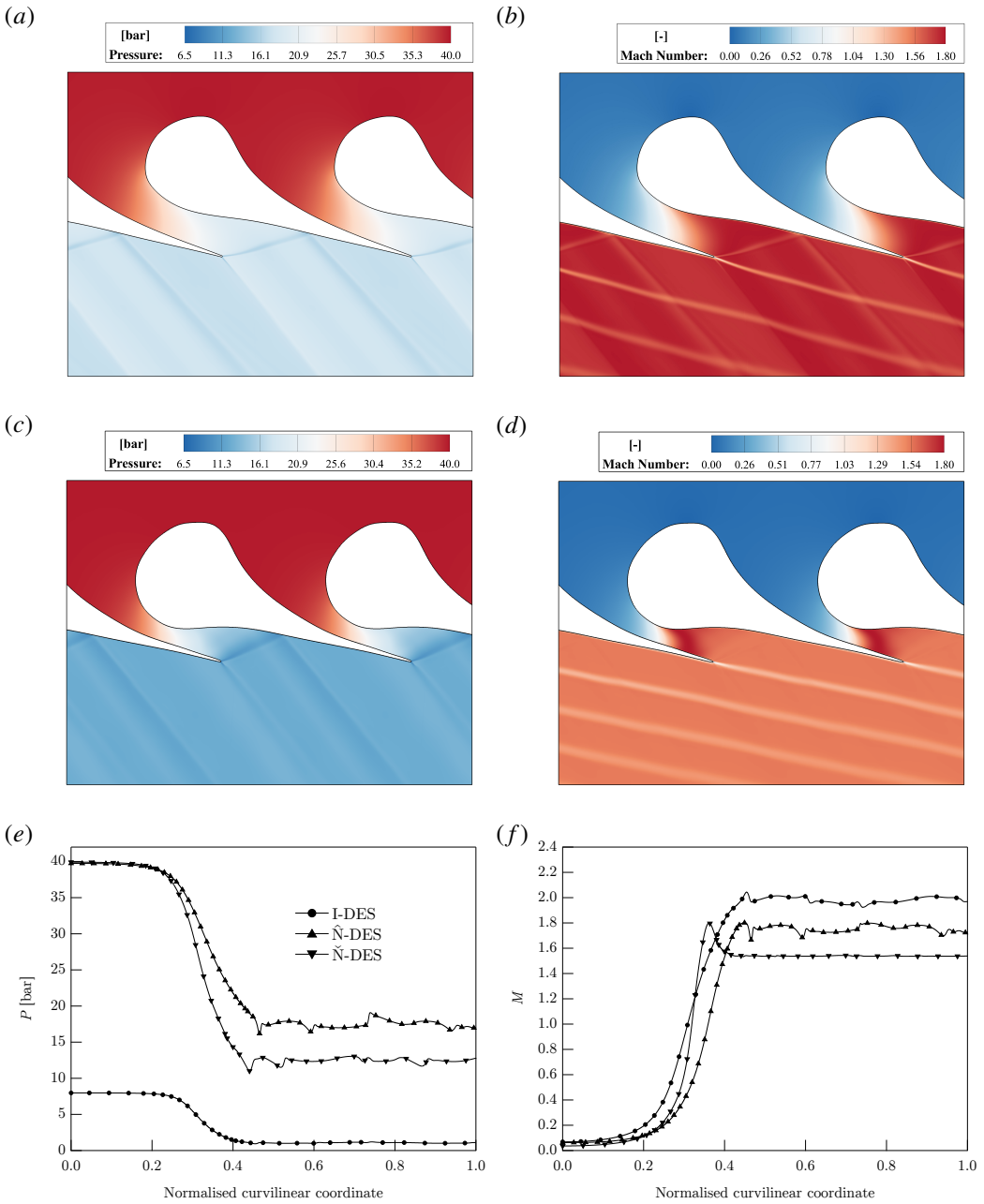
FIGURE 6.13. (*a*), (*b*) pressure and Mach number fields for N̂-DES; (*c*), (*d*) pressure and Mach number fields for Ň-DES; (*e*), (*f*) pressure and Mach number distributions along a reference streamline, approximately following the centreline of the blade channel, see figure 6.9(b). The working fluid is MM.

and $T_0^t = 270\,^\circ\mathrm{C}$ features a non-monotonic Mach number (see figure 6.3(*b*)) with a remarkable difference ($\Delta M \approx 0.26$) between the two stationary points. Moreover, if $J > 0$ in the neighbourhood of the trailing edge (i.e. the expansion through the blade channel end between the two extrema), non-ideal Prandtl-Meyer fans and oblique shocks may occur. This scenario is clarified using two

specific examples in which the expansion through the blade channel ends near a stationary point of the Mach number (local maximum for Ň-DES and local minimum for Ň-DES). Note that a possible advantage deriving from this situation is the enhanced uniformity of the Mach number distribution within the stator-rotor axial gap, due to the relatively low sensitivity of the Mach number to perturbations in the outlet pressure ($J \approx 0$).

Pressure and Mach number distributions for Ň-DES and Ň-DES are shown in figures 6.13(a–f). For both cases, a pattern of weak oblique waves occurs downstream of the trailing edge, evidenced in the pressure contours. Inspection of figures 6.13(b) and 6.13(f) reveals that Ň-DES features non-ideal oblique waves, consistently with the small positive values of J in the trailing edge region. For Ň-DES, see figures 6.13(d) and 6.13(f), no appreciable variation of the Mach number is observed across the oblique waves pattern, due to comparatively smaller values of J (very close to zero). Ň-DES features an outlet Mach number $M_{05} = 1.73$. As the blade is designed for a higher pressure ratio, the new optimal cascade features a lower outlet Mach number ($M_{05} = 1.51$ for Ň-DES) as the local maximum of the Mach number moves within the blade channel. Cascade performance, used in the following to assess the off-design behaviour, are equal between the two design cases and amount to $\zeta_S = 3.9\%$.

Ň-OFF-β_+ and Ň-OFF-β_-, analogously to I-OFF-β_+ and I-OFF-β_-, respectively, aim at determining the impact of different pressure ratios on the cascade performance, likewise computed by decreasing/increasing the condensation temperature of $20\,^\circ$C, with constant enthalpy drops across each single cascade. The upstream stagnation conditions are instead kept constant. As the nomenclatures suggests, the blades used in the off-design cases Ň-OFF-β_+ and Ň-OFF-β_- are those optimized for Ň-DES and Ň-DES, respectively.

The larger pressure ratio in Ň-OFF-β_+ is achieved by means of post-expansion, see figures 6.14(a–b) and 6.14(e–f). The actual features of the Mach number field downstream of the trailing edge differ significantly from those observed in the ideal-like operating regime. The Prandtl-Meyer fan generated on the pressure side of the trailing edge, and subsequently reflected on the suction side of the neighbouring blade, produces a non-ideal decrease of the Mach number. Past the trailing edge, the matching of pressure and flow direction across the wake is accomplished by a non-ideal oblique shock which increases the Mach number. The high amount of post-expansion can be further appreciated from the waviness of the wake. Overall, the prevailing effects is the Mach number decrease across the expansion waves downstream of the trailing edge, which ultimately results in $M_{05} = 1.62$ (while $M_{05} = 1.73$ in the design condition Ň-DES). The kinetic loss coefficient instead increases to $\zeta_S = 5.7\%$, as expected, due to onset of the relatively strong shock generated at the trailing edge.

Configuration Ň-OFF-β_-, which features a decreased pressure ratio, exhibits a reversed flow pattern with respect to the Ň-OFF-β_+ downstream of the trailing edge, as shown in figure 6.14(c–f). To accommodate the higher outlet pressure, an oblique shock stems from the pressure side of the trailing edge and is reflected on the suction side of the neighbouring blade, whereas a rarefaction fan is generated on the opposite side of the trailing edge. For both waves, a non-ideal variation of the Mach number is observed and the Mach number decreases across the Prandtl-Meyer expansion and it increases across the oblique, non-ideal shock wave. The overall Mach number variation follows the non-ideal character of the compression process, resulting in $M_{05} = 1.57$ (while $M_{05} = 1.51$ in Ň-DES). The stronger shock pattern in Ň-OFF-β_- than in Ň-OFF-β_+ is responsible for the comparatively larger increase of the loss coefficient ($\zeta_S = 8.0\%$).

The situation depicted above with Ň-OFF-β_+ and Ň-OFF-β_- is opposed to the ideal-gas like scenario. The non-ideal variation of the outlet Mach number with the outlet pressure might have remarkable consequences on the operation of the entire turbine. As a matter of fact, the present supersonic cascades are prototypes of first stators of ORC turbines. The nozzle is commonly followed by a transonic rotor, whose operational characteristics and performance are crucially
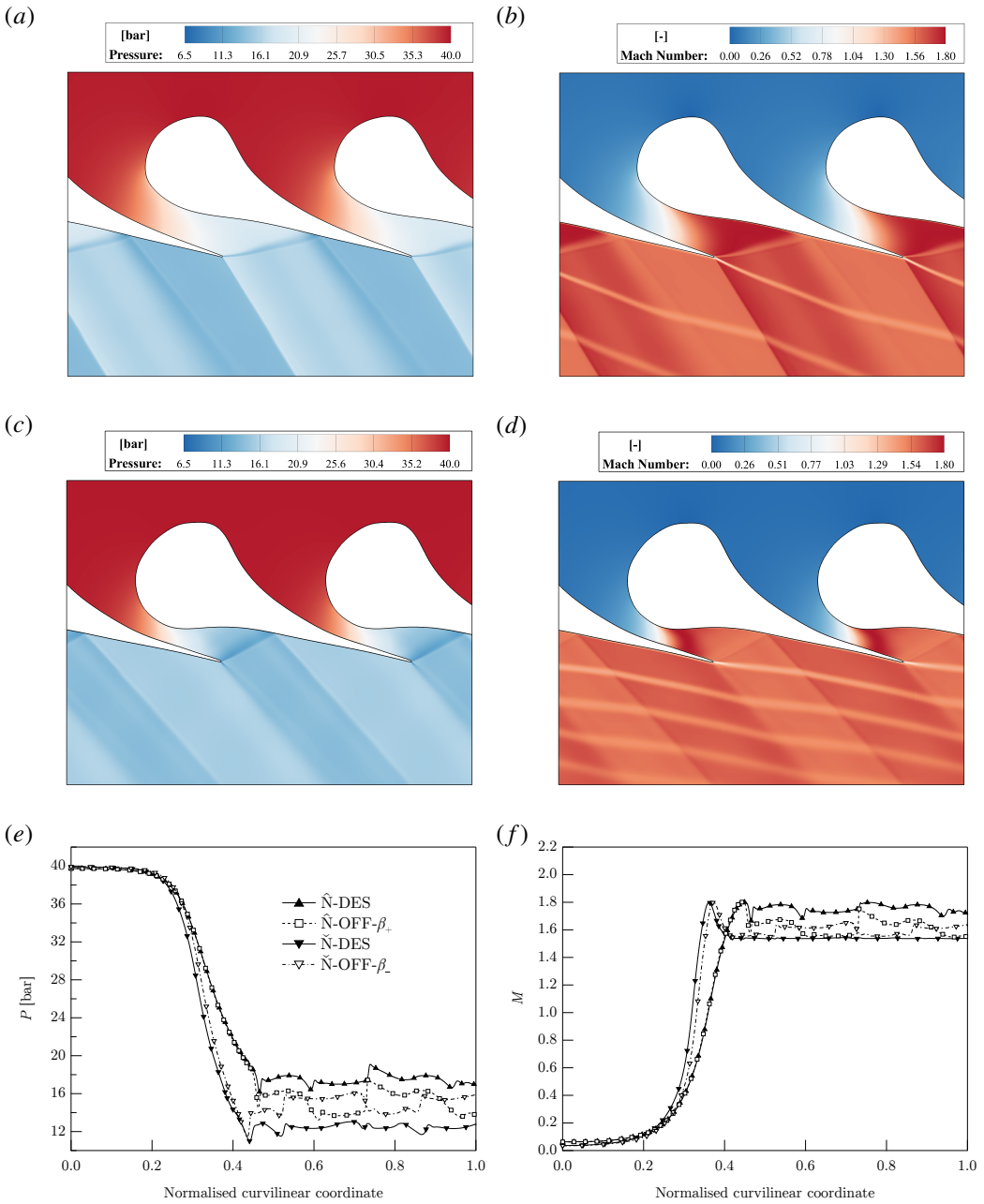
FIGURE 6.14. The effect of variations in the outlet static pressure for the non-ideal operating regime. (*a*), (*b*) pressure and Mach number fields for $\hat{\text{N}}$-OFF-β_+; (*c*), (*d*) pressure and Mach number fields for $\check{\text{N}}$-OFF-β_-; (*e*), (*f*) pressure and Mach number distributions along a reference streamline, approximately following the centreline of the blade channel, see figure 6.9(b). The working fluid is MM.

dependent on the flow regime (whether subsonic or supersonic) associated with the relative flow at the inlet. The rotor-inlet flow is indeed proportional to the (absolute) Mach number at the outlet of the stator, modulated by the rotational speed. Supersonic relative flow at the rotor inlet are

detrimental for the turbine flexibility and performance mainly due to the so-called unique-incidence phenomenon (Starken *et al.*, 1984). Within this supersonic flow regime, the rotor leading edge behaves as a bluff body, enabling the formation of a bow shock upstream of the leading edge. Both the shock strength and its distance from the rotor leading edge are function of the inlet relative Mach number and the leading edge radius. Under this condition the inlet flow angle is no longer a free parameter but it is given by the bow-shock interaction among adjacent rotor cascades. It can be proved that, for a given rotor geometry, a unique pattern of characteristic lines is feasible, thus admitting a unique inlet flow angle (Starken, 1993). Therefore, the flow is chocked in the rotor cascade and it is not possible to adjust the massflow by varying the upstream flow angle. Besides, supersonic rotor cascades may present a complex pattern of shock waves and shock-boundary layer interactions, which is likely to result in a lower stage efficiency as the Mach number at the rotor inlet increases (Rinaldi *et al.*, 2016). A proper design of the rotor cascade allows the mitigation of the aforementioned phenomena (see, e.g., Bufi & Cinnella, 2018), even though such design is valid only for a specific operating condition. From this point of view, operating conditions similar to Ň-DES, i.e. tuned to obtain a local maximum of the Mach number near to the trailing edge, are advantageous against the unique incidence phenomenon. Indeed, both an increase and a decrease of the outlet pressure would reduce the outlet Mach number, thus increasing the safety margin for unique incidence. On the contrary, for design conditions analogous to Ň-DES, a Mach number increase is expected for whatever pressure-ratio variation. In particular, a non-ideal effect that unexpectedly increases the stator-outlet/rotor-inlet Mach number for different pressure ratios (e.g. Ň-DES $\rightarrow$ Ň-OFF-β_-) might drive the rotor in unique-incidence condition, with severe detrimental effects on the turbine operation and performance. Recall that in the ideal-like operating regime a decrease/increase of the outlet pressure always increases/decreases the Mach number.

As anticipated in §6.1, the upstream stagnation quantities play a key role in the expansion process for non-ideal flows. The last two examples Ň-OFF-T_+^t and Ň-OFF-P_-^t aim at demonstrating the effect of a variation in the upstream stagnation conditions, at fixed pressure ratio. In the same spirit as I-OFF-T_+^t and I-OFF-P_-^t, the stagnation temperature and pressure are varied independently. The reference condition for this study is Ň-DES.

We first consider the impact of an increase of the upstream stagnation temperature on the cascade performance (Ň-OFF-T_+^t). The increase in the stagnation temperature is large enough that the isentropic pattern changes from $\mathscr{S}^{NI}$ to $\mathscr{S}^I$, thus the Mach number is monotonic in the supersonic expansion in the divergent section of the blade channel, as shown in figures 6.15(*b*) and 6.15(*f*). As a further consequence of the stagnation temperature increase, the adapted pressure ratio (across the blade channel only) increases as well, see figure 6.4(*b*) for expansions with a similar value of the stagnation pressure. In the present case, since the pressure ratio is fixed, the increase of stagnation temperature triggers a strong shock wave downstream of the cascade where the fish-tail reflects, see figures 6.15(*a–b*) and 6.15(*e–f*). The kinetic energy loss coefficient dramatically increases to $\zeta_s = 12.7\%$, resulting in more than three times the design loss coefficient and the outlet Mach number decreases to $M_{05} = 1.47$. Non-ideal oblique shocks are not observed in the present configuration because the shock adiabat centred on the thermodynamic state at the trailing edge no longer contains the $J > 0$ region necessary for the Mach number increase[1] (see §4.4.2.3). Note that in case of ideal-like operating conditions, the cascade loss coefficient remains nearly constant through an increase of the upstream stagnation temperature (I-DES $\rightarrow$ I-OFF-T_+^t), thus highlighting a severe distinction between the ideal and non-ideal operating conditions. Considering that inherent fluctuations of the set-point temperature are unavoidable, such turbines will most likely oscillate from strong shocks to shock-free conditions, compromising the stability,

---

[1]The fact that non-ideal oblique shocks are disallowed in Ň-OFF-T_+^t can also be deduced by noticing that the isentrope associated with the upstream stagnation conditions of Ň-OFF-T_+^t no longer contains a $J > 0$ region. Thus, for each pre-shock state A along the selected isentrope, the resulting shock adiabat is embedded in the thermodynamic region $\Gamma > 1 - 1/M_A^2$ and the Mach number is monotonically decreasing along the shock curve.
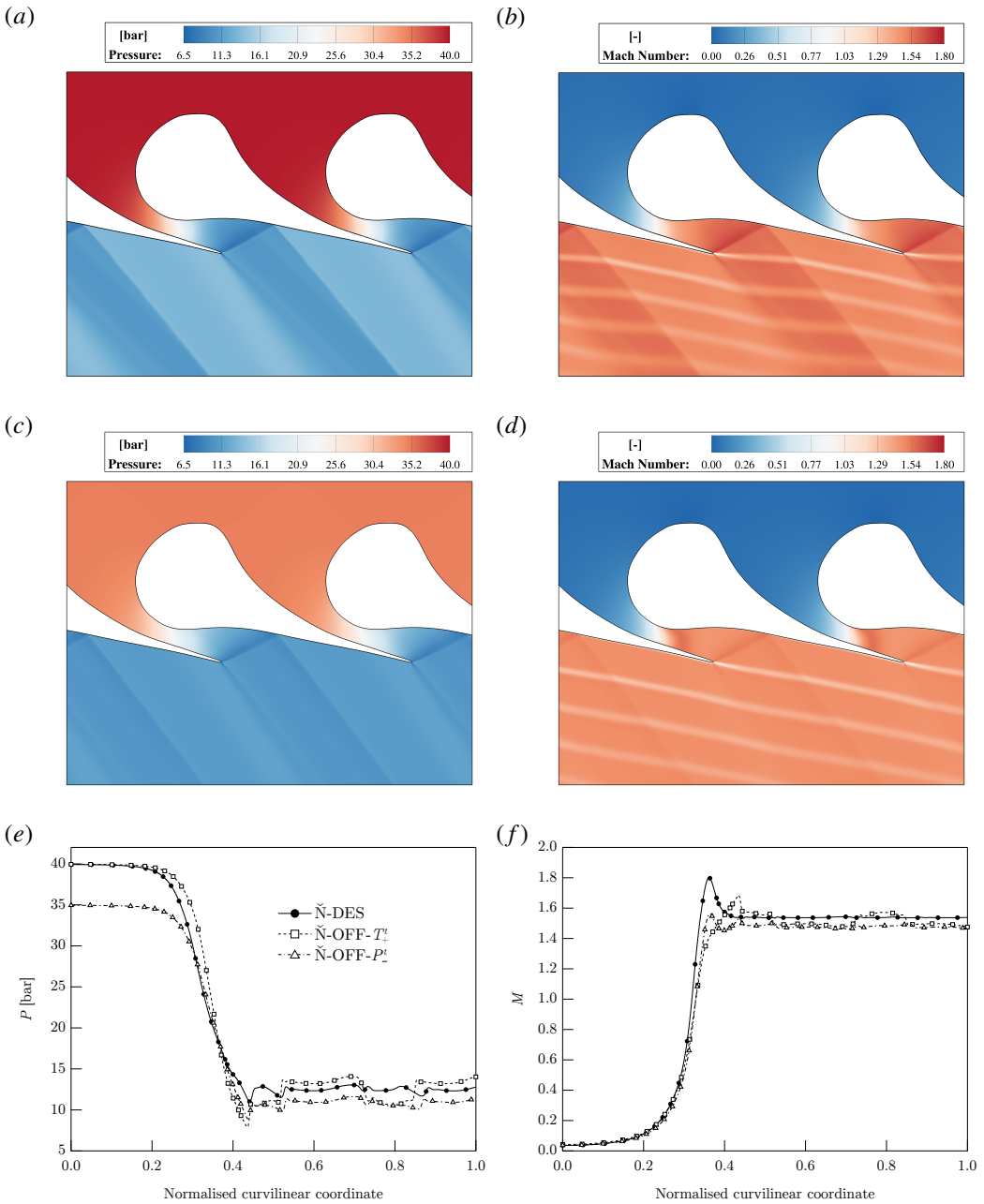
(a)

(b)

(c)

(d)

(e)

(f)

FIGURE 6.15. The effect of variations in the upstream stagnation conditions for the non-ideal operating regime. (a), (b) pressure and Mach number fields for Ň-OFF-T_+^t; (c), (d) pressure and Mach number fields for Ň-OFF-P_-^t; (e), (f) pressure and Mach number distributions along a reference streamline, approximately following the centreline of the blade channel, see figure 6.9(b). The working fluid is MM.

the performance and the mechanical integrity of the stage (especially from the fatigue standpoint).

Finally, Ň-OFF-P_-^t illustrates the consequences of a decrease in the upstream stagnation pressure. The pressure and Mach number fields, see figures 6.15(c–f), are qualitatively similar

to the design ones. On a quantitative level, the Mach number peak in the blade channel and the outlet Mach number ($M_{05} = 1.45$) are reduced and a stronger shock-wave pattern is generated at the trailing edge, confirmed by the increase of the loss coefficient ($\zeta_s = 4.6\%$). Compared to the variation in the upstream stagnation temperature ($\check{N}$-OFF-T_+^t), the variation of the upstream stagnation pressure affects the flow field and the cascade performance to a lower extent.

It is worth underlining that the flow-field dependence on the upstream stagnation quantities is not limited to a specific thermodynamic range, differently from the non-monotonic variation of the Mach number or the onset of oblique shocks featuring an increase of the Mach number.

6.3 Concluding remarks

Non-ideal flows of siloxane MM in converging-diverging nozzle cascades were investigated numerically. Steady-state numerical solutions were obtained by employing a Navier-Stokes flow solver, featuring k-ω SST turbulence model along with state-of-the-art thermodynamic treatment. By examining representative design points along with selected off-design conditions, two opposite scenarios were recognized within the non-ideal gasdynamic regime $\Gamma < 1$. In the range of pressures approximately up to the critical pressure, the expansion process in the nozzle cascade is qualitatively similar to that observed in the ideal-gas limit. In other words, despite the nozzle expansion occurs in the non-ideal gasdynamic regime, non-ideal effects do not play a major role and ideal-gas considerations can be applied in the design and performance analysis of the cascade. Quantitative differences with respect to the dilute-gas flow field are arguably negligible at relatively low pressures (e.g. $0.5P_c$) and increase approaching the supercritical regime. Expansion from supercritical conditions can instead exhibit strong non-ideal effects which determine a quantitative and qualitative deviation from the flow features characterizing subcritical expansions.

The main implications for nozzle-cascade flows in their non-ideal operating regime are:

 (i) a potentially advantageous design, involving stationary points of the Mach number in proximity of the blade trailing edge, leads to a nearly uniform outlet Mach number distribution in the stator-rotor axial gap with a low sensitivity to slight variations in the outlet pressure;

 (ii) if the above-mentioned stationary point is the local maximum/minimum, a decrease/increase in the outlet Mach number is observed with decreasing/increasing outlet pressure, achieved by means of non-ideal Prandtl-Meyer waves/oblique shocks;

 (iii) the cascade performance is highly sensitive to variations in the upstream stagnation pressure and temperature, at constant pressure ratio. The present analysis suggests a larger influence of stagnation temperature variations (e.g., $\Delta\zeta_s = +8.8\%$ with $\Delta T_0^t = +20°C$ against $\Delta\zeta_s = +0.7\%$ with $\Delta P_0^t = -5\,\text{bar}$).

The present analysis shows that the performance of nozzle cascades operating in the non-ideal gasdynamic regime may be strongly sensitive to departure from the design conditions. This suggests that including multiple operating conditions at the design stage (robust design optimization) might be crucial for the future development of turbomachinery for supercritical cycle applications.

Numerical results were found to be consistent with the predictions of the quasi-one-dimensional flow and oblique-wave theories, which are of general validity and mainly depend on the behaviour of the fundamental derivative of gasdynamics. Therefore, we expect that the present findings can be extended to most molecularly complex fluids featuring $\Gamma < 1$ in the single-phase vapour region.

CHAPTER 7

CONCLUSIONS AND OUTLOOK

7.1 Conclusions

The study documented in this thesis offers a comprehensive overview of phenomena arising in steady supersonic flows. An arbitrary equation of state of the gas was allowed (subject to physical constraints). Specifically, no assumption was made on the values of the fundamental derivative of gasdynamics Γ and indeed substances exhibiting non-ideal thermodynamic behaviour for which $\Gamma < 1$ (in contrast to the ideal-gas case, $\Gamma = \text{const} > 1$) were the focus of the research. In single-phase gases to which the discussion was limited, states featuring $\Gamma < 1$ are found in the neighbourhood of the saturation curve and critical point of molecularly complex fluids. In this context, three main topics were addressed: (i) quasi-one-dimensional flows in converging-diverging nozzles, (ii) two-dimensional oblique waves, (iii) shock reflections and interactions in two-dimensions. These are fundamental features of the flow expanding in supersonic stator cascades. Connected to this is the concluding application case where the flow through ORC turbine vanes was examined in the NICFD framework. The general conclusions of the research topics in this work are summarised in the following.

Steady flows in converging-diverging nozzles were investigated from a novel perspective which clarifies the connection between a general adiabatic flow field and the underlying local isentropic-flow features. This approach proved particularly useful in the computation of non-classical nozzle flows where a variety of isentropic flows is possible and can be combined into piece-wise isentropic flows (shocked flows) in several different ways. In order to enable the description of isentropic flows, the concept of isentropic pattern was introduced. The isentropic pattern encompasses each possible isentropic flow for a given stagnation state. Moving from the classification of isentropic flows, exact flows possibly including shock waves were computed using a shock-fitting technique. The layout of the exact solutions produced by monotonically decreasing values of the ambient pressure, namely the functioning regime of the nozzle, was examined using the van der Waals gas model. The following results were obtained:

- Two isentropic patterns ($\mathscr{S}^{I}$, $\mathscr{S}^{NI}$) were singled out in the classical gasdynamic regime and five ($\mathscr{S}^{I}$, $\mathscr{S}^{NI}$, $\mathscr{S}_{1}^{NC}$, $\mathscr{S}_{2}^{NC}$, $\mathscr{S}_{3}^{NC}$) in the non-classical gasdynamic regime. With the exception of $\mathscr{S}^{I}$, all the isentropic patterns feature a non-monotonic behaviour of the Mach number. In particular, $\mathscr{S}_{1}^{NC}$ and $\mathscr{S}_{2}^{NC}$ exhibit three sonic points.

- Following the study of the transitional criteria among the different isentropic patterns identified, a thermodynamic map of the stagnation states leading to each isentropic pattern was computed. Thermodynamic considerations and application of the second law of thermodynamics determined the direction in which shock-induced transitions of the isentropic pattern can occur.

- As many as ten functioning regimes were identified: the ideal-like regime $\mathscr{R}^{I}$, the non-ideal classical regime $\mathscr{R}^{NI}$ characterised by non-monotonic Mach number in supersonic flow and the non-classical regimes $\mathscr{R}_{3}^{NC}$, $\mathscr{R}_{2a}^{NC}$, $\mathscr{R}_{2b}^{NC}$, $\mathscr{R}_{2c}^{NC}$, $\mathscr{R}_{1a}^{NC}$, $\mathscr{R}_{1b}^{NC}$, $\mathscr{R}_{1c}^{NC}$, $\mathscr{R}_{0}^{NC}$. Except for $\mathscr{R}_{3}^{NC}$ which is distinguished for the non-monotonic Mach number in subsonic flow, the non-classical functioning regimes feature one or more of rarefaction shocks, sonic shocks and compression shocks splitting in two distinct entities (split-shock).

- In order to identify the thermodynamic region of interest for the observation of non-ideal nozzle flows, a thermodynamic map of the reservoir conditions resulting in each functioning regime was produced. The higher complexity of this map, compared to that associated with the isentropic patterns, is due to the occurrence of shock-induced transitions of the isentropic pattern. Reservoir states leading to non-ideal functioning regimes are found in the supercritical thermodynamic region along isentropes crossing the $\Gamma < 1$ region ($\Gamma < 0$

for non-classical functioning regimes). An important aspect to be considered in practical applications is that at such high temperatures, fluids composed by complex molecules might undergo thermal degradation.

- Each of the aforementioned functioning regimes can be observed with sufficiently large c_v/R values of the van der Waals gas, while some non-classical functioning regimes may in fact disappear if the molecular complexity is reduced. The predictions of the simple van der Waals model were verified against accurate thermodynamic models of selected fluids. Comparison between the different fluids considered indicated that good qualitative agreement, in terms of layout of the thermodynamic map of the functioning regimes, is found between fluids with similar values of Γ_{min}.

Scale-invariant oblique waves in steady supersonic flows were studied taking advantage of the qualitative equivalence with one-dimensional unsteady flows. On this basis, curves of oblique waves, which mirror the wave curves of the one-dimensional Riemann problem, were constructed. This was done using a two-step procedure where the projection of the wave curve onto the thermodynamic variables is first considered, and kinematic quantities are retrieved afterwards. The wave curve analysis allowed to determine all the downstream states connected to a given supersonic upstream state by means of oblique waves. In the classical gasdynamic regime, where the wave curve structure is well-known, the research focused on the non-ideal effect of the Mach number increase across oblique shocks (non-ideal oblique shocks). Moreover, a unified approach for the description of the geometrical properties of classical oblique waves was presented. In the non-classical gasdynamic regime, the attention was centred on the admissible wave curve configurations, which were studied using the van der Waals gas model. The following results were obtained:

- A detailed study of the necessary conditions for the occurrence of non-ideal oblique shocks allowed to determine a family of thermodynamic regions, parametrised by the upstream Mach number M_A, in which the upstream thermodynamic state must be selected in order to observe the discontinuous increase of the Mach number. The computational procedure of these thermodynamic domains was applied to several fluids of practical interest using accurate EoS, obtaining qualitatively similar results. For a given M_A, the admissibility region of non-ideal oblique shocks approximately coincides with the region $\Gamma < 1 - 1/M_A^2$.

- The typical shock angle–deflection angle diagram of oblique shocks was extended with an additional half-plane corresponding to Prandtl-Meyer fans, thanks to the definition of an equivalent-fan angle. The choice of this angle as the average slope of the leading and terminating Mach lines (guided by the bisector rule for oblique shocks) provided a smooth matching between the oblique-shock branch and the newly defined rarefaction-fan branch.

- Six non-classical wave curves were singled out: $\mathcal{N}_1, \mathcal{N}_2, \mathcal{N}_3, \mathcal{N}_4, \mathcal{N}_5, \mathcal{N}_6$. Key feature of these wave curves is the presence of inverted waves (rarefaction shocks and compression fans) and composite waves.

- Analysis of the transitional conditions among the different wave curves led to the definition of a map, in the parameter space of the thermodynamic quantities and Mach number, of the upstream states leading to each type of wave curve. The thermodynamic region of upstream states associated with non-classical wave curves extends approximately from the low-density neighbourhood of the negative-Γ region up to infinite pressures along isentropes featuring $\Gamma < 0$. As previously noticed for nozzle flows, from the practical point of view the high stagnation temperatures associated with these flows, combined with the high molecular complexity of the working fluid, may result in thermal stability issues.

145

- The computation of the upstream-state map of the wave curves using accurate thermodynamic models of fluid confirms the picture given by the van der Waals model.

The theory of oblique waves was applied to the investigation of shock reflections and interactions in non-ideal gasdynamics, offering an overview of the most relevant configurations. This was made possible by restricting the attention to the neighbourhood of the node where oblique waves intersect generating a scale-invariant flow. The same approach used in the study of oblique wave was adopted. In the classical gasdynamic regime, the research concentrated on the occurrence of non-ideal oblique shocks in the reflection or interaction pattern. In the non-classical case, the primary interest was on the structure of the shock reflection or interaction at the node. Due to the possibility of outgoing fans or composite waves at the node, the classical two-shock and three-shock theories of von Neumann were extended to the non-classical gasdynamic context. The van der Waals gas model was used in this study as previous results confirm its accuracy from the qualitative point of view. The following results were obtained:

- Flow fields that locally involve only non-ideal oblique shocks, and thus provide an overall increase of the flow Mach number, were detected in the case of regular reflection, cross node and overtake node. The large shock angles characterizing irregular reflections seemed to preclude this possibility.

- It was shown that in a wide range of incident-shock parameters, compression shocks undergo regular reflection generating a reflect fan or composite wave. The situation was quite different for irregular reflections. Reflected composite waves were observed in the case of Mach reflection, while non-classical waves were not encountered in the von Neumann, Guderley and Vasil'ev reflections.

- Regular reflections in which a rarefaction shock reflects as a fan or composite wave were observed. In contrast with the case of compression shocks, the study indicated that irregular reflections occur uniquely in the form of Guderley patterns. While no clear proof of the non-existence of other reflection mechanisms was given, arguments supporting this apparent scenario were provided.

- Several combinations of outgoing waves at a cross node were detected. For each pair of incident and reflected shocks, the configurations realizable in a regular reflection were recovered.

- In the overtake node, two main differences were noticed between the classical and non-classical configurations. On the one hand, non-classical overtake nodes were depicted in which the oblique waves are similar to those found in the classical case, except for an opposite pressure variation. On the other hand, it was shown that a compression shock can overtake a rarefaction shock generating a transmitted fan (no counterpart in classical gasdynamics).

Numerical simulations of non-ideal flows through supersonic stator vanes were performed, with particular reference to ORC turbines. Working fluid MM (hexamethyldisiloxane) was considered, which is classified as a non-BZT fluid by most modern thermodynamic models, as other fluids currently used in ORC power systems. This study, conducted using the most recent and accurate EoS for MM, addressed non-ideal but classical gasdynamic effects. Most flow features were anticipated and explained through the use of simpler models for specific flow regions analysed in the previous chapters, namely the quasi-one-dimensional flow, the generation of oblique shock waves by an abrupt turning of a supersonic stream and the shock reflection at a wall. Shape

optimization was applied to three operating conditions, one representing a subcritical, low turbine-inlet pressure ORC system while the other two featuring a supercritical cycle with high-pressure turbine inlet. The high-pressure cases involved stationary points of the Mach number in proximity of the trailing edge. For each configuration, the off-design behaviour was explored by imposing variations in the outlet pressure and in the inlet stagnation state. The following results were obtained:

- Remarkable differences were found between the flow fields of the design conditions considered. The low-pressure case provided an ideal-gas-like scenario, as a minimal departure from the corresponding ideal-gas flow could be noticed. On the contrary, the high-pressure cases involved a non-monotonic evolution of the Mach number in the blade channel and non-ideal oblique shocks and Prandtl-Meyer fans at the trailing edge.

- For the high-pressure operating conditions, the stationary point of the Mach number in proximity of the trailing edge allowed for a nearly uniform outlet Mach number distribution in the stator-rotor axial gap with a low sensitivity to slight variations in the outlet pressure.

- The response to variations in the outlet pressure, at fixed upstream stagnation state, was found to largely depend on the operating condition. If a local minimum of the Mach number occurs at the trailing edge, either a decrease or an increase in the outlet pressure can produce an increase of the Mach number at the rotor intake. Detrimental effects on the turbine flexibility and performances are possible due to the occurrence of the so-called unique incidence phenomenon affecting the rotor. Operating conditions characterised by a local maximum of the Mach number at the trailing edge exhibit the opposite behaviour, namely the outlet Mach number can decrease with both increasing and decreasing outlet pressure, thus improving the safety margin for unique incidence.

- In the high-pressure operating conditions, variations in the upstream stagnation temperature at fixed upstream pressure and pressure ratio caused a dramatic loss increase (more than three times the design loss) due to the formation of strong oblique shocks at the trailing edge. By contrast, no significant increase of the loss was noticed in the ideal-gas-like configuration.

7.2 Outlook

The original research presented in this thesis contributes to better knowledge and understanding of the theory of supersonic flows in the non-ideal gasdynamic regime. The practical implications of this study are numerous and challenging. Besides confirming the need of accounting for non-ideal effects in the design and analysis of aerodynamic devices operating with molecularly complex vapours in thermodynamic states close to the vapour-liquid saturation curve and critical point, it was clearly demonstrated that a wide variety of different phenomena is possible over a relatively narrow range of thermodynamic states. This remarkable degree of freedom offers the opportunity to exploit and control non-ideal effects with relatively small changes in the boundary conditions. On the other hand, depending on the specific context, the enhanced sensitivity to the operating conditions might represent a serious disadvantage.

This work will hopefully motivate further theoretical and experimental investigation. Importantly, attention was paid to develop concepts and analytical tools of general validity. In this sense, it was shown that the results and conclusions do not depend on the specific form of the EoS, except for the presence of the $\Gamma < 1$ region in the vapour phase. As a matter of fact, the relevance of this study extends beyond NICFD, arguably to all situations where locally non-convex isentropes in the pressure–density or pressure–specific volume planes can be found (e.g., porous-media flows,

supersonic reacting flows) and possibly outside the domain of fluid dynamics (generic hyperbolic systems of conservation laws featuring non-convex characteristic fields, e.g. nonlinear elasticity). Below, some perspectives, limitations and open questions of the presented analysis are discussed to suggest the direction of future research.

In the immediate vicinity of the critical point, analytical models such as those used in this work are qualitatively inaccurate and scaling laws, accounting for the non-analyticity of the Helmholtz free energy at the critical point, should be used (see, e.g., Levelt-Sengers, 1970). The $\Gamma < 1$ region predicted in molecularly complex vapours by analytical models may be partially overlapping with the region where long-range critical fluctuations affect the thermodynamic properties of the fluid, especially derivative properties such as Γ (Nannan et $al.$, 2016). Although the reference models in Span-Wagner form (used in this work to confirm the vdW predictions) are generally accurate even quite close to the critical point, the potential influence of critical effects deserves more careful examination.

Thermodynamic states exhibiting $\Gamma < 1$ are found also in the vapour-liquid equilibrium region, even in fluids composed by simple molecules. In particular, $\Gamma < 0$ in the near-critical two-phase region according to scaled fundamental EoS based on universal critical exponents (Nannan et $al.$, 2013). Some of the general considerations given above can be applied to the study of non-ideal and non-classical effects. The new aspect, and main difference with the present treatment, is that isentropes have a kink in their slope along the saturation curve. Among the others, this enables the formation of split waves (Menikoff & Plohr, 1989). Extension of the present study to the two-phase region would certainly provide a more complete picture of non-ideal steady supersonic flows, and is of sure interest for applications such as supercritical CO_2 power generation or refrigeration systems.

Another important problem for further study is the non-uniqueness of solutions for ramp/wedge flows subject to supersonic upstream conditions. The question is inherited from classical gasdynamics, where on a given compression ramp a weak and a strong shock (according to the pressure jump) are possible with the same upstream state. The issue is not the possibility of observing the strong solution locally, which in fact occurs in detached shock fronts, but rather if a straight strong shock on a wedge is physically admissible and can be realised. Recent investigations (Kraiko et $al.$, 2014; Kluwick & Cox, 2018a) point to the crucial role of the global geometry and boundary conditions at downstream infinity in determining the stability of the configuration and thus the possibility of realising it. Evidently, the non-uniqueness cannot be resolved by local analysis or isolated-shock stability arguments alone. In the non-classical context, the problem of multiple solutions is further complicated because up to three stationary points of the deflection angle are possible along the wave curve and by the presence of composite waves. Also of interest is the investigation of detached shocks and shock–boundary layer interaction in non-ideal flows. Development in this area might be useful to gain further insights into non-classical shock reflections.

The study of shock interactions could be extended by including the diffraction of a shock though a contact discontinuity. Among the others, this case is relevant for applications involving over/underexpanded jets (e.g., rocket propulsion, fuel injection, rapid expansion of supercritical solutions) and for supersonic turbine flows where the shock waves generated at the trailing edge interact with the wake, which might feature a shear layer (approximable as a slip line). Yet in the context of turbine flows, future efforts should be aimed at assessing the impact of non-classical effects on the blade design and performance when the working fluid is of the BZT class. The dedicated literature is scarce and thus further studies (e.g. numerical simulations, on the lines of those reported in this work) would be valuable in view of the possible use of more complex fluids in ORC power plants.

Lastly, some recommendations regarding the possibility that the non-classical effects described in this work might be observed experimentally in steady-state flows. Apart from the non-monotonic variation of the Mach number in subsonic expansions, these phenomena, in particular the long sought rarefaction shock, necessitate supersonic or at least sonic flow conditions. The requirement of steady supersonic flow in the neighbourhood of the BZT region implies higher stagnation enthalpies and temperatures, if compared to those associated with non-classical unsteady flows (e.g. shock tube experiments). High enthalpy implies high power required in the experimental facility, which could be eventually limited using small test chambers (in turn, thicker boundary layers). The values of the stagnation temperature might be close to the thermal stability limit of the substance, at least those which are currently indicated as candidate BZT fluids (e.g. complex siloxanes and perfluorocarbons). In this connection, advancements in the modelling and measurement of thermal and caloric properties of molecularly complex fluids (including mixtures) in the general neighbourhood of the critical point are of paramount importance.

Thermodynamic modelling

In this Appendix, the thermodynamic models considered in this work are briefly described. As is well-known, the equilibrium thermodynamic properties of a material are embodied in the relation

$$e = e(s, v) \tag{A.1}$$

expressing the specific internal energy e of an equilibrium state as a function of the specific entropy $s \geqslant 0$ and the specific volume $v > 0$, see Galgani & Scotti (1970). The above equation, known as the fundamental relation in the energy representation, is obtained under the assumption of single-constituent and simple thermodynamic system (Callen, 1985; Gyftopoulos & Beretta, 2005). The fundamental relation (A.1) is monotonic with respect to the entropy, being the temperature

$$T = \left(\frac{\partial e}{\partial s} \right)_v \tag{A.2}$$

non-negative. The energy fundamental relation can therefore be inverted to obtain the fundamental relation in the entropy representation $s = s(e, v)$. If the material is a fluid and thus it cannot sustain tension, the pressure

$$P = -\left(\frac{\partial e}{\partial v} \right)_s \tag{A.3}$$

is non-negative and thus the fundamental relation (A.1) is monotonic also with respect to the specific volume. Moreover, thermodynamic stability requires that the fundamental relations in the energy and entropy form are respectively convex and concave. This implies that the isochoric specific heat

$$c_v = T \left(\frac{\partial s}{\partial T} \right)_v \tag{A.4}$$

and the isentropic compressibility

$$K_s = -\frac{1}{v} \left(\frac{\partial v}{\partial P} \right)_s \tag{A.5}$$

are non-negative. Note that $c^2 = v/K_s \geqslant 0$.

Fundamental relations analogous to (A.1) are obtained through the Legendre transformation:

$$f(T, v) = \inf_s \left[e(s, v) - Ts \right] \qquad \text{specific Helmholtz free energy,} \tag{A.6a}$$

$$h(s, P) = \inf_v \left[e(s, v) + Pv \right] \qquad \text{specific enthalpy,} \tag{A.6b}$$

$$g(P, T) = \inf_{s,v} \left[e(s, v) - Ts + Pv \right] \qquad \text{specific Gibbs free energy.} \tag{A.6c}$$

From the thermodynamic stability requirements it follows that: the fundamental relation in the Helmholtz representation is convex in v and concave in T, the fundamental relation in the enthalpy representation is convex in s and concave in P, the fundamental relation in the Gibbs representation is concave.

The knowledge of two (compatible) equations of state (EoS) is equivalent to the knowledge of a fundamental relation. In practical applications, the thermal and caloric EoS

$$P = P(T,v) \quad \text{and} \quad e = e(T,v), \tag{A.7}$$

respectively, often represent the only available thermodynamic information on the system, because, differently from the fundamental relations or other EoS, they can be easily obtained from direct measurements on the system or from mathematical models based on physical reasoning. With the knowledge of the thermal and caloric EoS, the relation $s = s(T,v)$ is obtained from the Euler relation of thermodynamics $e = Ts - Pv$ and together with $e(T,v)$ the Helmholtz fundamental relation is constructed. An even more convenient choice is to specify the thermal EoS together with the ideal-gas isochoric specific heat

$$c_{v,\infty}(T) = \lim_{v \to \infty} c_v(T,v), \tag{A.8}$$

which can be used to construct the caloric EoS from

$$e(T,v) = e_0 + \int_{T_0}^{T} \left[c_{v,\infty}(\tau) - \tau \int_{v}^{\infty} \frac{\partial^2 P}{\partial T^2}(\tau,v) dv \right] d\tau + \int_{v_0}^{v} T^2 \frac{\partial}{\partial T} \left(\frac{P(T,v)}{T} \right) dv, \tag{A.9}$$

where subscript 0 indicates an arbitrary reference state.

In the following, the thermodynamic models adopted in this work are described in terms of thermal EoS, except for the Span-Wagner model which directly expresses the Helmholtz fundamental relation.

Ideal gas model

The widely diffused ideal-gas model, appropriate in dilute gases, is obtained by assuming that gases are composed of identical point-particles interacting with each other only through elastic collisions. The ideal-gas thermal EoS reads

$$P(T,v) = \frac{RT}{v} \tag{A.10}$$

where $R = R_u/M_m$ is the specific gas constant, being $R_u = 8.314 \ \mathrm{J\,mol^{-1}\,K^{-1}}$ and M_m the universal gas constant and the molecular mass, respectively. Since both derivatives of the thermal EoS appearing in (A.9) are identically zero, the caloric EoS assumes the simple form

$$e(T) = e_0 + \int_{T_0}^{T} c_{v,\infty}(\tau) d\tau. \tag{A.11}$$

If constant specific heat c_v is also assumed, the internal energy depends linearly on temperature and the model is called polytropic ideal gas model or perfect gas model.

van der Waals model

The van der Waals (vdW) model (van der Waals, 1873) is the simplest model capable of representing in a qualitative way both liquid and vapour homogeneous states. In the vdW model, particles have a finite volume and interact through elastic collisions, subject to weak long-range attractive forces

and strong short-range repulsive forces. The validity of model can be extended to the two-phase region by introducing a correction based on the Maxwell construction. The vdW thermal EoS is

$$P(T, v) = \frac{RT}{v - b} - \frac{a}{v^2}, \tag{A.12}$$

where the constants a and b can be expressed in terms of critical quantities (subscript c) as follows:

$$a = \frac{27}{64} \frac{R^2 T_c^2}{P_c}, \quad b = \frac{1}{8} \frac{RT_c}{P_c}. \tag{A.13}$$

Even in this case, the caloric EoS is particularly simple, namely

$$e(T, v) = e_0 + \int_{T_0}^{T} c_{v,\infty}(\tau) d\tau - \frac{a}{v}, \tag{A.14}$$

as $\partial^2 P / \partial T^2 (T, v) = 0$. The van der Waals model is often used in its polytropic form $c_v = $ const, which has the advantage that the reduced EoS

$$P_r(T_r, v_r) = \frac{8}{3} \frac{T_r}{v_r - 1} - \frac{3}{v_r^2}, \tag{A.15}$$

$$e_r(T_r, v_r) = \frac{8}{3} \frac{c_v}{R} T_r - \frac{3}{v_r}, \tag{A.16}$$

$$\tag{A.17}$$

where $P_r = P/P_c$, $v_r = v/v_c$, $T_r = T/T_c$ and $e_r = e/(P_c v_c)$, depend only on the value of the dimensionless specific heat at constant volume c_v/R.

Martin-Hou model

The Martin-Hou thermal EoS (Martin & Hou, 1955), later improved by Martin *et al.* (1959), reads

$$P(T, v) = \frac{RT}{v - b} + \sum_{i=2}^{5} \frac{Q_i(T)}{(v - b)^i}, \tag{A.18}$$

where $b = v_c - \epsilon RT_c/(15P_c)$ for a substance-specific constant $3 < \epsilon < 4$ and the functions Q_i are given by

$$Q_i(T) = A_i + B_i T + C_i e^{-kT_r}, \tag{A.19}$$

with $k = 5.475$ and substance-dependent coefficient A_i, B_i and C_i that can be expressed in terms of critical-point coordinates and of the properties of one state along the saturation curve (Martin & Hou, 1955).

Improved Peng-Robinson-Stryjek-Vera model

The improved Peng-Robinson-Stryjek-Vera (iPRSV) thermal Eos, devised by Van der Stelt *et al.* (2012) to enhance the original EoS by (Peng & Robinson, 1976) and it's modification by (Stryjek & Vera, 1986), reads

$$P(T, v) = \frac{RT}{v - b} - \frac{a}{v^2 + 2vb - b^2}, \tag{A.20}$$

where

$$a = \left(0.457235 \frac{R^2 T_c^2}{P_c}\right) \bar{\alpha}(T_r) \quad \text{and} \quad b = 0.077796 \frac{RT_c}{P_c}. \tag{A.21}$$

The $\bar{\alpha}$-function is given by

$$\bar{\alpha}(T_r) = \left[1 + \left(1 + \sqrt{T_r} \right) \kappa(T_r) \right]^2, \tag{A.22}$$

in which κ is defined by

$$\kappa(T_r) = \kappa_0 + \kappa_1 \left\{ \sqrt{[A - D(T_r + B)]^2 + E} + A - D(T_r + B) \right\} \sqrt{T_r + C}. \tag{A.23}$$

In the expression of κ, $\kappa_0 = 0.378893 + 1.4897153\omega - 0.17131848\omega^2 + 0.0196554\omega^3$ is a function of the acentric factor ω, κ_1 is a substance-specific parameter which can be obtained by regressing experimental data and the remaining constant coefficients read $A = 1.1, B = 0.25, C = 0.2, D = 1.2$ and $E = 0.01$.

Span-Wagner model

Span & Wagner (2003a,b) developed a class of multi-parameter model for non-polar and weakly polar fluids that can potentially provide highly accurate thermodynamic properties for technical applications. The thermodynamic model is expressed in terms of the Helmholtz energy in the reduced form $f_r = f/RT$ as a function of the inverse reduced temperature $\sigma = 1/T_r$ and reduced density $\rho_r = \rho/\rho_c$. The function $f_r(\sigma, \rho_r)$ is therefore a fundamental relation. The functional form $f_r(\sigma, \rho_r)$ comprises two terms, an ideal-gas contribution $f_r^{\mathrm{ig}}(\sigma, \rho_r)$ and a residual part $f_r^{\mathrm{r}}(\sigma, \rho_r)$ which accounts for the influence of intermolecular forces. The ideal-gas Helmholtz energy is obtained from

$$f_r^{\mathrm{ig}}(\sigma, \rho_r) = \frac{h_0 \sigma}{RT_c} - \frac{s_0}{R} - 1 + \ln\left(\frac{\rho_r}{\rho_{r,0}} \frac{\sigma_0}{\sigma} \right) - \frac{\sigma}{R} \int_{\sigma_0}^{\sigma} \frac{c_{p,\infty}}{\tau^2} d\tau + \frac{1}{R} \int_{\sigma_0}^{\sigma} \frac{c_{p,\infty}}{\tau} d\tau, \tag{A.24}$$

where $c_{p,\infty}$ is the ideal-gas isobaric specific heat defined analogously to (A.8), $\sigma_0 = T_c/T_0$ and $\rho_{r,0} = \rho_0/\rho_c$ are the inverse reduced temperature and the reduced density at a prescribed reference state (subscript 0), h_0 and s_0 are the ideal-gas specific enthalpy and entropy, computed in that state. The reduced residual Helmholtz energy for non-polar and weakly polar fluids reads

$$\begin{aligned} f_r^{\mathrm{r}}(\sigma, \rho_r) = \ & n_1 \rho_r \sigma^{0.25} + n_2 \rho_r \sigma^{1.125} + n_3 \rho_r \sigma^{1.5} \\ & + n_4 \rho_r^2 \sigma^{1.375} + n_5 \rho_r^3 \sigma^{0.25} + n_6 \rho_r^7 \sigma^{0.875} \\ & + n_7 \rho_r^2 \sigma^{0.675} e^{-\rho_r} + n_8 \rho_r^5 \sigma^{1.75} e^{-\rho_r} + n_9 \rho_r \sigma^{3.625} e^{-\rho_r^2} \\ & + n_{10} \rho_r^4 \sigma^{3.625} e^{-\rho_r^2} + n_{11} \rho_r^3 \sigma^{14.5} e^{-\rho_r^3} + n_{12} \rho_r^4 \sigma^{12.0} e^{-\rho_r^3}, \end{aligned} \tag{A.25}$$

where $n_i, i = 1, \ldots, 12$ are substance-specific parameters, which result from fitting or extrapolation of a set of experimental data.

Eigenvalue problem for the steady 2D Euler equations

The steady two-dimensional Euler equations (4.1) can be written in quasi-linear form as

$$\mathcal{A}_x(q)\frac{\partial q}{\partial x} + \mathcal{A}_y(q)\frac{\partial q}{\partial y} = 0, \tag{B.1}$$

for the unknown $q(x,t)$ defined in (4.2). In the above equation, $A_x(q) = \nabla_q F_x(q)$ and $A_y(q) = \nabla_q F_y(q)$ are the Jacobians of the fluxes, namely

$$\mathcal{A}_x(q) = \left(\frac{\partial F_{xi}}{\partial q_j}(q)\right)_{1\leqslant i,j\leqslant 4}, \tag{B.2}$$

$$\mathcal{A}_y(q) = \left(\frac{\partial F_{yi}}{\partial q_j}(q)\right)_{1\leqslant i,j\leqslant 4}, \tag{B.3}$$

where F_{xi} and F_{yi} denote the i-th element of the fluxes F_x and F_y, respectively (see definition 4.3), and q_j is the j-th element of q. The generalized eigenvalue problem

$$\left(\mathcal{A}_y(q) - \lambda_k(q)\mathcal{A}_x(q)\right)r_k(q) = 0, \tag{B.4}$$

where λ_k and r_k indicate the k-th eigenvalue and right eigenvector, respectively, is associated with the hyperbolicity of (4.1) and with the notions of genuinely nonlinear or linearly degenerate characteristic fields through the derived quantity $\alpha_k(q) = \nabla_q \lambda_k(q) \cdot r_k(q)$, known as the nonlinearity factor of the k-th field, where

$$\nabla_q \lambda_k(q) = \left(\frac{\partial \lambda_k}{\partial q_i}(q)\right)_{1\leqslant i\leqslant 4}, \tag{B.5}$$

is the vector of partial derivatives of the k-th eigenvalue with respect to q. Genuine nonlinearity of a characteristic field corresponds to $\alpha_k(q) \neq 0$ for all q, while linear degeneracy to $\alpha_k(q) = 0$ for all q. Since the properties of the characteristic fields do not depend on the chosen conservative or nonconservative form of the nonlinear hyperbolic system, a suitable change of variables may be advantageous (Godlewski & Raviart, 2013). Using the map

$$(\rho, \rho u_x, \rho u_y, \rho e + \rho u^2/2) \mapsto (P, u, \vartheta, s), \tag{B.6}$$

where $\vartheta = \tan^{-1}(u_y/u_x)$ is the angle formed by the particle path with the x-axis, the Jacobians in the mapped variables can be written as (the same notation is maintained for simplicity)

$$
\mathcal{A}_x(q) = \begin{bmatrix} u\cos\vartheta/c^2 & \rho\cos\vartheta & -\rho u\sin\vartheta & u\cos\vartheta \left(\frac{\partial\rho}{\partial s}\right)_P \\ 1/\rho & u\cos^2\vartheta & -u^2\cos\vartheta\sin\vartheta & 0 \\ 0 & u\cos\vartheta\sin\vartheta & u^2\cos^2\vartheta & 0 \\ 0 & 0 & 0 & u\cos\vartheta \end{bmatrix}
\tag{B.7}
$$

and

$$
\mathcal{A}_y(q) = \begin{bmatrix} u\sin\vartheta/c^2 & \rho\sin\vartheta & \rho u\cos\vartheta & u\sin\vartheta \left(\frac{\partial\rho}{\partial s}\right)_P \\ 0 & u\cos\vartheta\sin\vartheta & -u^2\sin^2\vartheta & 0 \\ 1/\rho & u\sin^2\vartheta & u^2\cos\vartheta\sin\vartheta & 0 \\ 0 & 0 & 0 & u\sin\vartheta \end{bmatrix}.
\tag{B.8}
$$

For supersonic flows, namely if $M > 1$, the eigenvalue problem (B.4) gives the well-known eigenvalues

$$
\lambda_1(q) = \tan(\vartheta - \mu), \quad \lambda_{2,3}(q) = \tan\vartheta, \quad \lambda_4(q) = \tan(\vartheta + \mu),
\tag{B.9}
$$

and eigenvectors

$$
r_1(q) = \begin{pmatrix} -\rho u^2 \\ u \\ \sqrt{M^2-1} \\ 0 \end{pmatrix}, \quad r_2(q) = \begin{pmatrix} 0 \\ 1 \\ 0 \\ 0 \end{pmatrix}, \quad r_3(q) = \begin{pmatrix} 0 \\ 0 \\ 0 \\ 1 \end{pmatrix}, \quad r_4(q) = \begin{pmatrix} \rho u^2 \\ -u \\ \sqrt{M^2-1} \\ 0 \end{pmatrix},
\tag{B.10}
$$

in which the angle $\mu = \sin^{-1}(1/M)$, is the Mach angle. In the mapped variables, the partial derivatives of the eigenvalues read

$$
\nabla_q\lambda_1(q) = \frac{1+\tan^2(\vartheta-\mu)}{\sqrt{M^2-1}}\left(-\frac{\Gamma-1}{\rho c^2}\frac{1}{u}, \sqrt{M^2-1}, -\frac{1}{c}\left(\frac{\partial c}{\partial s}\right)_P\right),
\tag{B.11}
$$

$$
\nabla_q\lambda_{2,3}(q) = \left(0,0,1+\tan^2\vartheta,0\right),
\tag{B.12}
$$

$$
\nabla_q\lambda_4(q) = \frac{1+\tan^2(\vartheta+\mu)}{\sqrt{M^2-1}}\left(\frac{\Gamma-1}{\rho c^2},-\frac{1}{u}, \sqrt{M^2-1}, \frac{1}{c}\left(\frac{\partial c}{\partial s}\right)_P\right),
\tag{B.13}
$$

so that to the above eigenpairs correspond the nonlinearity factors

$$
\alpha_{1,4}(q) = \Gamma, \quad \alpha_{2,3}(q) = 0,
\tag{B.14}
$$

where a proper rescaling of the eigenvectors is used to eliminate the multiplicative factor in (B.11) and (B.13). Relations (B.14) reflect the role of the fundamental derivative of gasdynamics in determining the nature of the 1–field and 4–field.

C^1 continuity of $\beta_g(\Theta)$ at $\Theta = 0$

The functions $\beta_s(\Theta, \mathbf{A})$ and $\beta_f(\Theta, \mathbf{A})$ graphed in the two halves of the unified (β_g, Θ)–plane and joining along the vertical axis $\Theta = 0$ are continuous up to first derivative with respect to Θ. Of the two shock branches, only the weak shock branch $\beta_{ws}(\Theta, \mathbf{A})$ will be considered as it is the one adjacent to the rarefaction curve. Continuity up to first order is analytically demonstrated hereunder. For simplicity, the case of left-running shocks and rarefaction fans is considered only; the same results will hold for the right-running counterparts because of rotational symmetry between the β_g–Θ relations for left-running and right-running waves. The same notation of 2.3 will be used, although the independent variable here is Θ rather than v_{B}. For ease of notation, the dependence of the shock angle function and of the equivalent-fan angle on the upstream state will be omitted. Firstly, it the deviation angle is zero, the oblique shock wave degenerates into an acoustic wave, so that $\beta_{ws}|_{\Theta=0} = \mu_{\mathrm{A}}$; at the same time, $\beta_f|_{\Theta=0} = \mu_{\mathrm{A}}$, according to (4.21). Thus, the piecewise function defined by (4.22) is continuous at the zero-deviation angle. In order to verify the C^1 continuity at $\Theta = 0$, the derivatives of the shock angle and its equivalent fan angle are compared.

To show this, we first combine the mass balance and tangential momentum balance equations across the shock into

$$\rho_{\mathrm{A}} \tan \beta_s = \rho_{\mathrm{B}} \tan(\beta_s - \Theta), \tag{C.1}$$

and we take the derivative with respect to Θ, thus obtaining

$$\left. \frac{\mathrm{d}\beta_{ws}}{\mathrm{d}\Theta} \right|_{\Theta=0} = -(1 + \tan \mu_{\mathrm{A}}) \left(\rho_{\mathrm{A}} \tan \mu_{\mathrm{A}} + \left. \frac{\mathrm{d}v_{\mathrm{B}}}{\mathrm{d}\beta_s} \right|_{\beta_s = \mu_{\mathrm{A}}} \right)^{-1}, \tag{C.2}$$

in which $\tan \mu_{\mathrm{A}} = (M_{\mathrm{A}}^2 - 1)^{-1/2}$ and taking the limit $[v] \to 0$ in relation (2.33) gives

$$\left. \frac{\mathrm{d}v_{\mathrm{B}}}{\mathrm{d}\beta_s} \right|_{\beta_s = \mu_{\mathrm{A}}} = -2 \frac{\sqrt{M_{\mathrm{A}}^2 - 1}}{\rho_{\mathrm{A}} \Gamma_{\mathrm{A}}}. \tag{C.3}$$

Upon substitution, one gets

$$\left. \frac{\mathrm{d}\beta_{ws}}{\mathrm{d}\Theta} \right|_{\Theta=0} = \frac{\Gamma_{\mathrm{A}}}{2} \frac{M_{\mathrm{A}}^2}{M_{\mathrm{A}}^2 - 1}. \tag{C.4}$$

For the equivalent-fan angle, the derivative of β_f with respect to Θ is simply

$$\frac{\mathrm{d}\beta_f}{\mathrm{d}\Theta} = \frac{1}{2} \left(1 + \frac{\mathrm{d}\mu_{\mathrm{B}}}{\mathrm{d}M_{\mathrm{B}}} \frac{\mathrm{d}M_{\mathrm{B}}}{\mathrm{d}\Theta} \right), \tag{C.5}$$

where $\mathrm{d}\mu_\mathrm{B}/\mathrm{d}M_\mathrm{B} = -\left(M_\mathrm{B} \sqrt{1 - M_\mathrm{B}^2} \right)^{-1}$ and, from the theory of characteristics (see, e.g., Thompson, 1988),

$$\frac{\mathrm{d}M_\mathrm{B}}{\mathrm{d}\Theta} = -\frac{M_\mathrm{B}(1 + (\Gamma_\mathrm{B} - 1)M_\mathrm{B}^2)}{\sqrt{M_\mathrm{B}^2 - 1}}. \tag{C.6}$$

Substitution into equation (C.5) yields, after evaluation at $\Theta = 0$,

$$\left. \frac{\mathrm{d}\beta_f}{\mathrm{d}\Theta} \right|_{\Theta=0} = \frac{\Gamma_\mathrm{A}}{2} \frac{M_\mathrm{A}^2}{M_\mathrm{A}^2 - 1}, \tag{C.7}$$

thus demonstrating, together with equation (C.4), the C^1 continuity of the piecewise function defined by (4.22) at the zero-deviation angle.

By further differentiation, it can be shown that C^2 continuity is not satisfied at $\Theta = 0$. The long calculations leading to this result for a general equation of state are not presented here. We report, as an example, the expression pertaining the perfect-gas case, which reads

$$\left. \frac{\mathrm{d}^2\beta_{ws}}{\mathrm{d}\Theta^2} \right|_{\Theta=0} = \left. \frac{\mathrm{d}^2\beta_f}{\mathrm{d}\Theta^2} \right|_{\Theta=0} + \frac{(\gamma + 1)^2}{16} \frac{M_\mathrm{A}^4(M_\mathrm{A}^2 - 2)}{(M_\mathrm{A}^2 - 1)^{5/2}}. \tag{C.8}$$

The above equation shows that for a perfect gas, unless $M_\mathrm{A} = \sqrt{2}$, a finite jump in the second derivative exists in passing through the no-deviation condition.

C.1 Bisector rule for steady oblique shock waves

In the neighbourhood of the $\Theta = 0$ axis, oblique shock waves are weak enough to be well approximated by isentropic compressions. In this limit, the bisector rule states that the slope of an oblique shock equals the average between the pre-shock and post-shock characteristic slopes. The bisector rule, which was originally addressed by Kluwick (1971) for the case of perfect gases, is extended here to non-ideal equations of state in the context of classical gasdynamics $\Gamma > 0$. For simplicity, the case of left-running shocks and rarefaction fans is considered only. Using (C.4) with $\Gamma_\mathrm{A} \neq 0$, the Taylor series expansion of the shock angle, in the neighbourhood of $\Theta = 0$, reads

$$\beta_s = \sin^{-1}(1/M_\mathrm{A}) + \frac{\Gamma_\mathrm{A}}{2} \frac{M_\mathrm{A}^2}{M_\mathrm{A}^2 - 1} \Theta + \mathcal{O}(\Theta^2), \tag{C.9}$$

where $\sin^{-1}(1/M_\mathrm{A}) = \mu_\mathrm{A} = \beta_{c\mathrm{A}}$ is the slope of the pre-shock characteristics lines with respect to the pre-shock flow direction. In the post-shock state, the slope of the characteristics lines (again with respect to the pre-shock flow direction) is

$$\beta_{c\mathrm{B}} = \Theta + \sin^{-1}(1/M_\mathrm{B}), \tag{C.10}$$

where the second term is expanded, in the neighbourhood of $\Theta = 0$, as

$$\sin^{-1}(1/M_\mathrm{B}) = \sin^{-1}(1/M_\mathrm{A}) - \frac{1}{M_\mathrm{A}\sqrt{M_\mathrm{A}^2 - 1}} \left. \frac{\mathrm{d}M_\mathrm{B}}{\mathrm{d}\Theta} \right|_{\Theta=0} \Theta + \mathcal{O}(\Theta^2). \tag{C.11}$$

Because of the isentropic limit, the Mach number derivative in the above expression has the same form as in Prandtl-Meyer waves (C.6), namely

$$\left. \frac{\mathrm{d}M_\mathrm{B}}{\mathrm{d}\Theta} \right|_{\Theta=0} = -\frac{M_\mathrm{A}(1 + (\Gamma_\mathrm{A} - 1)M_\mathrm{A}^2)}{\sqrt{M_\mathrm{A}^2 - 1}}. \tag{C.12}$$

Thus, the post-shock characteristic slope in the isentropic limit is given by

$$\beta_{c\mathrm{B}} = \sin^{-1}(1/M_{\mathrm{A}}) + \Gamma_{\mathrm{A}}\frac{M_{\mathrm{A}}^2}{M_{\mathrm{A}}^2 - 1}\Theta + \mathcal{O}(\Theta^2), \tag{C.13}$$

showing that, if oblique shock waves are weak enough that the isentropic approximation applies, namely in the neighbourhood of $\Theta = 0$,

$$(\beta_{c\mathrm{A}} + \beta_{c\mathrm{B}})/2 = \sin^{-1}(1/M_{\mathrm{A}}) + \frac{\Gamma_{\mathrm{A}}}{2}\frac{M_{\mathrm{A}}^2}{M_{\mathrm{A}}^2 - 1}\Theta + \mathcal{O}(\Theta^2) = \beta_s, \tag{C.14}$$

that is, the shock angle is the bisector of the pre-shock and post-shock characteristic lines.

Numerical simulations of quasi-1D nozzle flows: capturing sonic shocks

Selected contents from:

Vimercati, D. & Guardone, A. 2018. On the numerical simulation of non-classical quasi-1D steady nozzle flows: Capturing sonic shocks. *Applied Mathematics and Computation*, 319, 617-632.

In this Appendix, the numerical simulation of non-classical nozzle flows within the quasi-1D approximation is considered. Often, the numerical simulation of conservation laws with source terms, such as the quasi-1D Euler equations, is carried out using fractional step methods, in which one alternates the solution of the associated homogeneous system of conservation laws and the solution of a system of ordinary differential equations in which the source term is the vector field. However, fractional step methods can easily fail if the solution is close to a steady state, where the source term must exactly balance the flux gradient (LeVeque, 1998). In order to overcome these difficulties, several unsplit procedures have been proposed (see, e.g., Roe, 1987; Bermudez & Vazquez, 1994; LeVeque, 1998; Bale *et al.*, 2003; Caselles *et al.*, 2009), which mainly rely on upwinding techniques for both the flux gradient and the source term. Here, we focus on numerical schemes that combine an approximate Riemann solver of the Roe type, whose capability of simulating accurately nozzle flows is well assessed (Glaister, 1988; Liou *et al.*, 1990; Mottura *et al.*, 1997; Guardone & Vigevano, 2002; Cinnella, 2006), with an upwind treatment of the source term. In this respect, one of the main advantages of a Roe solver is the capability, rooted in the so-called Property U, of capturing steady shocks exactly, thus making this class of schemes particularly suitable for steady-state computations. The latter claim will be confirmed by numerical experiments with an approximate Roe solver (so called because Property U is not satisfied) adopting a simplified procedure for minimal implementation complexity and computational costs.

Since Roe schemes are approximate Riemann solvers, they all must be complemented with a suitable entropy fix in order to prevent the occurrence of entropy violating solutions whenever the flux computed from the approximate solver differs from the exact one. If the steady state includes shocks that are sonic either on the upstream or downstream side, there is possible that a transonic

expansion lies in the vicinity of these shocks during convergence to their final, steady-state position. The interaction between the entropy fix and the underlying source term is well-known to be crucial for the steady-state balancing. In this respect, standard corrections (e.g., the entropy fix of Harten & Hyman, 1983) modify the characteristic speed only in the attempt to generate sufficient numerical viscosity; a similar treatment, however, can easily lead to inaccuracies and balancing issues, as the source term is not handled accordingly. The prototypical synchronous entropy fix of van Leer *et al.* (1989), which operates simultaneously on the characteristic speed and on the source term, is considered. This transonic correction was devised in order to break down sonic glitches in the throat of choked nozzle flows, which are possibly generated by standard entropy corrections. Our numerical experiments will show that the synchronous splitting can efficiently enforce the numerical balance near sonic shocks and that the neighbouring transonic expansion can be cancelled provided that the numerical dissipation is adjusted.

D.1 Governing equations

The quasi-1D Euler equations, can be written in the general form of a balance law for the vector unknown $q(x,t)$ as

$$\frac{\partial q}{\partial t} + \frac{\partial}{\partial x} F(q) = \psi(q,x), \tag{D.1}$$

where

$$q = \left(\rho, \rho u, \rho e + \rho u^2/2 \right)^T \tag{D.2}$$

is the vector of balance variables density and

$$F(q) = \left(\rho u, \ \rho u^2 + P, \ \rho h^t u \right)^T \tag{D.3}$$

is the flux function, where the pressure is expressed as function of the balance variables, for instance, from the equation of state $P(e,\rho)$ for the internal energy $e = q_3 - q_2^2/(2q_1)$ and the density $\rho = q_1$. Other thermodynamic quantities encountered in the following are obtained likewise. Finally,

$$\psi(q,x) = -\frac{A'(x)}{A(x)} \left(\rho u, \ \rho u^2, \ \rho h^t u \right)^T \tag{D.4}$$

is the geometrical source term, where $A(x)$ is the known cross-sectional area distribution along the axial coordinate x. In order to account for discontinuous solutions, system (D.1) is replaced at the discontinuity location by the Rankine-Hugoniot relation, written in a laboratory reference frame as

$$[F(q)] = u_s[q], \tag{D.5}$$

where $[\cdot]$ indicates the jump between the post-shock and pre-shock states and u_s is speed of propagation of the discontinuity. Relations (D.5) must be complemented by suitable admissibility criteria that rule out unphysical shock waves, see 2.3.

The flux Jacobian $\mathcal{A}(q) = \left(\partial F_i(q)/\partial u_j \right)_{1 \leqslant i,j \leqslant 3}$ takes the form

$$\mathcal{A}(q) = \begin{bmatrix} 0 & 1 & 0 \\ \frac{\partial P}{\partial q_1} - u^2 & \frac{\partial P}{\partial q_2} + 2u & \frac{\partial P}{\partial q_3} \\ u\left(\frac{\partial P}{\partial q_1} - h^t \right) & h^t + u\frac{\partial P}{\partial q_2} & u\left(1 + \frac{\partial P}{\partial q_3} \right) \end{bmatrix} \tag{D.6}$$

where the partial derivatives of the pressure with respect to the conservative variables can be written as

$$\frac{\partial P}{\partial q_1} = \left(\frac{\partial P}{\partial \rho}\right)_e - \frac{1}{\rho}\left(e - \frac{u^2}{2}\right)\left(\frac{\partial P}{\partial e}\right)_\rho, \tag{D.7}$$

$$\frac{\partial P}{\partial q_2} = -\frac{u}{\rho}\left(\frac{\partial P}{\partial e}\right)_\rho, \tag{D.8}$$

$$\frac{\partial P}{\partial q_3} = \frac{1}{\rho}\left(\frac{\partial P}{\partial e}\right)_\rho. \tag{D.9}$$

and gives real eigenvalues

$$\lambda_1(q) = u - c, \qquad \lambda_2(q) = u, \qquad \lambda_3(q) = u + c. \tag{D.10}$$

In single-phase thermodynamic regions, the speed of sound is strictly positive, so that (D.1) constitutes a strictly hyperbolic system of balance laws. One can recognize the well-known left-facing characteristic waves ($dx/dt = u - c$) and right-facing waves ($u + c$), separated by the particle trajectories (see, e.g., Thompson, 1988). The nature of the characteristic fields (D.10) is determined by the nonlinearity factors, defined analogously to the steady 2D case (Appendix B), which read

$$\alpha_2(q) = 0, \qquad \alpha_{1,3}(q) = \mp\Gamma, \tag{D.11}$$

While the second characteristic field is linearly degenerate, the first and third fields could exhibit either genuine nonlinearity, if the flow fully evolves in the regime $\Gamma > 0$ or $\Gamma < 0$, or mixed nonlinearity, if fluid states features both $\Gamma > 0$ and $\Gamma \leqslant 0$[1]. The scale-invariant flows (functions of x/t) associated with the above characteristic fields can be: continuously differentiable simple waves, shock waves or their combinations (composite waves) in the left-facing or right-facing wave families and contact discontinuities in the degenerate field (Menikoff & Plohr, 1989). As discussed in §4.3, the scale-invariant wave patterns in the (x, y)–plane for 2D steady supersonic flow and in the (x, t)–plane for the present unsteady 1D case are qualitatively equivalent. In particular, the wave curve consisting of states connected to a given initial state by a scale-invariant solution are analogous to the extended wave curves computed in §4.4.1 and 4.5.1 (provided, of course, that the spreading of simple-wave fans is interpreted in 1D as time progresses, rather than in 2D and oblique shocks are replaced by unsteady normal shocks).

D.2   Upwind-differencing schemes for non-homogeneous hyperbolic systems

Let us define a uniform grid $x_j = x_0 + j\Delta x$, $j = 1, \ldots, N$, with cell interfaces $x_{j\pm1/2} = x_j \pm \Delta x/2$, and let $Q_j(t)$ denote the numerical approximation to the cell average of q over the jth cell, $x \in [x_{j-1/2}, x_{j+1/2}]$. We assume that the approximate solution of (D.1)-(D.5) is sought within the computational domain $x \in [x_0, x_N]$ by solving a sequence of interface Riemann problems (Toro, 2013), with initial data given by the piecewise constant states Q_j, of the form

$$\frac{\partial q}{\partial t} + \hat{\mathcal{A}}_{j+1/2}\frac{\partial q}{\partial x} = \Delta x\,\Psi_{j+1/2}\,\delta(x - x_{j+1/2}), \tag{D.12}$$

where $\hat{\mathcal{A}}_{j+1/2}$ is an approximate Jacobian and the source term has been replaced by a delta of amplitude $\Psi_{j+1/2}$ located at the cell interface. This treatment of the source term, introduced by

---

[1]Non-classical shock waves may feature $\Gamma > 0$ both at the pre-shock and at the post-shock state, see Zamfirescu *et al.* 2008. This, however, requires that the corresponding shock adiabat bridges the thermodynamic region $\Gamma < 0$.

Bale *et al.* (2003) in the context of wave-propagation methods for balance laws, leads naturally to the following wave decomposition,

$$\hat{\mathcal{A}}_{j+1/2}(Q_{j+1} - Q_j) - \Delta x\,\Psi_{j+1/2} = \sum_k \beta^k_{j+1/2}\,r^k_{j+1/2}, \tag{D.13}$$

where $r^k_{j+1/2}$ is the k-th right eigenvector of the approximate Jacobian (the notation is slightly different from that of §4 and Appendix B, here the index is displayed in the superscript for more clarity). The associated waves of intensity $\beta^k_{j+1/2}$ are thus distributed to the neighbouring cells based on the sign of the corresponding eigenvalues. This procedure yields a semi-discrete scheme of the form

$$Q'_j = -\frac{1}{\Delta x}\left(F_{j+1/2} - F_{j-1/2}\right) + \frac{1}{2}\left(\Psi_{j+1/2} + \Psi_{j-1/2}\right), \tag{D.14}$$

where the numerical flux $F_{j+1/2}$ is given by

$$F_{j+1/2} = \frac{1}{2}\left(F(Q_j) + F(Q_{j+1})\right) - \frac{1}{2}\sum_k \text{sgn}(\lambda^k_{j+1/2})\,\beta^k_{j+1/2}\,r^k_{j+1/2}, \tag{D.15}$$

showing the upwind character of both the flux difference and the source term integral. In the following sections are described the building blocks of our class of schemes, namely the choice of the approximate Jacobian and the discretization of the source term along with the related entropy conditions.

D.2.1 Roe linearization for non-ideal gases

One of the most popular and effective approximate Riemann solvers, based on a local linearization of the original nonlinear system, is due to Roe (1981). The basic theory behind the Riemann solver of Roe is here recalled; for a detailed review see, e.g., LeVeque (1992). Let q_l and q_r denote the left and right states, respectively, in the Riemann problem for the hyperbolic system with flux function $F(q)$ and flux Jacobian $\mathcal{A}(q)$. A Roe linearization matrix is a constant-coefficient matrix $\hat{\mathcal{A}}(q_l, q_r)$ satisfying the following properties, collectively referred to as Property U:

(i) $\hat{\mathcal{A}}(q_l, q_r)(q_r - q_l) = F(q_r) - F(q_l)$.

(ii) $\hat{\mathcal{A}}(q_l, q_r)$ is diagonalizable with real eigenvalues.

(iii) $\hat{\mathcal{A}}(q_l, q_r) \to \mathcal{A}(q)$ smoothly as $q_l, q_r \to q$.

The above conditions ensure, in the order specified, the conservation of the resulting algorithm, the hyperbolicity of the linearized system and the consistency of the approximation. In addition, in the special case where q_l and q_r are connected by a single discontinuity, conditions (i) and (ii) guarantee that the approximate Riemann solution agrees with the exact Riemann solutions.

   Once the Roe linearization matrix has been defined, the approximate Jacobian at $x_{j+1/2}$ is obtained by setting $\hat{\mathcal{A}}_{j+1/2} = \hat{\mathcal{A}}(Q_j, Q_{j+1})$. Despite the explicit form of $\hat{\mathcal{A}}(q_l, q_r)$ depends on the particular linearization procedure employed, it has been noticed (see Mottura *et al.*, 1997; Guardone & Vigevano, 2002) that two general classes of linearization techniques can be delineated. The first one includes Roe matrices, termed in *Jacobian form*, that are obtained by evaluating the flux Jacobian at a suitable intermediate state $\tilde{q}(q_l, q_r)$, namely

$$\hat{\mathcal{A}}(q_l, q_r) = \mathcal{A}\left(\tilde{q}(q_l, q_r)\right). \tag{D.16}$$

With such an approach, condition (ii) is automatically satisfied and (iii) reduces to $\tilde{q}(q_l, q_r) \to q$ as $q_l, q_r \to q$. The intermediate state is obtained from condition (i), which is easily seen to yield

a one-parameter family of solutions and thus requires that an additional constraint is specified. For a perfect gas, the additional constraint is an identity if u and h^t are chosen as the independent variables. In this case, the renowned Roe averages

$$\tilde{u} = \frac{\sqrt{\rho_l}u_l + \sqrt{\rho_r}u_r}{\sqrt{\rho_l} + \sqrt{\rho_r}} \qquad \text{and} \qquad \tilde{h}^t = \frac{\sqrt{\rho_l}h_l^t + \sqrt{\rho_r}h_r^t}{\sqrt{\rho_l} + \sqrt{\rho_r}},$$

are recovered. Roe linearizations in Jacobian form are rather uncommon for non-ideal fluids, because of the complexity of the system of equations stemming from condition (i). A notable example is the Roe linearization proposed by Guardone & Vigevano (2002), in which the supplementary condition is selected in order to reduce significantly the complexity associated with the definition of the intermediate state.

An alternative approach stems from the observation that, for a general non-ideal equation of state, only the elements of the *extended* state

$$p = \left(u, h^t, \frac{\partial P}{\partial q_1}, \frac{\partial P}{\partial q_2}, \frac{\partial P}{\partial q_3} \right) \tag{D.17}$$

explicitly appear into the definition (D.6) of the flux Jacobian (in the perfect-gas case, only u and h^t appear explicitly, owing to the first-degree homogeneity of the corresponding flux function). The so-called linearizations in *quasi-Jacobian form* assume the Roe matrix to be of the form

$$\hat{\mathcal{A}}(q_l, q_r) = \mathcal{A}\left(\tilde{p}(q_l, q_r)\right), \tag{D.18}$$

where each of the elements of the intermediate extended state $\tilde{p}$ is taken as independent unknown of the linearization problem, i.e. the velocity, the total enthalpy and the partial derivatives of the pressure which are no longer computed from some state $\tilde{q}$ (in which case the linearization would indeed be in Jacobian form). The definition of the five parameters is usually carried out by assuming the celebrated Roe averages for the velocity and total enthalpy along with relation

$$\widetilde{\frac{\partial P}{\partial q_1}} = -\tilde{u}\widetilde{\frac{\partial P}{\partial q_3}} \tag{D.19}$$

to enforce thermodynamic consistency. This procedure reduces the number of degrees of freedom resulting from the imposition of condition (i) to one. Based on the choice of the remaining parameter, many different methods have been derived that include most of the Roe linearizations available in the scientific literature, such as those due to Abgrall (1991), Cox & Cinnella (1994), Glaister (1988), Grossman & Walters (1989), Liou *et al.* (1990), Vinokur & Montagné (1990). As pointed out by Toumi (1992), one possible drawback of linearizations in quasi-Jacobian form, with respect to those in Jacobian form, is the lack of a compatible intermediate state, which may lead to inconsistencies whenever the elements of the extended state are used to compute derived thermodynamic quantities. In addition, this approach does not guarantee, in general, that conditions (ii) and (iii) are fulfilled and further constraints could be required.

It has been noticed (see, e.g., Abgrall, 1991; Mottura *et al.*, 1997), however, that none of these formulations was proved to be clearly superior to the others, while, on the other hand, the numerical efficiency is largely influenced by the complexity of a particular formulation. In this respect, most difficulties in the computation of $\hat{\mathcal{A}}$ lie with condition (i) of Property U. This ultimately led some researchers to adopt solvers which do not satisfy exactly condition (i), but only in some approximate manner (thus, they are not formally Roe schemes and will be referred to as approximate Roe solvers), still giving reasonably accurate results, see Masella *et al.* (1999), Buffard *et al.* (2000), Cinnella (2006). These simplified procedures sacrifice some of the advantages of

an exact (in the sense that Property U is satisfied exactly) linearization in order to minimize implementation complexity and computational costs.

To the best of the authors' knowledge, there does not exist any study of the performance of these Roe-type linearizations when applied to the computation of steady nozzle flows of non-ideal gases, that possibly include non-classical waves. Thus, numerical experiments will initially focus on the assessment of selected linearization procedures. Three formulations will be tested as representative of different linearization philosophies: the solvers of Guardone & Vigevano (2002) and of Vinokur & Montagné (1990) as representative of the exact linearizations in Jacobian and quasi-Jacobian form, respectively, and the simplified formulation of Cinnella (2006) as representative of the approximated linearization procedures.

D.2.2 Source term discretization

The Roe schemes described above require that some sort of discretized form of the source term $\Psi_{j+1/2}$ is defined at cell edges. Note that, if the interface values $\Psi_{j+1/2}$ approximate the source term to $\mathcal{O}(\Delta x^2)$, then the resulting scheme (D.14)-(D.15) is second-order accurate in space (it is easy to see that each flux difference and source term integral are centred on the same interval). In this work, we use the simple average

$$\Psi_{j+1/2} = \frac{1}{2} \left(\psi(Q_j, x_j) + \psi(Q_{j+1}, x_{j+1}) \right) \tag{D.20}$$

to discretize the source term, even though this choice will not yield a well-balanced scheme, i.e. initial equilibrium values would not be preserved by the method. As discussed by LeVeque (2011), a suitable average resulting in a well-balanced scheme can be conveniently defined for diverse problems; these, unfortunately, do not include the quasi-1D Euler equations. However, in most numerical experiments for which our scheme appropriately models the flow field (recognizing, for instance, transonic expansion or non-classical composite waves), the residual of the solution is as low as 10^{-10} and the scheme is found to be balanced almost to machine precision.

D.2.3 Sonic entropy correction

The upwind contribution to the interface flux along the k-th right eigenvector r^k in (D.15) can be written as

$$\text{sgn}(\lambda^k)\beta^k = |\lambda^k|\alpha^k - \text{sgn}(\lambda^k)z^k\Delta x, \tag{D.21}$$

where we have used $Q_{j+1} - Q_j = \sum_k \alpha^k r^k$ and $\Psi_{j+1/2} = \sum_k z^k r^k$ (subscript $j + 1/2$ has been dropped for brevity). If a transonic expansion occurs at the interface Riemann problem, namely if the data are such that $\lambda_j^k < 0 < \lambda_{j+1}^k$, the eigenvalue λ^k of the dissipation matrix can possibly vanish, thus leading to the formation of entropy-violating shocks (with outgoing characteristics). Popular transonic entropy fixes are those due to Harten (1983), Harten & Hyman (1983), LeVeque (1992) or Kermani & Plett (2001), which rely on the model of a smooth transonic expansion wave to generate a sufficient amount of numerical viscosity. These transonic fixes lead to redefine in some way the characteristic speed near a sonic point; for instance, in the case of the Harten & Hyman (1983) correction, $|\lambda^k|$ is replaced by

$$|\lambda^k|_{\text{HH}}^* = \frac{1}{2} \left(\frac{(\lambda^k)^2}{\delta_\lambda^k} + \delta_\lambda^k \right), \tag{D.22}$$

where $\delta_\lambda^k = \max(0, \lambda^k - \lambda_j^k, \lambda_{j+1}^k - \lambda^k)$ controls the band over which the entropy correction is enforced. The above mentioned entropy corrections have been successfully employed to break

Test Case	Inlet			Outlet		
	P/P_c	ρ/ρ_c	M	P/P_c	ρ/ρ_c	M
TC1	1.3295	1.3056	0.4655	1.3210	1.2955	0.3832
TC2	1.0708	1.1964	0.4695	1.0707	1.1946	0.3778
TC3	0.1658	0.0083	0.6070	0.0468	0.0024	1.7000
TC4	1.0726	1.2000	0.4561	1.0847	1.2253	0.3314
TC5	1.0829	1.2223	0.4415	0.3206	0.1418	1.5178

TABLE D.1. Inlet ($x = -1$) and outlet ($x = 1$) boundary conditions for each of the test cases.

down entropy-violating shocks in both unsteady and steady-state problems governed by hyperbolic conservation laws. However, direct application of any of these sonic fixes to systems incorporating source term may lead to unsatisfactory results, especially when a steady-state solution is sought. The most noticeable defect, as shown by van Leer *et al.* (1989), consists in a two-cell sonic plateau placed at the throat of steady nozzle flows in choked conditions, where the transition from subsonic to supersonic flow takes place. In the work of van Leer *et al.* (1989) a cure to this problem, known as the entropy bypass, is proposed. The entropy bypass consists in the synchronous splitting of the characteristic speed and of the source term near a sonic point. If a transonic rarefaction is detected, namely if $\lambda_j^k < 0 < \lambda_{j+1}^k$, the average values $\bar{\lambda}^k = (\lambda_j^k + \lambda_{j+1}^k)/2$, $\bar{z}^k = (z_j^k + z_{j+1}^k)/2$ and the spreading $\delta_\lambda^k = d_{\text{ef}}(\lambda_{j+1}^k - \lambda_j^k)$, $\delta_z^k = d_{\text{ef}}(z_{j+1}^k - z_j^k)$ for both the characteristic speed and the source term can be recognized. These are used to compute the effective absolute value $|\lambda^k|_{VL}^*$,

$$|\lambda^k|_{\text{VL}}^* = \frac{(\bar{\lambda}^k)^2}{\delta_\lambda^k} + \frac{\delta_\lambda^k}{4}, \tag{D.23}$$

which is used in place of $|\lambda^k|$ and the effective source term z^{k*},

$$z^{k*} = \frac{\bar{\lambda}^k}{\delta_\lambda^k}\left(2\bar{z}^k - \bar{\lambda}^k\frac{\delta_z^k}{\delta_\lambda^k}\right) + \frac{\delta_z^k}{4}, \tag{D.24}$$

which is used in place of $\text{sgn}(\lambda^k)z^k$ in (D.21). As pointed out by van Leer *et al.* (1989), adding a suitable splitting of the source term to that of the characteristic speed, in the presence of transonic expansions, allows to smoothly match the backward and forward facing parts of the fan while the sonic point is approaching its final position in the throat (where the source term vanishes), thus avoiding sonic plateaus in the steady-state solution. The above transonic flux formula contains a free parameter d_{ef} controlling the spreading of the expansion fan. In their numerical experiments, van Leer *et al.* (1989) report that $d_{\text{ef}} = 2 \div 4$ allows to reach the correct steady-state flow at a sonic throat, starting from arbitrary initial conditions, whereas lower values of d_{ef} would result in the formation of a sonic plateau. The analysis of Goodman & LeVeque (1988) also indicates that optimal robustness in handling a sonic throat is obtained with $d_{\text{ef}} = 4$.

In the following numerical experiments, scheme (D.14)-(D.15) for the Jacobian, quasi-Jacobian and simplified formulation of the Roe matrix will at first be tested along with different entropy corrections. To the best of our knowledge, there has been no investigation on the effectiveness of this class of schemes in steady-state computations of non-ideal, possibly non-classical, nozzle flows. Next, the performance of the synchronous splitting of van Leer *et al.* (1989) will be studied, with particular emphasis on the role of the artificial spreading of the expansion fan.

D.3   Numerical results

In this section, the upwind schemes described above are applied to the solution of a set of steady nozzle flows of BZT fluids, which are all modelled as van der Waals gases with $c_v/R = 50$. All computations refer to the converging-diverging geometry used in §3. A 400-cell uniform computational grid is used throughout this work. The boundary conditions for the test cases considered in the following are reported in Table D.1. Characteristic boundary treatment is used. Solutions are marched in time with the forward Euler time stepping (we are not interested in temporal accuracy). The CFL number is set to 0.8. The initial condition for each of the test cases is a constant distribution of the mass flow rate and a linear distribution of pressure and density matching the boundary conditions. No flux limiter will be used, insofar as scheme (D.14)-(D.15), in which any of the above-mentioned Roe solvers is used along with treatment (D.20) for the source term, will yield second-order accurate steady state solutions. Local time stepping is used to speed up convergence to the steady state. The 2-norm of the time derivative of the numerical solution is used as stopping criteria: when this residual is 10^{-10} times a reference residual (computed in the initial stages of the time marching), the flow is considered steady. The exact solutions to which our numerical results are compared, are computed using the technique described in §3.

D.3.1   Assessment of selected Roe solvers and entropy fixes

To begin with, the effect of one particular choice of the Roe solver and of the entropy correction is discussed. The Roe formulations examined here are the exact solvers due to Vinokur & Montagné (1990), Guardone & Vigevano (2002) and the approximate solver of Cinnella (2006). The shorthand "VM", "GV" and "CS", respectively, will be used for the three solvers to be tested. At sonic points, the entropy corrections of Harten & Hyman (1983), LeVeque (1992) and Kermani & Plett (2001) are considered, to be referred to as "HH", "LV" and "KP" corrections, respectively.

In our first test case, denoted as TC1, the inlet pressure and density are selected in the dense-gas thermodynamic region at slightly supercritical conditions. The exit boundary data is such that the steady-state solution features a subsonic to supersonic transition in the throat and a compression shock wave in the diverging section. The computed Mach number distributions are shown in figures D.1-D.3 along with the exact solutions; the corresponding convergence histories are reported in figures D.11(*a-c*). Note that the scheme obtained with the CS solver and LV entropy fix failed to converge; the Mach number distribution reported in figure D.2 is a snapshot extracted from the limit cycle in which the computation is trapped. The considered Roe formulations exhibit similar performances in smooth regions of the flow field: the solutions of the VM and GV solvers are always superposed and CS performs only slightly different, owing to the fact that the latter satisfies Property U to within $\mathcal{O}(\|q_r - q_l\|^2)$. However, none of the transonic entropy fix methods examined here is able to produce a perfectly smooth transition in the throat of the nozzle (see enlargements in figures D.1-D.3). Here, the closest agreement with the exact solutions is obtained with the KP correction, owing to the larger band over which the correction is enforced and the correspondingly larger artificial numerical viscosity introduced (see Kermani & Plett, 2001). The two-cell plateau that is computed when the sonic point is approaching the throat also causes slow convergence towards the steady state. This agrees with the analysis of van Leer *et al.* (1989). Regarding the behaviour of the three solvers near discontinuities (see enlargements in figures D.1-D.3), the exact solvers (VM and GV) are considerably more accurate than the simplified procedure. While the VM and GV formulations produce sharp shock profiles, the CS solver introduces large oscillations both upstream and downstream of the discontinuity. Presumably, this effect is a direct consequence of the larger numerical viscosity introduced by the simplified procedure, which is not capable of capturing steady shocks across a single cell interface and tends to smear the discontinuities across multiple cells.
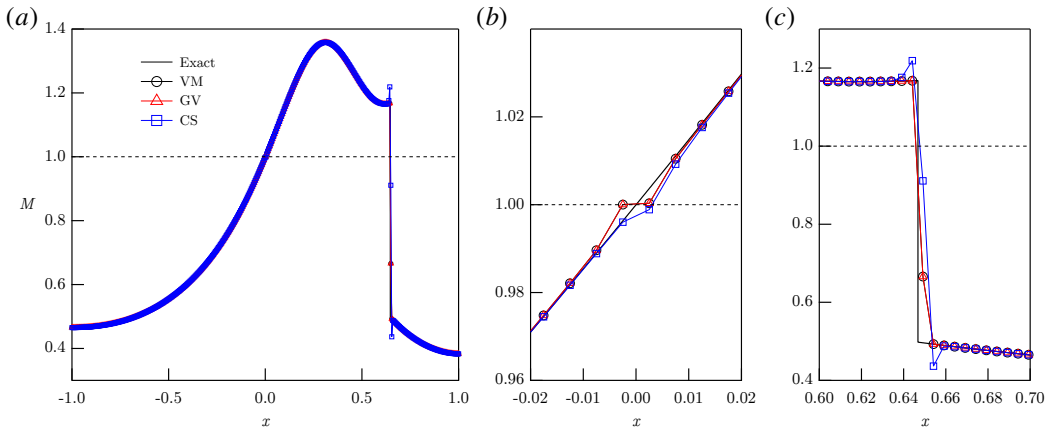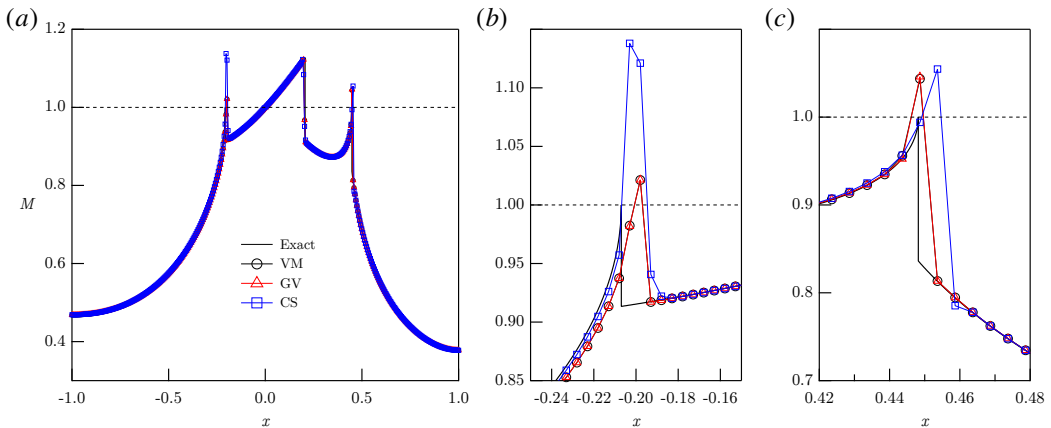
FIGURE D.1. TC1-HH: comparison of the Mach number distributions obtained with the Roe solvers evaluated and the entropy correction of Harten and Hyman on a non-ideal, yet classical, shocked nozzle flow. (*a*) Complete flow field; (*b*) enlargement of the throat region; (*c*) enlargement of the shock wave in the diverging section.
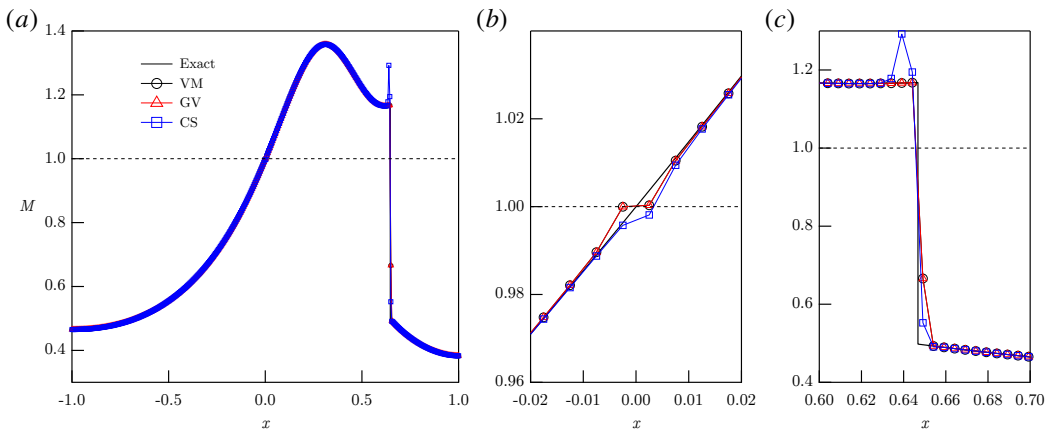
FIGURE D.2. TC1-LV: same as Figure D.1 but with LeVeque's entropy correction.

Next, a more challenging test case is considered. Boundary data for TC2 have been selected to obtain three discontinuities within the nozzle, as shown in figures D.4-D.6. The first one is a rarefaction shock with sonic upstream state, located upstream of the throat. The remaining ones are compression shocks downstream of the throat: the second one is a classical shock, whereas the third one is a non-classical shock with sonic upstream state. All the simulations carried out with the HH and LV entropy corrections failed to converge, see the convergence histories in figures D.11(*d*-*f*); the Mach number distribution reported in figures D.4 and D.5 are snapshots extracted from the limit cycle in which the computations ended. The analysis of the residual's distribution reveals that, using HH and LV fixes, balancing issues occur at cell interfaces neighbouring the sonic shocks on the upstream side, where a transonic expansion is computed in time marching from the initial distribution of the balance variables and prevents the solution from reaching a steady state. On the contrary, no balancing issues occur using the KP fix; the larger bandwidth of this correction guarantees a numerical steady state solution. Nevertheless, none of the considered
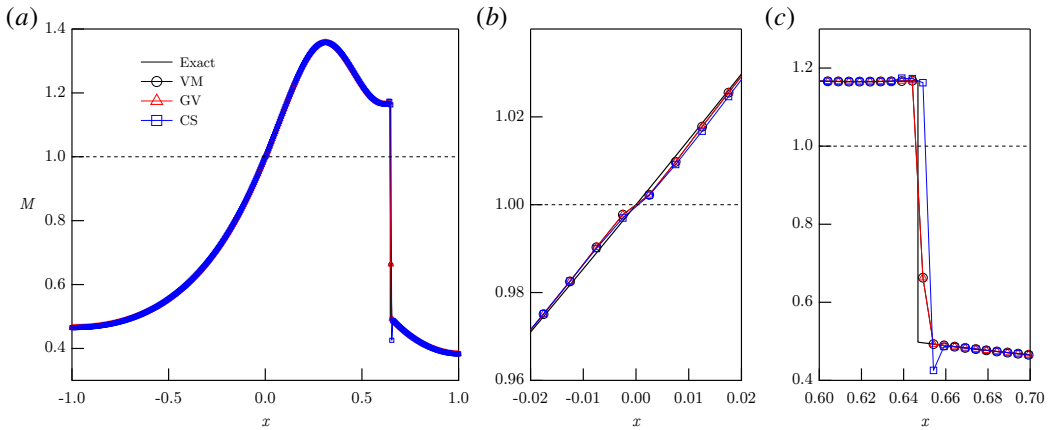
FIGURE D.3. TC1-KP: same as Figure D.1 but with Kermani and Plett's entropy correction.

FIGURE D.4. TC2-HH: comparison of the Mach number distributions obtained with the Roe solvers evaluated and the entropy correction of Harten and Hyman on a non-classical nozzle flow with three shock waves, two of which have sonic upstream state. (*a*) Complete flow field; (*b*) and (*c*) enlargements of the sonic shocks.

Roe solvers and entropy fixes is accurate in the close proximity of sonic shocks (the KP fix, in this respect, is the most inaccurate), nor in the throat section as already observed in the previous test case.

Similarly to TC1, the exact solvers seem to perform better than the simplified solver. Moreover, if the TC2 simulations are initialised using the exact steady-state solution, which does not include transonic expansions near the sonic shocks, the method equipped with either VM or GV solvers preserves the initial distribution without adding sonic points; on the other hand, the CS solver produces a distribution similar to that reported in figures D.4-D.6 (without converging to a steady state). The latter observation suggests that, for the exact solvers, the inaccuracies near sonic shocks and the lack of convergence to the steady state can be eliminated or reduced by using more sophisticated entropy corrections accounting for the presence of the background source term. In contrast, the glitches exhibited by the simplified solver should be ascribed not only to the entropy fix, but also to the solver itself, thus pointing again to the benefits (rooted in Property U) of a sharp-shock representation.
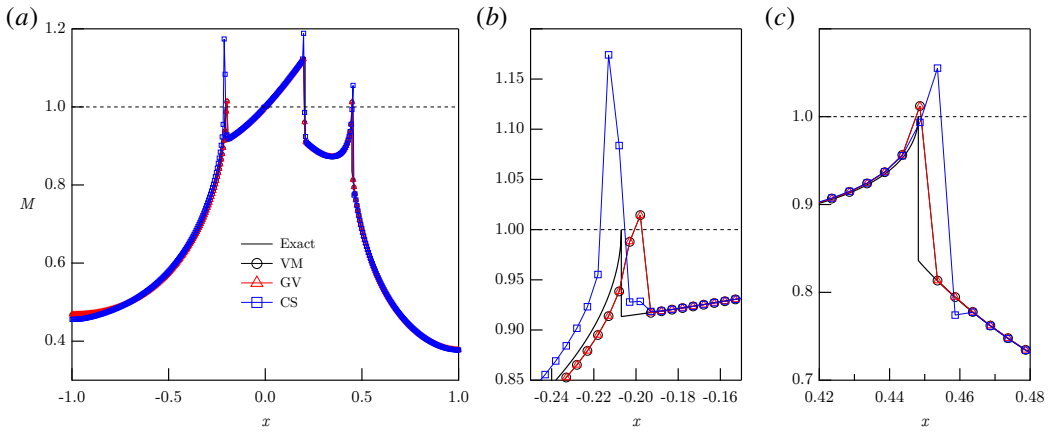
FIGURE D.5. TC2-LV: same as Figure D.4 but with LeVeque's entropy correction.
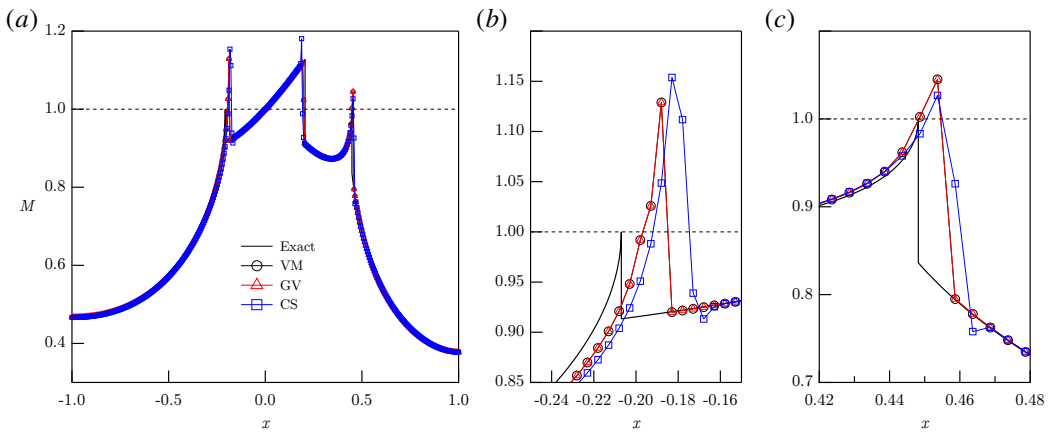
FIGURE D.6. TC2-KP: same as Figure D.4 but with Kermani and Plett's entropy correction.
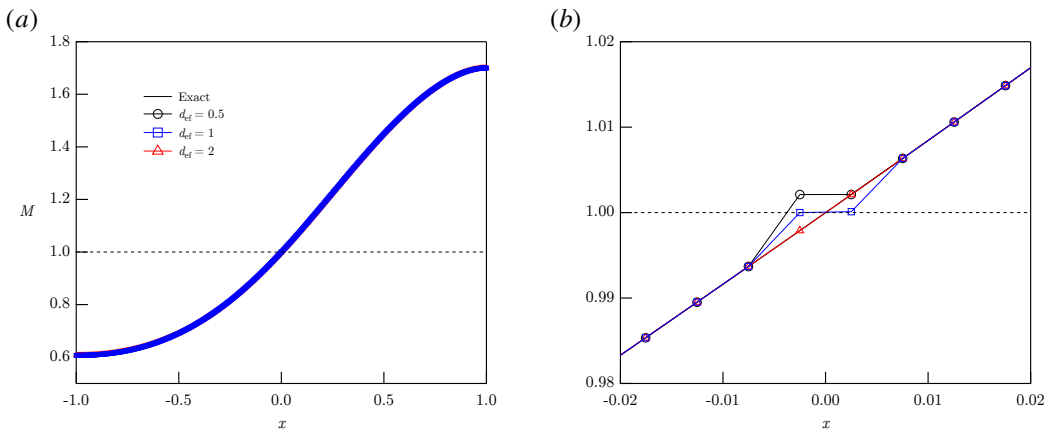
FIGURE D.7. TC3: Mach number distributions obtained from the GV solver with equipped with the entropy bypass on a smooth nozzle flow expanding from subsonic inlet conditions to supersonic exit conditions. (*a*) Complete flow field; (*b*) enlargement of the throat section.

D.3.2   The entropy bypass for capturing sonic shocks

The assessment of the different Roe solvers carried out in the previous section calls attention to the superior performances of the exact solvers for steady-state calculations. In this respect, the GV and VM solvers showed negligible differences in the numerical results. In the following, we will examine the behaviour of an exact Roe solver in conjunction with entropy corrections that are able to produce the desired steady state balance and accuracy near sonic shock waves. Without loss of generality, the GV solver will be considered herein (calculations performed with the VM solver, not shown here, show indeed minimal differences). The next series of numerical experiments will take advantage of the transonic treatment of van Leer *et al.* (1989), referred to by the authors themselves as the entropy bypass ("EB" in the following). The entropy bypass, see relations (D.23)-(D.24), is based on a synchronous splitting of the characteristic speed and source term integral near a sonic point. Such a joint treatment, devised in the context of classical nozzle flows to fix sonic glitches in the throat of choked nozzle flows, can be successfully applied to non-classical flows including sonic shocks, see below.

Before commenting on the possibility of obtaining accurate representation of sonic shocks, we consider a smooth choked flow, indicated as TC3 in Table D.1, expanding from subsonic inlet conditions to supersonic exit conditions. Thus, at the steady state, a transonic expansion is located in the throat of the nozzle, which is precisely the situation for which the EB transonic formula was originally formulated. The effectiveness of the simultaneous splitting of the characteristic speed and the source term is shown in figure D.7. Our numerical results are consistent with the previous findings: if the spreading parameter is sufficiently large, namely $d_{\text{ef}} = 2$ according to the analysis of van Leer *et al.* (1989), the sonic plateau is removed. On the contrary, the choices $d_{\text{ef}} = 0.5$ and $d_{\text{ef}} = 1$ lead to the same inaccuracies observed in TC1 (though here the convergence to the steady state was faster, see figure D.11(g)).

We turn now to a non-classical nozzle flow which represents, in a sense, the opposite scenario of the previous test case and it is used here to evaluate the behaviour of the synchronous splitting near sonic shocks. The flow field for TC4 includes two shock waves with sonic upstream states, but no supersonic points. Numerical results obtained with different values of the spreading parameter are shown in figure D.8 and the corresponding convergence histories are reported in figure D.11(h). The computations performed with $d_{\text{ef}} = 0.5$ and $d_{\text{ef}} = 1$ converged to the steady state, suggesting that the entropy bypass at sonic points can possibly balance transonic expansions even when these are located far from the throat, namely, where the source term does not vanish. Most importantly, the amplitude of the transonic expansion that is incorrectly computed during time marching can be reduced by decreasing the value of the spreading parameter of the model fan. Eventually, using $d_{\text{ef}} = 0.5$ the transonic expansion is completely removed and the errors in the location of the sonic shock is significantly reduced.

The effect of the parameter d_{ef} on the spreading of the transonic fan can be explained as follows. As the sonic shock approaches its steady-state position, the solution of the Riemann problem at the corresponding cell interface will have, in general, the structure of a composite wave. In this regard, the larger the spreading of the model expansion fan in the entropy correction formula, the larger will be the smooth fan in the composite wave. Thus, with large values of d_{ef}, the sonic shock will be wrongly captured as a sequence of transonic expansion and non-sonic shock.

D.3.3   An improved formula

The present analysis allows us to clarify two important aspects related to the treatment of sonic points in steady nozzle flows. Firstly, if the source term is not modified jointly with the characteristic speed, large inaccuracies can be found either in the throat of choked flows and in proximity of sonic shocks. In the latter condition, one also has to expect unbalancing problems that destroy the
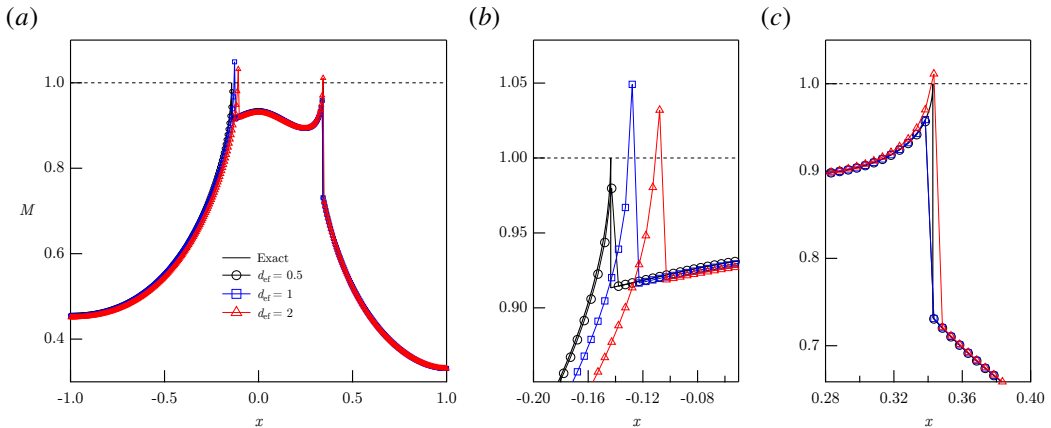
FIGURE D.8. TC4: Mach number distributions obtained from the GV solver with the entropy bypass on a non-classical flow including two sonic shocks (both on the upstream side) but no supersonic points. (*a*) Complete flow field; (*b*) and (*c*) enlargements of the leading and trailing sonic shocks, respectively.

convergence towards the steady state, unless a large band entropy fix, such as the KP one, is used. The second relevant consideration is that the synchronous splitting can efficiently break down sonic plateaus and provide steady-state balance even when a transonic rarefaction is computed in the time advance. However, in order to meet these goals and, in particular, to improve resolution of sonic shocks, the spreading of the transonic fan in the entropy correction should be specifically adjusted. On the one hand, large values of d_{ef} guarantee perfectly smooth subsonic to supersonic expansions in the throat of choked flows; on the other hand, lower values of d_{ef} allow to improve the resolution of sonic shocks. The fact that, at the steady state, subsonic to supersonic transition can take place only at the throat, while sonic shocks occur away from it (except for very special boundary data marking the transition of functioning regimes $\mathscr{R}_1^{NC}/\mathscr{R}_2^{NC}$), suggests that a possible way to deal with non-classical steady nozzle flows is to adapt d_{ef} to the the various regions of the nozzle. The simplest approach, in this sense, would consist in selecting a small value of d_{ef} everywhere except in the nozzle throat, where a larger spreading parameter is triggered to provide an appropriate amount of numerical dissipation in case a transonic expansion occurs at the steady state.

This simple treatment of the sonic points is tested again on TC2, see figure D.9. Here we have reported the numerical solutions obtained from the plain EB correction with $d_{ef} = 0.5$ and $d_{ef} = 2$, whose inaccuracies have been previously discussed, and the numerical results of the mixed approach, which is denoted as "improved". The improved procedure is constructed by imposing $d_{ef} = 0.5$ everywhere except for few interfaces neighbouring the throat, where $d_{ef} = 2$ is triggered. Here, the empirical choice $d_{ef} = 0.5$ for handling sonic shocks away from the throat is motivated by the parametric study shown in figure D.8. On the other hand, the choice of the throat value $d_{ef} = 2$ is consistent with the analysis of van Leer *et al.* (1989) and with our numerical experiments shown in figure D.7. The same procedure is applied to TC5, shown in figure D.10, which exhibits a post-sonic shock in the diverging section of the nozzle. In both cases, the improved treatment of transonic expansions makes it possible to combine the advantages of the choice $d_{ef} = 2$ in the sonic throat and the enhanced resolution of sonic shocks provided by $d_{ef} = 0.5$. For both TC2 and TC5, the improved method converges rapidly to the exact steady state, see figures D.11(*i-j*).

Admittedly, the simple modification described above can be unsatisfactory if the exact steady state contains a sonic shock at the throat, which can possibly occur for special boundary data marking the transition between functioning regimes $\mathscr{R}_1^{NC}$ and $\mathscr{R}_2^{NC}$. A more robust and general
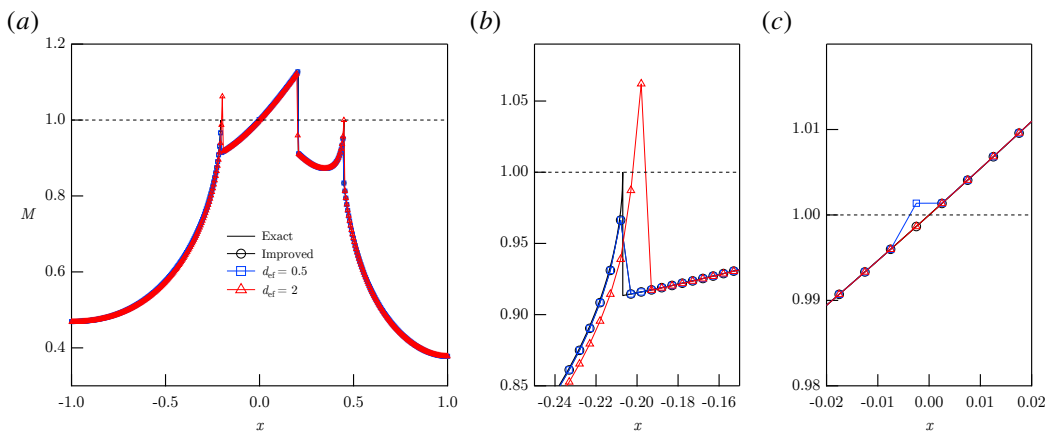
FIGURE D.9. TC2-EB: comparison of the Mach number distributions obtained from the GV solver equipped with the plain and improved entropy bypass. (*a*) Complete flow field; (*b*) enlargement of the leading sonic shock; (*c*) enlargement of the throat region.
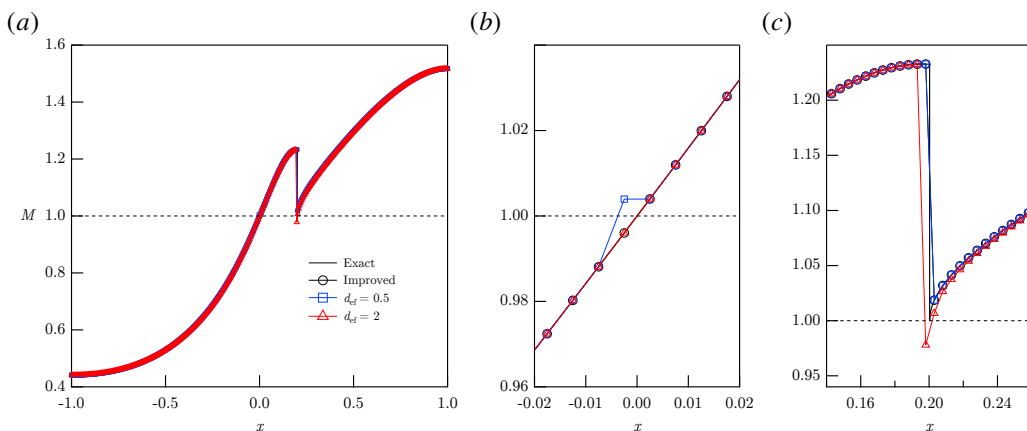
FIGURE D.10. TC5: comparison of the Mach number distributions obtained from the GV solver equipped with the plain and improved entropy bypass. The flow field features a shock with downstream sonic state in the diverging section and a subsonic to supersonic transition in the throat of the nozzle. (*a*) Complete flow field; (*b*) enlargement of the throat region; (*c*) enlargement of the sonic shock.

entropy correction would consist in adapting the spreading parameter only when a sonic or nearly sonic shock is detected. This would require, in turn, the definition of a general procedure for detecting sonic shocks. The design of such an enhanced treatment is left for future investigations.
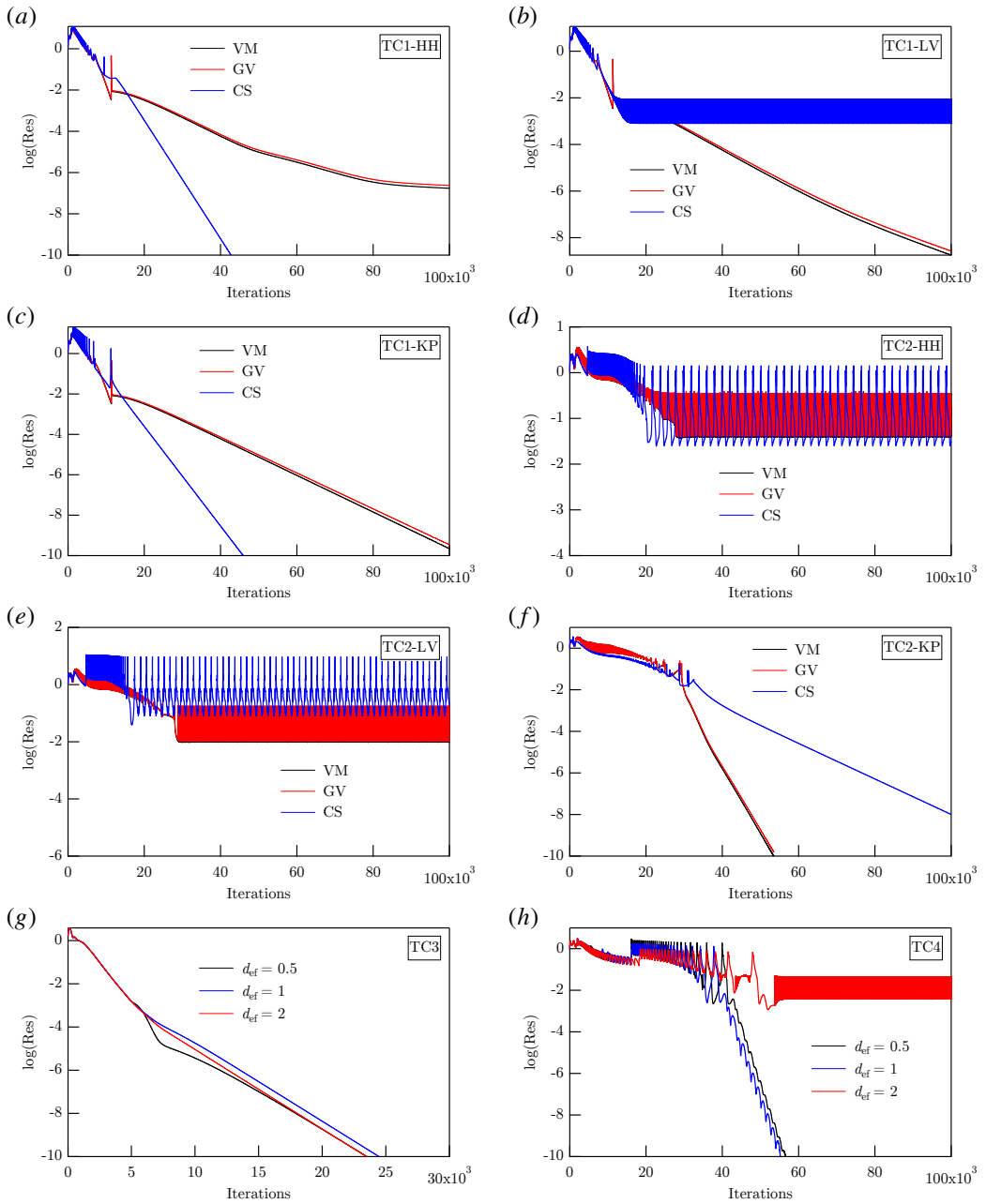
FIGURE D.11. Convergence history for each of the test cases.
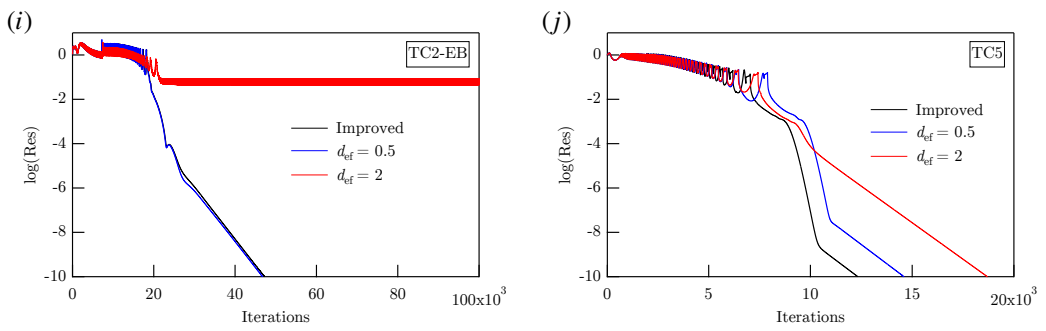
FIGURE D.11 (Cont.). Convergence history for each of the test cases.

REFERENCES

ABGRALL, R. 1991 An extension of Roe's upwind scheme to algebraic equilibrium real gas models. *Comput. & Fluids* **19** (2), 171–182.

ALFEREZ, N. & TOUBER, E. 2017 One-dimensional refraction properties of compression shocks in non-ideal gases. *J. Fluid Mech.* **814**, 185–221.

ANDERSON, J. D. 2010 *Fundamentals of aerodynamics*. Tata McGraw-Hill Education.

ANGELINO, G., INVERNIZZI, C. & MACCHI, E. 1991 Organic working fluid optimization for space power cycles. In *Modern research topics in aerospace propulsion*, pp. 297–326. Springer.

BALE, D. S., LEVEQUE, R. J., MITRAN, S. & ROSSMANITH, J. A. 2003 A wave propagation method for conservation laws and balance laws with spatially varying flux functions. *SIAM J. Sci. Comput.* **24** (3), 955–978.

BARTH, T. & JESPERSEN, D. 1989 The design and application of upwind schemes on unstructured meshes. In *27th Aerospace sciences meeting*, p. 366.

BARTOSIEWICZ, Y., AIDOUN, Z. & MERCADIER, Y. 2006 Numerical assessment of ejector operation for refrigeration applications based on CFD. *Appl. Therm. Eng.* **26** (5-6), 604–612.

BEN-DOR, G. 2007 *Shock wave reflection phenomena*. Springer.

BERMUDEZ, A. & VAZQUEZ, M. E. 1994 Upwind methods for hyperbolic conservation laws with source terms. *Comput. & Fluids* **23** (8), 1049–1071.

BETHE, H. A. 1942 The theory of shock waves for an arbitrary equation of state. Technical paper 545. Office Sci. Res. & Dev.

BINI, R. & COLOMBO, D. 2017 Large multistage axial turbines. *Energy Procedia* **129**, 1078 – 1084.

BORISOV, A. A., BORISOV, A. A., KUTATELADZE, S. S. & NAKORYAKOV, V. E. 1983 Rarefaction shock wave near the critical liquid-vapor point. *J. Fluid Mech.* **126**, 59–73.

BROWN, B. P. & ARGROW, B. M. 1997 Two-dimensional shock tube flow for dense gases. *J. Fluid Mech.* **349**, 95–115.

BROWN, B. P. & ARGROW, B. M. 2000 Application of Bethe-Zel'dovich-Thompson fluids in Organic Rankine Cycle engines. *J. Propul. Power* **16** (6), 1118–1123.

BUFFARD, T., GALLOUËT, T. & HÉRARD, J. M. 2000 A sequel to a rough Godunov scheme: application to real gases. *Comput. & Fluids* **29** (7), 813–847.

BUFI, E. A. & CINNELLA, P. 2018 Preliminary design method for dense-gas supersonic axial turbine stages. *J. Eng. Gas Turb. Power* **140** (11), 112605.

CALDERAZZI, L. & COLONNA, P. 1997 Thermal stability of R-134a, R-141b, R-13I1, R-7146, R-125 associated with stainless steel as a containing material. *Int. J. Refrig.* **20** (6), 381–389.

CALLEN, H. B. 1985 *Thermodynamics and an introduction to thermostatistics*, 2nd edn. Wiley.

CASELLES, V., DONAT, R. & HARO, G. 2009 Flux-gradient and source-term balancing for certain high resolution shock-capturing schemes. *Comput. & fluids* **38** (1), 16–36.

CHANDRASEKAR, D. & PRASAD, P. 1991 Transonic flow of a fluid with positive and negative nonlinearity through a nozzle. *Phys. Fluids A* **3** (3), 427–438.

CHPOUN, A., PASSEREL, D., LI, H. & BEN-DOR, G. 1995 Reconsideration of oblique shock wave reflections in steady flows. Part 1. Experimental investigation. *J. Fluid Mech.* **301**, 19–35.

CINNELLA, P. 2006 Roe-type schemes for dense gas flow computations. *Comput. & Fluids* **35** (10), 1264–1281.

CINNELLA, P. 2008 Transonic flows of dense gases over finite wings. *Phys. Fluids* **20** (4), 046103.

CINNELLA, P. & CONGEDO, P. M. 2007 Inviscid and viscous aerodynamics of dense gases. *J. Fluid Mech.* **580**, 179–217.

COLELLA, P. & HENDERSON, L. F. 1990 The von Neumann paradox for the diffraction of weak shock waves. *J. Fluid Mech.* **213**, 71–94.

COLONNA, P., CASATI, E., TRAPP, C., MATHIJSSEN, T., LARJOLA, J., TURUNEN-SAARESTI, T. & UUSITALO, A. 2015 Organic Rankine Cycle power systems: From the concept to current technology, applications, and an outlook to the future. *J. Eng. Gas Turb. Power* **137** (10), 100801–1–19.

COLONNA, P. & GUARDONE, A. 2006 Molecular interpretation of nonclassical gasdynamics of dense vapors under the van der Waals model. *Phys. Fluids* **18** (5), 056101–1–14.

COLONNA, P., GUARDONE, A. & NANNAN, N. R. 2007 Siloxanes: a new class of candidate Bethe-Zel'dovich-Thompson fluids. *Phys. Fluids* **19** (10), 086102–1–12.

COLONNA, P., GUARDONE, A., NANNAN, N. R. & ZAMFIRESCU, C. 2008*a* Design of the dense gas flexible asymmetric shock tube. *J. Fluid Eng.* **130** (3), 034501–1–6.

COLONNA, P., HARINCK, J., REBAY, S. & GUARDONE, A. 2008*b* Real-gas effects in organic Rankine cycle turbine nozzles. *J. Propul. Power* **24** (2), 282–294.

COLONNA, P., NANNAN, N. R., GUARDONE, A. & LEMMON, E. W. 2006 Multiparameter equations of state for selected siloxanes. *Fluid Phase Equilib.* **244** (2), 193–211.

COLONNA, P. & REBAY, S. 2004 Numerical simulation of dense gas flows on unstructured grids with an implicit high resolution upwind Euler solver. *Int. J. Numer. Meth.* **46** (7), 735–765.

COLONNA, P. & SILVA, P. 2003 Dense gas thermodynamic properties of single and multi-component fluids for fluid dynamics simulations. *J. Fluid Eng.-T. ASME* **125** (3), 414–427.

COLONNA, P., VAN DER STELT, T. P. & GUARDONE, A. 2012 FluidProp (Version 3.0): A program for the estimation of thermophysical properties of fluids. Asimptote, Delft, The Netherlands, http://www.fluidprop.com.

COURANT, R. & FRIEDRICHS, K. 1948 *Supersonic flow and shock waves*. New York: Interscience.

Cox, C. F. & Cinnella, P. 1994 General solution procedure for flows in local chemical equilibrium. *AIAA J.* **32** (3), 519–527.

Cramer, M. S. 1989*a* Negative nonlinearity in selected fluorocarbons. *Phys. Fluids A* **1** (11), 1894–1897.

Cramer, M. S. 1989*b* Shock splitting in single-phase gases. *J. Fluid Mech.* **199**, 281–296.

Cramer, M. S. 1991 Nonclassical dynamics of classical gases. In *Nonlinear Waves in Real Fluids* (ed. A. Kluwick), pp. 91–145. New York, NY: Springer-Verlag.

Cramer, M. S. 2006 Rayleigh processes in single-phase fluids. *Phys. Fluids* **18** (1), 016101.

Cramer, M. S. & Best, L. M. 1991 Steady, isentropic flows of dense gases. *Phys. Fluids A* **3** (4), 219–226.

Cramer, M. S. & Crickenberger, A. B. 1991 The dissipative structure of shock waves in dense gases. *J. Fluid Mech.* **223**, 325–355.

Cramer, M. S. & Crickenberger, A. B. 1992 Prandtl-Meyer function for dense gases. *AIAA Journal* **30** (2), 561–564.

Cramer, M. S. & Fry, N. R. 1993 Nozzle flows of dense gases. *Phys. Fluids A* **5** (5), 1246–1259.

Cramer, M. S. & Kluwick, A. 1984 On the propagation of waves exhibiting both positive and negative nonlinearity. *J. Fluid Mech.* **142**, 9–37.

Cramer, M. S., Kluwick, A., Watson, L. T. & Pelz, W. 1986 Dissipative waves in fluids having both positive and negative nonlinearity. *J. Fluid Mech.* **169**, 323–336.

Cramer, M. S., Monaco, J. F. & Fabeny, B. M. 1994 Fanno processes in dense gases. *Phys. Fluids* **6** (2), 674–683.

Cramer, M. S. & Park, S. 1999 On the suppression of shock-induced separation in Bethe–Zel'dovich–Thompson fluids. *J. Fluid Mech.* **393**, 1–21.

Cramer, M. S. & Sen, R. 1986 Shock formation in fluids having embedded regions of negative nonlinearity. *Phys. Fluids* **29**, 2181–2191.

Cramer, M. S. & Sen, R. 1987 Exact solutions for sonic shocks in van der Waals gases. *Phys. Fluids* **30**, 377–385.

Cramer, M. S. & Tarkenton, G. M. 1992 Transonic flows of Bethe–Zel'dovich–Thompson fluids. *J. Fluid Mech.* **240**, 197–228.

Dafermos, C. M. 2010 *Hyperbolic Conservation Laws in Continuum Physics*. Springer-Verlag, Berlin.

D'Angelo, S., Vimercati, D. & Guardone, A. 2018 A unified description of oblique waves in ideal and non-ideal steady supersonic flows around compressive and rarefactive corners. *Acta Mechanica* **229** (6), 2585–2595.

Defina, A., Susin, F. M. & Viero, D. P. 2008 Numerical study of the Guderley and Vasil'ev reflections in steady two-dimensional shallow water flow. *Phys. Fluids* **20** (9), 097102.

DENTON, J. D. & XU, L. 1989 The trailing edge loss of transonic turbine blades. In *ASME 1989 International Gas Turbine and Aeroengine Congress and Exposition*, pp. V001T01A097–V001T01A097. ASME.

DUHEM, P. 1909 On the propagation of shock waves in fluids. *Z. Phys. Chem.* **69**, 169–186.

D'YAKOV, S. P. 1954 On the stability of shock waves. *Zh. Eksp. Teor. Fiz* **27** (3), 288–295.

ERPENBECK, J. J. 1962 Stability of step shocks. *Phys. Fluids* **5** (10), 1181–1187.

ERPENBECK, J. J. 1963 Reply to comments by Gardner. *Phys. Fluids* **6** (9), 1368–1368.

FEHER, E. G. 1968 The supercritical thermodynamic power cycle. *Energy Conversion* **8** (2), 85–90.

FERGASON, S. H., GUARDONE, A. & ARGROW, B. M. 2003 Construction and validation of a dense gas shock tube. *J. Thermophys. Heat Tr.* **17** (3), 326–333.

FOWLES, G. R. 1981 Stimulated and spontaneous emission of acoustic waves from shock fronts. *Phys. Fluids* **24** (2), 220–227.

GALGANI, L. & SCOTTI, A. 1970 On subadditivity and convexity properties of thermodynamic functions. *Pure Appl. Chem.* **22** (3-4), 229–236.

GALIANA, F. J. D., WHEELER, A. P. S. & ONG, J. 2016 A study of trailing-edge losses in Organic Rankine Cycle turbines. *J. Turbomach.* **138** (12), 121003.

GARDNER, C. S. 1963 Comment on "Stability of step shocks". *Phys. Fluids* **6** (9), 1366–1367.

GEDANITZ, H., DAVILA, M. J. & LEMMON, E. W. 2015 Speed of sound measurements and a fundamental equation of state for cyclopentane. *J. Chem. Eng. Data* **60** (5), 1331–1337.

GILBARG, D. 1951 The existence and limit behavior of the one-dimensional shock layer. *Am. J. Math.* **73** (2), 256–274.

GLAISTER, P. 1988 An approximate linearised Riemann solver for the Euler equations for real gases. *J. Comput. Phys.* **74** (2), 382–408.

GLIMM, J., KLINGENBERG, C., MCBRYAN, O., PLOHR, B., SHARP, D. & YANIV, S. 1985 Front tracking and two-dimensional Riemann problems. *Advances in Applied Mathematics* **6** (3), 259–290.

GLIMM, J. & MAJDA, A. J. 2012 *Multidimensional hyperbolic problems and computations*. Springer Science & Business Media.

GODLEWSKI, E. & RAVIART, P. A. 2013 *Numerical approximation of hyperbolic systems of conservation laws*. Springer Science & Business Media.

GOODMAN, J. B. & LEVEQUE, R. J. 1988 A geometric approach to high resolution TVD schemes. *SIAM J. Numer. Anal.* **25** (2), 268–284.

GORI, G., GUARDONE, A., VITALE, S., HEAD, A., PINI, M. & COLONNA, P. 2015 Non-ideal compressible-fluid dynamics simulation with SU2: Numerical assessment of nozzle and blade flows for Organic Rankine Cycle applications. In *3rd International Seminar on ORC Power Systems. Brussels, Belgium*.

GORI, G., VIMERCATI, D. & GUARDONE, A. 2017*a* Non-ideal compressible-fluid effects in oblique shock waves. *Journal of Physics: Conference Series* **821** (1), 012003.

GORI, G., ZOCCA, M., CAMMI, G., SPINELLI, A. & GUARDONE, A. 2017*b* Experimental assessment of the open-source SU2 CFD suite for ORC applications. *Energy Procedia* **129**, 256–263.

GROSSMAN, B. & WALTERS, R. W. 1989 Analysis of flux-split algorithms for Euler's equations with real gases. *AIAA J.* **27** (5), 524–531.

GUARDONE, A. 2007 Three-dimensional shock tube flows for dense gases. *J. Fluid Mech.* **583**, 423–442.

GUARDONE, A. 2011 Nozzle design for supersonic flows of N2O at supercritical and close-to-critical conditions. In *8th International Conference on Flow Dynamics*, pp. 1–2.

GUARDONE, A. & ARGROW, B. M. 2005 Nonclassical gasdynamic region of selected fluorocarbons. *Phys. Fluids* **17** (11), 116101–1–17.

GUARDONE, A., SPINELLI, A. & DOSSENA, V. 2013 Influence of molecular complexity on nozzle design for an organic vapor wind tunnel. *J. Eng. Gas Turb. Power* **135**, 042307.

GUARDONE, A. & VIGEVANO, L. 2002 Roe linearization for the van der Waals gas. *J. Comput. Phys.* **175** (1), 50–78.

GUARDONE, A., VIGEVANO, L. & ARGROW, B. M. 2004 Assessment of thermodynamic models for dense gas dynamics. *Phys. Fluids* **16** (11), 3878–3887.

GUARDONE, A. & VIMERCATI, D. 2016 Exact solutions to non-classical steady nozzle flows of Bethe-Zel'dovich-Thompson fluids. *J. Fluid Mech.* **800**, 278–306.

GUARDONE, A., ZAMFIRESCU, C. & COLONNA, P. 2010 Maximum intensity of rarefaction shock waves for dense gases. *J. Fluid Mech.* **642**, 127–146.

GUDER, C. & WAGNER, W. 2009 A reference equation of state for the thermodynamic properties of sulfur hexafluoride (SF6) for temperatures from the melting line to 625 K and pressures up to 150 MPa. *J. Phys. Chem. Ref. Data* **38** (1), 33–94.

GUDERLEY, K. G. 1962 *The theory of transonic flow*. Pergamon Press.

GYFTOPOULOS, E. P. & BERETTA, G. P. 2005 *Thermodynamics: foundations and applications*. Courier Corporation.

HARTEN, A. 1983 High resolution schemes for hyperbolic conservation laws. *J. Comput. Phys.* **49** (3), 357–393.

HARTEN, A. & HYMAN, J. M. 1983 Self adjusting grid methods for one-dimensional hyperbolic conservation laws. *J. Comput. Phys.* **50** (2), 235–269.

HAYES, W. D. 1958 The basic theory of gasdynamic discontinuities. In *Fundamentals of gasdynamics* (ed. H W Emmons), *High speed aerodynamics and jet propulsion*, vol. 3, pp. 416–481. Princeton, N.J.: Princeton University Press.

HEAD, A. J., DE SERVI, C., CASATI, E., PINI, M. & COLONNA, P. 2016 Preliminary design of the ORCHID: A facility for studying non-ideal compressible fluid dynamics and testing ORC expanders. In *ASME Turbo Expo 2016: Turbomachinery Technical Conference and Exposition*, pp. V003T25A001–V003T25A001. ASME.

HELFGEN, B., TÜRK, M. & SCHABER, K. 2003 Hydrodynamic and aerosol modelling of the rapid expansion of supercritical solutions (RESS-process). *J. Supercrit Fluids* **26** (3), 225–242.

HENDERSON, L. F. & MENIKOFF, R. 1998 Triple-shock entropy theorem and its consequences. *J. Fluid Mech.* **366**, 179–210.

HOFFREN, J., TALONPOIKA, T., LARJOLA, J. & SIIKONEN, T. 2002 Numerical simulation of real-gas flow in a supersonic turbine nozzle ring. *J. Eng. Gas Turb. Power* **124**, 395–403.

IVANOV, M. S., BONDAR, Y. A., KHOTYANOVSKY, D. V., KUDRYAVTSEV, A. N. & SHOEV, G. V. 2010 Viscosity effects on weak irregular reflection of shock waves in steady flow. *Prog. Aerosp. Sci.* **46** (2-3), 89–105.

IVANOV, M. S., GIMELSHEIN, S. F. & BEYLICH, A. E. 1995 Hysteresis effect in stationary reflection of shock waves. *Phys. Fluids* **7** (4), 685–687.

IVANOV, M. S., MARKELOV, G. N., KUDRYAVTSEV, A. N. & GIMELSHEIN, S. F. 1998 Numerical analysis of shock wave reflection transition in steady flows. *AIAA Journal* **36** (11), 2079–2086.

IVANOV, M. S., SHOEV, G., KHOTYANOVSKY, D., BONDAR, Y. & KUDRYAVTSEV, A. 2012 Supersonic patches in steady irregular reflection of weak shock waves. In *28th International Symposium on Shock Waves*, pp. 543–548. Springer.

JASSIM, E., ABEDINZADEGAN ABDI, M. & MUZYCHKA, Y. 2008 Computational fluid dynamics study for flow of natural gas through high-pressure supersonic nozzles: Part 1. Real gas effects and shockwave. *Petroleum Science and Technology* **26** (15), 1757–1772.

KERMANI, M. & PLETT, E. 2001 Modified entropy correction formula for the Roe scheme. In *39th Aerospace Sciences Meeting and Exhibit*, p. 83.

KEULEN, L., GALLARINI, S., LANDOLINA, C., SPINELLI, A., IORA, P., INVERNIZZI, C., LIETTI, L. & GUARDONE, A. 2018 Thermal stability of hexamethyldisiloxane and octamethyltrisiloxane. *Energy* **165**, 868 – 876.

KLUWICK, A. 1971 Zur ausbreitung schwacher Stöße in dreidimensionalen instationären Strömungen. *ZAMM* **51** (3), 225–232.

KLUWICK, A. 1993 Transonic nozzle flow of dense gases. *J. Fluid Mech.* **247**, 661–688.

KLUWICK, A 1994 Interacting laminar boundary layers of dense gases. In *Fluid- and Gasdynamics*, pp. 335–349. Springer.

KLUWICK, A. 2001 Rarefaction shocks. In *Handbook of Shock Waves* (ed. G. Ben-Dor, O. Igra & T. Elperin), pp. 339–411. Academic Press.

KLUWICK, A. 2004 Internal flows of dense gases. *Acta Mech.* **169**, 123–143.

KLUWICK, A. 2017 Non-ideal compressible fluid dynamics: A challenge for theory. *Journal of Physics: Conference Series* **821** (1), 012001.

KLUWICK, A. & COX, E. A. 2018*a* Steady small-disturbance transonic dense gas flow past two-dimensional compression/expansion ramps. *J. Fluid Mech.* **848**, 756–787.

KLUWICK, A. & COX, E. A. 2018*b* Weak shock reflection in channel flows for dense gases. *J. Fluid Mech.* (Submitted).

KONTOROVICH, V. M. 1958 Concerning the stability of shock waves. *Soviet Phys. JETP* **6**.

Kraiko, A. N., P'yankov, K. S. & Yakovlev, Ye. A. 2014 The flow of a supersonic ideal gas with 'weak' and 'strong' shocks over a wedge. *J. Appl. Math. Mech.* **78** (4), 318–330.

Kutateladze, S. S., Nakoryakov, V. E. & Borisov, A. A. 1987 Rarefaction waves in liquid and gas-liquid media. *Ann. Rev. Fluid Mech.* **19**, 577–600.

Lai, N. A., Wendland, M. & Fischer, M 2011 Working fluids for high-temperature organic Rankine cycles. *Energy* **36** (1), 199 – 211.

Landau, L. D. & Lifshitz, E. M. 1987 *Fluid mechanics, 2nd edn*. Pergamon Press.

Lax, P. D. 1957 Hyperbolic systems of conservation laws II. *Commun. Pur. Appl. Math.* **10** (4), 537–566.

van Leer, B., Lee, W. T. & Powell, K. G. 1989 Sonic-point capturing. *AIAA paper* **1945**, 1989.

Lemmon, E. W., Huber, M. L. & McLinden, M. O. 2013 NIST reference database 23: reference fluid thermodynamic and transport properties–REFPROP, version 9.1. *Standard Reference Data Program* .

Lemmon, E. W. & Span, R. 2006 Short fundamental equations of state for 20 industrial fluids. *J. Chem. Eng. Data* **51** (3), 785–850.

Levelt-Sengers, J. M. H. 1970 Scaling predictions for thermodynamic anomalies near the gas-liquid critical point. *Ind. Eng. Chem. Fundam.* **9** (3), 470–480.

LeVeque, R. J. 1992 *Numerical methods for conservation laws*, chap. 9, pp. 151–156. Springer.

LeVeque, R. J 1998 Balancing source terms and flux gradients in high-resolution Godunov methods: the quasi-steady wave-propagation algorithm. *J. Comput. Phys.* **146** (1), 346–365.

LeVeque, R. J. 2011 A well-balanced path-integral f-wave method for hyperbolic problems with source terms. *J. Sci. Comput.* **48** (1-3), 209–226.

Liou, M. S., Van Leer, B. & Shuen, J.-S. 1990 Splitting of inviscid fluxes for real gases. *J. Comput. Phys.* **87** (1), 1–24.

Liu, T. P. 1976 The entropy condition and the admissibility of shocks. *J. Math. Anal. Appl.* **53** (1), 78–88.

Macchi, E. & Astolfi, M. 2016 *Organic Rankine Cycle (ORC) power systems: technologies and applications*. Woodhead Publishing.

Mach, E. 1878 Uber den verlauf von funkenwellen in der ebene und im raume. *Sitzungsbr. Akad. Wiss. Wien* **78**, 819–838.

Majda, A. 1983 *The existence of multi-dimensional shock fronts*. Am. Math. Soc.

Martin, J. J. & Hou, Y. C. 1955 Development of an equation of state for gases. *AIChE J.* **1** (2), 142–151.

Martin, J. J., Kapoor, R. M. & De Nevers, N. 1959 An improved equation of state for gases. *AIChE J.* **5** (2), 159–160.

Masella, J. M., Faille, I. & Gallouet, T. 1999 On an approximate Godunov scheme. *Int. J. Comput. Fluid Dyn.* **12** (2), 133–149.

Mathijssen, T. 2017 Experimental observation of non-ideal compressible fluid dynamics with application in Organic Rankine Cycle power systems. PhD thesis, Delft University of Technology.

Mathijssen, T., Gallo, M., Casati, E., Nannan, N. R., Zamfirescu, C., Guardone, A. & Colonna, P. 2015 The flexible asymmetric shock tube (FAST): a Ludwieg tube facility for wave propagation measurements in high-temperature vapours of organic fluids. *Exp. Fluids* **56** (10), 1–12.

Mee, D. J., Baines, N. C., Oldfield, M. L. G. & Dickens, T. E. 1990 An examination of the contributions to loss on a transonic turbine blade in cascade. In *ASME 1990 International Gas Turbine and Aeroengine Congress and Exposition*, pp. V005T16A012–V005T16A012. ASME.

Meier, K., Laesecke, A. & Kabelac, S. 2004 Transport coefficients of the Lennard-Jones model fluid. I. Viscosity. *J. Chem. Phys.* **121** (8), 3671–3687.

Menikoff, R. & Plohr, B. J. 1989 The Riemann problem for fluid flow of real materials. *Rev. Mod. Phys.* **61(1)**, 75–130.

Meroni, A., Andreasen, J. G., Persico, G. & Haglind, F. 2018 Optimization of organic Rankine cycle power systems considering multistage axial turbine design. *Applied Energy* **209**, 339 – 354.

Monaco, J. F., Cramer, M. S. & Watson, L. T. 1997 Supersonic flows of dense gases in cascade configurations. *J. Fluid Mech.* **330**, 31–59.

Mottura, L., Vigevano, L. & Zaccanti, M, . 1997 An evaluation of Roe's scheme generalizations for equilibrium real gas flows. *J. Comput. Phys.* **138** (2), 354–399.

Nannan, N. R., Guardone, A. & Colonna, P. 2013 On the fundamental derivative of gas dynamics in the vapor–liquid critical region of single-component typical fluids. *Fluid Phase Equilib.* **337**, 259–273.

Nannan, N. R., Sirianni, C., Mathijssen, T., Guardone, A. & Colonna, P. 2016 The admissibility domain of rarefaction shock waves in the near-critical vapour-liquid equilibrium region of pure typical fluids. *J. Fluid Mech.* **795**, 241–261.

von Neumann, J. 1943 Oblique reflection of shocks. *John von Neumann Collected Works* **6**, 238–299.

von Neumann, J. 1945 Refraction, intersection and reflection of shock waves. *NAVORD Rep. 203-45* .

Palacios, F., Alonso, J. J., Duraisamy, F., Colonno, M., Hicken, J., Aranake, A., Campos, A., Copeland, S., Economon, T., Lonkar, A. & others 2013 Stanford University Unstructured (SU 2): an open-source integrated computational environment for multi-physics simulation and design. In *51st AIAA Aerospace Sciences Meeting Including the New Horizons Forum and Aerospace Exposition*, p. 287.

Pasetti, M., Invernizzi, C. & Iora, P. 2014 Thermal stability of working fluids for Organic Rankine Cycles: an improved survey method and experimental results for cyclopentane, isopentane and n-butane. *Appl. Therm. Eng.* **73** (1), 764–774.

Pego, R. L. 1986 Nonexistence of a shock layer in gas dynamics with a nonconvex equation of state. *Arch. Ration. Mech. Anal.* **94** (2), 165–178.

PENG, D. Y. & ROBINSON, D. B. 1976 A new two-constant equation of state. *Ind. Eng. Chem. Fundam.* **15**, 59–64.

PERKINS, R. A., SENGERS, J. V., ABDULAGATOV, I. M. & HUBER, M. L. 2013 Simplified model for the critical thermal-conductivity enhancement in molecular fluids. *Int. J. Thermophys.* **34** (2), 191–212.

PERSICO, G. 2017 Evolutionary optimization of centrifugal nozzles for organic vapours. *Journal of Physics: Conference Series* **821** (1), 012015.

PINI, M., SPINELLI, A., PERSICO, G. & REBAY, S. 2015 Consistent look-up table interpolation method for real-gas flow simulations. *Comput. Fluids* **107**, 178 – 188.

PINI, M., VITALE, S., COLONNA, P., GORI, G., GUARDONE, A., ECONOMON, T., ALONSO, J. J. & PALACIOS, F. 2017 SU2: the open-source software for non-ideal compressible flows. *Journal of Physics: Conference Series* **821** (1), 012013.

PREISSINGER, M. & BRUGGEMANN, D. 2016 Thermal stability of hexamethyldisiloxane (MM) for high-temperature organic Rankine cycle (ORC). *Energies* **9** (3).

RE, B., DOBRZYNSKI, C. & GUARDONE, A. 2017 An interpolation-free ALE scheme for unsteady inviscid flows computations with large boundary displacements over three-dimensional adaptive grids. *J. Comput. Phys.* **340**, 26–54.

RE, B., DOBRZYNSKI, C. & GUARDONE, A. 2018 Assessment of grid adaptation criteria for steady, two-dimensional, inviscid flows in non-ideal compressible fluids. *Appl. Math. Comput.* **319**, 337–354.

RE, B. & GUARDONE, A. 2018 An adaptive ALE scheme for non-ideal compressible fluid dynamics over dynamic unstructured meshes. *Shock Waves* pp. 1–27.

REINKER, F., KENIG, E. Y., PASSMANN, M. & AUS DER WIESCHE, S. 2017 Closed Loop Organic Wind Tunnel (CLOWT): design, components and control system. *Energy Procedia* **129**, 200–207.

RINALDI, E., PECNIK, R. & COLONNA, P. 2015 Computational fluid dynamic simulation of a supercritical CO2 compressor performance map. *J. Eng. Gas Turb. Power* **137** (7), 072602.

RINALDI, E., PECNIK, R. & COLONNA, P. 2016 Unsteady operation of a highly supersonic ORC turbine. *J. Turbomach.* **128**.

RODRIGUEZ-FERNANDEZ, P. & PERSICO, G. 2015 Automatic design of ORC turbine profiles using evolutionary algorithms. In *3rd International Seminar on ORC Power Systems*.

ROE, P. L. 1981 Approximate Riemann solvers, parameter vectors, and difference schemes. *J. Comput. Phys.* **43** (2), 357–372.

ROE, P. L. 1987 *Upwind differencing schemes for hyperbolic conservation laws with source terms*, pp. 41–51. Berlin, Heidelberg: Springer Berlin Heidelberg.

SAGNIER, P. & VÉRANT, J. L. 1998 On the validation of high enthalpy wind tunnel simulations. *Aerospace science and technology* **2** (7), 425–437.

SANDERSON, S. R. 2004 Gasdynamic wave interaction in two spatial dimensions. *J. Fluid Mech.* **506**, 187–205.

SCHNERR, G.H. & LEIDNER, P. 1991 Diabatic supersonic flows of dense gases. *Phys. Fluids A* **3** (10), 2445–2458.

SCHUSTER, A., KARELLAS, S. & AUMANN, R. 2010 Efficiency optimization potential in supercritical Organic Rankine Cycles. *Energy* **35** (2), 1033 – 1039, eCOS 2008.

SERRE, D. 2007 Shock reflection in gas dynamics. In *Handbook of mathematical fluid dynamics*, pp. 39–122. Elsevier.

SETZMANN, U. & WAGNER, W. 1991 A new equation of state and tables of thermodynamic properties for methane covering the range from the melting line to 625 K at pressures up to 100 MPa. *J. Phys. Chem. Ref. Data* **20** (6), 1061–1155.

SKEWS, B. W. & ASHWORTH, J. T. 2005 The physical nature of weak shock wave reflection. *J. Fluid Mech.* **542**, 105–114.

SMITH, R. G. 1979 The Riemann problem in gas dynamics. *Transactions of the American Mathematical Society* **249** (1), 1–50.

SPAN, R. & WAGNER, W. 2003*a* Equations of state for technical applications. I. Simultaneously optimized functional forms for nonpolar and polar fluids. *Int. J. Thermophys.* **24** (1), 1–39.

SPAN, R. & WAGNER, W. 2003*b* Equations of state for technical applications. II. Results for nonpolar fluids. *Int. J. Thermophys.* **24** (1), 41–109.

SPINELLI, A., DOSSENA, V., GAETANI, P., OSNAGHI, C. & COLOMBO, D. 2010 Design of a test rig for organic vapours. In *ASME Turbo Expo 2010: Power for Land, Sea and Air GT2010*.

SPINELLI, A., PINI, M., DOSSENA, V., GAETANI, P. & CASELLA, F. 2013 Design, simulation, and construction of a test rig for organic vapours. *J. Eng. Gas Turb. Power* **135**, 042303.

STARKEN, H. 1993 Basic fluid dynamic boundary conditions of cascade wind tunnels. In *Advanced Methods of Cascade Testing*.

STARKEN, H., YONGXING, Z. & SCHREIBER, H.A. 1984 Mass flow limitation of supersonic blade rows due to leading edge blockage. In *ASME 1984 International Gas Turbine Conference and Exhibit*.

VAN DER STELT, T. P., NANNAN, N. R. & COLONNA, P. 2012 The iPRSV equation of state. *Fluid Phase Equilib.* **330**, 24–35.

STRYJEK, R. & VERA, J. H. 1986 PRSV: An improved Peng–Robinson equation of state for pure compounds and mixtures. *Can. J. Chem. Eng.* **64** (2), 323–333.

STUPOCHENKO, Y. V., LOSEV, S. A. & OSIPOV, A. I. 1967 *Relaxation Processes in Shock Waves*, *Applied physics and engineering*, vol. 1. Springer.

SUTTON, G. P. & BIBLARZ, O. 2016 *Rocket propulsion elements*. John Wiley & Sons.

TAYLOR, G. I. 1910 The conditions necessary for discontinuous motion in gases. *Proc. R. Soc. Lond. A* **84** (571), 371–377.

TCHANCHE, B. F., LOONIS, P., PÉTRISSANS, M. & RAMENAH, H. 2013 Organic Rankine Cycle systems principles, opportunities and challenges. In *Microelectronics (ICM), 2013 25th International Conference on*, pp. 1–4. IEEE.

Tchanche, B. F, Pétrissans, M. & Papadakis, G. 2014 Heat resources and Organic Rankine Cycle machines. *Renewable and Sustainable Energy Reviews* **39**, 1185–1199.

Tesdall, A. M. & Hunter, J. K. 2002 Self-similar solutions for weak shock reflection. *SIAM Journal on Applied Mathematics* **63** (1), 42–61.

Tesdall, A. M., Sanders, R. & Popivanov, N. 2015 Further results on Guderley Mach reflection and the triple point paradox. *J. Sci. Comput.* **64** (3), 721–744.

Teshukov, V. M. 1989 Stability of the regular reflection of shock waves. *PMTF Zh. Prikl. Mekhan. Tekhn. Fiz* pp. 26–33.

Thol, M., Dubberke, F. H., Baumhögger, E., Vrabec, J. & Span, R. 2017 Speed of sound measurements and fundamental equations of state for octamethyltrisiloxane and decamethyltetrasiloxane. *J. Chem Eng. Data* **62** (9), 2633–2648.

Thol, M., Dubberke, F. H., Rutkai, G., Windmann, T., Köster, A., Span, R. & Vrabec, J. 2016 Fundamental equation of state correlation for hexamethyldisiloxane based on experimental and molecular simulation data. *Fluid Phase Equilib.* **418**, 133 – 151.

Thol, M., Javed, M. A.., Baumhögger, E., Span, R. & Vrabec, J. 2018 Thermodynamic properties of dodecamethylpentasiloxane, tetradecamethylhexasiloxane and decamethylcyclopentasiloxane. *Fluid Phase Equilib.* (Submitted).

Thol, M., Lemmon, E. W. & Span, R. 2012 Equation of state for benzene for temperatures from the melting line up to 725 K with pressures up to 500 MPa. *High Temperatures–High Pressures* **41** (2).

Thompson, P. A. 1971 A fundamental derivative in gasdynamics. *Phys. Fluids* **14** (9), 1843–1849.

Thompson, P. A. 1988 *Compressilbe Fluid Dynamics*. McGraw-Hill.

Thompson, P. A. 1991 Liquid-vapor adiabatic phase changes and related phenomena. In *Nonlinear Waves in Real Fluids* (ed. A. Kluwick), pp. 147–213. New York, NY: Springer-Verlag.

Thompson, P. A., Carofano, G. C. & Kim, Y. G. 1986 Shock waves and phase changes in a large-heat-capacity fluid emerging from a tube. *J. Fluid Mech.* **166**, 57–92.

Thompson, P. A. & Lambrakis, K. C. 1973 Negative shock waves. *J. Fluid Mech.* **60**, 187–208.

Toro, E. F. 2013 *Riemann solvers and numerical methods for fluid dynamics: a practical introduction*. Springer Science & Business Media.

Toumi, I. 1992 A weak formulation of Roe's approximate Riemann solver. *J. Comput. Phys,* **102** (2), 360–373.

Turunen-Saaresti, T., Uusitalo, A. & Honkatukia, J. 2017 Design and testing of high temperature micro-ORC test stand using siloxane as working fluid. *Journal of Physics: Conference Series* **821** (1), 012024.

Uusitalo, A., Honkatukia, J. & Turunen-Saaresti, T. 2017 Evaluation of a small-scale waste heat recovery organic Rankine cycle. *Applied Energy* **192**, 146–158.

Vasil'ev, E. I. 2016 The nature of the triple point singularity in the case of stationary reflection of weak shock waves. *Fluid Dynamics* **51** (6), 804–813.

Vasil'ev, E. I., Elperin, T. & Ben-Dor, G. 2008 Analytical reconsideration of the von Neumann paradox in the reflection of a shock wave over a wedge. *Phys. Fluids* **20** (4), 046101.

Vasil'ev, E. I. & Kraiko, A. N. 1999 Numerical simulation of weak shock diffraction over a wedge under the von Neumann paradox conditions. *Zh. Vychisl. Mat. Mat. Fiz.* **39** (8), 1393–1404.

Viero, D. P., Susin, F. M. & Defina, A. 2013 A note on weak shock wave reflection. *Shock Waves* **23** (5), 505–511.

Vimercati, D., Gori, G. & Guardone, A. 2018*a* Non-ideal oblique shock waves. *J. Fluid Mech.* **847**, 266–285.

Vimercati, D., Gori, G., Spinelli, A. & Guardone, A. 2017 Non-ideal effects on the typical trailing edge shock pattern of ORC turbine blades. *Energy Procedia* **129**, 1109–1116.

Vimercati, D., Kluwick, A. & Guardone, A. 2018*b* Oblique waves in steady supersonic flows of Bethe-Zeldovich-Thompson fluids. *J. Fluid Mech.* **855**, 445–468.

Vinokur, M. & Montagné, J. L. 1990 Generalized flux-vector splitting and Roe average for an equilibrium real gas. *J. Comput. Phys.* **89** (2), 276–300.

Vitale, S., Albring, T. A., Pini, M., Gauger, N. R. & Colonna, P. 2017 Fully turbulent discrete adjoint solver for non-ideal compressible flow applications. *Journal of the Global Power and Propulsion Society* **1**, 252–270.

Vitale, S., Gori, G., Pini, M., Guardone, A., Economon, T. D., Palacios, F., Alonso, J. J. & Colonna, P. 2015 Extension of the SU2 open source CFD code to the simulation of turbulent flows of fuids modelled with complex thermophysical laws. In *22nd AIAA Computational Fluid Dynamics Conference*, p. 2760.

van der Waals, J. D. 1873 Over de Continuiteit van den Gas-en Vloeistoftoestand (on the continuity of the gas and liquid state). PhD thesis, Leiden University.

Wendroff, B. 1972*a* The Riemann problem for materials with nonconvex equations of state I: isentropic flow. *J. Math. Anal. Appl.* **38** (2), 454–466.

Wendroff, B. 1972*b* The riemann problem for materials with nonconvex equations of state II: general flow. *J. Math. Anal. Appl.* **38** (3), 640–658.

Weyl, H. 1949 Shock waves in arbitrary fluids. *Comm. Pure Appl. Math.* **2** (2-3), 103–122.

Wheeler, A. P. S. & Ong, J. 2013 The role of dense gas dynamics on organic Rankine cycle turbine performance. *J. Eng Gas Turb. Power* **135** (10), 102603.

Zamfirescu, C. & Dincer, I. 2009 Performance investigation of high-temperature heat pumps with various BZT working fluids. *Thermochim. Acta* **488** (1), 66–77.

Zamfirescu, C., Guardone, A. & Colonna, P. 2008 Admissibility region for rarefaction shock waves in dense gases. *J. Fluid Mech.* **599**, 363–381.

Zel'dovich, Y.B & Raizer, Y. P. 1968 *Physics of shock waves and high-temperature hydrodynamic phenomena*. Academic Press.

Zel'dovich, Y. B. 1946 On the possibility of rarefaction shock waves. *Zh. Eksp. Teor. Fiz.* **4**, 363–364.

Zucrow, M. J. & Hoffman, J. D. 1976 *Gas dynamics*. New York: Wiley.

NOMENCLATURE

Acronyms/Abbreviations

BZT	Bethe-Zel'dovich-Thompson
CFL	Courant-Friedrichs-Lewy
CS	Cinnella's solver
D_6	Dodecamethylcyclohexasiloxane
DKLL	D'yakov-Kontorovich limit locus
DS	Double-sonic shock
DLS	Locus of DS points double-sonic locus
EB	Entropy bypass
EoS	Equation of state
GV	Guardone and Vigevano (Roe solver)
HH	Harten and Hyman (entropy fix)
iPRSV	Improved Peng-Robinson-Stryjek-Vera
KP	Kermani and Plett (entropy fix)
LuT	Look up table
LV	LeVeque (entropy fix)
MDM	Octamethyltrisiloxane
MD_4M	Tetradecamethylhexasiloxane
MM	Hexamethyldisiloxane
MH	Martin-Hou
NICFD	Non-ideal compressible-fluid dynamics
ORC	Organic Rankine cycle
PP10	Perfluoroperhydrofluorene
PS_{max}	Pre-shock state of maximum-intensity post-sonic shock
PS_{sat}	Pre-shock state of post-sonic shock with post-shock saturated conditions
PSL_{max}	Locus of PS_{max} points
PSL_{sat}	Locus of PS_{sat} points
PSLL	Pre-shock limit locus
R245fa	1,1,1,3,3-Pentafluoropropane
Re	Reynolds number
SD	Sonic-shock disintegration
SW	Span-Wagner
TI	Turbulence intensity
TVD	Total variation diminishing
vdW	van der Waals
VL	Van Leer et. al. (entropy fix)
VLE	Vapour-liquid equilibrium
VM	Vinokur and Montagné (Roe solver)

Latin alphabet

a	Parameter of the vdW and MH EoS
A	Upstream or pre-shock state
A	Triplet of independent variables describing the pre-shock state
A	Nozzle cross-sectional area; parameter of the MH and iPRSV EoS
A^*	Critical cross-sectional area
A^J_τ	Point of maximum entropy along $J_A = 0$ locus
$A^V_{dM,0}$	Pre-shock state for stationary post-shock Mach number on the VLE line
$A^J_{V,1}$	High-density intersection between $J_A = 0$ locus and VLE line
$A^J_{V,2}$	Low-density intersection between $J_A = 0$ locus and VLE line
$\mathcal{A}$	Flux Jacobian
$\hat{A}$	Approximate Jacobian
b	Parameter of the vDW, MH and iPRSV EoS
B	Downstream or post-shock state
B	Parameter of the MH and iPRSV EoS
c	Speed of sound
c_b	Blade chord
$c_{p,\infty}$	Ideal-gas isobaric specific heat
c_v	Specific heat at constant volume
$c_{v,\infty}$	Ideal-gas isochoric specific heat
C	Parameter of the MH and iPRSV EoS
$\mathcal{C}$	Classical wave curve
C	Contact discontinuity
d_{ef}	Fan-spreading parameter for entropy correction
D	Parameter of the iPRSV EoS
e	Specific internal energy
E	Parameter of the iPRSV EoS
f	Specific Helmholtz free energy
f^{ig}_r	Ideal-gas Helmholtz energy (SW EoS)
f^{r}_r	Residual Helmholtz energy (SW EoS)
F	Flux of conservative or balance variables; numerical flux
F_v	v-component of the vector field of the shock layer equations
F_T	T-component of the vector field of the shock layer equations
F	Reflected rarefaction fan
g	Specific Gibbs free energy
G	Grüneisen coefficient
h	Specific enthalpy
I	intersection between the local isentrope and $\Gamma = 0$ locus
$\mathscr{S}$	Isentropic pattern
I	Incident shock
j	Mass flux function
J	Dimensionless isentropic derivative of the M w.r.t. ρ at constant h^t
k	Thermal conductivity; Parameter of the MH EoS
K_s	Isentropic compressibility
$\mathcal{K}$	Dimensionless isochoric derivative of c w.r.t. s
l	Characteristic length of relaxation processes
l_0	Mean-free path
L	Characteristic macroscopic length
m	Mass flux across discontinuity

$\dot{m}$	Mass flow rate
$\dot{m}_c$	Critical mass flow rate
$\dot{m}_s$	Mass flow rate for choked nozzle
$\dot{m}_{max}$	Maximum mass flow rate dischargeable by the nozzle
M	Mach number
M_A^{tr}	Transitional upstream Mach number
M_m	Molecular mass
$\boldsymbol{M}$	Mach stem
n	Parameter of the SW EoS
$\boldsymbol{n}$	Normal unit vector
$\mathcal{N}$	Non-classical wave curve
p	Extended state for quasi-Jacobian linerization
P	Pressure
P_a	Ambient pressure downstream of the nozzle
q	Conservative variables or balance variables
Q	Numerical approximation of the cell average of q; parameter of the MH EoS
r	Right eigenvector
R	Specific gas constant
R_u	Universal gas constant
$\mathscr{R}$	Functioning regime
$\boldsymbol{R}$	Reflected shock
s_τ	Isentrope tangent to the $J = 0$ locus
$s_{\tau,1}$	Isentrope tangent to the $\Gamma = 1$ locus
$s_{\tau,0}$	Isentrope tangent to the $\Gamma = 0$ locus
s_{vle}	Isentrope tangent to the vapour-liquid saturation curve
S	Downstream state of double-sonic oblique shock
S$^+$	Downstream state of post-sonic oblique shock
S$^-$	Downstream state of pre-sonic oblique shock
T	Temperature
$\boldsymbol{T}$	Transmitted shock
$\boldsymbol{u}$	Velocity vector
u	Velocity magnitude
v	Specific volume
V	Volume
w	Conservative variables (scale-invariant form)
x	Streamwise coordinate (1D, Quasi-1D) or cartesian coordinate (2D)
y	Cartesian coordinate
y^+	Wall unit
z	Wave component of approximate source term

Greek alphabet

α	Nonlinearity factor; wave component of cell average difference
$\bar{\alpha}$	Parameter of the iPRSV EoS
β	Outlet pressure to upstream stagnation pressure ratio;
	wave component of numerical flux difference and source term contribution
β_c	Characteristic line angle w.r.t upstream flow direction
β_f	Equivalent-fan angle w.r.t upstream flow direction
β_g	Generalized wave angle w.r.t upstream flow direction
β_s	Shock angle w.r.t pre-shock flow direction

β_{ws}	Shock angle w.r.t pre-shock flow direction (weak oblique shock)
β_{ss}	Shock angle w.r.t pre-shock flow direction (strong oblique shock)
$\beta_{s,\text{sat}}$	Shock angle leading to post-shock saturated conditions
$\tilde{\beta}_s$	Shock angle of Mach number–preserving oblique shock
γ	Specific heats ratio
Γ	Fundamental derivative of gasdynamics
Γ_{min}	Minimum value of Γ in the vapour region
δ	Delta function
δ_λ	Entropy correction band
∂V	Volume surface
Δ	Shock thickness
ε	Ambient to reservoir pressure ratio
ϵ	Parameter of the MH EoS
ζ	Volume viscosity
ζ_S	Kinetic energy loss coefficient
ϑ	Flow direction angle
Θ	Flow deflection angle across oblique waves or ramp/wedge angle
κ	Parameter of the iPRSV EoS
κ_0	Parameter of the iPRSV EoS
κ_1	Parameter of the iPRSV EoS
λ	Eigenvalue
Λ	Dimensionless isentropic derivative of Γ w.r.t ρ
μ	Mach angle; shear viscosity
μ_t	Eddy viscosity
ν	Prandtl-Meyer function
ξ	Similarity variable (2D steady flow)
Π	Relative slope Rayleigh line/shock adiabat
ρ	Density
σ	Inverse reduced temperature
ψ	Source term
Ψ	Relative mass flux function w.r.t post-sonic shock mass flux; approximate source term
ω	Acentric factor

Superscripts

$\mathcal{H}$	Evaluation on the Hugoniot locus
t	Total or stagnation thermodynamic state
$\sim$	Roe average; Intermediate state for quasi-Jacobian linerization
$-$	Average value between neighbouring cells
$*$	Effective value for the entropy correction

Subscripts

0	Variable at a reference state; variable upstream of the turbine cascade
05	Variable at half axial chord downstream of the trailing edge
1	Variable downstream of the turbine cascade
A	Upstream or pre-shock state
B	Downstream or post-shock state
c	Thermodynamic variable at the critical point
d	Detachment condition

e	Variable at the nozzle exit section
j ± 1/2	Variable at the cell interface $j/j + 1$
l	Left state in the Riemann problem
n	Normal component
out	Mass flow averaged variable at the domain outlet
q	Gradient w.r.t the *q*-variables
r	Reservoir variable (nozzle flow); reduced thermodynamic variable; right state in the Riemann problem
s	Sonic point
S$^+$	Variables at downstream state of post-sonic oblique shock
SD	Variable at the sonic-shock disintegration locus
t	Tangential component
tr	Variables at the nozzle throat
x	*x*-component; *x*-Jacobian
y	*y*-component; *y*-Jacobian

Mathematical symbols

∇	Gradient
$\times$	Vector product
·	Scalar product
$\mathcal{O}$	Big O

Other symbols

[]	Jump across shock wave (from pre-shock to post-shock)

LIST OF FIGURES

LIST OF TABLES